INTELLIGENT DIAGNOSIS WITH ADVERSARIAL MACHINE LEARNING IN MULTIMODAL BIOMEDICAL BRAIN IMAGES

EDITED BY: Yuhui Zheng, Zexuan Ji, Heye Zhang and Jonathan Wu

PUBLISHED IN: Frontiers in Neuroinformatics

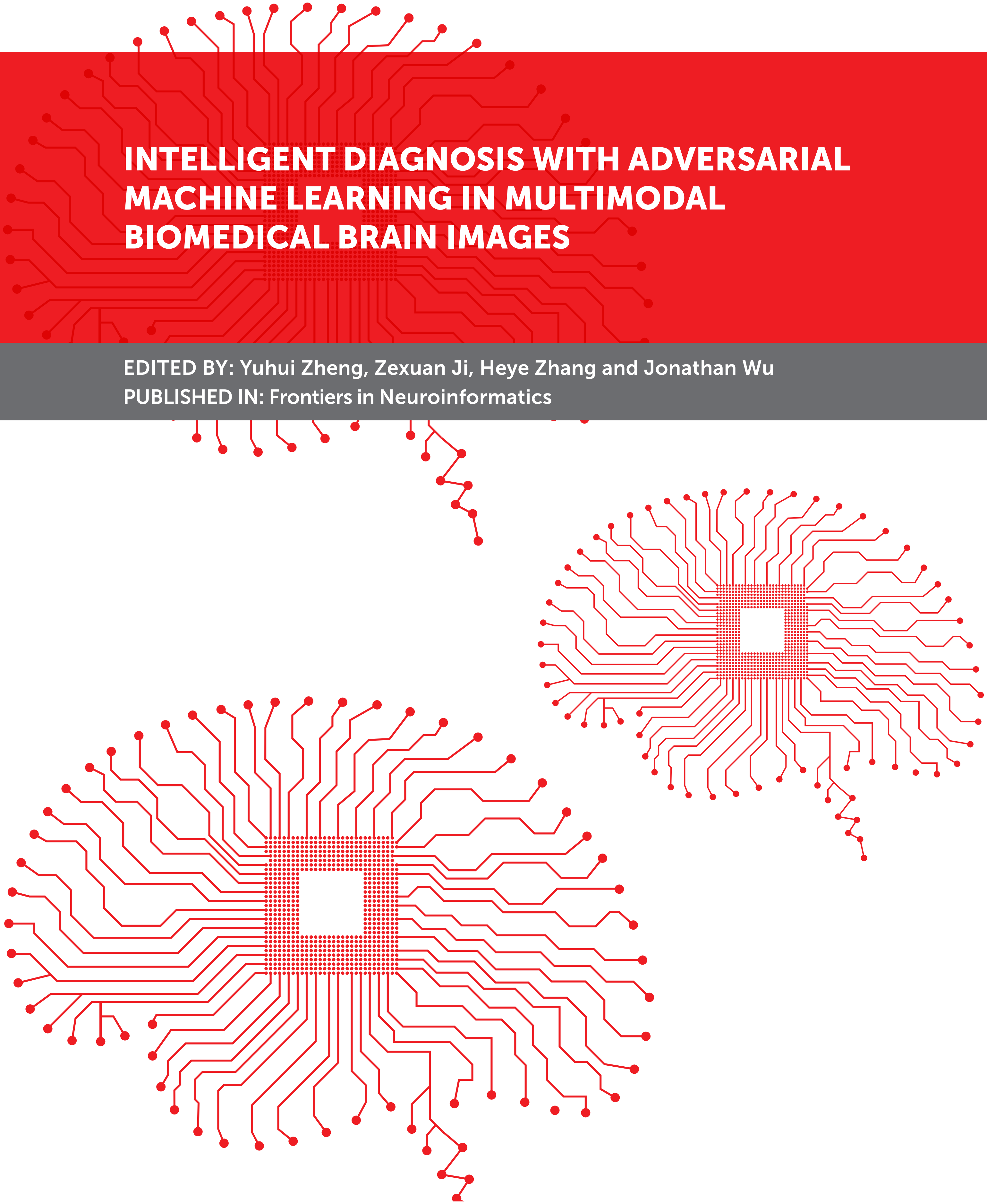

frontiers Research Topics

Frontiers eBook Copyright Statement

ISSN 1664-8714
ISBN 978-2-88971-349-3
DOI 10.3389/978-2-88971-349-3

About Frontiers

Frontiers is more than just an open-access publisher of scholarly articles: it is a pioneering approach to the world of academia, radically improving the way scholarly research is managed. The grand vision of Frontiers is a world where all people have an equal opportunity to seek, share and generate knowledge. Frontiers provides immediate and permanent online open access to all its publications, but this alone is not enough to realize our grand goals.

Frontiers Journal Series

The Frontiers Journal Series is a multi-tier and interdisciplinary set of open-access, online journals, promising a paradigm shift from the current review, selection and dissemination processes in academic publishing. All Frontiers journals are driven by researchers for researchers; therefore, they constitute a service to the scholarly community. At the same time, the Frontiers Journal Series operates on a revolutionary invention, the tiered publishing system, initially addressing specific communities of scholars, and gradually climbing up to broader public understanding, thus serving the interests of the lay society, too.

Dedication to Quality

Each Frontiers article is a landmark of the highest quality, thanks to genuinely collaborative interactions between authors and review editors, who include some of the world's best academicians. Research must be certified by peers before entering a stream of knowledge that may eventually reach the public - and shape society; therefore, Frontiers only applies the most rigorous and unbiased reviews.
Frontiers revolutionizes research publishing by freely delivering the most outstanding research, evaluated with no bias from both the academic and social point of view. By applying the most advanced information technologies, Frontiers is catapulting scholarly publishing into a new generation.

What are Frontiers Research Topics?

Frontiers Research Topics are very popular trademarks of the Frontiers Journals Series: they are collections of at least ten articles, all centered on a particular subject. With their unique mix of varied contributions from Original Research to Review Articles, Frontiers Research Topics unify the most influential researchers, the latest key findings and historical advances in a hot research area! Find out more on how to host your own Frontiers Research Topic or contribute to one as an author by contacting the Frontiers Office: frontiersin.org/about/contact

INTELLIGENT DIAGNOSIS WITH ADVERSARIAL MACHINE LEARNING IN MULTIMODAL BIOMEDICAL BRAIN IMAGES

Topic Editors:
Yuhui Zheng, Nanjing University of Information Science and Technology, China
Zexuan Ji, Nanjing University of Science and Technology, China
Heye Zhang, Sun Yat-sen University, China
Jonathan Wu, University of Windsor, Canada

Citation: Zheng, Y., Ji, Z., Zhang, H., Wu, J., eds. (2021). Intelligent Diagnosis With Adversarial Machine Learning in Multimodal Biomedical Brain Images. Lausanne: Frontiers Media SA. doi: 10.3389/978-2-88971-349-3

Table of Contents

frontiers in Neuroinformatics

ORIGINAL RESEARCH
published: 07 October 2020
doi: 10.3389/fninf.2020.00040

Classification of Schizophrenia by Functional Connectivity Strength Using Functional Near Infrared Spectroscopy

Jiayi Yang[1,2†], *Xiaoyu Ji*[1†], *Wenxiang Quan*[3†], *Yunshan Liu*[1,4], *Bowen Wei*[1,5] *and Tongning Wu*[1*]

[1]China Academy of Information and Communications Technology, Beijing, China, [2]Institute of Electrical Engineering, Chinese Academy of Sciences, Beijing, China, [3]Peking University Sixth Hospital, Peking University Institute of Mental Health, NHC Key Laboratory of Mental Health (Peking University), National Clinical Research Center for Mental Disorders (Peking University Sixth Hospital), Beijing, China, [4]School of Computer Science and Technology, Donghua University, Shanghai, China, [5]School of Computer Science and Technology, Xidian University, Xian, China

Functional near-infrared spectroscopy (fNIRS) has been widely employed in the objective diagnosis of patients with schizophrenia during a verbal fluency task (VFT). Most of the available methods depended on the time-domain features extracted from the data of single or multiple channels. The present study proposed an alternative method based on the functional connectivity strength (FCS) derived from an individual channel. The data measured 100 patients with schizophrenia and 100 healthy controls, who were used to train the classifiers and to evaluate their performance. Different classifiers were evaluated, and support machine vector achieved the best performance. In order to reduce the dimensional complexity of the feature domain, principal component analysis (PCA) was applied. The classification results by using an individual channel, a combination of several channels, and 52 ensemble channels with and without the dimensional reduced technique were compared. It provided a new approach to identify schizophrenia, improving the objective diagnosis of this mental disorder. FCS from three channels on the medial prefrontal and left ventrolateral prefrontal cortices rendered accuracy as high as 84.67%, sensitivity at 92.00%, and specificity at 70%. The neurophysiological significance of the change at these regions was consistence with the major syndromes of schizophrenia.

Keywords: functional near infrared spectroscopy (fNIRS), schizophrenia, functional connectivity strength (FCS), support machine vector, classification

Edited by:
Heye Zhang,
Sun Yat-sen University, China

Reviewed by:
Zicheng Liu,
Arctic University of Norway, Norway
Xi Cheng,
Télécom ParisTech, France

Correspondence:
Tongning Wu
wutongning@caict.ac.cn

† These authors have contributed equally to this work

Received: *02 June 2020*
Accepted: *22 July 2020*
Published: *07 October 2020*

Citation:
Yang J, Ji X, Quan W, Liu Y, Wei B and Wu T (2020) Classification of Schizophrenia by Functional Connectivity Strength Using Functional Near Infrared Spectroscopy. Front. Neuroinform. 14:40. doi: 10.3389/fninf.2020.00040

INTRODUCTION

Schizophrenia is a kind of psychiatric disorder characterized by a series of positive/psychotic (e.g., hallucinations and delusions), negative/deficit (e.g., insufficiency of thought and loss of motivation), and cognitive (e.g., impairment of memory and attention) symptoms (Buckley et al., 2009). Conventionally, clinical diagnostic criteria are predominately based on the relative subjective approaches, for example, according to the diagnostic manuals (American Psychiatric Association, 1994). With the development of neuroimaging, a number of objective methods to identify schizophrenia patients have emerged, e.g., single photon emission computed tomography (SPECT; Gordon et al., 1994), diffusion tensor imaging (DTI; Ohtani et al., 2014), functional magnetic resonance imaging (fMRI; Weiss et al., 2004; Deng et al., 2017; Tréhout et al., 2017), and functional near infrared spectroscopy (fNIRS; Kubota et al., 2005; Rosenbaum et al., 2017).

fNIRS is a noninvasive hemodynamic imaging technique used to assess functional activities in the human brain (Hoshi, 2003). It detects the concentration of oxygenated hemoglobin (Oxy-Hb) and deoxygenated hemoglobin (Deoxy-Hb) by measuring the absorption and reflection of specific near infrared spectrums in the cortices during tasks. Compared to other neuroimaging instruments, fNIRS has the benefit of being low cost with a high portability. These advantages have enabled its application in the diagnosis of schizophrenia, which was mainly based on the effect of hypofrontality (reduced activation around the bilateral prefrontal cortex) during various verbal fluency tasks (VFTs; Suto et al., 2004; Ehlis et al., 2007; Takizawa et al., 2008; Ji et al., 2020). In practice, the majority of these studies extracted the time-domain features from single or multiple channels of healthy subjects and patients with schizophrenia (Suto et al., 2004; Kanahara et al., 2013; Sugimura et al., 2014; Tian et al., 2019). As a consequence, diverse machine learning classifiers (Li et al., 2015) were trained and distinguished the patients with schizophrenia from the healthy subjects.

In contrast, substantial neuroimaging studies of other modalities have found abnormal dysconnectivity between the prefrontal cortex and temporal cortex in schizophrenia patients (Friston and Frith, 1995; Maguire et al., 2000; Greicius, 2008; Bullmore and Sporns, 2009; Whitfield-Gabrieli et al., 2009), and these experiments using EEG and fMRI have proposed classification methods based on brain network properties (Demirci et al., 2008; Yang et al., 2010; Arbabshirani et al., 2013). Nevertheless, the method on whole-brain network properties cannot be directly applied to fNIRS analysis because the conventional clinical fNIRS only measures signals from the frontotemporal cortex. One fNIRS study discriminated patients with schizophrenia using four global network properties (Song et al., 2016). The achieved overall accuracy was 85.5%, but the local changes could not be investigated with the approach. Hence, the analysis on regional functional connectivity (FC), integrating both the spatial and temporal relation of brain activities, is hypothesized to provide new insights on classifying schizophrenia.

In this article, we provided an FC-based method to identify schizophrenia patients. Oxy-Hb data from 100 schizophrenia patients and 100 healthy subjects during VFT were used in the experiment. functional connectivity strength (FCS) from single channel, from the ensemble 52 channels, from the dimensional reduced 52 channels, and from different combinations of 2–5 channels were used to trained four popular classifiers (Linear Discriminant Analysis: LDA, k-Nearest Neighbor: KNN, Gaussian Processes classifier: GPC, and Support Vector Machine: SVM), respectively. The best accuracy was 85.00% (LOOCV), with sensitivity as 87.00% (LOOCV) and specificity as 83.00% (LOOCV), by using FCS from three channels. Theneurophysiological significance was discussed. The FCS-based method provided a new and effective approach for schizophrenic identification.

MATERIALS AND METHODS

Subject

The Oxy-Hb dataset included 100 schizophrenic (male/female: 50/50, 33.81 ± 11.52 years old and ranging from 18 to 53 years old) and 100 healthy subjects (male/female: 47/53, 34.43 ± 12.36 years old and ranging by 18–78 years old) who were recruited from Peking University Sixth Hospital. The diagnosis for schizophrenia was based on DSM-IV and conducted by two clinical doctors. All subjects were native Chinese speakers and right-handed. This study was carried out in conformity with the Declaration of Helsinki and was sustained by the ethics committee of Peking University Sixth Hospital. All subjects provided written consent after being fully informed of the procedures in the study.

VFT Experiment

The experiment was conducted in a quiet room and no entry was permitted during the experiment. The Chinese VFT (Quan et al., 2015) was initiated by a 30-s pre-task baseline period, followed by a 60-s task period and a 30-s post-task baseline period (**Figure 1**). There was a screen 1 m in front of the participants. During the pre-task and post-task baseline periods, the participants were asked to stare at the center of the screen and count from 1 to 5. During the 60-s task period, three Chinese characters ("白," "天," and "大," indicating white, sky, and big, respectively) were displayed on the screen and changed every 20 s. The participants were instructed to produce as many phrases or four-character idioms starting with these characters as they could.

fNIRS Measurement and Data Preprocessing

The measurement was conducted using a 52-channel near infrared spectrometer (ETG-4000, Hitachi Medical Co., Japan). The instrument had 33 probes (17 emitters and 16 detectors; **Figure 2**). The positioning of the receivers emitters was referred to an international 10-20 system of Electroencephalography (Oostenveld and Praamstra, 2001). To specify, the detector between Channel #5 and #6 was located at Fz, the emitters close to #43 and #52 were fitted around T4 and T3, and #46 and #49 were placed in Fp2 and Fp1, respectively. The measurement area covered the bilateral prefrontal and temporal cortices (**Figure 2**). The separation between the channels was 3 cm. In the experiments, each subject was measured with 120 s (30 s pre-task baseline, 60 s VFT and 30 s post-task baseline) at a sampling rate of 10 Hz. Hence, there were 1,200 signal points for each channel per subject. The measured Oxy-Hb signal was organized as a matrix with 300 × 1,200 × 52 (number of subjects × signal points × amount of channels).

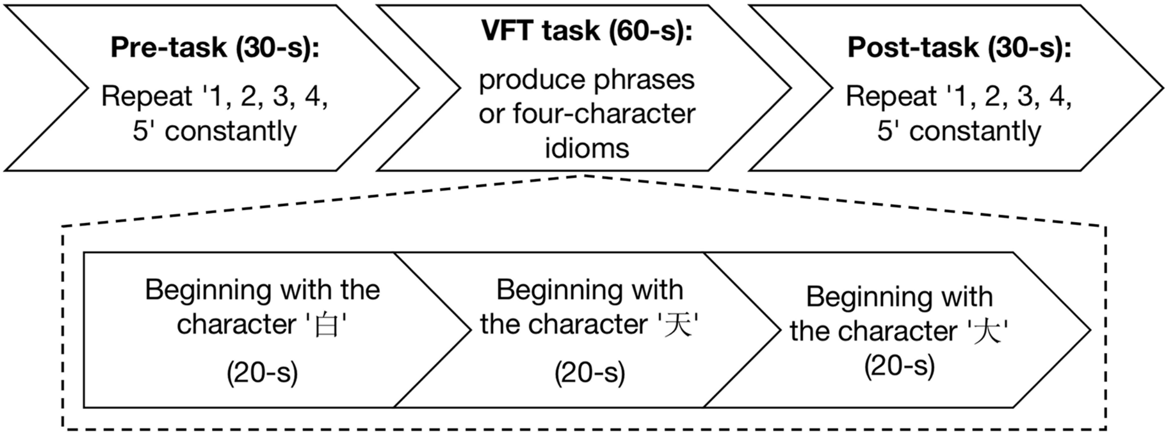

FIGURE 1 | Experimental flowchart. The experiment has three procedures: 30-s pre-task, 60-s verbal fluency task (VFT) task, and 30-s post-task.

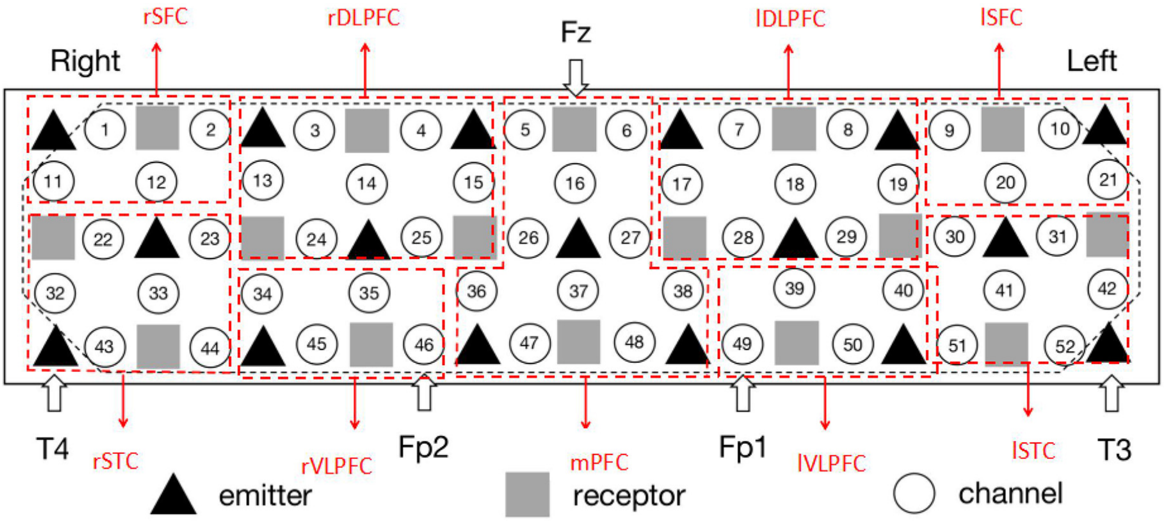

FIGURE 2 | The setting of functional near infrared spectroscopy (fNIRS) probe and channel. Hexagons stand for near-infrared light emitters, diamonds stand for near-infrared light receptors, and cycles stand for fNIRS channels. T3, T4, Fp1, Fp2, and Fz are the electrode positions in the international 10-20 system. rSFC, right superior frontal cortex; rSTC, right superior temporal cortex; rDLPFC, right dorsolateral prefrontal cortex; rVLPFC, right ventrolateral prefrontal cortex; mPFC, medial prefrontal cortex; lDLPFC, left dorsolateral prefrontal cortex; lVLPFC, left ventrolateral prefrontal cortex; lSFC, left superior frontal cortex; lSTC, left superior temporal cortex. The placement is in line with the configuration of Schecklmann et al. (2010).

The raw Oxy-Hb data were preprocessed through a band-pass filter of 0.009–0.08 Hz to remove the motion artifacts. The least square method was used to eliminate and remove the linear trend from the Oxy-Hb signals. MATLAB toolkit HomER2 (Huppert et al., 2009) was used to preprocess the original data.

Feature Extraction for Classification

The conventional classification methods usually utilized the time-domain features (for example, mean amplitude of Oxy-Hb during VFT). Frontal functional dysconnectivity is a salient feature of schizophrenia but it has not yet been applied for identifying schizophrenia. FCS was selected to characterize the effect and the following steps were used to obtain the value:

(1) Pearson's correlation among the data from 52 channels was calculated by:

$$r_{xy} = \frac{\sum x_i y_i - n\overline{xy}}{(n-1)S_x S_Y} \tag{1}$$

where $\overline{x}$, $\overline{y}$ are the mean, and S_x, S_y are the standard deviations of the measured data x_i and y_i, respectively; n is the number of the data.

(2) FCS was calculated by:

$$FCS = \frac{\sum_y r_{x,y}}{51} \quad (2)$$

As a consequence, 52 FCSs were derived *per* subject. We assessed the results from three kinds of approaches to identify schizophrenia.

- Single-feature: FCS from single channel
- Ensemble 52 FCSs: FCSs from 52 channels with or without dimensional reduction techniques
- Combine-features: FCS from the combination of several single-features

Four widely used classifiers in schizophrenic identification, LDA, GPC, KNN, and SVM, were trained and applied in the study. Since the details of these classifiers were extensively discussed previously (Mourão-Miranda et al., 2005; Yoon et al., 2007; Azechi et al., 2010; Tanaka and Katura, 2011; Dai et al., 2012; Arbabshirani et al., 2013; Hahn et al., 2013), we will not repeat them again. The MATLAB toolkits, GPML (v3.4[1]; Rasmussen and Nickisch, 2010), LIBSVM (v3.1.2[2], and LDA (V1.0.0.0[3]) were used in the analysis. KNN was realized by MATLAB function KNNCLASSIFY.

Note that the major parameters of these toolkits and functions used default or empirical values, with the exceptions of:

- KNN: $k = (100)^{1/2} = 10$; Euclidean distance is adopted to calculate the distances between the unlabeled sample and the labeled training samples. Traditionally, the Euclidean distance is appropriate when the issue included mutually correlated observations. As such, this distance needs to consider every variable and does not remove redundancies. The situation is very similar to our situation: the data from 52 channels are highly correlated and none can be simply removed. k is to set $k = \sqrt{n}$ The method has been proposed by Mitra et al. (2002);
- SVM: RBF kennel; C and gamma were optimized by automated grid search and evaluated *via* 10-fold cross-validation. The optimization was conducted per case and the best RBF factors were provided along with the results.

Evaluation of the Classification Performance

To evaluate the performance of the individual classifier, both leave-one-out cross-validation (LOOCV) and 10-fold/20-fold CV were used to estimate the performance of the classifier. The subjects involved in the experiments were schizophrenia patients (positive, P) and the healthy controls (negative, N). The true positive (TP) and the true negative (TN) are the number of patients and healthy people being correctly classified, respectively. The false positive (FP) is the number of healthy people being classified as patients. The false negative (FN) is the number of patients being classified as healthy people. The performance of the classification method was assessed in terms of accuracy, sensitivity, and specificity as shown in:

$$accuracy = \frac{TP + TN}{(TP + FP + FN + TN)} \quad (3)$$

$$sensitivity = \frac{TP}{(TP + FN)} \quad (4)$$

$$specificity = \frac{TN}{(FP + TN)} \quad (5)$$

RESULTS

FC Matrices

Figure 3 shows the waveform of Oxy-Hb from 52 channels. The results were averaged across the healthy control and schizophrenic group. The reduced Oxy-Hb during VFT was obvious in patients with schizophrenia, being consistent with previous literature. The derived FCs were mapped in **Figure 4**. It was revealed that functional connections with high intensity were observed in the healthy controls, indicating dysconnectivity of schizophrenia.

Classification Results

Single-FCS Results

The overall accuracy from the top five channels to identify schizophrenia is shown in **Figure 5** and is summarized in **Table 1**. LDA, KNN, and SVM demonstrated similar overall levels of accuracy, i.e., LDA: 72.50–81.00% (LOOCV), KNN: 78.00–82.00% (LOOCV), and SVM: 77.50–83.50% (LOOCV). GPC had the lowest accuracy at 67.00–69.50% (LOOCV). In terms of spatial distribution of the channels, although LDA, KNN, and SVM demonstrated laterality (left or right sidedness), in general, the best channels identified by these three classifiers were on the ventral part of the frontal cortices. In contrast, GPC utilized the FCS from the dorsal channels.

52-FCS Results

Figure 6 shows the 52-feature results from different classifiers. Again, GPC achieved the lowest results (accuracy at 51.00% (LOOCV), with sensitivity at 55.00% (LOOCV) and specificity at 47.0% (LOOCV)). The other three classifiers had similar performances whilst SVM slightly outperformed the other two. In summary, SVM achieved the best accuracy at 86.50% (LOOCV), sensitivity at 91.00% (LOOCV), and specificity at 82% (LOOCV). LDA had the best accuracy at 83.00% (LOOCV), sensitivity at 85.00% (LOOCV), and specificity at 81.00% (LOOCV). KNN yielded the best accuracy at 77.00% (LOOCV), sensitivity at 84.00% (LOOCV), and specificity at 70.00% (LOOCV). The performance of the classifiers initially increased with the numbers of channels but stabilized when more channels were taken into consideration. It may indicate the existence of redundancy in this feature space.

---

[1] http://www.gaussianprocess.org/gpml

[2] http://www.csie.ntu.edu.tw/∼cjlin/libsvm/

[3] https://ww2.mathworks.cn/matlabcentral/fileexchange/29673-lda-linear-discriminant-analysis

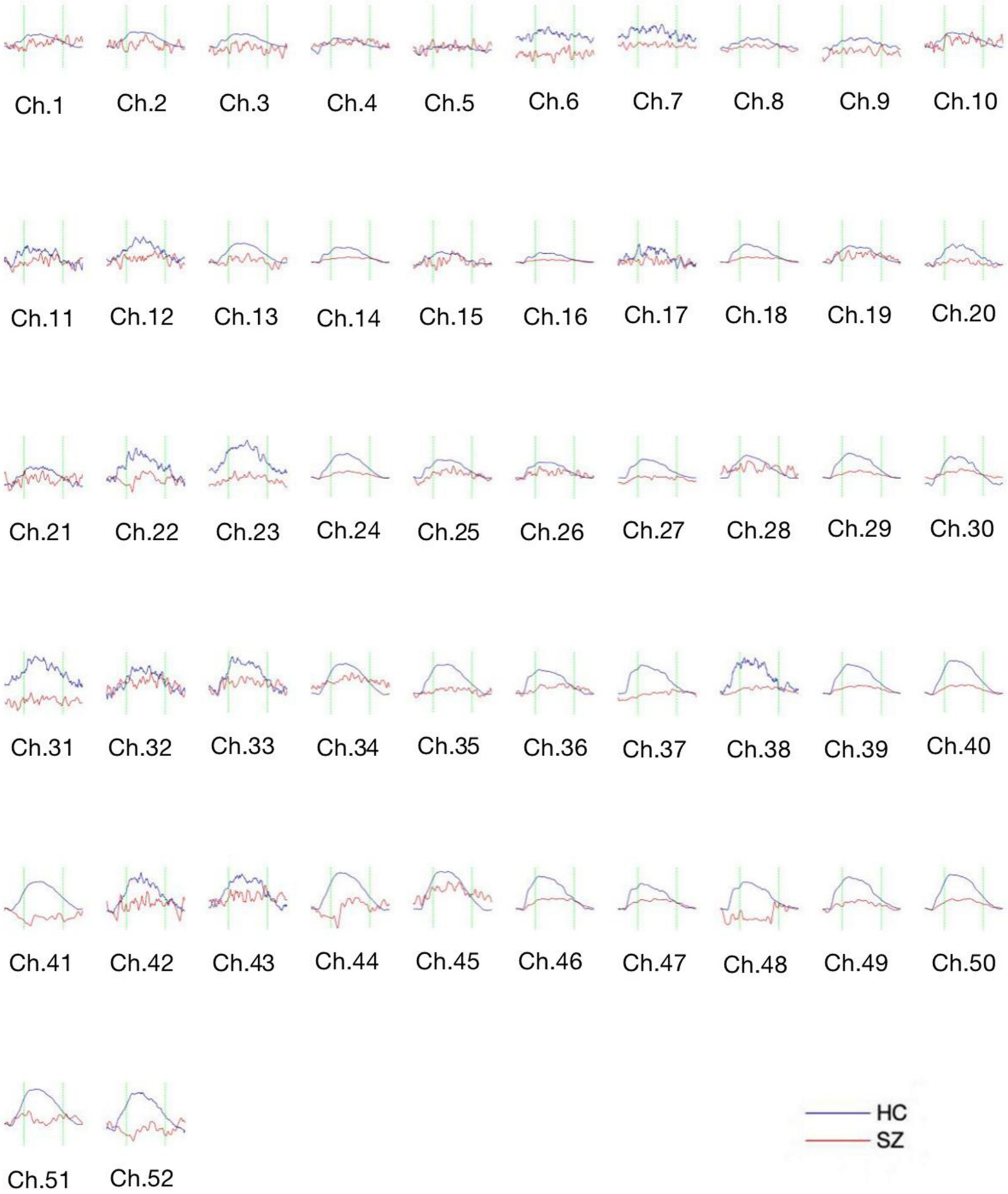

FIGURE 3 | The concentration curve of Oxy-Hb from 52 channels averaged from the healthy controls (blue lines) and the schizophrenic group (red lines). SZ, schizophrenic patients; HC, healthy controls.

Dimensional Reduced 52-FCS Results

Principal component analysis (PCA) can convert multiple observations of potentially correlated variables into a set of linearly independent components. It implemented singular value decomposition to reduce the dimensionality of a dataset that consisted of a large number of interrelated variables, while retaining as much variation present in the dataset as possible (Abdi and Williams, 2010). For comparison, we also used two other variants of PCA in the analysis: Kernel PCA and Sparse PCA. Kernel PCA uses various kernel functions to project datasets into a higher dimensional feature space, where it is linearly separable. We selected Gaussian kernel in this case.

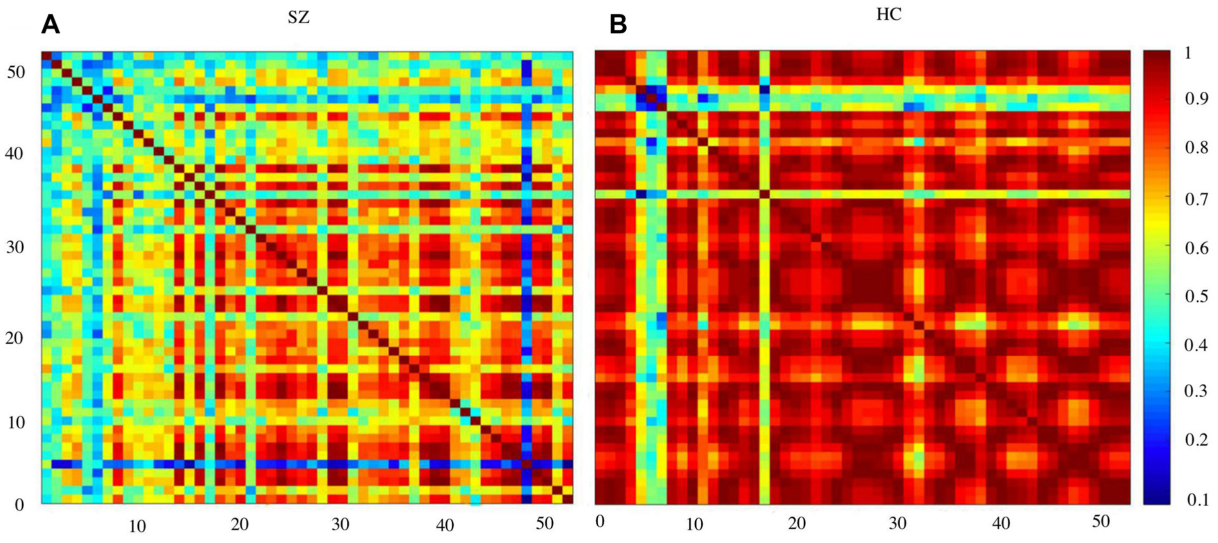

FIGURE 4 | Functional connectivity (FC) matrices averaged over schizophrenia group and healthy controls. SZ, schizophrenic patients **(A)**; HC, healthy controls **(B)**.

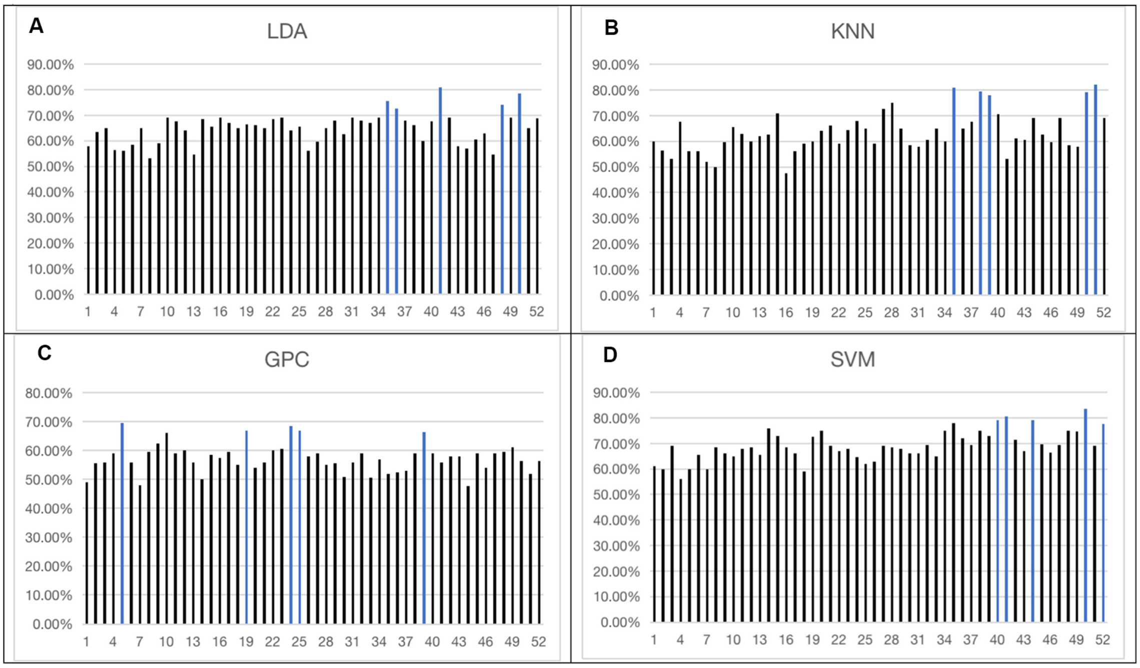

FIGURE 5 | Overall accuracy achieved by single-channel feature using four classifiers [LDA **(A)**, KNN **(B)**, GPC **(C)**, SVM **(D)**]. The top five channels were indicated by blue (the optimized C and gamma of the top five channels of SVM are shown in the **Supplementary Figures 1–5**). LDA, Linear Discriminant Analysis; KNN, k-Nearest Neighbor; GPC, Gaussian Processes classifier.

It was realized by MATLAB function KernelPca.m (Kitayama, 2020). Sparse PCA is implemented on the basis of the inverse power method for nonlinear eigenproblems, which is introduced in detail by Hein and Bühler (2010). Moreover, the deflation scheme proposed by Bühler (2015) is adopted to compute multiple principal components. It was realized by the free software sparsePCA developed by Matthias Hein and Thomas Bühler [Copyright 2010–2020 Thomas Bühler and Matthias Hein (hein@cs.uni-saarland.de). Machine Learning Group, Saarland University, Germany[4]].

---

[4] http://www.ml.uni-saarland.de

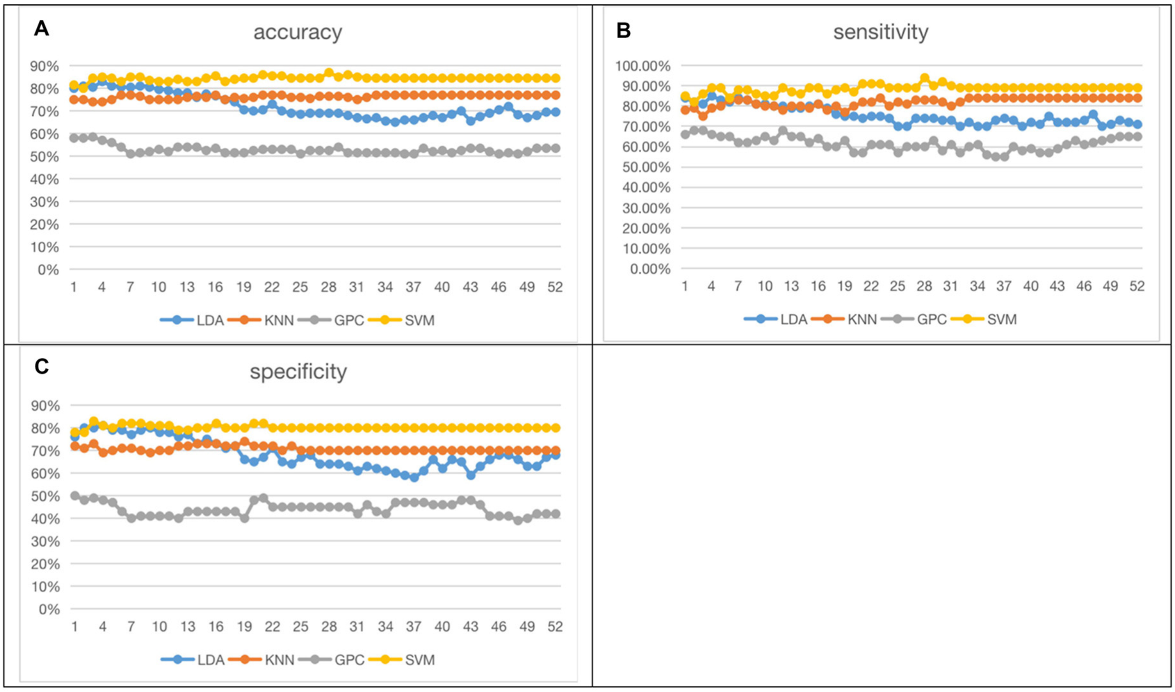

FIGURE 6 | Fifty-two functional connectivity strength (FCS) results [accuracy **(A)**, sensitivity **(B)**, specificity **(C)**; the optimized C and gamma of best accuracy as 86.50% of SVM are shown in **Supplementary Figure 6**].

TABLE 1 | Top five channels with functional connectivity strength (FCS) representing the best overall accuracy from the four classifiers (the optimized C and gamma of five channels of Support Vector Machine (SVM) are shown in **Supplementary Figures 1–5**).

LDA	Channel	Brain region	Accuracy
	#41	lSTC	81.00%
	#50	lVLPFC	78.50%
	#35	rVLPFC	75.50%
	#48	mPFC	74.00%
	#36	mPFC	72.50%
KNN			
	#51	lSTC	82.00%
	#35	rVLPFC	81.00%
	#38	mPFC	79.50%
	#50	lVLPFC	79.00%
	#39	lVLPFC	78.00%
GPC			
	#5	mPFC	69.50%
	#24	rDLPFC	68.50%
	#39	lVLPFC	66.50%
	#25	rDLPFC	67.00%
	#19	lDLPFC	67.00%
SVM			
	#50	lVLPFC	83.50%
	#41	lSTC	80.50%
	#40	lVLPFC	79.00%
	#44	rSTC	79.00%
	#52	lSTC	77.50%

We derived the first 21 principal components representing cumulative rates exceeding 93.4%. Classification based on the selected principal components is shown in **Table 2**. The results of 10-fold and 20-fold cross validation were provided for comparison.

Combined FCS Results

Further effort was made to assess the capability of schizophrenic identification using a certain combination of the channels. Since SVM yielded the best overall accuracy, the experiments were conducted only using this classifier. FCSs from 2, 3, 4, and 5 channels were selected from the five channels presenting the top capability on schizophrenic identification (presented in **Figure 5**). The results are shown in **Table 3**. Classification using FCS from three channels can achieve accuracy at 85.00% (LOOCV), sensitivity at 87.00% (LOOCV), and specificity at 83.00% (LOOCV).

DISCUSSIONS

Schizophrenia has been considered a disorder of connectivity between various brain units (Elvevåg and Goldberg, 2000). The connections were found to be reduced by schizophrenia, as shown in **Figure 4**. This finding was consistent with studies using other imaging modalities (Bellani et al., 2010; Deng et al., 2017).

FCS measures the connectivity across different brain units, so as to identify the hubs playing important roles in information processing and communication during cognitive tasks (van den Heuvel and Sporns, 2013; Mears and Pollard, 2016). As shown in **Table 1**, the capability of discriminating schizophrenia was evident for the FCS at VLPFC and mPFC. mPFC relates

TABLE 2 | Classification performance of leave-one-out cross-validation (LOOCV), 10-fold, and 20-fold by using three dimensionality reduction methods (the optimized C and gamma of SVM are shown in **Supplementary Figures 7–15**).

		LOOCV	10-fold	20-fold
LDA	Accuracy (PCA KernelPCA SparsePCA)	80.50% 80.00% 82.00%	79.00% 80.50% 80.50%	81.50% 82.00% 82.50%
	Sensitivity (PCA KernelPCA SparsePCA)	82.00% 81.00% 83.00%	81.00% 82.00% 83.00%	83.00% 84.00% 83.00%
	Specificity (PCA KernelPCA SparsePCA)	79.00% 79.00% 81.00%	77.00% 79.00% 78.00%	80.00% 80.00% 82.00%
KNN	Accuracy (PCA KernelPCA SparsePCA)	79.00% 82.00% 79.50%	80.50% 80.50% 82.00%	80.00% 81.00% 80.50%
	Sensitivity (PCA KernelPCA SparsePCA)	82.00% 83.00% 81.00%	81.00% 82.00% 84.00%	82.00% 83.00% 81.00%
	Specificity (PCA KernelPCA SparsePCA)	76.00% 81.00% 78.00%	80.00% 79.00% 80.00%	78.00% 79.00% 80.00%
GPC	Accuracy (PCA KernelPCA SparsePCA)	72.00% 73.50% 75.00%	68.50% 70.00% 70.50%	70.00% 71.50% 70.50%
	Sensitivity (PCA KernelPCA SparsePCA)	73.00% 75.00% 77.00%	70.00% 72.00% 72.00%	72.00% 73.00% 72.00%
	Specificity (PCA KernelPCA SparsePCA)	71.00% 72.00% 73.00%	67.00% 68.00% 70.00%	68.00% 70.00% 69.00%
SVM	Accuracy (PCA KernelPCA SparsePCA)	87.50% 89.00% 88.00%	85.50% 87.00% 88.50%	87.50% 86.00% 89.50%
	Sensitivity (PCA KernelPCA SparsePCA)	89.00% 90.00% 89.00%	86.00% 88.00% 89.00%	86.00% 87.00% 90.00%
	Specificity (PCA KernelPCA SparsePCA)	86.00% 88.00% 87.00%	85.00% 86.00% 88.00%	89.00% 85.00% 89.00%

TABLE 3 | Overall accuracy of different combinations of FCS using SVM (the optimized C and gamma are shown in **Supplementary Figures 16–41**).

Selection of the channels					Accuracy	Sensitivity	Specificity
#40	**#41**	**#44**	**#50**	**#52**			
x	x				82.00%	84.00%	80%
x		x			81.50%	82.00%	81%
x			x		80.50%	82.00%	79%
x				x	83.00%	85.00%	81%
	x	x			78.50%	79.00%	78%
	x		x		82.00%	83.00%	79%
	x			x	83.00%	83.00%	83%
		x	x		79.00%	80.00%	78%
		x		x	80.50%	81.00%	80%
			x	x	83.50%	85.00%	82%
x	x	x			81.50%	83.00%	80%
x	x		x		85.00%	87.00%	83%
x	x			x	84.00%	86.00%	82%
x		x	x		82.00%	82.00%	80%
x			x	x	84.50%	85.00%	84%
x		x		x	83.00%	85.00%	81%
	x	x	x		80.00%	82.00%	78%
	x	x		x	79.50%	81.00%	78%
	x		x	x	80.00%	81.00%	79%
		x	x	x	81.00%	84.00%	78%
x	x	x	x		83.50%	86.00%	81%
x	x	x		x	83.00%	84.00%	82%
x	x		x	x	84.50%	85.00%	84%
x		x	x	x	82.00%	85.00%	79%
	x	x	x	x	83.00%	84.00%	82%
x	x	x	x	x	84.50%	86.00%	83%

to decision making and short- and long-term memory (Euston et al., 2012), and coordinates VLPFC and DLPFC functions (Peng et al., 2018). The neurophysiological functions of this cortex are associated with the symptoms of schizophrenia. The left VLPFC associates with the production of articulate language and in nonlinguistic tasks (Hickok and Poeppel, 2004, 2007), while the right VLPFC plays a role in linking working memory with episodic memory and in a series of complicated social behaviors (He et al., 2020). The reduced FCS of VLPFC in patients with schizophrenia may relate to the impairment of both verbal skills and social functions, which are the major symptoms of schizophrenia. In contrast, some channels were at STC, which mediates spatial awareness and exploration (Karnath, 2001). To summarize, these changes during VFT corresponded to the perturbed performance of schizophrenia patients (difficulty or incapability to produce four-character idioms).

PCA reduced the dimension of the feature space and saved the computational cost, while achieving satisfactory accuracy. The disadvantage of PCA was that the principle components could not be attributed to the data from the specific channel, thus concealing the regional neurophysiological changes. Using the FCS from three channels, the achieved performance was comparable to the current results: accuracy at 70–86%, sensitivity at 70–84%, and specificity at 65–93% (Arbabshirani et al., 2013; Chuang et al., 2014; Li et al., 2015; Pina-Camacho et al., 2015;

Song et al., 2017). The method was not calculated from the time-domain values on single or multiple channels. It means that reliable results could be provided when integrated with the time-domain approaches.

There are some limitations to the present study. First, the individual schizophrenic episode was not identified and taken into analysis. However, it may have implications on the effected sites (Zhu et al., 2010). Second, the patients receiving medications and physical treatment were not ruled out from the study. Although previous studies have revealed a negligible medication effect on fNIRS signals, investigations of drug-free patients or of those receiving physical treatment (e.g., transcranial magnetic stimulation, electroconvulsive therapy, and neurofeedback) will be needed to allow further clinical applications of fNIRS (Fujita et al., 2011; Mihara et al., 2012; Monden et al., 2012). Third, educational background may have an impact on language ability. In our study, we did not categorize the subjects into more educational background groups because the number of subjects in each group would be sparse. But the two groups matched their educational backgrounds (the schizophrenia group included 14 graduate degrees, 20 undergraduate degrees, 20 college degrees, 31 senior high school degrees, and 15 junior high school degrees, and the healthy group included 15 graduate degrees, 20 undergraduate degrees, 20 college degrees, 30 high school degrees, and 15 junior high school degrees). Lastly, only three machine-learning classifiers, LDA, KNN, and SVM, were used in the study because they were the most popular machine-learning classifiers in discriminating patients with schizophrenia. The comparison of their performance was a topic being widely discussed while the individual performance seemed to be signal- and feature-dependent (Mourão-Miranda et al., 2005; Hahn et al., 2013; Li et al., 2015). In the present study, we conducted a similar comparison. Other classifiers, such as artificial neural networking, has not yet been applied but theoretically could be utilized in the identification of schizophrenia (Zheng et al., 2019a,b, 2020). We will try it in our future study.

CONCLUSION

The study proposed an FCS-based method to identify patients with schizophrenia. 52-channel Oxy-Hb data of fronto-temporal fNIRS were obtained during VFT from healthy and schizophrenic subjects. The FCS of each channel was calculated as features for classification. We investigated the performance of different classifiers, from FCS of all the 52 channels or from several channels. The method was in sharp contrast to most previous studies using the time-average data obtained from multiple channels. The classification results were comparable to the existing results. In addition, the method can detect the changes of hubs during VFT, which was in consistency with the symptoms of schizophrenia.

DATA AVAILABILITY STATEMENT

The datasets presented in this article are not readily available because dataset are strictly restricted to non-commercial uses. Requests to access the datasets should be directed to wutongning@caict.ac.cn.

ETHICS STATEMENT

The studies involving human participants were reviewed and approved by the ethics committee of Peking University Sixth Hospital. The patients/participants provided their written informed consent to participate in this study.

AUTHOR CONTRIBUTIONS

TW conceptualized the experiments and supervised their implementation. JY and XJ contributed code to the project. WQ contributed to data acquisition. YL and BW validated the results and visualized them. XJ wrote the first version of the manuscript with input from JY and TN. TW and JY wrote the final version of the manuscript.

FUNDING

This study was supported by grants from the National Natural Science Foundation Project (No. 61971445), the National Key Research and Development Program of China (Nos. 2018YFC1314200 and 2019YFF0216302), and the National Science and Technology Major Project (No. 2018ZX10301201).

SUPPLEMENTARY MATERIAL

The Supplementary Material for this article can be found online at: https://www.frontiersin.org/articles/10.3389/fninf.2020.00040/full#supplementary-material.

REFERENCES

Abdi, H., and Williams, L. J. (2010). Principal component analysis. *Wiley Interdiscip. Rev. Comput. Stat.* 2, 433–450. doi: 10.1002/wics.101

American Psychiatric Association. (1994). *Diagnostic and Statistical Manual of Mental Disorders*, Washington DC: American Psychiatric Association.

Arbabshirani, M. R., Kiehl, K. A., Pearlson, G. D., and Calhoun, V. D. (2013). Classification of schizophrenia patients based on resting-state functional network connectivity. *Front. Neurosci.* 7:133. doi: 10.3389/fnins.2013.00133

Azechi, M., Iwase, M., Ikezawa, K., Takahashi, H., Canuet, L., Kurimoto, R., et al. (2010). Discriminant analysis in schizophrenia and healthy subjects using prefrontal activation during frontal lobe tasks: a near-infrared spectroscopy. *Schizophr. Res.* 117, 52–60. doi: 10.1016/j.schres.2009.10.003

Bellani, M., Cerruti, S., and Brambilla, P. (2010). Orbitofrontal cortex abnormalities in schizophrenia. *Epidemiol. Psichiatr. Soc.* 19, 23–25. doi: 10.1017/s1121189x00001561

Buckley, P. F., Miller, B. J., Lehrer, D. S., and Castle, D. J. (2009). Psychiatric comorbidities and schizophrenia. *Schizophr. Bull.* 35, 383–402. doi: 10.1093/schbul/sbn135

Bühler, T. (2015). *A Flexible Framework for Solving Constrained Ratio Problems in Machine Learning.* Germany: Saarland University. Ph.D. Thesis. Available online at: http://scidok.sulb.uni-saarland.de/volltexte/2015/6159/.

Bullmore, E., and Sporns, O. (2009). Complex brain networks: graph theoretical analysis of structural and functional systems. *Nat. Rev. Neurosci.* 10, 186–198. doi: 10.1038/nrn2575

Chuang, C. C., Nakagome, K., Pu, S., Lan, T. H., Lee, C. Y., and Sun, C. W. (2014). Discriminant analysis of functional optical topography for schizophrenia diagnosis. *J. Biomed. Opt.* 19:011006. doi: 10.1117/1.jbo.19.1.011006

Dai, D., Wang, J., Hua, J., and He, H. (2012). Classification of ADHD children through multimodal magnetic resonance imaging. *Front. Syst. Neurosci.* 6:63. doi: 10.3389/fnsys.2012.00063

Demirci, O., Clark, V. P., and Calhoun, V. D. (2008). A projection pursuit algorithm to classify individuals using fMRI data: application to schizophrenia. *NeuroImage* 39, 1774–1782. doi: 10.1016/j.neuroimage.2007.10.012

Deng, S. P., Hu, W., Calhoun, V. D., and Wang, Y.-P. (2017). Integrating imaging genomic data in the quest for biomarkers for schizophrenia disease. *IEEE/ACM Trans. Comput. Biol. Bioinform.* 15, 1480–1491. doi: 10.1109/TCBB.2017.2748944

Ehlis, A. C., Herrmann, M. J., Plichta, M. M., and Fallgatter, A. J. (2007). Cortical activation during two verbal fluency tasks in schizophrenic patients and healthy controls as assessed by multi-channel near-infrared spectroscopy. *Psychiatry Res.* 156, 1–13. doi: 10.1016/j.pscychresns.2006.11.007

Elvevåg, B., and Goldberg, T. E. (2000). Cognitive impairment in schizophrenia is the core of the disorder. *Crit. Rev. Neurobiol.* 14, 1–21. doi: 10.1615/critrevneurobiol.v14.i1.10

Euston, D., Gruber, A., and McNaughton, B. (2012). The role of medial prefrontal cortex in memory and decision making. *Neuron* 76, 1057–1070. doi: 10.1016/j.neuron.2012.12.002

Friston, K. J., and Frith, C. D. (1995). Schizophrenia: a disconnection syndrome. *J. Clin. Neurosci.* 3, 89–97.

Fujita, Y., Takebayashi, M., Hisaoka, K., Tsuchioka, M., Morinobu, S., and Yamawaki, S. (2011). Asymmetric alternation of the hemodynamic response at the prefrontal cortex in patients with schizophrenia during electroconvulsive therapy: a near-infrared spectroscopy study. *Brain Res.* 1410, 132–140. doi: 10.1016/j.brainres.2011.06.052

Gordon, E., Barry, R. J., Anderson, J., Fawdry, R., Yong, C., Grunewald, S., et al. (1994). Single photon emission computed tomography (SPECT) measures of brain function in schizophrenia. *Aust. N. Z. J. Psychiatry* 28, 446–452. doi: 10.3109/00048679409075872

Greicius, M. (2008). Resting-state functional connectivity in neuropsychiatric disorders. *Curr. Opin. Neurol.* 21, 424–430. doi: 10.1097/WCO.0b013e328306f2c5

Hahn, T., Marquand, A. F., Plichta, M. M., Ehlis, A. C., Schecklmann, M. W., Dresler, T., et al. (2013). A novel approach to probabilistic biomarker-based classification using functional near-infrared spectroscopy. *Hum. Brain Mapp.* 34, 1102–1114. doi: 10.1002/hbm.21497

He, Z., Zhao, J., Shen, J., Muhlert, N., Elliott, R., and Zhang, D. (2020). The right VLPFC and downregulation of social pain: a TMS study. *Hum. Brain Mapp.* 41, 1362–1371. doi: 10.1002/hbm.24881

Hein, M., and Bühler, T. (2010). "An inverse power method for nonlinear eigenproblems with applications in 1-spectral clustering and sparse PCA," in *Advances in Neural Information Processing Systems 23 (NIPS 2010), Neural Information Processing Systems Conference*, 847–855.

Hickok, G., and Poeppel, D. (2004). Dorsal and ventral streams: a framework for understanding aspects of the functional anatomy of language. *Cognition* 92, 67–99. doi: 10.1016/j.cognition.2003.10.011

Hickok, G., and Poeppel, D. (2007). The cortical organization of speech processing. *Nat. Rev. Neurosci.* 8, 393–402. doi: 10.1038/nrn2113

Hoshi, Y. (2003). Functional near-infrared optical imaging: utility and limitations in human brain mapping. *Psychophysiology* 40, 511–520. doi: 10.1111/1469-8986.00053

Huppert, T. J., Diamond, S. G., Franceschini, M. A., and Boas, D. A. (2009). HomER: a review of time-series analysis methods for near-infrared spectroscopy of the brain. *Appl. Opt.* 48, D280–D298. doi: 10.1364/ao.48.00d280

Ji, X. Y., Quan, W. X., Yang, L., Chen, J., Wang, J. J., and Wu, T. N. (2020). Classification of schizophrenia by seed-based functional connectivity using prefronto-temporal functional near infrared spectroscopy. *J. Neurosci. Meth.* 344. doi: 10.1016/j.jneumeth.2020.108874

Kanahara, N., Sekine, Y., Haraguchi, T., Uchida, Y., Hashimoto, K., Shimizu, E., et al. (2013). Orbitofrontal cortex abnormality and deficit schizophrenia. *Schizophr. Res.* 143, 246–252. doi: 10.1016/j.schres.2012.11.015

Karnath, H. O. (2001). New insights into the functions of the superior temporal cortex. *Nat. Rev. Neurosci.* 2, 568–576. doi: 10.1038/35086057

Kitayama, M. (2020). *MATLAB-Kernel-PCA*. GitHub. Available online at: https://github.com/kitayama1234/MATLAB-Kernel-PCA. Accessed July 9, 2020.

Kubota, Y., Toichi, M., Shimizu, M., Mason, R. A., Coconcea, C. M., Findling, R. L., et al. (2005). Prefrontal activation during verbal fluency tests in schizophrenia—a near-infrared spectroscopy (NIRS) study. *Schizophr. Res.* 77, 65–73. doi: 10.1016/j.schres.2005.01.007

Li, Z., Wang, Y., Quan, W., Wu, T., and Lv, B. (2015). Evaluation of different classification methods for the diagnosis of schizophrenia based on functional near-infrared spectroscopy. *J. Neurosci. Methods* 241, 101–110. doi: 10.1016/j.jneumeth.2014.12.020

Maguire, E. A., Gadian, D. G., Johnsrude, I. S., Good, C. D., Ashburner, J., Frackowiak, R. S. J., et al. (2000). Navigation-related structural change in the hippocampi of taxi drivers. *Proc. Natl. Acad. Sci. U S A* 97, 4398–4403. doi: 10.1073/pnas.070039597

Mears, D., and Pollard, H. B. (2016). Network science and the human brain: using graph theory to understand the brain and one of its hubs, the amygdala, in health and disease. *J. Neurosci. Res.* 94, 590–605. doi: 10.1002/jnr.23705

Mihara, M., Miyai, I., Hattori, N., Hatakenaka, M., Yagura, H., Kawano, T., et al. (2012). Neurofeedback using real-time near-infrared spectroscopy enhances motor imagery related cortical activation. *PLoS One* 7:e32234. doi: 10.1371/journal.pone.0032234

Mitra, P., Murthy, C. A., and Pal, S. K. (2002). Unsupervised feature selection using feature similarity. *IEEE Trans. Pattern Anal. Mach. Intell.* 24, 301–312. doi: 10.1109/34.990133

Monden, Y., Dan, H., Nagashima, M., Dan, I., Kyutoku, Y., Okamoto, M., et al. (2012). Clinically-oriented monitoring of acute effects of methylphenidate on cerebral hemodynamics in ADHD children using fNIRS. *Clin. Neurophysiol.* 123, 1147–1157. doi: 10.1016/j.clinph.2011.10.006

Mourão-Miranda, J., Bokde, A. L., Born, C., Hampel, H., and Stetter, M. (2005). Classifying brain states and determining the discriminating activation patterns: support vector machine on functional MRI data. *NeuroImage* 28, 980–995. doi: 10.1016/j.neuroimage.2005.06.070

Ohtani, T., Bouix, S., Hosokawa, T., Saito, Y., Eckbo, R., Ballinger, T., et al. (2014). Abnormalities in white matter connections between orbitofrontal cortex and anterior cingulate cortex and their associations with negative symptoms in schizophrenia: a DTI study. *Schizophr. Res.* 157, 190–197. doi: 10.1016/j.schres.2014.05.016

Oostenveld, R., and Praamstra, P. (2001). The five percent electrode system for high-resolution EEG and ERP measurements. *Clin. Neurophysiol.* 112, 713–719. doi: 10.1016/s1388-2457(00)00527-7

Peng, K., Steele, S. C., Becerra, L., and Borsook, D. (2018). Brodmann area 10: collating, integrating and high level processing of nociception and pain. *Prog. Neurobiol.* 161, 1–22. doi: 10.1016/j.pneurobio.2017.11.004

Pina-Camacho, L., Prieto, J. G., Parellada, M., Castro-Fornieles, J., Gonzalez-Pinto, A. M., Bombin, I., et al. (2015). Predictors of schizophrenia spectrum disorders in early-onset first episodes of psychosis: a support vector machine model. *J. Eur. Child Adolesc. Psychiatry* 24, 427–440. doi: 10.1007/s00787-014-0593-0

Quan, W., Wu, T., Li, Z., Wang, Y., Dong, W., and Lv, B. (2015). Reduced prefrontal activation during a verbal fluency task in Chinese-speaking patients with schizophrenia as measured by near-infrared spectroscopy. *Prog. Neuropsychopharmacol. Biol. Psychiatry* 58, 51–58. doi: 10.1016/j.pnpbp.2014.12.005

Rasmussen, C. E., and Nickisch, H. (2010). Gaussian processes for machine learning (GPML) toolbox. *J. Mach. Learn. Res.* 11, 3011–3015. doi: 10.1115/1.4002474

Rosenbaum, D., Haipt, A., Fuhr, K., Haeussinger, F. B., Metzger, F. G., Nuerk, H.-C., et al. (2017). Aberrant functional connectivity in depression as an index of state and trait rumination. *Sci. Rep.* 7:2174. doi: 10.1038/s41598-017-02277-z

Schecklmann, M., Romanos, M., and Bretscher, F. (2010). Prefrontal oxygenation during working memory in ADHD. *J. Psychiatr. Res.* 44, 621–628. doi: 10.1016/j.jpsychires.2009.11.018

Song, H., Bogdan, I. I. M., Wang, S., Dong, W., Quan, W., Dang, W., et al. (2016). "Automatic schizophrenia discrimination on fNIRS by using PCA and SVM," in *Proceedings of the 2016 IEEE International Conference on Bioinformatics and Biomedicine (BIBM)*, (Shenzhen, China: IEEE), 389–394.

Song, H., Chen, L., Gao, R. Q., Mihaita Bogdan, I. I., Yang, J., Wang, S., et al. (2017). Automatic schizophrenic discrimination on fNIRS by using complex brain network analysis and SVM. *BMC Med. Inform. Decis. Mak.* 17:166. doi: 10.1186/s12911-017-0559-5

Sugimura, Y., Watanabe, K., Ogawa, S., Kodama, T., Takeshita, M., Noda, T., et al. (2014). A discriminant model of mental disorders based on wave form patterns obtained by multi-channel near-infrared spectroscopy. *Rinsho Byori* 62, 147–152.

Suto, T., Fukuda, M., Ito, M., Uehara, T., and Mikuni, M. (2004). Multichannel near- infrared spectroscopy in depression and schizophrenia: cognitive brain activation study. *Biol. Psychiatry* 55, 501–511. doi: 10.1016/j.biopsych.2003.09.008

Takizawa, R., Kasai, K., Kawakubo, Y., Marumo, K., Kawasaki, S., Yamasue, H., et al. (2008). Reduced frontopolar activation during verbal fluency task in schizophrenia: a multi-channel near-infrared spectroscopy study. *Schizophr. Res.* 99, 250–262. doi: 10.1016/j.schres.2007.10.025

Tanaka, H., and Katura, T. (2011). Classification of change detection and change blindness from near-infrared spectroscopy signals. *J. Biomed. Opt.* 16:087001. doi: 10.1117/1.3606494

Tian, J., Wang, J., Quan, W., Lv, B., Liu, J., Hobbie, C., et al. (2019). The functional near-infrared spectroscopy in the diagnosis of schizophrenia. *Eur. J. Psychiatry* 33, 97–103. doi: 10.1016/j.ejpsy.2019.05.001

Tréhout, M., Leroux, E., Delcroix, N., and Dollfus, S. (2017). Relationships between corpus callosum and language lateralization in patients with schizophrenia and bipolar disorders. *Bipolar Disord.* 19, 496–504. doi: 10.1111/bdi.12526

van den Heuvel, M. P., and Sporns, O. (2013). An anatomical substrate for integration among functional networks in human cortex. *J. Neurosci.* 33, 14489–14500. doi: 10.1523/JNEUROSCI.2128-13.2013

Weiss, E. M., Hofer, A., Golaszewski, S., Siedentopf, C., Brinkhoff, C., Kremser, C., et al. (2004). Brain activation patterns during a verbal fluency test—a functional MRI study in healthy volunteers and patients with schizophrenia. *Schizophr. Res.* 70, 287–291. doi: 10.1016/j.schres.2004.01.010

Whitfield-Gabrieli, S., Thermenos, H. W., Milanovic, S., Tsuang, M. T., Faraone, S. V., McCarley, R. W., et al. (2009). Hyperactivity and hyperconnectivity of the default network in schizophrenia and in first-degree relatives of persons with schizophrenia. *Proc. Natl. Acad. Sci. U S A* 106, 1279–1284. doi: 10.1073/pnas.0809141106

Yang, H., Liu, J., Sui, J., Pearlson, G., and Calhoun, V. D. (2010). A hybrid machine learning method for fusing fMRI and genetic data: combining both improves classification of schizophrenia. *Front. Hum. Neurosci.* 4:192. doi: 10.3389/fnhum.2010.00192

Yoon, U., Lee, J.-M., Im, K., Shin, Y.-W., Cho, B. H., Kim, I. Y., et al. (2007). Pattern classification using principal components of cortical thickness and its discriminative pattern in schizophrenia. *NeuroImage* 34, 1405–1415. doi: 10.1016/j.neuroimage.2006.11.021

Zheng, Y. H., Song, H. H., Zhang, K. H., Zhang, K., Fan, J., and Liu, X. (2020). Dynamically spatio-temporal regularized correlation tracking. *IEEE Trans. Neural Netw. Learn. Syst.* 31, 2336–2347. doi: 10.1109/TNNLS.2019.2929407

Zheng, Y. H., Sun, L., Wang, S. F., Zhang, J., and Ning, J. (2019a). Spatially regularized structural support vector machine for robust visual tracking. *IEEE Trans. Neural Netw. Learn. Syst.* 30, 3024–3034. doi: 10.1109/TNNLS.2018.2855686

Zheng, Y. H., Wang, X. L., Zhang, G. Q., Xiao, B. H., Xiao, F., and Zhang, J. W. (2019b). Multi-kernel coupled projections for domain adaptive dictionary learning. *IEEE Trans. Mult.* 21, 2292–2304. doi: 10.1109/tmm.2019.2900166

Zhu, Y., Liu, X., Wang, H., Jiang, T., Fang, Y., Hu, H., et al. (2010). Reduced prefrontal activation during tower of London in first-episode schizophrenia: a multi-channel near-infrared spectroscopy study. *Neurosci. Lett.* 478, 136–140. doi: 10.1016/j.neulet.2010.05.003

Conflict of Interest: The authors declare that the research was conducted in the absence of any commercial or financial relationships that could be construed as a potential conflict of interest.

frontiers
in Neuroinformatics

PERSPECTIVE
published: 21 October 2020
doi: 10.3389/fninf.2020.571039

ANSH: Multimodal Neuroimaging Database Including MR Spectroscopic Data From Each Continent to Advance Alzheimer's Disease Research

Pravat K. Mandal[1,2]*, **Kanika Sandal**[1], **Deepika Shukla**[1]*, **Manjari Tripathi**[3], **Kuldeep Singh**[1] **and Saurav Roy**[1]

[1] *NeuroImaging and NeuroSpectroscopy (NINS) Laboratory, National Brain Research Centre, Manesar, India,* [2] *Florey Institute of Neuroscience and Mental Health, Parkville, VIC, Australia,* [3] *Department of Neurology, All Indian Institute of Medical Sciences, New Delhi, India*

Edited by:
Heye Zhang,
Sun Yat-sen University, China

Reviewed by:
Zhifan Gao,
University of Western Ontario, Canada
Menglin Wu,
Nanjing Tech University, China

***Correspondence:**
Pravat K. Mandal
pravat.mandal@gmail.com;
pravat.mandal@florey.edu.au
Deepika Shukla
deepika.shukla0914@gmail.com

Received: *09 June 2020*
Accepted: *31 August 2020*
Published: *21 October 2020*

Citation:
Mandal PK, Sandal K, Shukla D, Tripathi M, Singh K and Roy S (2020) ANSH: Multimodal Neuroimaging Database Including MR Spectroscopic Data From Each Continent to Advance Alzheimer's Disease Research. Front. Neuroinform. 14:571039. doi: 10.3389/fninf.2020.571039

Alzheimer's disease (AD) is a devastating neurodegenerative disorder affecting millions of people worldwide. The etiology of AD is not known, and intense research involving multimodal neuroimaging data (e.g., MRI, functional MRI, PET etc.) is extensively used to identify the causal molecular process for AD. In this context, various imaging-based databases accessible to researchers globally, are useful for an independent analysis. Apart from MRI-based brain imaging data, the neurochemical data using magnetic resonance spectroscopy (MRS) provide early molecular processes before the structural or functional changes are manifested. The existing imaging-based databases in AD lack the integration of MRS modality and, thus, limits the availability of neurochemical information to the AD research community. This perspective is an initiative to bring attention to the development of the neuroimaging database, "ANSH," that includes brain glutathione (GSH), gamma aminobutyric acid (GABA) levels, and other neurochemicals along with MRI-based information for AD, mild cognitive impairment (MCI), and healthy subjects. ANSH is supported by a JAVA-based workflow environment and python providing a simple, dynamic, and distributed platform with data security. The platform consists of two-tiered architecture for data collection and management further supporting quality control, report generation for analyzed data, and data backup with a dedicated storage system. The ANSH database aims to present a single neuroimaging data platform incorporating diverse data types from healthy control and patient groups to provide better insights pertaining to disease progression. This data management platform provides flexible data sharing across users with continuous project monitoring. The development of ANSH platform will facilitate collaborative research and multi-site data sharing across the globe.

Keywords: Alzheimer's disease, diagnostic marker, neurochemical, glutathione, neuroimaging, behavioural database

INTRODUCTION

Alzheimer's disease (AD) is a major neurodegenerative disorder, and the number of AD patients is increasing globally with each passing year, and disease-modifying treatment is not available. Although pathophysiologic knowledge of AD from existing hypotheses like amyloid beta deposition (Hardy and Higgins, 1992) has helped immensely to understand the disease process, the causal process for AD has not been identified. Neuroimaging modalities involving MRI, fMRI, PET, and behavioral studies have provided the associated structural and behavioral changes in the disease process (Gorgolewski et al., 2016). The first such database was reported by the National Alzheimer's Coordinating Center (NACC), which mainly involved MRI, and the genetic and behavioral dataset of healthy old (HO), and AD patients (Cronin-Stubbs et al., 2000; Beekly et al., 2004). These databases created an opportune situation for the sharing of imaging-based data with researchers. There are other databases from Image Data Archive, Laboratory of NeuroImaging (IDA LONI; Rex et al., 2003; Neu et al., 2005), Longitudinal Online Research Imaging System (LORIS; Das et al., 2011), Extensible Neuroimaging Archive Toolkit (XNAT; Marcus et al., 2007), Open Access Series of Imaging Study (OASIS; Marcus et al., 2007), Biomedical Informatics Research Network (BIRN; Keator et al., 2008), and Collaborative Informatics and Neuroimaging Suite (COINS; Scott et al., 2011). The list of databases is expanding, and only a few specific features mainly structural and functional related to AD are presented in **Figure 1**. Subsequently, neurochemical data is added in the present dataset "ANSH" to bridge the gap (**Figure 1**). MR spectroscopy (MRS) is a potent non-invasive modality to identify the various neurochemicals involved in the early disease process. MRS-driven outcomes provide information that is critically involved in the transition of normal healthy person to mild cognitive impairment (MCI).

Various neurochemicals [e.g., *N*-acetyl aspartate (NAA), myo-Inositol (mI), creatine (Cr), choline (Cho), etc.; Doraiswamy et al., 1998; Mandal et al., 2015], neurotransmitter [e.g., gamma aminobutyric acid (GABA), glutamate, glutamine, etc.; Bai et al., 2015), antioxidant, and glutathione (GSH) level (Mandal et al., 2012, 2015; Shukla et al., 2020] can be quantified in AD brain using MRS. The NAA/mI ratio and the GSH levels from the hippocampus are correlated to cognitive decline in various behavioral studies (Doraiswamy et al., 1998; Mandal et al., 2015). In MRS studies, the depletion of GSH in the hippocampus, frontal cortices, and anterior cingulate cortices (Mandal et al., 2012, 2015; Shukla et al., 2020) has been validated from various independent postmortem studies (Gu et al., 1998; Sultana et al., 2008; Ansari and Scheff, 2010).

Hence, the inclusion of neurochemical data is required and will play a profound role in AD research for identifying a causal molecular process for AD, possible therapeutic development, and monitoring disease progression. ANSH is the first platform where antioxidant, neurotransmitter, and energy metabolites are discussed and will be available to the research community.

A CHRONOLOGICAL DEVELOPMENT OF VARIOUS AD-BASED DATABASE

Database and associated data-processing platforms are powerful tools for supporting medical data mining and discovery from the wealth of routinely acquired clinical and imaging data. This facilitates better information, individualized and optimized patient care (Bui et al., 2013).

Since then, many initiatives progressed toward the open sharing and reusability of the original data. This section briefly describes more details of these databases. The University of Washington School of Public Health supported by the National Institute of Health (NIH) started the Alzheimer's Disease Research Center (ADRC) with a mandate to provide a comprehensive advanced AD research and related disorders from 39 ADRCs at various medical schools across the United States. NACC started with a behavioral and genetic dataset platform and then gradually incorporated MR imaging (Cronin-Stubbs et al., 2000; Beekly et al., 2004). Subsequently, an increasing number of experiments led to the generation of heterogeneous datasets, with an urgent need for standardization and distribution of this information. This initiative resulted in the creation of IDA-LONI for data sharing concerning the disease progression from various research sites globally[1]. IDA-LONI is a hub comprising approximately 138 studies from various disease datasets with new studies added overtime (Petersen et al., 2010). LONI is fortified with upload, download, quality check (QC), processing, and various other user-level sharing features. The Alzheimer's disease neuroimaging initiative (ADNI; Petersen et al., 2010) and the human connectome projects are associated with this platform (Rex et al., 2003). LORIS is a web-based platform for neuroimaging studies (Das et al., 2011). LORIS consists of a wide range of datasets including neurological, behavioral, and imaging data from anatomical, functional maps, atlases, and MRI models. LORIS streamlined a framework for storing and processing behavioral, clinical, neuroimaging, and genetic data. The combination of the software platform and web-based approach for data management, throughput task, and data sharing to the approved users was supported by the Neuroimaging Archive Toolkit (XNAT; Marcus et al., 2007), Analysis of Functional Neuroimages (AFNI; Cox, 1996), Human Imaging Database (HID; Marcus et al., 2011), and Brain Imaging Data Structure (BIDS; Gorgolewski et al., 2016), which provide the user with the data management tools for a better analysis of data across a diverse number of neuroimaging datasets. The Neuro-Imaging Tools and Resource Collaboratory (NITRC) has played a vital role in hosting all the neuroimaging software repository, data, and toolboxes under one platform[2].

OASIS (Marcus et al., 2007) is a dedicated project involving brain MRI and PET longitudinal data available to the scientific community. The BIRN package offers an amalgamated and distributed infrastructure for the storage, retrieval, analysis, and documentation of biomedical imaging datasets (Keator et al., 2008). BIRN uses XNAT and

---

[1] https://ida.loni.usc.edu

[2] https://www.nitrc.org

FIGURE 1 | The chronological development of various neuroimage-based database pertaining to Alzheimer's disease (AD) research with a variety of modalities. (1) National Alzheimer's Coordinating Center (NACC; Cronin-Stubbs et al., 2000; Beekly et al., 2004). (2) IDA-LONI (Rex et al., 2003; Neu et al., 2005). (3) Longitudinal Online Research Imaging System (LORIS; Das et al., 2011). (4) Neuroimaging Archive Toolkit (XNAT; Marcus et al., 2007). (5) Open Access Series of Imaging Study (OASIS; Marcus et al., 2007). (6) Biomedical Informatics Research Network (BIRN; Keator et al., 2008). (7) Collaborative Informatics and Neuroimaging Suite (COINS; Scott et al., 2011). (8) ANSH: a dynamic comprehensive database management system. Abbreviations: DTI, diffusion tensor imaging; ECoG, electrocorticography; EEG, electroencephalogram; fMRI, functional magnetic resonance imaging; MEG, magnetoencephalography; MRS, magnetic resonance spectroscopy; PET, positron emission tomography; QSM, quantitative susceptibility mapping; SPECT, single-photon emission computerized tomography. MRS data specifically critical antioxidant, receptors, and brain energy metabolites will be available through the ANSH.

HID for data acquisition and management (Keator et al., 2008). In progression, COINS is comprised of 300 studies consisting of 19,000 MRI, magnetoencephalography (MEG), and electroencephalogram (EEG) scans with more than 180,000 clinical assessments (Bockholt et al., 2010). The COINS database provides an optimized platform for data mining from multiorganization sources shared with added security and data tracking portal with Public Health Information (PHI; Bockholt et al., 2010).

IMPORTANCE OF MR SPECTROSCOPY DATA AND APPLICATION

MRS data can be generated from any part of the brain using single-voxel mode or multivoxel mode (Mandal, 2007). MRS data is generally smaller in size and easy to handle compared to MRI-based data. Various advanced packages are available to process MRS data, and absolute quantitation of various neurochemicals is also possible (Mandal and Shukla, 2020). These MRS-processing packages can be added with a suitable plugin so that processed MRS data can be utilized in multimodel big data analytics (Sharma et al., 2019). Various MRS pulse sequences are now available to detect specific neurochemicals (GABA, GSH, glutamate/glutamine) without any ambiguity (Terpstra et al., 2003). **Figure 2A** represents the MRS spectra from the left hippocampus by placing the single-voxel ($25 \times 25 \times 25$ mm^3), MRS data was acquired using a 3T MRI (Achieva, Philips) scanner, and processed using the KALPANA software (Mandal and Shukla, 2020). **Figure 2B** represents absolute quantitation of GSH in relevant amount (mM) from the left hippocampus of HO, MCI, and AD patients (Mandal et al., 2015). Significant depletion of GSH level from the left hippocampus, as detected by *in vivo* MRS, is sensitive for comparing HO, MCI, and AD patients. MRS is also the only technique that can be used to detect the GSH conformers *in vivo*, and these conformers are likely to play an important role in the AD disease process (Mandal et al., 2017, 2019; Shukla et al., 2020). The changes in the GSH level are susceptible to AD pathology only. Data indicated that, GSH level in the left cerebellum of AD and HO did not alter significantly ($p = 0.536$); however, the specific change in GSH in the hippocampal regions in the same AD and HO groups was found to be significant ($p < 0.001$; Mandal et al., 2015). The database involving ^{31}P MRS is critical to understand the impaired energy metabolism process (e.g., increased hippocampal pH) in the AD brain in contrast to the age-matched normal brain (Mandal et al., 2012; Rijpma et al., 2018).

This perspective will bridge the gap providing the unique neurochemical data in AD research.

TECHNICAL DETAILS OF THE ANSH DATABASE IN BRIEF

Key Features

ANSH, a dynamic and distributed data management platform, follows a two-tired architecture that includes a graphical user interface, processing pipeline, and database server. The ANSH supports a JAVA-based workflow environment and python for storage with flexible data access and data sharing among users. In addition, QC ensures an improved database management. The ANSH also provides a report generation feature with the additional functionality of continuous project monitoring using data visualization and statistical analysis.

Some key features of the ANSH are: (1) distributive platform; (2) user login with privacy implementations; (3) quality check; (4) image viewer; (5) centralized approach to fetch data; (6) real-time tracking and backup of the database; (7) heterogeneous data; (8) effortless import/export of data with the use of data-processing pipelines; and (9) report generation.

Data Types and Quality Control

ANSH provides a dynamic and comprehensive database management system for the heterogeneous neuroimaging datasets, specifically MRI and multinuclear MRS for HO, MCI, and AD categories along with the neuropsychological test scores. The MRI data consist of diverse 3D T1, T2-weighted, Flair, and QSM images for different age groups of healthy young as well as HO subjects. Other imaging modalities such as PET, fMRI, and DTI will also be added to the ANSH database. MRS data for GSH and GABA are provided for age-matched HO, MCI, and AD groups along with T1, T2-weighted, and Flair MRI dataset. The neuropsychological score broadly constitutes from the mini-mental state examination, clock drawing test, trail making tests. The flow diagram of the ANSH is presented in **Figure 2C**.

ANSH User-Flow Schematic

The ANSH incorporates three levels of users including administrator, write/read privileged, and read privileged only. The administrator is the top-level user, responsible for assigning other user's rights as well as creating and managing the new and existing project information. The administrator only holds the right to completely remove the specific project data from the database. Users with the read and write privileges can read and write the specific data according to the permission given to them by the administrator, whereas the user with the read privileges will only be able to read a selective database for the specific projects as permitted by the administrator. Each user can export the selected data from the specified project.

Dataset Handling

Data entry in the ANSH database can be accomplished individually using data entry forms or imported in bulk. Data insertion and updation rights are held by the administrator and given to the write-privileged users for the specified projects. Data retrieval rights are entitled to all users. The ANSH also provides detailed data report, data visualization plots (i.e., bar and pie charts) as image files and statistical

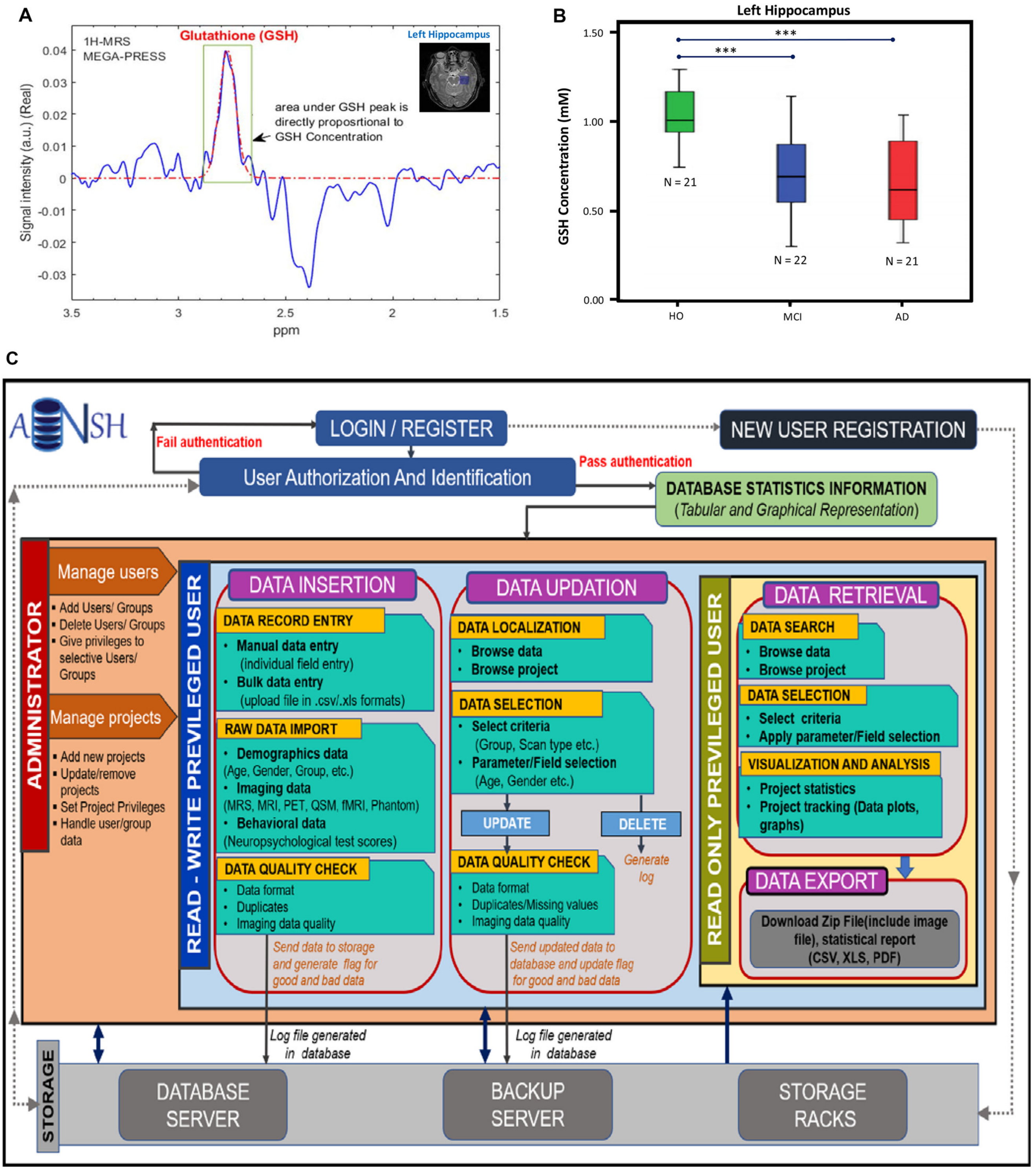

FIGURE 2 | (A) 1H-MRS MEGA-PRESS edited spectra for *in vivo* glutathione (GSH) estimation in the left hippocampus of a HO brain. **(B)** Box–whisker plot showing significant GSH concentration depletion in the mild cognitive impairment (MCI) and AD groups compared to the HO group. ***The significance level was set at $p < 0.001$ (Mandal et al., 2015). **(C)** This workflow illustrates the conventions for the construction of database and management of data. The access of data is provided by the user authentication. The privileged user is provided with two main segments, i.e., data insertion and updation, where the user can review data and can make appropriate changes. Both segments follow the raw image quality control (QC) before putting the data in the backup servers. It will also keep a track of the data usage and generate logs for the changes. Read-only privileged users are enriched with the segment for data retrieval to export image data and the data reports using various search filters and data selection parameters. All segments are interconnected by the backend server and the rack system of the ANSH.

information in the form of pdf and excel which can be exported afterwards.

Data Processing, Storage, and Security

In the ANSH database management system, the user can access the database through a secure desktop application. Data imported or entered, undergoes a rigorous quality assurance process with a quality flag level. This quality tagged data is sent to the server for storage and subsequently history logs are maintained and stored in the ANSH server tracking associated changes.

Data security is provided in multiple steps: (1) authorized users will be granted access to the database, (2) quarantine of sensitive files (e.g., user password file), where files are encrypted and hashed, (3) tracking user behavior against data, (4) successful/failed attempts to establish connection are logged to track intruders, (5) restricting user access by designing and granting appropriate user with limited administrative privileges, and (6) database backups are taken as a part of security protocol, where these backups allow to recover the lost data that may have resulted from hardware failure, data corruption, theft, or natural disasters.

CONCLUSION AND FUTURE DIRECTIONS

The ANSH database construction is a sincere attempt to bring the critical neurochemical information from HO, MCI, and AD patients to the global researchers for comparative analysis. WE will also add Parkinson disease data and other mental disorders data in ANSH database. This novel program is in an expanding stage and needs further infrastructure support to build a robust system to cater to the Indian and global brain research community.

DATA AVAILABILITY STATEMENT

The original contributions presented in the study are included in the article, further inquiries can be directed to PM through email pravat.mandal@gmail.com.

AUTHOR CONTRIBUTIONS

PM and DS conceptualized the idea and were involved in the manuscript writing and figure design. KSa was involved in the database design, manuscript writing, analysis of various databases and preparation of **Figure 1**. MT was involved in discussion as a clinical collaborator. KSi was involved in programming of the database development and expansion and preparation of **Figure 2**. SR was involved in Web-based application and front-end generation.

FUNDING

PM (Principal Investigator) is grateful for the financial support (Tata Innovation Fellow, No. BT/HRD/01/05/2015) from the Ministry of Science and Technology, Government of India, and the Indo-Australian Biotechnology Fund (Grant No. BT/Indo-Aus/10/31/2016). PM (Principal Investigator) and DS (Co-Investigator) also thank the Ministry of Electronics and Information Technology [4(5)/2019/ITEA] for funding support.

ACKNOWLEDGMENTS

PM thanks Ms. Avantika Samkaria (Researcher, NINS lab) and Ms. Komal Jindal (Senior R&D Engineer, NINS lab) for critical comments and editorial support. PM and DS dedicate this article to their parents.

REFERENCES

Ansari, M. A., and Scheff, S. W. (2010). Oxidative stress in the progression of Alzheimer disease in the frontal cortex. *J. Neuropathol. Exp. Neurol.* 69, 155–167. doi: 10.1097/nen.0b013e3181cb5af4

Bai, X., Edden, R. A. E., Gao, F., Wang, G., Wu, L., Zhao, B., et al. (2015). Decreased γ-aminobutyric acid levels in the parietal region of patients with Alzheimer's disease. *J. Magn. Reson. Imaging* 41, 1326–1331. doi: 10.1002/jmri.24665

Beekly, D. L., Ramos, E. M., van Belle, G., Deitrich, W., Clark, A. D., Jacka, M. E., et al. (2004). The national Alzheimer's coordinating center (NACC) database: an Alzheimer disease database. *Alzheimer Dis. Assoc. Disord.* 18, 270–277.

Bockholt, H. J., Scully, M., Courtney, W., Rachakonda, S., Scott, A., Caprihan, A., et al. (2010). Mining the mind research network: a novel framework for exploring large scale, heterogeneous translational neuroscience research data sources. *Front. Neuroinform.* 3:36. doi: 10.3389/neuro.11.036.2009

Bui, A. A., Hsu, W., Arnold, C., El-Saden, S., Aberle, D. R., and Taira, R. K. (2013). Imaging-based observational databases for clinical problem solving: the role of informatics. *J. Am. Med. Inform. Assoc.* 20, 1053–1058. doi: 10.1136/amiajnl-2012-001340

Cox, R. W. (1996). AFNI: software for analysis and visualization of functional magnetic resonance neuroimages. *Comput. Biomed. Res.* 29, 162–173. doi: 10.1006/cbmr.1996.0014

Cronin-Stubbs, D., DeKosky, S. T., Morris, J. C., and Evans, D. A. (2000). Promoting interactions with basic scientists and clinicians: the NIA Alzheimer's disease data coordinating center. *Stat. Med.* 19, 1453–1461. doi: 10.1002/(sici)1097-0258(20000615/30)19:11/12<1453::aid-sim437>3.0.co;2-7

Das, S., Zijdenbos, A. P., Harlap, J., Vins, D., and Evans, A. C. (2011). LORIS: a web-based data management system for multi-center studies. *Front. Neuroinform.* 5:37. doi: 10.3389/fninf.2011.00037

Doraiswamy, P. M., Charles, H. C., and Krishnan, K. R. (1998). Prediction of cognitive decline in early Alzheimer's disease. *Lancet* 352:1678. doi: 10.1016/S0140-6736(05)61449-3

Gorgolewski, K. J., Auer, T., Calhoun, V. D., Craddock, R. C., Das, S., Duff, E. P., et al. (2016). The brain imaging data structure, a format for organizing and describing outputs of neuroimaging experiments. *Sci. Data* 3:160044. doi: 10.1038/sdata.2016.44

Gu, M., Owen, A. D., Toffa, S. E., Cooper, J. M., Dexter, D. T., Jenner, P., et al. (1998). Mitochondrial function, GSH and iron in neurodegeneration and Lewy body diseases. *J. Neurol. Sci.* 158, 24–29. doi: 10.1016/s0022-510x(98)00095-1

Hardy, J. A., and Higgins, G. A. (1992). Alzheimer's disease: the amyloid cascade hypothesis. *Science* 256, 184–185. doi: 10.1126/science.1566067

Keator, D. B., Grethe, J. S., Marcus, D., Ozyurt, B., Gadde, S., Murphy, S., et al. (2008). A national human neuroimaging collaboratory enabled by the biomedical informatics research network (BIRN). *IEEE Trans. Inf. Technol. Biomed.* 12, 162–172. doi: 10.1109/TITB.2008.917893

Mandal, P. K. (2007). Magnetic resonance spectroscopy (MRS) and its application in Alzheimer's disease. *Concept Magn. Reson.* 30A, 40–64. doi: 10.1002/cmr.a.20072

Mandal, P. K., Akolkar, H., and Tripathi, M. (2012). Mapping of hippocampal pH and neurochemicals from *in vivo* multi-voxel 31P study in healthy normal young male/female, mild cognitive impairment and Alzheimer's disease. *J. Alzheimers Dis.* 31, S75–S86. doi: 10.3233/jad-2012-120166

Mandal, P. K., and Shukla, D. (2020). KALPANA: advanced spectroscopic signal processing platform for improved accuracy to aid in early diagnosis of brain disorders in clinical setting. *J. Alzheimers Dis.* 75, 397–402. doi: 10.3233/jad-191351

Mandal, P. K., Saharan, S., Tripathi, M., and Murari, G. (2015). Brain glutathione levels—a novel biomarker for mild cognitive impairment and Alzheimer's disease. *Biol. Psychiatry* 78, 702–710. doi: 10.1016/j.biopsych.2015.04.005

Mandal, P. K., Shukla, D., Govind, V., Boulard, Y., and Ersland, L. (2017). Glutathione conformations and its implications for *in vivo* magnetic resonance spectroscopy. *J. Alzheimers Dis.* 59, 537–541. doi: 10.3233/jad-170350

Mandal, P. K., Shukla, D., Tripathi, M., and Ersland, L. (2019). Cognitive improvement with glutathione supplement in Alzheimer's disease: a way forward. *J. Alzheimers Dis.* 68, 531–535. doi: 10.3233/jad-181054

Mandal, P. K., Tripathi, M., and Sugunan, S. (2012). Brain oxidative stress: detection and mapping of anti-oxidant marker "glutathione" in different brain regions of healthy male/female, MCI and Alzheimer patients using non-invasive magnetic resonance spectroscopy. *Biochem. Biophys. Res. Commun.* 417, 43–48. doi: 10.1016/j.bbrc.2011.11.047

Marcus, D. S., Harwell, J., Olsen, T., Hodge, M., Glasser, M. F., Prior, F., et al. (2011). Informatics and data mining tools and strategies for the human connectome project. *Front. Neuroinform.* 5:4. doi: 10.3389/fninf.2011.00004

Marcus, D. S., Olsen, T. R., Ramaratnam, M., and Buckner, R. L. (2007). The extensible neuroimaging archive toolkit: an informatics platform for managing, exploring and sharing neuroimaging data. *Neuroinformatics* 5, 11–34. doi: 10.1385/ni:5:1:11

Marcus, D. S., Wang, T. H., Parker, J., Csernansky, J. G., Morris, J. C., and Buckner, R. L. (2007). Open access series of imaging studies (OASIS): cross-sectional MRI data in young, middle aged, nondemented and demented older adults. *J. Cogn. Neurosci.* 19, 1498–1507. doi: 10.1162/jocn.2007.19.9.1498

Neu, S. C., Valentino, D. J., and Toga, A. W. (2005). The LONI Debabeler: a mediator for neuroimaging software. *NeuroImage* 24, 1170–1179. doi: 10.1016/j.neuroimage.2004.10.035

Petersen, R. C., Aisen, P. S., Beckett, L. A., Donohue, M. C., Gamst, A. C., Harvey, D. J., et al. (2010). Alzheimer's disease neuroimaging initiative (ADNI): clinical characterization. *Neurology* 74, 201–209. doi: 10.1212/WNL.0b013e3181cb3e25

Rex, D. E., Ma, J. Q., and Toga, A. W. (2003). The LONI pipeline processing environment. *NeuroImage* 19, 1033–1048. doi: 10.1016/s1053-8119(03)00185-x

Rijpma, A., van der Graaf, M., Meulenbroek, O., Olde Rikkert, M. G. M., and Heerschap, A. (2018). Altered brain high-energy phosphate metabolism in mild Alzheimer's disease: a 3-dimensional ^{31}P MR spectroscopic imaging study. *Neuroimage Clin.* 18, 254–261. doi: 10.1016/j.nicl.2018.01.031

Scott, A., Courtney, W., Wood, D., de la Garza, R., Lane, S., King, M., et al. (2011). COINS: an innovative informatics and neuroimaging tool suite built for large heterogeneous datasets. *Front. Neuroinform.* 5:33. doi: 10.3389/fninf.2011.00033

Sharma, A., Shukla, D., Goel, T., and Mandal, P. K. (2019). BHARAT: an integrated big data analytic model for early diagnostic biomarker of Alzheimer's disease. *Front. Neurol.* 10:9. doi: 10.3389/fneur.2019.00009

Shukla, D., Mandal, P. K., Tripathi, M., Vishwakarma, G., Mishra, R., and Sandal, K. (2020). Quantitation of *in vivo* brain glutathione conformers in cingulate cortex among age-matched control, MCI and AD patients using MEGA-PRESS. *Hum. Brain Mapp.* 41, 194–217. doi: 10.1002/hbm.24799

Sultana, R., Piroddi, M., Galli, F., and Butterfield, D. A. (2008). Protein levels and activity of some antioxidant enzymes in hippocampus of subjects with amnestic mild cognitive impairment. *Neurochem. Res.* 33, 2540–2546. doi: 10.1007/s11064-008-9593-0

Terpstra, M., Henry, P.-G., and Gruetter, R. (2003). Measurement of reduced glutathione (GSH) in human brain using LCModel analysis of difference-edited spectra. *Magn. Reson. Med.* 50, 19–23. doi: 10.1002/mrm.10499

Conflict of Interest: The authors declare that the research was conducted in the absence of any commercial or financial relationships that could be construed as a potential conflict of interest.

frontiers
in Neuroinformatics

ORIGINAL RESEARCH
published: 10 November 2020
doi: 10.3389/fninf.2020.601829

Semi-Supervised Learning in Medical Images Through Graph-Embedded Random Forest

Lin Gu[1,2], *Xiaowei Zhang*[3], *Shaodi You*[4], *Shen Zhao*[5], *Zhenzhong Liu*[6,7]* and *Tatsuya Harada*[1,2]

[1] RIKEN AIP, Tokyo, Japan, [2] Research Center for Advanced Science and Technology (RCAST), The University of Tokyo, Tokyo, Japan, [3] Bioinformatics Institute (BII), A*STAR, Singapore, Singapore, [4] Faculty of Science, Institute of Informatics, University of Amsterdam, Amsterdam, Netherlands, [5] Department of Medical Physics, Western University, London, ON, Canada, [6] Tianjin Key Laboratory for Advanced Mechatronic System Design and Intelligent Control, School of Mechanical Engineering, Tianjin University of Technology, Tianjin, China, [7] National Demonstration Center for Experimental Mechanical and Electrical Engineering Education, Tianjin University of Technology, Tianjin, China

One major challenge in medical imaging analysis is the lack of label and annotation which usually requires medical knowledge and training. This issue is particularly serious in the brain image analysis such as the analysis of retinal vasculature, which directly reflects the vascular condition of Central Nervous System (CNS). In this paper, we present a novel semi-supervised learning algorithm to boost the performance of random forest under limited labeled data by exploiting the local structure of unlabeled data. We identify the key bottleneck of random forest to be the information gain calculation and replace it with a graph-embedded entropy which is more reliable for insufficient labeled data scenario. By properly modifying the training process of standard random forest, our algorithm significantly improves the performance while preserving the virtue of random forest such as low computational burden and robustness over over-fitting. Our method has shown a superior performance on both medical imaging analysis and machine learning benchmarks.

Keywords: vessel segmentation, semi-supervised learning, manifold learning, central nervous system (CNS), retinal image

Edited by:
Heye Zhang,
Sun Yat-sen University, China

Reviewed by:
Chenxi Huang,
Xiamen University, China
Guang Yang,
Imperial College London,
United Kingdom

Correspondence:
Zhenzhong Liu
zliu@email.tjut.edu.cn

Received: *01 September 2020*
Accepted: *23 September 2020*
Published: *10 November 2020*

Citation:
Gu L, Zhang X, You S, Zhao S, Liu Z and Harada T (2020) Semi-Supervised Learning in Medical Images Through Graph-Embedded Random Forest. Front. Neuroinform. 14:601829. doi: 10.3389/fninf.2020.601829

1. INTRODUCTION

Machine learning has been widely applied to analyze medical images such as an image of the brain. For example, the automatic segmentation of brain tumor (Soltaninejad et al., 2018) could help predict Patient Survival from MRI data. However, traditional methods usually require a large number of diagnosed examples. Collecting raw data during routine screening is possible but making annotations and diagnoses for them is costly and time-consuming for medical experts. To deal with this challenge, we propose a novel graph-embedded semi-supervised algorithm that makes use of the unlabeled data to boost the performance of the random forest. We specifically evaluate the proposed method on both a neuronal image and the retinal image analysis that is highly related to diabetic retinopathy (DR) (Niu et al., 2019) and Alzheimer's Disease (AD) (Liao et al., 2018), and make the following specific contributions:

1. We empirically validate that the performance bottleneck of random forest under limited training samples is the biased information gain calculation.
2. We propose a new semi-supervised entropy calculation by incorporating local structure of unlabeled data.
3. We propose a novel semi-supervised random forest which shows advantage performance of the state-of-the-art in both medical imaging analysis and machine learning benchmarks.

Among various supervised algorithms, random forest or random decision trees (Breiman et al., 1984; Criminisi et al., 2012) are one of the state-of-the-art machine learning algorithms for medical imaging applications. Despite its robustness and efficiency, its performance relies heavily on sufficiently labeled training data. However, annotating a large amount of medical data is time-consuming and requires domain knowledge. To alleviate the challenge of having enough labeled data, a class of learning methods named semi-supervised learning (SSL) (Joachims, 1999; Zhu et al., 2003; Belkin and Niyogi, 2004; Zhou et al., 2004; Chapelle et al., 2006; Zhu, 2006) were proposed to leverage unlabeled data to improve the performance. Leistner et al. (2009) proposed a semi-supervised random forest which maximizes the data margin via deterministic annealing (DA). Liu et al. (2015) showed that the splitting strategy appears to be the bottleneck of performance in a random forest. The authors estimate the unlabeled data through kernel density estimation (KDE) on the projected subspace, and when constructing the internal node, they progressively refine the splitting function with the acquired labels through KDE until it converges. Without explicit affinity relation, CoForest (Li and Zhou, 2007) iteratively guesses the unlabeled data with the rest of the trees in the forest and then uses the new labeled data to refine the tree. Semi-supervised based super-pixel (Gu et al., 2017) has proved to be effective in the segmentation of both a retinal image and a neuronal image.

Following the research line of a previous semi-supervised random forest (RF), we identify that RF's performance bottleneck, under insufficient data, is the biased information gain calculation when selecting an optimal splitting parameter (shown as blue in **Figure 1**). Therefore, as illustrated in red in **Figure 1**, we slightly modified the training procedure of RF to relieve this bias. We replace the original information gain with our novel graph-embedded entropy which exploits the data structure of unlabeled data. Specifically, we first use both labeled and unlabeled data to construct a graph whose weights measure local similarity among data and then minimize a loss function that sums the supervised loss over labeled data and a graph Laplacian regularization term. From the optimal solution, we can get label information of unlabeled data which is utilized to estimate a more accurate information gain for node splitting. Since a major part of training and the whole testing remains unchanged, our graph-embedded random forest could significantly improve the performance without losing the virtue of a standard random forest such as low computational burden and robustness over over-fitting.

2. ANALYSIS OF PERFORMANCE BOTTLENECK

Let us first review the construction of the random forest (Breiman et al., 1984) to figure out why random forest fails under limited training data. A random forest is an ensemble of decision trees: $\{t_1, t_2, ..., t_T\}$, of which an individual tree is independently trained and tested.

Training Procedure: Each decision tree t, as illustrated in **Figure 1**, learns to classify a training sample $x \in X$ to the corresponding label y by recursively branching it to the left or right child until reaching a leaf node. In particular, each node is associated with a binary split function $h(x_i, w, \tau)$, e.g., oblique linear split function

$$h(x_i, w, \tau) = [\langle w, x_i \rangle < \tau], \tag{1}$$

where [.] is an indicative function and τ is a scaler threshold. $w \in R^d$ serves as a feature weight parameter that projects the high dimension data $x \in R^d$ to a one dimensional subspace.

Given a candidate splitting function $h(x, w_j, \tau_j)$, its splitting quality is measured by information gain $G(w_j, \tau_j)$. In practice, given the training data X and their labels Y, the construction of the splitting node, as illustrated in the left side of **Figure 1**, comprises the following three stages:

Algorithm 1 : Training of node splitting.

```
Randomly generates a set of feature subspace candidates $\{w_j\}$
For each $w_j$, find the optimal $\tau_j^* = \arg\max_{\tau} G(w_j, \tau, X, Y)$ that best splits the data.
Among all $\{w_j, \tau_j^*\}$, pick the one with largest information gain: $j^* = \arg\max_{j} G(w_j, \tau_j^*, X, Y)$
```

Through the above stages, each split node is associated with a splitting function $h(x, w, \tau)$ that best splits the training data.

Testing Procedure: When testing data x, the trained random forest predicts the probability of its label by averaging the ensemble prediction as $\hat{p}(y|x) = \sum_t p_t(y|x)$, where $p_t(y|x)$ denotes the empirical label distribution of the training samples that reach leaf note of tree t.

2.1. Performance Bottleneck Under Insufficient Data

According to the study of Liu et al. (2015), insufficient training data would impact the performance of RF in three ways (Liu et al., 2015): (1) limited forest depth; (2) inaccurate prediction model of leaf nodes; (3) sub-optimal splitting strategy. Among them, Liu et al. (2015) identified that (1) is inevitable, and (2) is solvable with their proposed strategy. In this paper, we further improve the method by tackling (3).

We claim that the performance bottleneck of random forest is its sub-optimal splitting strategy in Algorithm 1. To empirically support this claim, we build three random forests, similar to Liu et al. (2015), for comparison: the first one, the **Control** is trained with a small size of a training set $S1$ as control; the second one, the

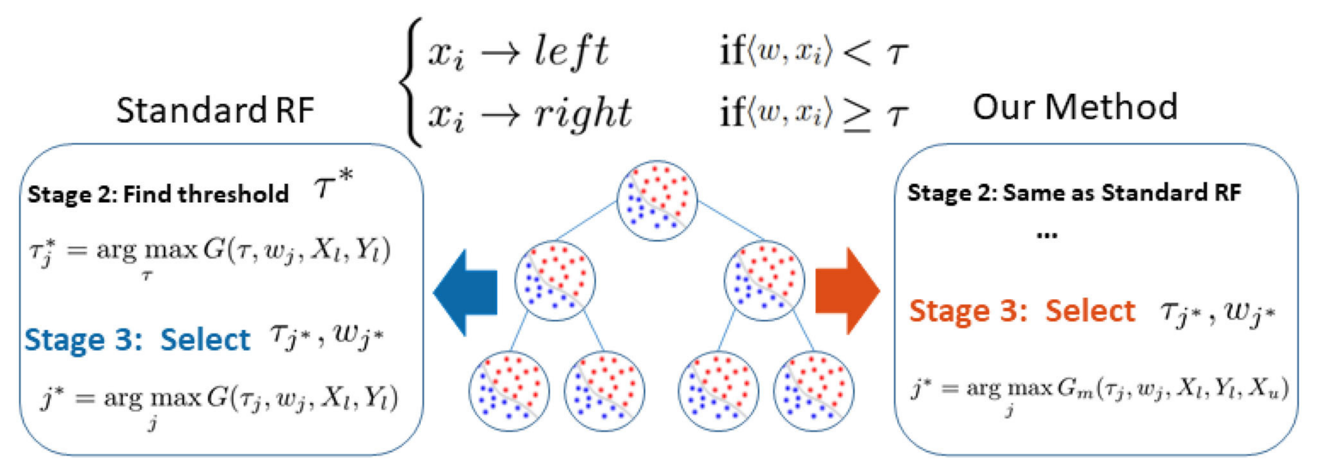

FIGURE 1 | Difference between our method and standard random forest. Noting that the performance bottleneck (shown in blue) is the biased information gain $G(\tau_j, w_j, X_l, Y_l)$ calculation based on limited labeled data X_l, Y_l in Stage 3, we replace $G(.)$ with our novel graph-embedded $G_m(., X_u)$ which considers unlabeled data X_u (shown in red).

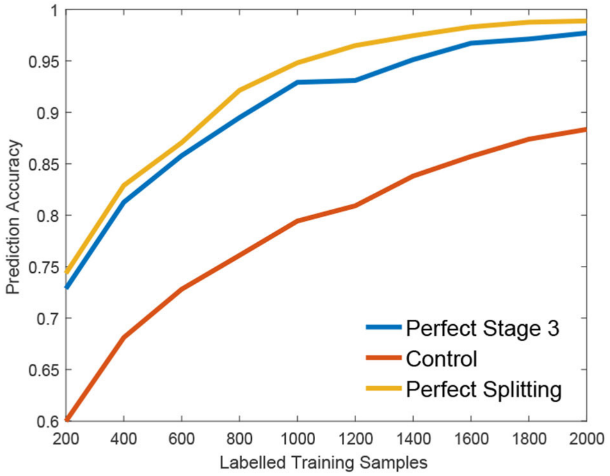

FIGURE 2 | Empirical validation of performance Bottleneck.

Perfect Stage 3 is constructed with the same training set $S1$ but its node splitting uses a large training set $S2$ to select the optimal parameter in stage 3 of Algorithm 1, to simulate the case that random forest selects the optimal parameter of stage 3 with full information; the third one, the **Perfect Splitting** is constructed with $S1$ while $S2$ was used for both Stage 2 and 3 of Algorithm 1.

Following the protocol of Liu et al. (2015), each random forest comprises 100 trees and the same entropy gain is adopted as the splitting criterion. We evaluate three random forests on Madelon (Guyon et al., 2004), a widely used machine learning benchmark. As shown in **Figure 2**, Perfect Stage 3, which only uses the full information to select the best parameter set, significantly improves the performance compared to the control group. Interestingly, the Perfect Splitting one, which utilizes the full information for both optimal parameter proposing (Stage 2) and optimal parameter decision (Stage 3), only makes a subtle improvement compared to Perfect Stage 3.

From **Figure 2**, we found that Stage 3, optimal parameter selection, is the performance bottleneck of the splitting node construction, which is also the keystone of random forest construction (Liu et al., 2015). When deciding the optimal parameter, random forest often fails to find the best one as its information gain calculation $g(w, \tau)$ is biased under insufficient training data. Interestingly, insufficient data has a smaller effect on the Stage 2, parameter proposal. Motivated by this observation, we propose a new information calculation which exploits unlabeled data to make a better parameter selection in Stage 3 of Algorithm 1.

3. GRAPH-EMBEDDED REPRESENTATION OF INFORMATION GAIN

In the previous section, we show that gain estimation appears to be the performance bottleneck of random forests. Empirically, we show that more label information helps to obtain more accurate gain estimation. This encourages us to consider the possibility of mining label information from unlabeled data through structural connections between labeled and unlabeled data. In particular, we perform a graph-based semi-supervised learning to get label information of unlabeled data, and compute information gain from both labeled and unlabeled data. To achieve a better gain estimation, we embed all data into a graph. Moreover, we assume the underlying structure of all data form a manifold, and compute data similarity based on the assumption.

Let l and u be the number of labeled and unlabeled instances, respectively. Let $X_l = [x_1, \cdots, x_l]^\top \in \mathbb{R}^{d\times l}$ be the matrix of feature vectors of labeled instances, and $X_u = [x_{l+1}, \cdots, x_{l+u}]^\top \in \mathbb{R}^{d\times u}$ be the matrix of unlabeled instances. To accommodate label information, we define a label matrix $Y \in \mathbb{R}^{(l+u)\times K}$ (assuming there are K class labels available), with each entry Y_{ik} containing 1 provided the i-th data belongs to X_l and is labeled with class k, and 0 otherwise. Besides, we define Y_l as a submatrix of Y corresponding to the labeled data, $y_i \in \mathbb{R}^K$ as the i-th row of Y corresponding to x_l, and $\boldsymbol{y}_l \in \mathbb{R}^l$ as the vector of class labels for X_l.

Based on both labeled and unlabeled instances, our purpose is to learn a mapping $f : \mathbb{R}^d \rightarrow \mathbb{R}^K$ and predict the label of instance x as $k^* := \arg\max_k f_k(x)$. Many semi-supervised learning algorithms use the following regularized framework

$$\sum_{i=1}^{l} loss(y_i, f(x_i)) + \lambda \sum_{i,j=l+1, i\neq j}^{l+u} s(x_i, x_j)\|f(x_i) - f(x_j)\|_2^2,$$

where $loss()$ is a loss function and $s(x_i, x_j)$ is a similarity function. In this paper, we apply the idea of graph embedding to learn f. We construct a graph $\mathcal{G} = (V, E, W)$, where each node in V denotes a training instance and $W \in \mathbb{R}^{(l+u)\times(l+u)}$ denotes a symmetric weight matrix. W is computed as follows: for each point find t nearest neighbors, and $W_{ij} = exp(-\|x_i - x_j\|_2^2/\sigma^2)$ if (x_i, x_j) are neighbors, 0 otherwise. Such construction of graph implicitly assumes that all data resides on some manifold and exploits local structure. Based on the graph embedding, we propose to minimize

$$\mathcal{L}(\{f_i\}) = \frac{1}{2}\left(\sum_{i=1}^{l+u}\|f_i - y_i\|_2^2 + \lambda \sum_{i,j=1}^{l+u} W_{ij}\|\frac{f_i}{\sqrt{D_{ii}}} - \frac{f_j}{\sqrt{D_{jj}}}\|_2^2\right), \tag{2}$$

where D is a diagonal matrix with its D_{ii} equal to the sum of the i-th row of W. Let $F^* = [f_1^*, \cdots, f_{l+u}^*] = \arg\min_{\{f_i\}} \mathcal{L}(\{f_i\})$ be the optimal solution, it has been shown in Zhou et al. (2004) that

$$F^* = ((1+\lambda)I - \lambda D^{-1/2}WD^{-1/2})^{-1}Y. \tag{3}$$

Based on the learned functions F^*, we can predict the label information of X_u and then utilize such information to estimate more accurate information gain. Specifically, we let $\hat{\boldsymbol{y}}_u$ denotes the predicted label of X_u, and for node S we compute Gini index $G_m(S) = \sum_{k=1}^{K} p_k(1-p_k)$, where

$$p_k = \frac{1}{|S|}\Big(\sum_{x_i\in S, 1\le i\le l} \mathbb{1}_{\{(\boldsymbol{y}_l)_i = k\}} + \sum_{x_i\in S, l+1\le i\le l+u} \mathbb{1}_{\{(\hat{\boldsymbol{y}}_u)_i = k\}}\Big)$$

is the proportion of data from class k. Note that we utilize information from both labeled and unlabeled data to compute the Gini index. For each node, we estimate information gain as

$$G_m(w, \tau, X_l, Y_l, X_u) = G_m(S) - \big(|S_l|G_m(S_l) + |S_u|G_m(S_u)\big)/|S|, \tag{4}$$

where S_l and S_u are left and right child nodes, respectively.

4. CONSTRUCTION OF SEMI-SUPERVISED RANDOM FOREST

In our framework, we preserve the major structure of the standard random forest where the testing stage is exactly the same as the standard one. As illustrated in the right part of **Figure 1**, we only make a small modification in stage 3 of Algorithm 1 where the splitting efficiency is now evaluated by our novel graph-embedded based information gain $G_m(\tau_j, w_j, X_l, Y_l, X_u)$ from Equation (4). Specifically, we leave stage 2 unchanged that the threshold τ of each subspace candidate w is still based on standard information gain such as the Gini index. Now with a set of parameter candidates w, τ, the stage 3 calculates the corresponding manifold based information score $\hat{g}(w, \tau)$ instead and select the optimal one through $\max_{w_j, \tau_j} \hat{g}(w_j, \tau_j)$.

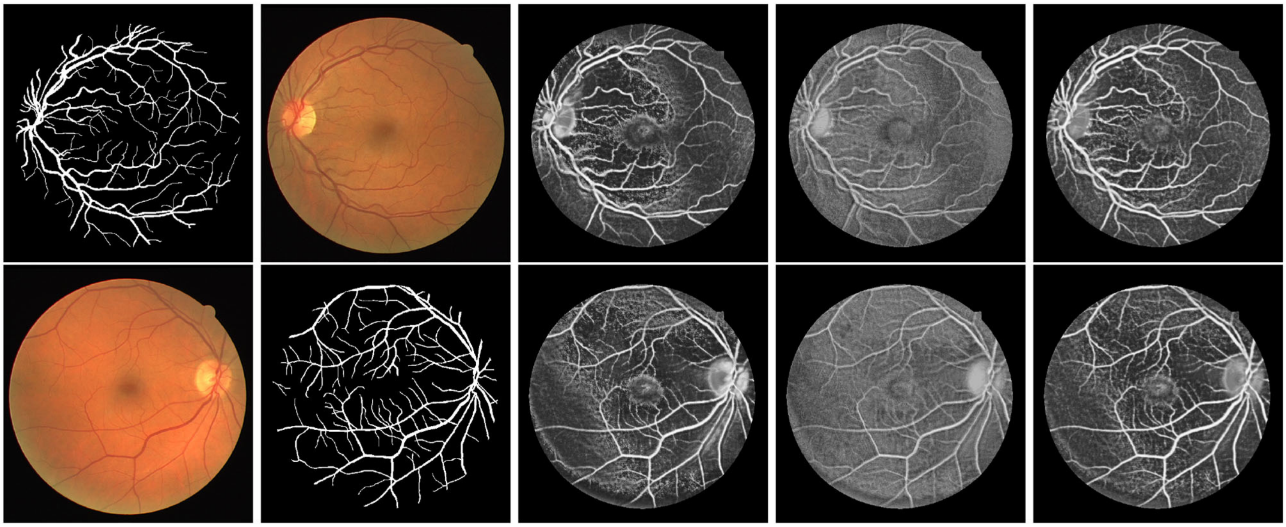

FIGURE 3 | Exemplar estimation of vessel on the DRIVE dataset with 800 labeled samples. From left to right: Input images; Ground-truth; Estimation of our method; Estimation of Standard RF; Estimation of Optimal RF.

5. EXPERIMENTS

We evaluate our method on both 2D, and 3D brain related medical image segmentation tasks as well as two machine learning benchmarks.

The retinal vessel, a part of the Central Nervous System (CNS), directly reflects the vascular condition of CNS. The accurate segmentation of vessels is important for this analysis. Much progress has been made based on either random forest (Gu et al., 2017) or deep learning (Liu et al., 2019). The DRIVE dataset (Staal et al., 2004) is a widely used 2D retinal vessel segmentation dataset that comprises of 20 training images and 20 testing ones. Each image is a 768 × 584 color image along with manual segmentation. For the image, we extract two types of widely used features: 1, local patch $x_1 \in R^{15\times15\times3}$ of target. 2, $x_2 \in R^{4\times7\times3}$ Gabor wavelets (Soares et al., 2006). We also investigate the single neuron segmentation in a brain image. BigNeuron project[1] (Peng et al., 2015) is a 3D neuronal dataset with ground truth annotation from experts. For BigNeuron data, we manually picked 13 images among which a random 10 were used for training while the rest were left for testing, because this dataset is designed for tracing rather than segmentation. For example, some annotation is visibly thinner than the actual neuron. Furthermore, the image may contain multiple neurons but only one is properly annotated. For both datasets, we randomly collected 40,000 (20,000 positive and 20,000 negative) samples from the training and testing sets, respectively. For 3D data, our feature is $x_1 \in R^{15\times15\times7}$ local cube similar to the setting of Gu et al. (2017).

Apart from the medical imaging, we also demonstrate the generality of our method on two binary machine learning benchmark, IJCNN1 (Prokhorov, 2001) and Madelon (Guyon et al., 2004), in Libsvm Repository (Chang and Lin, 2011).

During the evaluation, we randomly selected a certain number n of labeled samples from the whole training set while leaving the rest unlabeled. Standard Random Forest (RF) is trained with n labeled training data only. Our method and RobustNode (Liu et al., 2015) are trained with both labeled data and unlabeled

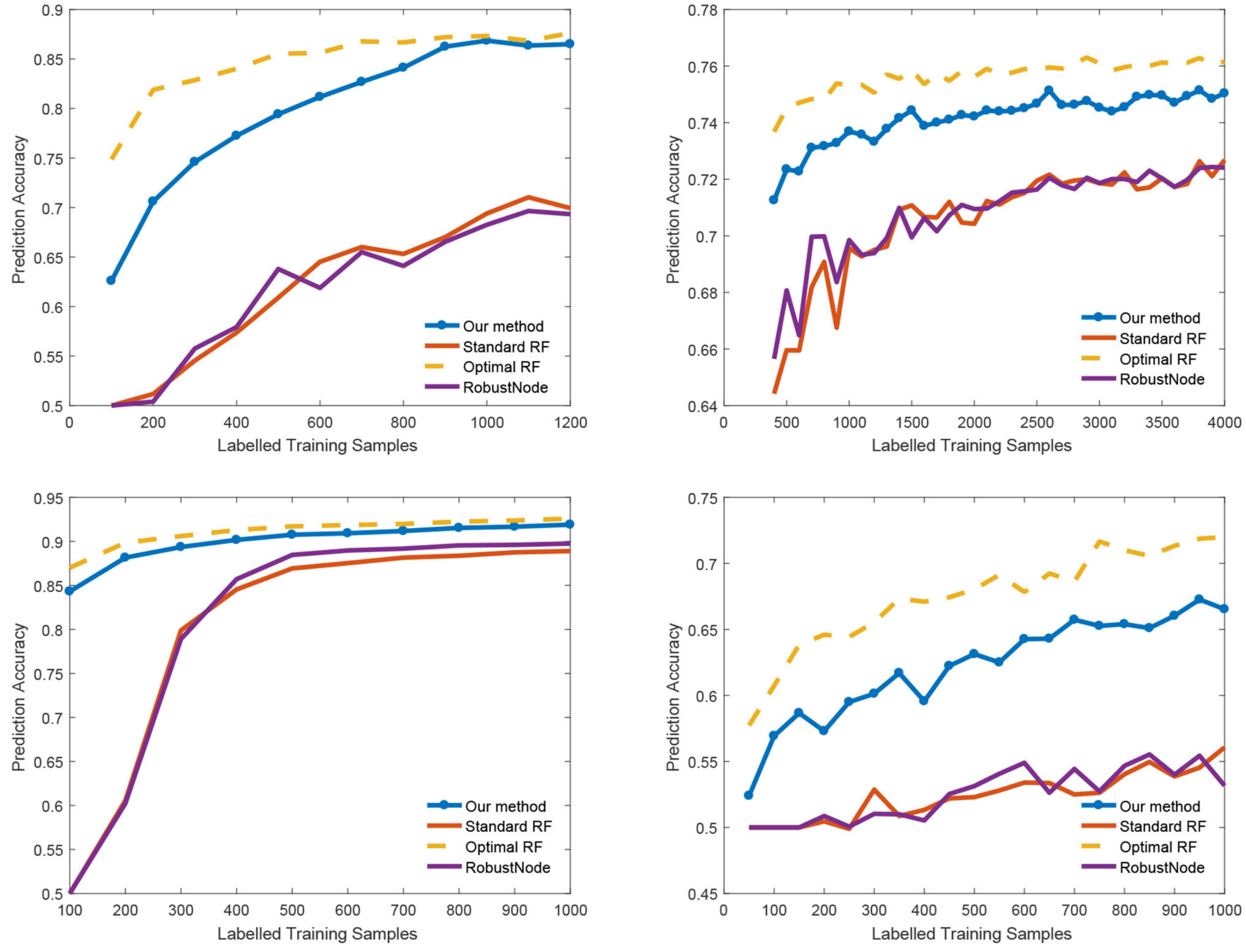

FIGURE 4 | Classification accuracy vs. number of labeled samples.

---

[1] https://www.alleninstitute.org/bigneuron/about/

TABLE 1 | Classification accuracy (represented in percentage %) on different dataset.

	Drive	Big neuron	IJCNN1	Madelon
Our method	79.42	74.16	89.36	59.57
Standard RF	60.90	70.93	79.89	51.33
Robust node RF	63.79	70.99	78.92	50.53
Optimal RF	85.53	75.55	91.29	67.10

We show the accuracy on the training sample of 400 (DRIVE), 1,500 (Big Neuron), 300 (IJCNN1), and 400 (Madelon).

data. For reference, we also compared it with Optimal RF which is trained with labeled data as a standard RF. However, its node splitting is supervised with the whole training samples and their label. Optimal RF indicates the upper bound for all of semi-supervised learning algorithms.

5.1. Medical Imaging Segmentation

First, we illustrate the visual performance of segmentation in **Figure 3**. The estimated score is the possibility of the vessel given by the individual method. Our algorithm has consistently improved the estimation compared to the standard RF.

5.2. Quantitative Analysis

We also report the classification accuracy with respect to the number of labeled data in **Figure 4**, **Table 1**. We compared our method with alternatives on both medical imaging segmentation and machine learning benchmarks. **Figure 4** shows that our algorithm significantly outperformed alternative methods. Specifically, in the DRIVE dataset, our algorithm approaches the upper bound at 1,000 labeled samples. In the IJCNN1 dataset, our method quickly approaches the optimal one while the alternatives take 400 samples to approach.

6. CONCLUSION

In this paper, we propose a novel semi-supervised random forest to tackle the challenging problem of the lacking annotation in the analysis of medical imaging such as a brain image. Observing that the bottleneck of the standard random forest is the biased information gain estimation, we replaced it with a novel graph-embedded entropy which incorporates information from both labeled and unlabeled data. Empirical results show that our information gain is more reliable than the one used in traditional random forest under insufficient labeled data. By slightly modifying the training process of the standard random forest, our algorithm significantly improves the performance while preserving the virtue of the random forest. Our method has shown a superior performance with very limited data in both brain imaging analysis and machine learning benchmarks.

DATA AVAILABILITY STATEMENT

All datasets generated for this study are included in the article/supplementary material.

AUTHOR CONTRIBUTIONS

All authors listed have made a substantial, direct and intellectual contribution to the work, and approved it for publication.

FUNDING

This research was supported by JST, ACT-X Grant Number JPMJAX190D, Japan and the National Natural Science Foundation of China (Grant No. 61873188).

REFERENCES

Belkin, M., and Niyogi, P. (2004). Semi-supervised learning on Riemannian manifolds. *Mach. Learn.* 56, 209–239. doi: 10.1023/B:MACH.0000033120.25363.1e

Breiman, L., Friedman, J., Stone, C. J., and Olshen, R. A. (1984). *Classification And Regression Trees*. CRC Press.

Chang, C.-C., and Lin, C.-J. (2011). Libsvm: A library for support vector machines. *ACM Trans. Intell. Syst. Technol.* 2:27. doi: 10.1145/1961189.1961199

Chapelle, O., Scholkopf, B., and Zien, A. (2006). *Semi-Supervised Learning*. London: MIT Press. doi: 10.7551/mitpress/9780262033589.001.0001

Criminisi, A., Shotton, J., and Konukoglu, E. (2012). Decision forests: a unified framework for classification, regression, density estimation, manifold learning and semi-supervised learning. *Found. Trends. Comput. Graph. Vis.* 7, 81–227. doi: 10.1561/0600000035

Gu, L., Zhang, X., Zhao, H., Li, H., and Cheng, L. (2017). Segment 2D and 3D filaments by learning structured and contextual features. *IEEE Trans. Med. Imaging* 36, 596–606. doi: 10.1109/TMI.2016.2623357

Gu, L., Zheng, Y., Bise, R., Sato, I., Imanishi, N., and Aiso, S. (2017). "Semi-supervised learning for biomedical image segmentation via forest oriented super pixels(voxels)," in *Medical Image Computing and Computer Assisted InterventionŠ MICCAI 2017*, eds M. Descoteaux, L. Maier-Hein, A. Franz, P. Jannin, D. L. Collins, and S. Duchesne (Quebec City, QC: Springer International Publishing), 702–710. doi: 10.1007/978-3-319-66182-7_80

Guyon, I., Gunn, S., Hur, A. B., and Dror, G. (2004). "Result analysis of the NIPS 2003 feature selection challenge," in *Proceedings of the 17th International Conference on Neural Information Processing Systems, NIPS'04* (Cambridge, MA: MIT Press), 545–552.

Joachims, T. (1999). "Transductive inference for text classification using support vector machines," in *Proceedings of the Sixteenth International Conference on Machine Learning, ICML '99* (San Francisco, CA: Morgan Kaufmann Publishers Inc.), 200–209.

Leistner, C., Saffari, A., Santner, J., and Bischof, H. (2009). "Semi-supervised random forests," in *2009 IEEE 12th International Conference on Computer Vision* (Kyoto), 506–513. doi: 10.1109/ICCV.2009.5459198

Li, M., and Zhou, Z. H. (2007). Improve computer-aided diagnosis with machine learning techniques using undiagnosed samples. *IEEE Trans. Syst. Man Cybern.* 37, 1088–1098. doi: 10.1109/TSMCA.2007.904745

Liao, H., Zhu, Z., and Peng, Y. (2018). Potential utility of retinal imaging for AlzheimerŠs disease: a review. *Front. Aging Neurosci.* 10:188. doi: 10.3389/fnagi.2018.00188

Liu, B., Gu, L., and Lu, F. (2019). "Unsupervised ensemble strategy for retinal vessel segmentation," in *Medical Image Computing and Computer Assisted Intervention-MICCAI 2019*, eds D. Shen, T. Liu, T. M. Peters, L. H. Staib, C. Essert, S. Zhou, P. T. Yap, and A. Khan (Shenzhen: Springer International Publishing), 111–119. doi: 10.1007/978-3-030-32239-7_13

Liu, X., Song, M., Tao, D., Liu, Z., Zhang, L., Chen, C., et al. (2015). Random forest construction with robust semisupervised node splitting. *IEEE Trans. Image Process*. 24, 471–483. doi: 10.1109/TIP.2014.2378017

Niu, Y., Gu, L., Lu, F., Lv, F., Wang, Z., Sato, I., et al. (2019). "Pathological evidence exploration in deep retinal image diagnosis," in *AAAI conference on artificial intelligence (AAAI)* (Honolulu: AAAI Press), 1093–1101. doi: 10.1609/aaai.v33i01.33011093

Peng, H., Hawrylycz, M., Roskams, J., Hill, S., Spruston, N., Meijering, E., et al. (2015). Bigneuron: large-scale 3D neuron reconstruction from optical microscopy images. *Neuron* 87, 252–256. doi: 10.1016/j.neuron.2015.06.036

Prokhorov, D. (2001). *IJCNN 2001 Neural Network Competition*. Washington, DC: IJCNN2001.

Soares, J. V. B., Leandro, J. J. G., Cesar, R. M., Jelinek, H. F., and Cree, M. J. (2006). Retinal vessel segmentation using the 2-D gabor wavelet and supervised classification. *IEEE Trans. Med. Imaging* 25, 1214–1222. doi: 10.1109/TMI.2006.879967

Soltaninejad, M., Zhang, L., Lambrou, T., Yang, G., Allinson, N., and Ye, X. (2018). "MRI brain tumor segmentation and patient survival prediction using random forests and fully convolutional networks," in *Brainlesion: Glioma, Multiple Sclerosis, Stroke and Traumatic Brain Injuries*, eds A. Crimi, S. Bakas, H. Kuijf, B. Menze, and M. Reyes (Cham: Springer International Publishing), 204–215. doi: 10.1007/978-3-319-75238-9_18

Staal, J., Abramoff, M. D., Niemeijer, M., Viergever, M. A., and van Ginneken, B. (2004). Ridge-based vessel segmentation in color images of the retina. *IEEE Trans. Med. Imaging* 23, 501–509. doi: 10.1109/TMI.2004.825627

Zhou, D., Bousquet, O., Lal, T., Weston, J., and Scholkopf, B. (2004). "Learning with local and global consistency," in *NIPS* (Vancouver, BC).

Zhu, X. (2006). *Semi-Supervised Learning Literature Survey*. Technical report, University of Wisconsin-Madison.

Zhu, X., Ghahramani, Z., Lafferty, J., et al. (2003). "Semi-supervised learning using Gaussian fields and harmonic functions," in *ICML, Vol. 3* (Washington, DC), 912–919.

Conflict of Interest: The authors declare that the research was conducted in the absence of any commercial or financial relationships that could be construed as a potential conflict of interest.

frontiers in Neuroinformatics

ORIGINAL RESEARCH
published: 16 November 2020
doi: 10.3389/fninf.2020.607365

Non-invasive Evaluation of Brain Death Caused by Traumatic Brain Injury by Ultrasound Imaging

Ningning Niu, Ying Tang, Xiaoye Hao and Jing Wang*

Department of Ultrasound, Tianjin First Center Hospital, Tianjin, China

Objectives: To investigate the clinical value of non-invasive ultrasound imaging in the evaluation of brain death caused by traumatic brain injury.

Methods: Thirty-four patients with acute severe traumatic brain injury were admitted to hospital within 48 h after injury. All patients were monitored intracranial pressure, transcranial Doppler, echocardiography examination, collection intracranial pressure, MCA-Vs, MCA-Vd, MCA-Vm, EF, LVMPI, RVMPI and other indicators, and combined with clinical conditions and other related data for comparative study and statistical analysis.

Results: The blood flow spectrum was characterized by diastolic retrograde blood flow spectrum pattern and nail waveform spectrum shape when the patient had clinical brain death. For the parameters of transcranial Doppler, there were significant differences in MCA-Vm and PI between clinical brain death group and normal control group ($P < 0.05$). For the parameters of echocardiography, there were statistically significant differences in EF, LVMPI, and RVMPI between clinical brain death group and normal control group ($P < 0.05$).

Conclusion: Non-invasive dynamic monitoring of cerebral hemodynamics and cardiac function parameters in patients with severe craniocerebral injury can provide a high accuracy and reliability for the preliminary diagnosis of brain death in patients with severe craniocerebral injury. It is helpful for early evaluation of prognosis and provides effective monitoring methods and guidance for clinical treatment.

Keywords: brain death, ultrasound, echocardiography, intracranial pressure, transcranial Doppler

Edited by:
Heye Zhang,
Sun Yat-sen University, China

Reviewed by:
Chenchu Xu,
Western University (Canada), Canada
Kexiang Li,
University of Wisconsin–Milwaukee,
United States

****Correspondence:***
Ying Tang
doctortang2010@aliyun.com

Received: *17 September 2020*
Accepted: *12 October 2020*
Published: *16 November 2020*

Citation:
Niu N, Tang Y, Hao X and Wang J (2020) Non-invasive Evaluation of Brain Death Caused by Traumatic Brain Injury by Ultrasound Imaging. Front. Neuroinform. 14:607365. doi: 10.3389/fninf.2020.607365

INTRODUCTION

With the rapid development of economic construction, urbanization and transportation, the incidence of traumatic brain injury increasing gradually and the number of patients who died due to craniocerebral trauma are also increasing gradually. However, the mortality rate of patients with severe traumatic brain injury is extremely high. In clinical work, we found that many patients with severe traumatic brain injury have been in the state of spontaneous breathing arrest, deep coma, dilation and fixation of double pupil due to intracranial hypertension or other reasons, and they are completely dependent on the ventilator to maintain breathing, that is, the brain function has been completely irreversible damage. In this case, the maintenance of respiration and drug circulation by ventilator often can maintain the heart rate and circulation for a long time until the organs of the whole body fail. This not only wastes valuable medical resources, but also limits the development of organ transplantation. Brain death will produce a series of pathophysiological changes including hemodynamics, endocrine, metabolism, inflammatory reaction, among which the most prominent manifestation is hemodynamic disorder. Non-invasive dynamic monitoring of cerebral hemodynamics and cardiac function parameters in patients with severe traumatic brain injury by ultrasound imaging is conducive to early evaluation of the prognosis of patients, providing effective monitoring means and guiding methods for clinical treatment, so as to provide a favorable opportunity for organ transplantation.

MATERIALS AND METHODS

Subjects

Thirty-four patients with acute severe traumatic brain injury were admitted to hospital within 48 hours after injury. There were 30 males and 4 females, aged 26–53 years old. The injury mechanism included 17 cases of accelerated injury, 13 cases of deceleration injury and 4 cases of mixed injury. Among them, 18 cases were injured by traffic accidents, 8 cases were caused by falling, 5 cases were injured by striking, and 3 cases were injured by other reasons. All cases were diagnosed by CT examination before or after admission. According to CT diagnosis, brain injury was classified. The main injury types included: 15 cases of cerebral contusion and laceration combined with acute subdural hematoma, 11 cases of cerebral contusion and laceration with intracerebral hematoma, 6 cases of acute epidural hematoma, and 2 cases of extensive brain contusion and brain swelling. According to the state of consciousness, 19 patients with GCS score of 6-8 and 15 patients with GCS score less than 6. Among them, 9 patients with multiple injuries, 5 patients with closed fractures of extremities (early manual reduction and plaster fixation in orthopedics department, and then open reduction and internal fixation according to the condition of neurosurgery) and 4 patients with pulmonary contusion were treated conservatively (**Figure 1**).

All the patients were monitored intracranial pressure and dynamic cerebral hemodynamic indexes of transcranial Doppler after admission. According to the prognosis of the patients, they were divided into clinical brain death group (see the following clinical brain death diagnostic criteria) and survival group. Another 20 healthy subjects were selected as the control group, and laboratory, transcranial Doppler and echocardiography were performed respectively. All measurements were performed by a physician with 5 years of experience in ultrasonography.

Inclusive Criteria and Exclusion Criteria

Inclusive criteria: Admission within 48 h after injury; age 20–60 years old; GCS $\leq$ 8 points at admission.

FIGURE 1 | The CT examination of one patient with cerebral contusion and laceration with intracerebral hematoma.

Exclusion criteria: Patients with severe multiple trauma, combined injury and shock; those who have been transferred to our hospital after craniotomy in another hospital; patients with heart, lung, liver, and kidney dysfunction; patients with stenosis of internal carotid artery system and vertebrobasilar artery system; patients whose temporal window was completely closed and could not detect blood flow signals; patients whose family members gave up treatment.

Clinical Diagnostic Criteria for Brain Death

The patients were clinically diagnosed as brain death. The criteria for brain death were referred to the criteria for brain death (adult) (Revised Version) drafted by the drafting group of the Ministry of Health in 2003 and the criteria and technical specifications for brain death (adult quality control version) in 2013. (i) Deep shock; (ii) disappearance of the papillary light reflex and corneal reflection; (iii) absence of spontaneous respiration; (iv) electroencephalogram displaying resting potential; (v) negative atropine test; (vi) no change in all of these conditions for 12 h after initial observation, then brain death was determined (Su et al., 2018).

Intracranial Pressure Detection Monitoring

Intracranial pressure detection monitoring was carried out by intracranial pressure monitor (Canimo MPM-1, United States), with an intracerebral probe, and the patients who needed outdoor drainage used intraventricular probe. ICP monitoring lasted for 1 week, and some patients were slightly prolonged according to their needs. Head wounds should be cleaned and disinfected daily to prevent intracranial infection. If the baseline of intracranial pressure monitor is shifted due to the patient's turning over or other nursing work, the baseline should be adjusted to zero according to the situation.

Transcranial Doppler Examination

The cerebral hemodynamics was detected by transcranial Doppler (TCD) (DWL Multi-Dop X_2, Germany). The middle cerebral artery was examined from the temporal window with a 2 MHz probe at a sampling depth of 45–60 mm. When the spectrum shape is smooth and the sound in the frequency window is loud was taken as the parameter index. All patients were placed in supine position with the head of bed raised 30 degrees. The detection time was 9:00 a.m. (before mannitol) and 4:00 p.m. (1 h after mannitol) for 7 days. After reaching the standard of clinical brain death, the patients were checked every 2–6 h according to their circulatory system. In order to exclude the influence of human subjective factors and technical factors on the experimental value, the cerebral blood flow detector was relatively fixed. The indexes included pulsatility index (PI), resistance index (RI), systolic blood flow velocity (MCA-Vs), diastolic blood flow velocity (MCA-Vd), and mean middle cerebral artery velocity (MCA-Vm).

Echocardiography

Echocardiography was detected by ultrasound diagnostic system (Mindray M7, China) with a S4 probe at a frequency of 1–4 MHz. The patient was in supine position. The weight, height and blood pressure were recorded and BSA was calculated. The indexes of echocardiographic parameters included left ventricular end diastolic diameter (LVDd), left ventricular end systolic diameter (LVDs), and ejection fraction (EF). The myocardial performance index (MPI) was calculated by the ratio of the sum of isovolumic systolic (ICT) and isovolumic diastolic (IRT) to ejection time (ET), MPI = (ICT + IRT)/ET. The blood flow spectrum of mitral valve, tricuspid valve, aortic valve, and pulmonary valve was clearly displayed to calculate left ventricular (LVMPI) and right ventricular (RVMPI) according to the formula. In order to reduce the error of echocardiography as much as possible, the average value of three consecutive cardiac cycles was taken for each index. All examinations were completed by one doctor and the images were stored at the same time.

Statistical Analysis

Statistical analysis was performed using SPSS Version 19.0 (IBM, Armonk, NY, United States). Continuous variables (normally distributed) were expressed as the mean ± standard deviation (SD). The differences between the two groups were compared by independent sample *t* test. The correlations were analyzed using Spearman's correlation analysis, and the correlation coefficients (r) were calculated. A two-sided P-value < 0.05 was considered to indicate statistical significance.

RESULTS

Changes of ICP and Cerebral Blood Flow Spectrum During Clinical Brain Death

In the control group, the cerebral blood flow spectrum was characterized by high flow velocity and low resistance, the spectrum pattern was smooth, and the sound of blood flow signal was loud (**Figure 2**). In the acute stage of traumatic brain injury, the spectrum of cerebral blood flow in this group showed high peak in systolic phase, low and high in diastolic phase, which was the characteristic spectrum manifestation of increased intracranial pressure, ICP was positively correlated with PI ($r = 0.872$, $P < 0.001$) and MCA-Vm ($r = 0.562$, $P = 0.003$). With the increase of ICP, the amplitude of cerebral blood flow spectrum gradually decreased, and the MCA-Vm gradually decreased, showing a low flow rate and high resistance spectrum morphology. When the patient had clinical brain death, the blood flow spectrum was characterized by diastolic retrograde blood flow spectrum pattern and nail waveform spectrum shape (**Figure 3**). At this time, ICP of intracranial pressure monitoring was more than 70 mmHg, which exceeded the average arterial pressure of the patient. The ICP of some patients fluctuate at about 100 mmHg before clinical death.

Comparisons of TCD Parameters

In this series of data, 15 patients with severe cerebral trauma has the characteristic performance of sum or nail spectrum by TDI before clinical brain death, and 14 patients were confirmed to have clinical brain death. The characteristic spectrum changes of cerebral perfusion arrest appeared earlier than clinical brain death. After the diagnosis of clinical brain death was established, the spectrum pattern of cerebral blood flow showed the spectrum pattern of nail spectrum or characteristic cerebral perfusion stop without blood flow signal. There were significant differences in MCA-Vm and PI between clinical brain death group and normal control group. The cerebral blood flow index was significantly lower after severe traumatic brain injury, than that of the normal control group, and PI was significantly higher than that of the normal control group ($P < 0.05$) (**Table 1**).

Comparisons of Echocardiography Parameters

Echocardiography parameters were performed in brain death group and normal control group (**Figures 4–5**). There were statistically significant differences in EF, LVMPI, and RVMPI between clinical brain death group and normal control group. LVMPI and RVMPI were higher in clinical brain death group than those in normal control group, and EF was lower than that in normal control group ($P < 0.05$) (**Table 2**).

DISCUSSION

Severe craniocerebral trauma patients die because of the sharp increase of intracranial pressure and the formation of cerebral hernia, which is the difficulty of clinical treatment in neurosurgery. With the continuous development of Neurosurgery, the effect of rescue treatment has been improved, but the effect is not satisfactory (Shrestha et al., 2018). The maintenance of cerebral perfusion and cerebral circulation depends on reasonable intracranial pressure and mean arterial blood pressure. The cerebral hemodynamic state changes with the increase of intracranial pressure. The main pathophysiological manifestations are insufficient cerebral perfusion, ischemia and

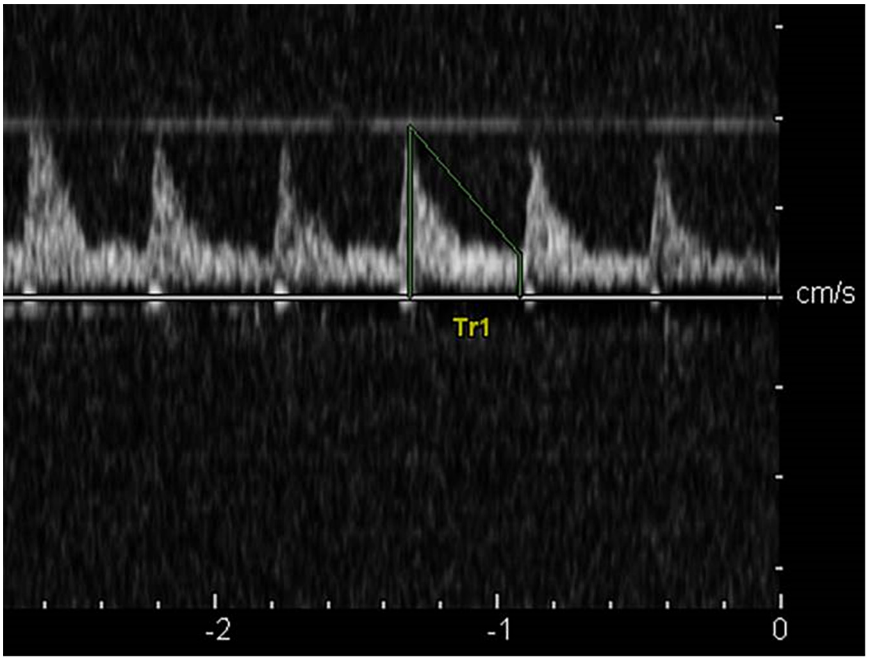

FIGURE 2 | The cerebral blood flow spectrum in the control group.

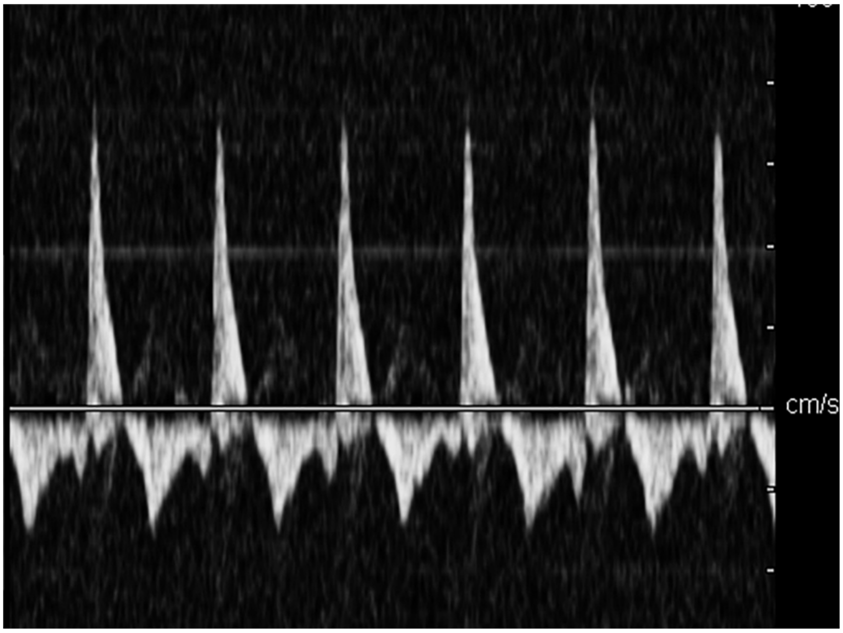

FIGURE 3 | The diastolic retrograde blood flow spectrum pattern when patient had clinical brain death.

hypoxia of brain tissue, aggravation of brain edema, even cerebral circulation stop, resulting in clinical brain death.

Brain death refers to the irreversible stop of whole brain function due to persistent and severe cerebral ischemia, hypoxia or other reasons (Tang et al., 2019). The diagnosis of brain death requires comprehensive clinical conditions and a variety of examination methods (Mullaguri et al., 2018). At present, there are a variety of detection methods to help confirm brain death, including radionuclide scanning, cerebral angiography and so on. These examination methods have important value for the diagnosis of brain death. However, the instruments and equipment for these examinations are expensive, and

TABLE 1 | Parameters of TCD in brain death group and normal group.

Group	*N*	MCA-Vm (cm/s)	PI	ICP (mmHg)
Normal	20	58.55 ± 7.05	0.81 ± 0.16	
Brain death	14	15.82 ± 7.99	3.56 ± 1.13	68.18 ± 19.62
t		18.89	2.46	
P		0.001	0.001	

Statistically significant difference compared with control group (P-value < 0.05). TCD, transcranial Doppler; MCA-Vm, mean middle cerebral artery velocity; PI, pulsatility index; ICP, intracranial pressure detection.

most of them are invasive examinations, which need to be transported to specific examination rooms. There are many inconveniences in clinical application, which limit these methods as routine examination methods. Electroencephalogram (EEG) can continuously monitor patients with craniocerebral injury, but EEG detection is based on EEG resting as the diagnostic criteria of brain death, and there are still many problems in EEG resting as the diagnostic criteria, which has been controversial in clinical practice (Kasapoglu et al., 2019). In recent years, some scholars have found that not all patients with clinical brain death have EEG resting state, but some patients have extensive EEG activities.

Transcranial Doppler can monitor the cerebral hemodynamic status of patients with severe traumatic brain injury, describe the cerebral hemodynamic state combined with mean arterial blood pressure, and evaluate the cerebral perfusion and intracranial pressure (Cacciatori et al., 2018; Berthoud et al., 2019). Invasive intracranial pressure monitoring is the most direct and accurate detection method for patients with intracranial pressure, which is currently recognized as the gold standard for intracranial pressure detection (Roth et al., 2019). In this study, we continuously monitored the changes of intracranial pressure in patients with severe traumatic brain injury, combined with the monitoring of mean arterial blood pressure. At the same time, the relevant parameters of cerebral hemodynamics were dynamically detected by TCD.

The results showed that, with the slight increase of intracranial pressure, the condition was aggravated, MCA-Vd decreased in the early stage, while MCA-Vs increased slightly, and MCA-Vm was normal; with the moderate and severe increase of intracranial pressure, the condition was further aggravated, MCA-Vd and MCA-Vs decreased, MCA-Vd decreased more significantly, and PI increased gradually. When the blood pressure reaches the mean arterial blood pressure level and continues, diastolic regurgitation or nail spectrum may appear finally. The changes of parameters of cerebral blood flow state were significantly corresponding to the changes of intracranial pressure and disease condition. When patients with complete diastolic reverse blood flow or nail waveform, clinical brain death will occur in a short period of time. This indicates that the brain function of the patients has undergone serious and completely irreversible changes when the above-mentioned manifestations

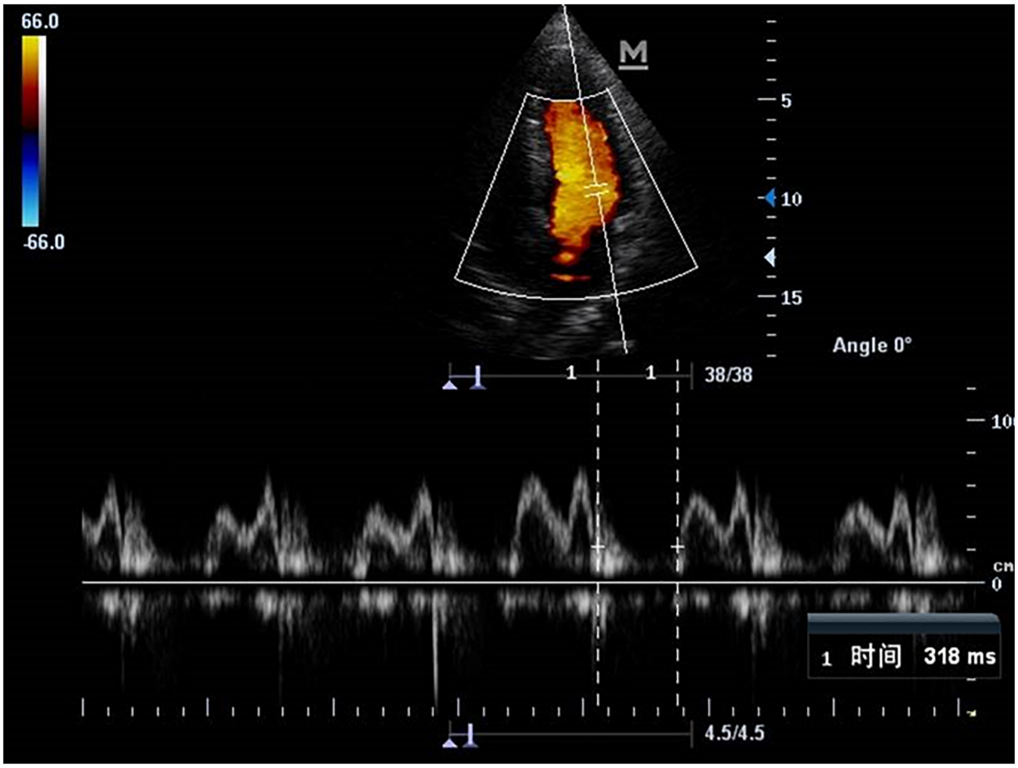

FIGURE 4 | The blood flow spectrum of mitral valve in patient with clinical brain death.

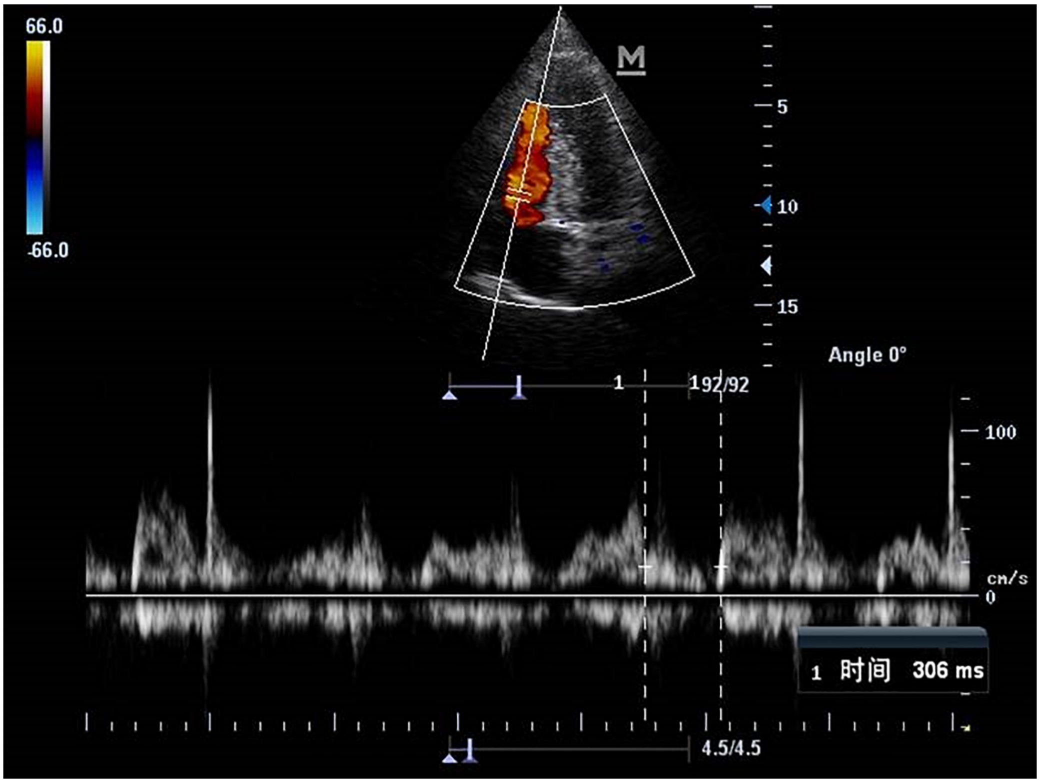

FIGURE 5 | The blood flow spectrum of tricuspid valve in patient with clinical brain death.

of cerebral blood flow state detected by non-invasive detection, indicating that the patient is about to or has suffered from clinical brain death.

Therefore, in the process of clinical treatment, before the typical spectrum of complete diastolic reverse blood flow or nail spectrum appears in TCD detection, active treatment should be taken as soon as possible to effectively control and reduce the improvement of cerebral perfusion and cerebral ischemia and hypoxia, which is of great significance for improving the prognosis and reducing the mortality of patients.

TABLE 2 | Parameters of echocardiography in brain death group and normal group.

Group	LVDd (cm)	LVDs (cm)	EF	LVMPI	RVMPI
Normal	45.61 ± 10.37	30.64 ± 10.15	61.57 ± 3.27	0.56 ± 0.13	0.25 ± 0.11
Brain death	46.33 ± 11.25	32.16 ± 10.82	59.38 ± 3.54	0.66 ± 0.16	0.41 ± 0.12
t	0.893	2.048	−2.667	1.507	3.902
P	0.377	0.084	0.01	0.05	0.008

Statistically significant difference compared with control group (P-value < 0.05). LVDd, left ventricular end diastolic diameter; LVDs, left ventricular end systolic diameter; EF, ejection fraction; LVMPI, the myocardial performance index of left ventricular; RVMPI, the myocardial performance index of right ventricular.

As an important organ to maintain hemodynamics, the heart can cause secondary heart injury in severe brain injury, especially in brain death (El-Battrawy et al., 2018). The lower the Lasco score is, the greater the decrease of EF would be. Brain death can lead to decreased cardiac systolic function, left ventricular ejection fraction, and ventricular wall motion.

As a non-invasive and rapid technique, ultrasound can dynamically monitor the structure and function of the heart. Myocardial performance index (MPI) as a comprehensive index to evaluate the overall systolic and diastolic function of the heart can be used to evaluate the overall ventricular function (Askin et al., 2018; Maria et al., 2019). When left ventricular systolic or diastolic dysfunction occurs, the isovolumic systolic period (ICT), isovolumic diastolic period (IRT), and ejection time (ET) change accordingly. Therefore, the measured value of MPI will also change accordingly, but it is not affected by many conditions such as age, heart rate, valve regurgitation, preload and afterload, cardiac geometry, two-dimensional image quality and angle between sampling line and blood flow direction. For patients with no change in left ventricular configuration, the change of global ventricular function can be evaluated only when diastolic function changes. In this study, the results showed that EF was lower in clinical brain death group than that in normal control group, LVESD, LVMPI, and RVMPI were higher than those in normal control group. There were significant differences in LVESD, EF, LVMPI, and RVMPI between clinical brain death group and normal control group.

Therefore, once the typical spectrum of complete diastolic reverse blood flow or nail spectrum appear in TCD detection, EF decreases and LVMPI, RVMPI increased in Echocardiography, that the patient has entered the state of brain death, and it is of no medical significance to continue treatment. With the informed consent of patients' families, we should improve the systematic examination methods of brain death as soon as possible, such as EEG and brainstem evoked potential, to further diagnose brain death and save limited medical resources. Whether the patients who died of non-traumatic brain injury also have the characteristic blood flow changes of the above mentioned brain death needs further data collection and research. Non-invasive dynamic monitoring of cerebral hemodynamics and cardiac function parameters in patients with severe craniocerebral injury can provide a high accuracy and reliability for the preliminary diagnosis of brain death in patients with severe craniocerebral injury. It is helpful for early evaluation of prognosis and provides effective monitoring methods and guidance for clinical treatment. With the development of medical image data, it is helpful to further dig out the biometrics and other information in the image, which will further improve the accuracy of prediction (Zheng et al., 2020a,b).

DATA AVAILABILITY STATEMENT

The original contributions presented in the study are included in the article/supplementary material, further inquiries can be directed to the corresponding author.

ETHICS STATEMENT

The studies involving human participants were reviewed and approved by the Medical Ethics Committee of the Tianjin First Central Hospital. The patients/participants provided their written informed consent to participate in this study.

AUTHOR CONTRIBUTIONS

YT contributed to the conception of the study and helped perform the analysis with constructive discussions. XH, NN, and JW performed the experiment. NN contributed to the data analysis and wrote the manuscript. All authors contributed to the article and approved the submitted version.

FUNDING

This study was supported by the project of the Tianjin First Central Hospital (2019CF39).

ACKNOWLEDGMENTS

We thank Miss Jing Liu and Miss Yang Liu for collaboration in data acquisition.

REFERENCES

Askin, L., Cetin, M., Tasolar, H., and Akturk, E. (2018). Left ventricular myocardial performance index in prediabetic patients without coronary artery disease. *Echocardiography* 35, 445–449. doi: 10.1111/echo.13822

Berthoud, V., Ellouze, O., Constandache, T., Martin, A., and Guinot, P. G. (2019). Transcranial doppler waveform patterns in nonpulsatile blood flow under venoarterial extracorporeal membrane oxygenation for brain death diagnosis. *ASAIO J.* 66:e64. doi: 10.1097/mat.0000000000001031

Cacciatori, A., Godino, M., and Mizraji, R. (2018). Utility of transcranial doppler in the coordination of transplants: 10 years of experience. *Trans. Proc.* 50, 408–411.

El-Battrawy, I., Borggrefe, M., and Akin, I. (2018). Myocardial dysfunction following brain death. *J. Am. Coll. Cardiol.* 71:368. doi: 10.1016/j.jacc.2017.09.1160

Kasapoglu, U. S., Haliloglu, M., Bilgili, B., and Cinel, I. (2019). The role of transcranial doppler ultrasonography in the diagnosis of brain death. *Turk Anesteziyoloji Ve Reanimasyon* 47, 367–374. doi: 10.5152/TJAR.2019.82258

Maria, D., Javier, O. F., Chantal, D. K. M., Thomas, F. H., Rasmus, M., Saed, A. A., et al. (2019). Myocardial performance index by tissue doppler echocardiography predicts adverse events in patients with atrial fibrillation. *Eur. Heart J. Cardiovasc. Imaging* 21, 560–566. doi: 10.1093/ehjci/jez173

Mullaguri, N., Sarwal, A., Katyal, N., Nattanamai, P., and Newey, C. R. (2018). Trans-cranial doppler as an ancillary study supporting irreversible brain injury in a post cardiac arrest patient on extracorporeal membrane oxygenation. *Cureus* 10:e2161. doi: 10.7759/cureus.2161

Roth, C., Ferbert, A., and Matthaei, J. (2019). Progress of intracranial pressure and cerebral perfusion pressure in patients during the development of brain death. *J. Neurol. Sci.* 398, 171–175. doi: 10.1016/j.jns.2019.01.048

Shrestha, P., Ansari, S. R., and Ghimire, R. K. (2018). Transcranial doppler ultrasonography cerebral blood flow dynamics study of neurosurgical patients in peri-agonal period with fixed dilated or non-reacting pupils. *Br. J. Neurosurg.* 32, 182–187. doi: 10.1080/02688697.2018.1467374

Su, Y.-Y., Chen, W.-B., Liu, G., Fan, L.-L., Zhang, Y., Ye, H., et al. (2018). An investigation and suggestions for the improvement of brain death determination in china. *Chin. Med. J.* 131, 2910–2914. doi: 10.4103/0366-6999.247193

Tang, Y., Zhao, J., Niu, N., Liu, Y., and Liu, J. (2019). A comparison study of real-time ultrasound elastography and electron microscopy for the assessment of liver damage induced by brain death. *Ultrasound Med. Biol.* 45, 935–943. doi: 10.1016/j.ultrasmedbio.2018.10.017

Zheng, Y., Song, H., Zhang, K., Fan, J., and Liu, X. (2020a). "Dynamically spatiotemporal regularized correlation tracking," in *IEEE Transactions on Neural Networks and Learning Systems*, Piscataway, NJ: IEEE, doi: 10.1109/TNNLS.2019.2929407

Zheng, Y., Sun, Y., Muhammad, K., and de Albuquerque, V. H. C. (2020b). "Weighted LIC-based structure tensor and its applications in image content perception and processing," in *IEEE Transactions on Industrial Informatics* Piscataway, NJ: IEEE.

Conflict of Interest: The authors declare that the research was conducted in the absence of any commercial or financial relationships that could be construed as a potential conflict of interest.

frontiers in Neuroinformatics

SYSTEMATIC REVIEW
published: 20 November 2020
doi: 10.3389/fninf.2020.610967

Review of Deep Learning Approaches for the Segmentation of Multiple Sclerosis Lesions on Brain MRI

Chenyi Zeng[1], *Lin Gu*[2,3], *Zhenzhong Liu*[4,5] *and Shen Zhao*[1]*

[1] *School of Intelligent Systems Engineering, Sun Yat-Sen University, Guangzhou, China,* [2] *RIKEN AIP, Tokyo, Japan,* [3] *The University of Tokyo, Tokyo, Japan,* [4] *Tianjin Key Laboratory for Advanced Mechatronic System Design and Intelligent Control, School of Mechanical Engineering, Tianjin University of Technology, Tianjin, China,* [5] *National Demonstration Center for Experimental Mechanical and Electrical Engineering Education, Tianjin University of Technology, Tianjin, China*

In recent years, there have been multiple works of literature reviewing methods for automatically segmenting multiple sclerosis (MS) lesions. However, there is no literature systematically and individually review deep learning-based MS lesion segmentation methods. Although the previous review also included methods based on deep learning, there are some methods based on deep learning that they did not review. In addition, their review of deep learning methods did not go deep into the specific categories of Convolutional Neural Network (CNN). They only reviewed these methods in a generalized form, such as supervision strategy, input data handling strategy, etc. This paper presents a systematic review of the literature in automated multiple sclerosis lesion segmentation based on deep learning. Algorithms based on deep learning reviewed are classified into two categories through their CNN style, and their strengths and weaknesses will also be given through our investigation and analysis. We give a quantitative comparison of the methods reviewed through two metrics: Dice Similarity Coefficient (DSC) and Positive Predictive Value (PPV). Finally, the future direction of the application of deep learning in MS lesion segmentation will be discussed.

Keywords: deep learning, multiple sclerosis, brain MRI, review, segmentation

Edited by:
Yuhui Zheng,
Nanjing University of Information Science and Technology, China

Reviewed by:
Chenchu Xu,
Western University, Canada
Zhiming Luo,
Xiamen University, China

Correspondence:
Shen Zhao
z-s-06@163.com

Received: *28 September 2020*
Accepted: *26 October 2020*
Published: *20 November 2020*

Citation:
Zeng C, Gu L, Liu Z and Zhao S (2020) Review of Deep Learning Approaches for the Segmentation of Multiple Sclerosis Lesions on Brain MRI. Front. Neuroinform. 14:610967. doi: 10.3389/fninf.2020.610967

1. INTRODUCTION

Multiple sclerosis (MS) is a chronic, autoimmune, and demyelinating disease with great clinical significance that affects the central nervous system (CNS). MS is a chronic disease that changes the morphology and structure of the brain due to the harm to the myelin sheath (Zhao et al., 2018). More importantly, MS can cause disability in young adults (Lladó et al., 2012). MS is relatively common in Europe, New Zealand, the United States, and parts of Australia. It has a major impact on the quality of life of the patients and their families due to its pathological characteristics.

The automatic segmentation of MS lesions through Magnetic Resonance Imaging (MRI) is of great clinical and engineering significance. Automatic segmentation of MS lesions is very important to help to detect diagnostic criteria for the disease which contains the spatial pattern of MS lesions in MRI (dissemination in space) and the emergence of new MS lesions(dissemination in time) (Polman et al., 2011). Besides, the automatic segmentation of MS lesions is essential for the quantitative analysis of the disease which is of great value in analyzing the progression of the disease and treatment options. Therefore, identifying and segmenting MS lesions is an indispensable step to characterize the disease and calculate and interpret more professional damage metrics. Before the emergence of the automatic segmentation of MS lesions, segmentation of the MS lesions were finished by experienced neuroradiologists. However, manual segmentation is a time-consuming and tedious process, and more importantly, it is poor efficiency due to intra-observer and inter-observer variability. Therefore, designing an excellent method for automatically segmenting MS lesions has great engineering significance. **Figure 1** shows the morphology of MS lesions in MRI.

Although many methods for automatically segmenting MS lesions have been proposed in recent years, none of them are widely used in clinical practice. This is because this task still encounters many technical problems and challenges. The crucial difficulty is that the intensity distribution of MS and brain gray matter overlap in MRI (Sahraian and Radue, 2007). This is due to the limited resolution of the image, the heterogeneity of the lesion, and the complex shape of the brain tissue, which affects a large number of voxels located at the boundary of different tissues (Mortazavi et al., 2012). In addition, the variability of the appearance of the lesion and the magnetic resonance (MR) acquisitions are also a major challenge (García-Lorenzo et al., 2013). For example, MS lesions present hypointensities in T1-w MRI sequences, and hyperintensities in T2-w, Proton Density weighted(PD-w), and Fluid Attenuated Inversion Recovery T2(T2-FLAIR) MRI sequences, with respect to normal intensities (Hashemi et al., 2012). Due to these severe challenges, the performance of manual segmentation performed by experts outperforms automatic segmentation in most cases. Thus, there is still a demand for a better automatic segmentation method to be proposed to meet the requirements of clinical practice.

A comprehensive review is very important to help future generations design better automatic segmentation models based on the predecessors. In the past few years, there have also been related reviews (Danelakis et al., 2018; Kaur et al., 2020; Shanmuganathan et al., 2020) published. Danelakis et al. (2018) reviews the methods of automatically segmenting MS lesions and pointed out that MRI data acquisition and the injection of the contrast medium during data acquisition are great challenges in the future. Kaur et al. (2020) reviews the state-of-the-art methods by 2019 and lists the future directions obtained from these methods for future reference. Shanmuganathan et al. (2020) reviews the classification and segmentation methods of MS lesions and compares the classification and segmentation methods separately. Their comparison of various strategies shows that the segmentation methods based on deep learning achieve better performance.

Although the previous reviews (Danelakis et al., 2018; Kaur et al., 2020; Shanmuganathan et al., 2020) have done a great job, there are still no reviews that give a comprehensive overview of the deep learning-based automatic segmentation methods individually which achieve excellent performance. Although the previous review also included methods based on deep learning, there are some methods based on deep learning that they did not review. In addition, their review of deep learning methods did not go deep into the specific categories of CNN. They only reviewed these methods in a generalized form, such as supervision strategy, input data handling strategy, etc. In this paper, we focus on reviewing the deep learning-based MS lesion segmentation methods. Compared to previous reviews that categorize these methods based on supervision strategy, we divided these methods into two categories according to their CNN style: patch-wise segmentation and semantic-wise segmentation. The strengths and weaknesses of these two classifications are also given through our investigation and analysis. The fundamental goal of this survey is to help determine the most promising research direction of deep learning in this field.

The rest of this review is organized as follows: In section 2, public datasets and metrics for evaluating algorithm performance will be elucidated. Section 3 reviews various segmentation methods by classifying them into two different categories and presents a qualitative comparison of the algorithms reviewed. A discussion of the future directions is given in section 4.

2. DATASETS AND METRICS

In this section, we will introduce the datasets and metrics used by the methods we reviewed.

2.1. Datasets

The public datasets used by the deep learning-based MS lesion segmentation method has three: MICCAI 2008 (Styner et al., 2008), MICCAI 2016 (Commowick et al., 2018), ISBI 2015 (Carass et al., 2017). In **Table 1**, we illustrate these three public datasets.

2.2. Metrics

There are many evaluation measures used in the literature to quantify the performance of their methods. These evaluation measures are generally obtained by comparing the results of automatic segmentation with ground truth, and most of them are calculated by four basic terms (Goldberg-Zimring et al., 1998):

- TP(True Positive): The prediction is the MS lesion area, and the prediction is correct.
- TN(True Negative): The prediction is not the MS lesion area, and the prediction is not correct.
- FP(False Positive): The prediction is the MS lesion area, and the prediction is not correct.
- FN(False Negative): The prediction is not the MS lesion area, and the prediction is not correct.

We list the commonly used metrics in **Table 2**. In this review, we use DSC and PPV to compare various methods.

3. METHOD

In this section, we first discuss the classification methods of all algorithms, and then we review the MS lesion segmentation methods based on deep learning and analyze their strengths and weaknesses according to the categorizations. Finally, we make a quantitative comparison of the methods we reviewed.

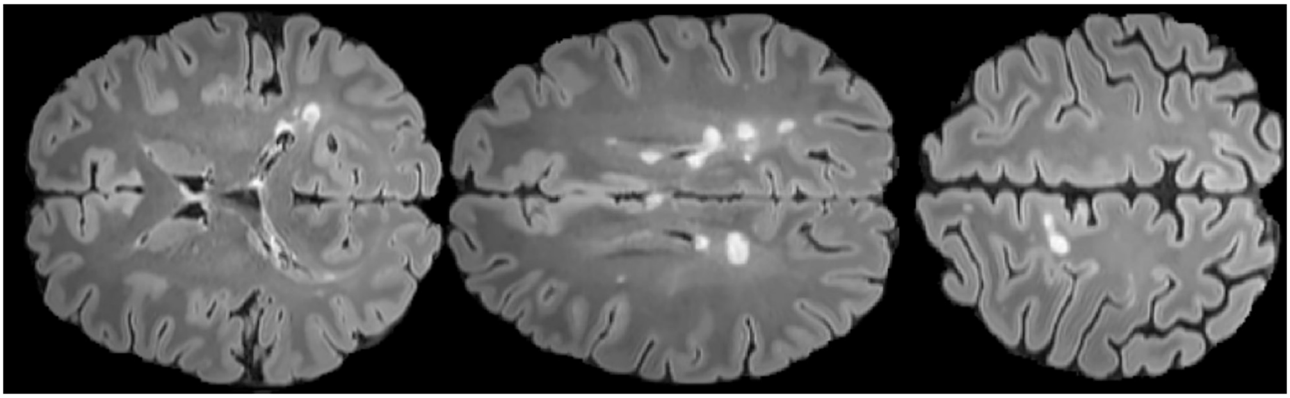

FIGURE 1 | FLAIR axial MRIs of brain slices with MS lesions (white area) The figure comes from the public data set MICCAI2016 (Commowick et al., 2018).

TABLE 1 | Public datasets used by the deep learning-based MS lesion segmentation.

Dataset	Num of subjects	Training set:Test set	MRI sequence	MRI scan
MICCAI 2008 (Styner et al., 2008)	45	20:25	T1-w, T2-w FLARE	3T Siemens Allegra 3T Siemens
MICCAI 2016 (Commowick et al., 2018)	53	15:38	T1-w T2-w PD-w T1-w Gd FLARE	Siemens Aera 1.5T Siemens Verio 3T Philips Ingenia 3T General Electric Discovery 3T
ISBI 2015 (Carass et al., 2017)	19	5:14	T1-w, T2-w FLARE, PD-w	3T Philips

TABLE 2 | Metrics for the reviewed methods.

Metrics	Calculation	Substitute name
Sensitivity (SEN) (Goldberg-Zimring et al., 1998)	$SEN = \frac{TP}{TP+FN}$	True positive rate
Specificity (SPE) (Goldberg-Zimring et al., 1998)	$SPE = \frac{TN}{TN+FP}$	True negative rate
Accuracy (ACC) (Wu et al., 2006)	$ACC = \frac{TN+TP}{TN+FP+TP+FN}$	
Dice similarity coefficient (DSC) (Dice, 1945)	$DSC = \frac{2TP}{FP+2TP+FN}$	F_1 Score
Positive predictive value (PPV) (Altman and Bland, 1994)	$PPV = \frac{TP}{TP+FP}$	Precision
Fallout (FALL) (Udupa et al., 2006)	$FALL = \frac{FP}{TN+FP}$	False positive rate

3.1. Categorization

The MS lesion segmentation task can be regarded as a semantic segmentation task, and each pixel (or voxel in 3D) of the input image needs to be classified as lesion or non-lesion. The methods we reviewed fall into two categories: patch-wise segmentation, semantic-wise segmentation. Patch-wise segmentation trains a CNN classifier to use the information of the pixel-centered patch to classify the pixel into two categories (lesions or non-lesions). Semantic segmentation trains a fully convolutional network to directly predict the lesion mask of the input image, so as to classify each pixel of the input image in a single forward propagation.

Patch-wise segmentation is the simplest segmentation strategy used when deep learning is just beginning to be applied to the segmentation of MS lesions. The segmentation strategy takes the pixel as the center and extracts a small patch of size N × N as the classifier input, and then they use the classifier to traverse the entire image. This strategy can make better use of contextual information around pixels. For example, Valverde et al. (2016) extracts 15×15×15 patches around each voxel from the MRI as input and then processes the input through two 3D convolutional layers. Then it output the probability of two possible classes(lesion and not lesion) through a fully connected layer and a softmax layer. In the patch-wise segmentation, a large number of redundant calculations are caused by overlapping patches, which decreases the calculation efficiency greatly. **Semantic-wise segmentation** is first proposed by Brosch et al. (2015). The input of semantic-wise segmentation can be the entire MRI volume or a relatively large patch. In semantic-wise segmentation, there will be no redundant calculations caused by overlapping patches. In Brosch et al. (2015), it takes the entire MRI volumes as input. Then feed the input into the network consists of a convolutional layer (LeCun et al., 1998) and a deconvolution layer (Zeiler et al., 2011) to predict the lesion mask.

3.2. Patch-Wise Segmentation

Patch-wise segmentation potentially converges faster when training the model because it randomly samples the patches over the dataset (LeCun et al., 1998). Besides, it is easier to deal with the problem of class imbalance. However, the time required to train a complicated patch-wise method can make the method infeasible when the number and size of patches are large. In addition, it has a lot of redundant calculations due to patch overlap.

Yoo et al. (2014) uses deep learning for feature learning and random forest for classification. They first train a model on a large amount of unlabeled data to recognize common patterns and then add labels to the training subset so that both features and labels can be used for segmentation tasks. Vaidya et al. (2015) uses 3D patches as input, via 3D convolutional network to classify each patch into two categories. Havaei et al. (2016) proposed a CNN network that can segment images from systematic multi-modal datasets. The method maps the input image to an embedding space. In this embedding space, arithmetic calculations (such as computing moments of a collection of vectors) are well-defined and can be used for different modalities available during inference time. These calculated moments can be further used to predict the final segmentation. This algorithm improves the robustness against missing input data modalities. Method in Birenbaum and Greenspan (2016) takes patches from multiple images, multiple views and multiple time points as input. It can be divided into two stages. The first stage uses FLARE and white matter (WM) prior to calculating the candidate voxel, and the second stage uses multi-view CNN to predict lesion probability for each voxel in MRI. It is the first deep learning method that uses longitudinal data for segmentation. Valverde et al. (2017) proposed a cascade structure consisting of two stages to segment MS lesions. When training the model, they manually select the training data to solve the problem of imbalance between positive and negative samples. The first stage is used to output voxels with a large probability of being a lesion, and the second stage further infers whether the voxels output by the first stage are lesions, and finally via set threshold to get binary output masks. On the basis of the previous work, Valverde et al. (2017, 2019) studied the influence of intensity domain adaptation on model performance. Alshayeji et al. (2018) proposed an effective method to simplify the pre-processing steps and reduce the processing time using heterogeneous single-channel MRI. They extract the features of the lesion use mathematical operations and morphological operations, and train an Multilayer Perceptron (MLP) for classification to reduce processing time. Essa et al. (2020) performs patch-wise R-CNN on the input image of each modality to generate a probabilistic output of locations of MS lesion, they input the extracted patches as the proposed regions into the RCNN output probabilistic output of lesion existence. They propose an adaptive neuro-fuzzy inference system to show how different MRI modalities are integrated, and they use this system to fuse the output of each MRI modality to get the final segmentation result.

3.3. Semantic-Wise Segmentation

Compared with patch-wise segmentation, semantic-wise segmentation requires only one forward propagation to classify all pixels of the input image and it has higher computational efficiency. But for the task of MS lesion segmentation, semantic-wise segmentation is prone to overfitting during training due to class imbalance, because in the MRI of MS lesions, the area of the lesion area is much smaller than the non-lesion area.

Brosch et al. (2016) combines the advantages of Brosch et al. (2015) and U-net (Ronneberger et al., 2015). It contains two paths: one is an encoding path composed of convolutional layers and pooling layers, and the other is a decoding path composed of deconvolutional layers and unpooling layers. A shortcut connection is built between the two paths. Compared with U-net (Ronneberger et al., 2015), it uses a deconvolution layer instead of upsampling, so there is no need to specially process the boundary regions. McKinley et al. (2016) introduces the nabla net, which combines the low-level features learned by the fully convolutional network and the high-level features learned by the encoder-decoder network to output a probability map. Zhang et al. (2018) uses LinkNet (Chaurasia and Culurciello, 2017) as their base segmentation network. LinkNet is an encoder-decoder network with an additional link between encoder and decoder. They add a loss function related to classification to the conditional generative adversarial network (cGAN) to achieve semantic segmentation more efficiently. Roy et al. (2018) uses parallel pathways to process different MRI image patches, and then concatenate the outputs of these pathways to predict the membership function of the patch through another convolution filter. It does not have a fully connected layer, it replaces the fully connected layer with a fully convolutional layer to get less false positives. In order to solve the problem of MS lesions have huge variability in size and DSC is not differentiable which result in can not be used directly for gradient descent, Wang et al. (2018) segments large and small lesions separately and propose a new activation function to facilitate network training. Aslani et al. (2018)uses 2D slices as input and a 2D encoder-decoder network to segment MS lesions to avoid the problems like the oversight of global information of patch-wise methods and the overfitting of 3D segmentation due to the problem of class imbalance. Kumar et al. (2018) combines the advantages of SegNet (Badrinarayanan et al., 2017) and U-net (Ronneberger et al., 2015) that U-net captures multi-scale information more effectively and SegNet has fewer parameters and faster training. Aslani et al. (2019) focuses on whole-brain slice-based segmentation in order to prevent the overfitting problem of 3D-based segmentation and the problem that patch-based segmentation cannot use global information. In addition, it also uses multi-level feature fusion to better use contextual information for segmentation. Zhang et al. (2019a) uses fully convolutional densely connected networks (Jégou et al., 2017) for MS lesion segmentation, and uses 2.5D stacked slices as input to improve segmentation performance. The term 2.5D is defined as slices stacked along three orthogonal planes (axial, sagittal, and coronal). Zhang et al. (2019b) proposes a recurrent slice-wise attention network by repeatedly using the contextual information of MS lesions to respond to the problem that Recurrent Neural Network (RNN) and long short-term memory (LSTM) have inherent flaws to capture long-term dependencies. Aslani et al. (2020) proposed a regularized network with an auxiliary loss function which makes the model ignore domain-specific information to handle the problem of domain shift. Gessert et al. (2020a) proposes a 4D deep learning network to improve the activity segmentation performance of MS lesions. It adds a 3D volume of historical time point to the input of the network and designs a new multi-encoder-decoder architecture that uses convolutional-recurrent units for time aggregation. In addition, they also explored whether adding an additional past time point to the input can improve segmentation performance. La Rosa et al. (2020) uses magnetization-prepared 2 rapid acquisition with gradient echo(MP2RAGE) MRI to segment cortical lesions(CLs). Compared to this method, other methods just segment white matter lesions(WMLs). Its network structure is based on 3D U-net (Çiçek et al., 2016). For the domain shift problem in MS lesion segmentation, Ackaouy et al. (2020) proposes an unsupervised method that learns a shared representation of the source and target domains. Gessert et al. (2020b) segment the newly emerging MS lesions by attention mechanism with two paths network while the general method only considers MS lesions segmentation in a single MRI volume. This task is particularly challenging because new lesions are minute, changes are subtle. Gabr et al. (2020) study how deep learning based on full convolutional neural networks (FCNN) performs when there is more data. They train, verify, and test on a dataset containing 1,000 MRI and got great results(DSC:0.95). Coronado et al. (2020) evaluates the performance of deep learning in segmenting gadolinium-enhancing lesions using a large cohort of MS patients.

3.4. Quantitative Comparation

In this subsection, reviewed MS lesion segmentation methods based on deep learning will be compared. **Table 3** shows the main performance comparison of various methods. Each method is analyzed through the dataset used, the input data dimension, the CNN style, and the performance (DSC Dice, 1945, PPV Altman and Bland, 1994).

It can be seen from **Table 3** that there are many methods that still use their private datasets which is not convenient to compare the performance of the methods quantitatively.

4. FUTURE DIRECTION

Although deep learning has achieved great performance in MS lesion segmentation tasks compared with traditional methods (Danelakis et al., 2018), there are still some problems that limit the potential of deep learning in this field: dataset scale, data imbalance, domain shift. Deep learning has also achieved great performance in other fields of medical images (Zhao et al., 2017, 2019a,b; Xu et al., 2018). We believe that borrowing deep learning methods from other fields into MS automatic segmentation can help design better segmentation methods. In the later part of this section, we will discuss some possible solutions to these problems as well as some new research problems in this field.

TABLE 3 | Comparison of reviewed methods.

Methods	Database	Dim	CNN style	DSC	PPV
Roy et al. (2018)	ISBI 2015	3D	Semantic-wise	0.524	0.866
Birenbaum and Greenspan (2016)	ISBI 2015	3D	Patch-wise	0.627	0.789
Valverde et al. (2019)	ISBI 2015	3D	Patch-wise	0.63	0.840
Aslani et al. (2019)	ISBI 2015	2D	Semantic-wise	0.61	0.899
Aslani et al. (2018)	ISBI 2015	2D	Semantic-wise	0.698	0.74
Zhang et al. (2019a)	ISBI 2015	2.5D	Semantic-wise	0.693	0.908
Havaei et al. (2016)	MICCAI 2008	2D	Patch-wise	0.832	N/A
Valverde et al. (2017)	MICCAI 2008	3D	Patch-wise	0.871	0.786
Brosch et al. (2016)	MICCAI 2008	3D	Semantic-wise	0.840	N/A
Valverde et al. (2016)	MICCAI 2016	3D	Patch-wise	0.541	N/A
McKinley et al. (2016)	MICCAI 2016	3D	Semantic-wise	0.591	N/A
Kazancli et al. (2018)	Proprietary	3D	Patch-wise	0.575	N/A
La Rosa et al. (2020)	Proprietary	3D	Semantic-wise	0.60	0.64
Brosch et al. (2015)	Proprietary	3D	Semantic-wise	0.355	0.414
Gabr et al. (2020)	Proprietary	3D	Semantic-wise	0.95	N/A
Coronado et al. (2020)	Proprietary	3D	Semantic-wise	0.77	N/A
Zhang et al. (2018)	Proprietary	2D	Semantic-wise	0.672	0.724
Aslani et al. (2020)	Proprietary	3D	Semantic-wise	0.50	0.519
Gessert et al. (2020a)	Proprietary	4D	Semantic-wise	0.64	N/A
Gessert et al. (2020b)	Proprietary	3D	Semantic-wise	0.656	N/A
Zhang et al. (2019b)	Proprietary	2D	Semantic-wise	0.660	N/A

Transfer learning can be a future direction to deal with the problem of small data sets. This problem not only exists in the study of MS lesion segmentation, but it is also a coexisting problem in medical image processing due to the difficulty of medical image acquisition and labeling. To solve the problem of a small dataset scale, it can be achieved through transfer learning (Pan et al., 2011). Transfer learning is a learning method for small datasets. First, a deep learning network with great performance is trained on a large dataset, and then the network is fine-tuned on a smaller dataset for specific problems. For example, Shin et al. (2016) reported that they performed transfer learning from pre-trained models on the ImageNet dataset and then fine-tuned on lymph node and interstitial lung diseases instead of training from scratch to achieve great performance. But we believe that directly transferring from natural images to medical images may not be the best transfer learning solution, because natural images and medical images are very different. We think it is possible to perform transfer learning from large medical image data sets, such as DeepLesion (Yan et al., 2018).

Designing a specific loss function may be a direction to solve the problem of data imbalance in the future. The pattern of manifestation of data imbalance in MS lesion segmentation is class imbalance. In a single MRI volume, the number of voxels with lesions is much smaller than the number of voxels without lesions, which will bring problems such as overfitting to the network training (Li et al., 2019). The impact of this problem on the patch-wise CNN style is less than that of the semantic-wise CNN style because the patch-wise CNN style classifies each voxel separately. In the patch-wise CNN style, the ratio of positive samples and negative samples of training data can be adjusted artificially to balance the class (Valverde et al., 2017). However, for the semantic-wise CNN style, all voxels are classified in a forward propagation, which makes it difficult to artificially adjust the ratio of positive and negative samples in the training data. Therefore, the class imbalance problem of the semantic-wise CNN style requires to be solved from another aspect. Through our investigation of imbalance problems in other fields, we found that the current mainstream method to solve this problem is to design a loss function carefully (e.g., Sudre et al., 2017; Wong et al., 2018; Kervadec et al., 2019; Li et al., 2019). They have achieved great results in other segmentation tasks such as ischemic stroke injury by proposing a loss function for class imbalance. We believe that this will also help reduce the impact of overfitting caused by the data imbalance in the segmentation of MS lesions.

Collaborative image and feature adaptation can improve the performance of the domain adaptive model to a certain extent. The domain shift refers to the problem that the model performs well on the source domain, but performs much worse on the target domain. Although there are some methods (Valverde et al., 2019; Ackaouy et al., 2020) in MS lesion segmentation that proposes domain adaptation models to solve the problem of domain shift, they only implement domain adaptation from the perspective of feature adaptation. Chen et al. (2019) proposes a domain adaptive method from two perspectives of image and feature, and verified their method on a cross-modal heart structure segmentation challenge. They choose the source domain as MRI modal data and the target domain as computed tomography(CT) modal data. They restored the performance degradation from 17.2 to 73.0%. We think that improving the performance of the domain adaptive model from both image and feature aspects is a future direction in MS segmentation.

Through our research, we found that some recent work began to introducing the sequence model (Gessert et al., 2020a,b) to segment the activity of MS lesions. The task of segmentation of multiple sclerosis lesion activity is to detect the appearance of new and enlarged lesions between the baseline and subsequent brain MRI scans (Gessert et al., 2020b). We think this is also a future direction for the segmentation task. More sequence models can be used to analyze the improvement and deterioration of patient lesions (e.g., LSTM). Cai et al. (2017) applies contextual LSTM (CLSTM) to the output layer of deep CNN and achieves sharper pancreas segmentation by capturing the context information of adjacent slices. Spatiotemporal regularization (Zheng et al., 2019) may improve the performance of activity segmentation and structure tensor (Zheng et al., 2020) can help more accurately capture the changes in the edge of the lesion.

5. CONCLUSION

In this review, we have done a detailed survey on the method of MS lesion segmentation based on deep learning, and we reviewed the commonly used public datasets and evaluation metrics of this segmentation task. We categorize these methods according to the CNN style they use. It is difficult to compare various methods because the datasets they use are not only public datasets but also their own proprietary data sets. We use DSC and PPV for quantitative comparisons including those that use proprietary datasets. The future direction and some potential problems are also illustrated.

Although deep learning greatly improves the performance of automatic segmentation methods, it is still challenging to directly use in clinical analysis. Collecting large-scale data sets to tap the potential of deep learning can help accelerate its application in clinical medicine, and there is still a lot of room for improvement for deep learning-based methods. The automatic segmentation method with better performance and stronger robustness is undoubtedly beneficial to the doctor's pre-diagnosis and post-treatment of the patient's condition.

DATA AVAILABILITY STATEMENT

Publicly available datasets were analyzed in this study. This data can be found here: http://www.ia.unc.edu/MSseg/; https://smart-stats-tools.org/lesion-challenge-2015; https://portal.fli-iam.irisa.fr/msseg-challenge/overview.

AUTHOR CONTRIBUTIONS

CZ was responsible for writing the paper. ZL was responsible for consulting the literature. LG was responsible for method comparison. SZ was responsible for revising the article. All authors contributed to the article and approved the submitted version.

REFERENCES

Ackaouy, A., Courty, N., Vallée, E., Commowick, O., and Galassi, F. (2020). Unsupervised domain adaptation with optimal transport in multi-site segmentation of multiple sclerosis lesions from MRI data. *Front. Comput. Neurosci.* 14:19. doi: 10.3389/fncom.2020.00019

Alshayeji, M. H., Al-Rousan, M. A., Ellethy, H., and Abed, S. (2018). An efficient multiple sclerosis segmentation and detection system using neural networks. *Comput. Electr. Eng.* 71, 191–205. doi: 10.1016/j.compeleceng.2018.07.020

Altman, D. G., and Bland, J. M. (1994). Statistics notes: diagnostic tests 2: predictive values. *BMJ* 309:102. doi: 10.1136/bmj.309.6947.102

Aslani, S., Dayan, M., Murino, V., and Sona, D. (2018). "Deep 2D encoder-decoder convolutional neural network for multiple sclerosis lesion segmentation in brain MRI," in *International MICCAI Brainlesion Workshop* (Berlin: Springer), 132–141. doi: 10.1007/978-3-030-11723-8_13

Aslani, S., Dayan, M., Storelli, L., Filippi, M., Murino, V., Rocca, M. A., et al. (2019). Multi-branch convolutional neural network for multiple sclerosis lesion segmentation. *NeuroImage* 196, 1–15. doi: 10.1016/j.neuroimage.2019.03.068

Aslani, S., Murino, V., Dayan, M., Tam, R., Sona, D., and Hamarneh, G. (2020). "Scanner invariant multiple sclerosis lesion segmentation from MRI," in *2020 IEEE 17th International Symposium on Biomedical Imaging (ISBI)* (Piscatawa, NJ), 781–785. doi: 10.1109/ISBI45749.2020.9098721

Badrinarayanan, V., Kendall, A., and Cipolla, R. (2017). SegNet: a deep convolutional encoder-decoder architecture for image segmentation. *IEEE Trans. Pattern Anal. Mach. Intell.* 39, 2481–2495. doi: 10.1109/TPAMI.2016.2644615

Birenbaum, A., and Greenspan, H. (2016). "Longitudinal multiple sclerosis lesion segmentation using multi-view convolutional neural networks," in *Deep Learning and Data Labeling for Medical Applications* (Berlin: Springer), 58–67. doi: 10.1007/978-3-319-46976-8_7

Brosch, T., Tang, L., Yoo, Y., Li, D. K. B., Traboulsee, A., and Tam, R. (2016). Deep 3D convolutional encoder networks with shortcuts for multiscale feature integration applied to multiple sclerosis lesion segmentation. *IEEE Trans. Med. Imaging* (Piscataway, NJ) 35, 1229–1239. doi: 10.1109/TMI.2016.2528821

Brosch, T., Yoo, Y., Tang, L. Y., Li, D. K., Traboulsee, A., and Tam, R. (2015). "Deep convolutional encoder networks for multiple sclerosis lesion segmentation," in *International Conference on Medical Image Computing and Computer-Assisted Intervention* (Springer), 3–11. doi: 10.1007/978-3-319-24574-4_1

Cai, J., Lu, L., Xie, Y., Xing, F., and Yang, L. (2017). Improving deep pancreas segmentation in CT and MRI images via recurrent neural contextual learning and direct loss function. *arXiv[preprint]arXiv:1707.04912*. doi: 10.1007/978-3-030-13969-8_1

Carass, A., Roy, S., Jog, A., Cuzzocreo, J. L., Magrath, E., Gherman, A., et al. (2017). Longitudinal multiple sclerosis lesion segmentation: resource and challenge. *NeuroImage* 148, 77–102. doi: 10.1016/j.neuroimage.2016.12.064

Chaurasia, A., and Culurciello, E. (2017). "Linknet: Exploiting encoder representations for efficient semantic segmentation," in *2017 IEEE Visual Communications and Image Processing (VCIP)* (Piscataway, NJ), 1–4. doi: 10.1109/VCIP.2017.8305148

Chen, C., Dou, Q., Chen, H., Qin, J., and Heng, P.-A. (2019). "Synergistic image and feature adaptation: towards cross-modality domain adaptation for medical image segmentation," in *Proceedings of the AAAI Conference on Artificial Intelligence, Vol. 33* (Menlo Park, CA), 865–872. doi: 10.1609/aaai.v33i01.3301865

Çiçek, Ö., Abdulkadir, A., Lienkamp, S. S., Brox, T., and Ronneberger, O. (2016). "3D U-net: learning dense volumetric segmentation from sparse annotation," in *International Conference on Medical Image Computing and Computer-Assisted Intervention* (Berlin: Springer), 424–432. doi: 10.1007/978-3-319-46723-8_49

Commowick, O., Istace, A., Kain, M., Laurent, B., Leray, F., Simon, M., et al. (2018). Objective evaluation of multiple sclerosis lesion segmentation using a data management and processing infrastructure. *Sci. Rep.* 8:13650. doi: 10.1038/s41598-018-31911-7

Coronado, I., Gabr, R. E., and Narayana, P. A. (2020). Deep learning segmentation of gadolinium-enhancing lesions in multiple sclerosis. *Multip. Scleros. J.* doi: 10.1177/1352458520921364

Danelakis, A., Theoharis, T., and Verganelakis, D. A. (2018). Survey of automated multiple sclerosis lesion segmentation techniques on magnetic resonance imaging. *Computer. Med. Imaging Graph*. 70, 83–100. doi: 10.1016/j.compmedimag.2018.10.002

Dice, L. R. (1945). Measures of the amount of ecologic association between species. *Ecology* 26, 297–302. doi: 10.2307/1932409

Essa, E., Aldesouky, D., Hussein, S. E., and Rashad, M. (2020). Neuro-fuzzy patch-wise R-CNN for multiple sclerosis segmentation. *Med. Biol. Eng. Comput*. 58, 2161–2175. doi: 10.1007/s11517-020-02225-6

Gabr, R. E., Coronado, I., Robinson, M., Sujit, S. J., Datta, S., Sun, X., et al. (2020). Brain and lesion segmentation in multiple sclerosis using fully convolutional neural networks: a large-scale study. *Multip. Scler. J.* 26, 1217–1226. doi: 10.1177/1352458519856843

García-Lorenzo, D., Francis, S., Narayanan, S., Arnold, D. L., and Collins, D. L. (2013). Review of automatic segmentation methods of multiple sclerosis white matter lesions on conventional magnetic resonance imaging. *Med. Image Anal.* 17, 1–18. doi: 10.1016/j.media.2012.09.004

Gessert, N., Bengs, M., Krüger, J., Opfer, R., Ostwaldt, A.-C., Manogaran, P., et al. (2020a). 4D deep learning for multiple sclerosis lesion activity segmentation. *arXiv[preprint]arXiv:2004.09216*.

Gessert, N., Krüger, J., Opfer, R., Ostwaldt, A.-C., Manogaran, P., Kitzler, H. H., et al. (2020b). Multiple sclerosis lesion activity segmentation with attention-guided two-path CNNs. *Comput. Med. Imaging Graph*. 84:101772. doi: 10.1016/j.compmedimag.2020.101772

Goldberg-Zimring, D., Achiron, A., Miron, S., Faibel, M., and Azhari, H. (1998). Automated detection and characterization of multiple sclerosis lesions in brain MR images. *Magnet. Reson. Imaging* 16, 311–318. doi: 10.1016/S0730-725X(97)00300-7

Hashemi, R. H., Bradley, W. G., and Lisanti, C. J. (2012). *MRI: the Basics: The Basics*. Lippincott Williams & Wilkins.

Havaei, M., Guizard, N., Chapados, N., and Bengio, Y. (2016). "Hemis: Hetero-modal image segmentation," in *International Conference on Medical Image Computing and Computer-Assisted Intervention* (Berlin: Springer), 469–477. doi: 10.1007/978-3-319-46723-8_54

Jégou, S., Drozdzal, M., Vazquez, D., Romero, A., and Bengio, Y. (2017). "The one hundred layers tiramisu: fully convolutional densenets for semantic segmentation," in *Proceedings of the IEEE Conference on Computer Vision and Pattern Recognition Workshops* (Piscataway, NJ), 11–19. doi: 10.1109/CVPRW.2017.156

Kaur, A., Kaur, L., and Singh, A. (2020). State-of-the-art segmentation techniques and future directions for multiple sclerosis brain lesions. *Arch. Comput. Methods Eng*. 1–27. doi: 10.1007/s11831-020-09403-7

Kazancli, E., Prchkovska, V., Rodrigues, P., Villoslada, P., and Igual, L. (2018). "Multiple sclerosis lesion segmentation using improved convolutional neural networks," in *VISIGRAPP (4: VISAPP)* (Portugal), 260–269. doi: 10.5220/0006540902600269

Kervadec, H., Bouchtiba, J., Desrosiers, C., Granger, E., Dolz, J., and Ayed, I. B. (2019). "Boundary loss for highly unbalanced segmentation," in *International Conference on Medical Imaging With Deep Learning* (Amsterdam), 285–296.

Kumar, P., Nagar, P., Arora, C., and Gupta, A. (2018). "U-segNet: fully convolutional neural network based automated brain tissue segmentation tool," in *2018 25th IEEE International Conference on Image Processing (ICIP)* (Piscataway, NJ), 3503–3507. doi: 10.1109/ICIP.2018.8451295

La Rosa, F., Abdulkadir, A., Fartaria, M. J., Rahmanzadeh, R., Lu, P.-J., Galbusera, R., et al. (2020). Multiple sclerosis cortical and WM lesion segmentation at 3T MRI: a deep learning method based on FLAIR and MP2RAGE. *NeuroImage* 27:102335. doi: 10.1016/j.nicl.2020.102335

LeCun, Y., Bottou, L., Bengio, Y., and Haffner, P. (1998). Gradient-based learning applied to document recognition. *Proc. IEEE* 86, 2278–2324. doi: 10.1109/5.726791

Li, Z., Kamnitsas, K., and Glocker, B. (2019). "Overfitting of neural nets under class imbalance: analysis and improvements for segmentation," in *International Conference on Medical Image Computing and Computer-Assisted Intervention* (Berlin: Springer), 402–410. doi: 10.1007/978-3-030-32248-9_45

Lladó, X., Oliver, A., Cabezas, M., Freixenet, J., Vilanova, J. C., Quiles, A., et al. (2012). Segmentation of multiple sclerosis lesions in brain MRI: a review of automated approaches. *Inform. Sci.* 186, 164–185. doi: 10.1016/j.ins.2011.10.011

McKinley, R., Wepfer, R., Gundersen, T., Wagner, F., Chan, A., Wiest, R., et al. (2016). "Nabla-net: A deep dag-like convolutional architecture for biomedical image segmentation," in *International Workshop on Brainlesion: Glioma, Multiple Sclerosis, Stroke and Traumatic Brain Injuries* (Berlin: Springer), 119–128. doi: 10.1007/978-3-319-55524-9_12

Mortazavi, D., Kouzani, A. Z., and Soltanian-Zadeh, H. (2012). Segmentation of multiple sclerosis lesions in MR images: a review. *Neuroradiology* 54, 299–320. doi: 10.1007/s00234-011-0886-7

Pan, S. J., Tsang, I. W., Kwok, J. T., and Yang, Q. (2011). Domain adaptation via transfer component analysis. *IEEE Trans. Neural Netw*. 22, 199–210. doi: 10.1109/TNN.2010.2091281

Polman, C. H., Reingold, S. C., Banwell, B., Clanet, M., Cohen, J. A., Filippi, M., et al. (2011). Diagnostic criteria for multiple sclerosis: 2010 revisions to the Mcdonald criteria. *Ann. Neurol.* 69, 292–302. doi: 10.1002/ana.22366

Ronneberger, O., Fischer, P., and Brox, T. (2015). "U-net: Convolutional networks for biomedical image segmentation," in *International Conference on Medical Image Computing and Computer-Assisted Intervention* (Berlin: Springer), 234–241. doi: 10.1007/978-3-319-24574-4_28

Roy, S., Butman, J. A., Reich, D. S., Calabresi, P. A., and Pham, D. L. (2018). Multiple sclerosis lesion segmentation from brain MRI via fully convolutional neural networks. *arXiv arXiv:1803.09172*. doi: 10.1109/ISBI.2018.8363545

Sahraian, M. A., and Radue, E.-W. (2007). *MRI Atlas of MS Lesions*. Berlin: Springer Science & Business Media.

Shanmuganathan, M., Almutairi, S., Aborokbah, M. M., Ganesan, S., and Ramachandran, V. (2020). Review of advanced computational approaches on multiple sclerosis segmentation and classification. *IET Signal Process*. 14, 333–341. doi: 10.1049/iet-spr.2019.0543

Shin, H.-C., Roth, H. R., Gao, M., Lu, L., Xu, Z., Nogues, I., et al. (2016). Deep convolutional neural networks for computer-aided detection: CNN architectures, dataset characteristics and transfer learning. *IEEE Trans. Med. Imaging* 35, 1285–1298. doi: 10.1109/TMI.2016.2528162

Styner, M., Lee, J., Chin, B., Chin, M., Commowick, O., Tran, H., et al. (2008). 3D segmentation in the clinic: a grand challenge II: MS lesion segmentation. *Midas J.* 2008, 1–6.

Sudre, C. H., Li, W., Vercauteren, T., Ourselin, S., and Cardoso, M. J. (2017). "Generalised dice overlap as a deep learning loss function for highly unbalanced segmentations," in *Deep Learning in Medical Image Analysis and Multimodal Learning for Clinical Decision Support* (Berlin: Springer), 240–248. doi: 10.1007/978-3-319-67558-9_28

Udupa, J. K., LeBlanc, V. R., Zhuge, Y., Imielinska, C., Schmidt, H., Currie, L. M., et al. (2006). A framework for evaluating image segmentation algorithms. *Comput. Med. Imaging Graph.* 30, 75–87. doi: 10.1016/j.compmedimag.2005.12.001

Vaidya, S., Chunduru, A., Muthuganapathy, R., and Krishnamurthi, G. (2015). "Longitudinal multiple sclerosis lesion segmentation using 3D convolutional neural networks," in *Proceedings of the 2015 Longitudinal Multiple Sclerosis Lesion Segmentation Challenge*, 1–2.

Valverde, S., Cabezas, M., Roura, E., González-Villá, S., Pareto, D., Vilanova, J. C., et al. (2017). Improving automated multiple sclerosis lesion segmentation with a cascaded 3D convolutional neural network approach. *NeuroImage* 155, 159–168. doi: 10.1016/j.neuroimage.2017.04.034

Valverde, S., Cabezas, M., Roura, E., González-Villa, S., Salvi, J., Oliver, A., et al. (2016). "Multiple sclerosis lesion detection and segmentation using a convolutional neural network of 3D patches," in *MSSEG Challenge Proceedings: Multiple Sclerosis Lesions Segmentation Challenge Using a Data Management and Processing Infrastructure*, 75.

Valverde, S., Salem, M., Cabezas, M., Pareto, D., Vilanova, J. C., Ramió-Torrentá, L., et al. (2019). One-shot domain adaptation in multiple sclerosis lesion segmentation using convolutional neural networks. *NeuroImage* 21:101638. doi: 10.1016/j.nicl.2018.101638

Wang, Z., Smith, C. D., and Liu, J. (2018). "Ensemble of multi-sized FCNs to improve white matter lesion segmentation," in *International Workshop on Machine Learning in Medical Imaging* (Berlin: Springer), 223–232. doi: 10.1007/978-3-030-00919-9_26

Wong, K. C., Moradi, M., Tang, H., and Syeda-Mahmood, T. (2018). "3D segmentation with exponential logarithmic loss for highly unbalanced object sizes," in *International Conference on Medical Image Computing and Computer-Assisted Intervention* (Berlin: Springer), 612–619. doi: 10.1007/978-3-030-00931-1_70

Wu, Y., Warfield, S. K., Tan, I. L., Wells, W. M. III, Meier, D. S., van Schijndel, R. A., et al. (2006). Automated segmentation of multiple sclerosis lesion subtypes with multichannel MRI. *NeuroImage* 32, 1205–1215. doi: 10.1016/j.neuroimage.2006.04.211

Xu, C., Xu, L., Gao, Z., Zhao, S., Zhang, H., Zhang, Y., et al. (2018). Direct delineation of myocardial infarction without contrast agents using a joint motion feature learning architecture. *Med. Image Anal.* 50, 82–94. doi: 10.1016/j.media.2018.09.001

Yan, K., Wang, X., Lu, L., and Summers, R. M. (2018). Deeplesion: automated mining of large-scale lesion annotations and universal lesion detection with deep learning. *J. Med. Imaging* 5:036501. doi: 10.1117/1.JMI.5.3.036501

Yoo, Y., Brosch, T., Traboulsee, A., Li, D. K., and Tam, R. (2014). "Deep learning of image features from unlabeled data for multiple sclerosis lesion segmentation," in *International Workshop on Machine Learning in Medical Imaging* (Berlin: Springer), 117–124. doi: 10.1007/978-3-319-10581-9_15

Zeiler, M. D., Taylor, G. W., and Fergus, R. (2011). "Adaptive deconvolutional networks for mid and high level feature learning," in *2011 International Conference on Computer Vision* (Piscataway, NJ), 2018–2025. doi: 10.1109/ICCV.2011.6126474

Zhang, C., Song, Y., Liu, S., Lill, S., Wang, C., Tang, Z., et al. (2018). "MS-GAN: GAN-based semantic segmentation of multiple sclerosis lesions in brain magnetic resonance imaging," in *2018 Digital Image Computing: Techniques and Applications (DICTA)* (Piscataway, NJ), 1–8. doi: 10.1109/DICTA.2018.8615771

Zhang, H., Valcarcel, A. M., Bakshi, R., Chu, R., Bagnato, F., Shinohara, R. T., et al. (2019a). "Multiple sclerosis lesion segmentation with tiramisu and 2.5 D stacked slices," in *International Conference on Medical Image Computing and Computer-Assisted Intervention* (Berlin: Springer), 338–346. doi: 10.1007/978-3-030-32248-9_38

Zhang, H., Zhang, J., Zhang, Q., Kim, J., Zhang, S., Gauthier, S. A., et al. (2019b). "RsaNet: Recurrent slice-wise attention network for multiple sclerosis lesion segmentation," in *International Conference on Medical Image Computing and Computer-Assisted Intervention* (Berlin: Springer), 411–419. doi: 10.1007/978-3-030-32248-9_46

Zhao, S., Gao, Z., Zhang, H., Xie, Y., Luo, J., Ghista, D., et al. (2017). Robust segmentation of intima-media borders with different morphologies and dynamics during the cardiac cycle. *IEEE J. Biomed. Health Inform.* 22, 1571–1582. doi: 10.1109/JBHI.2017.2776246

Zhao, S., Wu, X., Chen, B., and Li, S. (2019a). Automatic spondylolisthesis grading from mris across modalities using faster adversarial recognition network. *Med. Image Anal.* 58:101533. doi: 10.1016/j.media.2019.101533

Zhao, S., Wu, X., Chen, B., and Li, S. (2019b). "Automatic vertebrae recognition from arbitrary spine mri images by a hierarchical self-calibration detection framework," in *International Conference on Medical Image Computing and Computer-Assisted Intervention* (Springer), 316–325. doi: 10.1007/978-3-030-32251-9_35

Zhao, Y., Guo, S., Luo, M., Shi, X., Bilello, M., Zhang, S., et al. (2018). A level set method for multiple sclerosis lesion segmentation. *Magn. Reson. Imaging* 49, 94–100. doi: 10.1016/j.mri.2017.03.002

Zheng, Y., Song, H., Zhang, K., Fan. J., and Liu, X. (2019). Dynamically spatiotemporal regularized correlation tracking. *IEEE Trans. Neural Netw. Learn. Syst.* 1–12. doi: 10.1109/tnnls.2019.2929407

Zheng, Y., Sun, Y., Muhammad, K., and De Albuquerque, V. H. C. (2020). Weighted LIC-based structure tensor with application to image content perception and processing. *IEEE Trans. Ind. Inf.* 1. doi: 10.1109/tii.2020.2980577

Conflict of Interest: The authors declare that the research was conducted in the absence of any commercial or financial relationships that could be construed as a potential conflict of interest.

frontiers in Neuroinformatics

ORIGINAL RESEARCH
published: 24 November 2020
doi: 10.3389/fninf.2020.596340

Studying the Factors of Human Carotid Atherosclerotic Plaque Rupture, by Calculating Stress/Strain in the Plaque, Based on CEUS Images: A Numerical Study

Zhenzhou Li[1†], *Yongfeng Wang*[2†], *Xinyin Wu*[1†], *Xin Liu*[3], *Shanshan Huang*[1], *Yi He*[4], *Shuyu Liu*[5*] *and Lijie Ren*[6]

[1] Department of Ultrasound, Shenzhen Second People's Hospital, The First Affiliated Hospital of Shenzhen University Health Science Center, Shenzhen, China, [2] School of Biomedical Engineering, Sun Yat-sen University, Guangzhou, China, [3] Guangdong Academy Research on Virtual Reality (VR) Industry, Foshan University, Foshan, China, [4] Department of Neurosurgery, Shenzhen Second People's Hospital, The First Affiliated Hospital of Shenzhen University Health Science Center, Shenzhen, China, [5] School of Pharmacy, Sun Yat-sen University, Guangzhou, China, [6] Department of Neurology, Shenzhen Second People's Hospital, The First Affiliated Hospital of Shenzhen University Health Science Center, Shenzhen, China

Edited by:
Jonathan Wu,
University of Windsor, Canada

Reviewed by:
Zhonghua Sun,
Curtin University, Australia
Chenchu Xu,
Western University, Canada

***Correspondence:**
Shuyu Liu
lsy@mail.sysu.edu.cn

†These authors have contributed equally to this work

Received: *19 August 2020*
Accepted: *11 September 2020*
Published: *24 November 2020*

Citation:
Li Z, Wang Y, Wu X, Liu X, Huang S, He Y, Liu S and Ren L (2020) Studying the Factors of Human Carotid Atherosclerotic Plaque Rupture, by Calculating Stress/Strain in the Plaque, Based on CEUS Images: A Numerical Study.
Front. Neuroinform. 14:596340.
doi: 10.3389/fninf.2020.596340

Carotid plaque neovascularization is one of the major factors for the classification of vulnerable plaque, but the axial force effects of the pulsatile blood flow on the plaque with neovessel and intraplaque hemorrhage was unclear. Together with the severity of stenosis, the fibrous cap thickness, large lipid core, and the neovascularization followed by intraplaque hemorrhage (IPH) have been regarded as high-risk features of plaque rupture. In this work, the effects of these factors were evaluated on the progression and rupture of the carotid atherosclerotic plaques. Five geometries of carotid artery plaque were developed based on contrast-enhanced ultrasound (CEUS) images, which contain two types of neovessel and IPH, and geometry without neovessel and IPH. A one-way fluid-structure interaction model was applied to compute the maximum principal stress and strain in the plaque. For that hyper-elastic and non-linear material, Yeoh 3rd Order strain energy density function was used for components of the plaque. The simulation results indicated that the maximum principal stress of plaque in the carotid artery was higher when the degree of the luminal stenosis increased and the thickness of the fibrous cap decreased. The neovessels within the plaque could introduce a 2.5% increments of deformation in the plaque under the pulsatile blood flow pressure. The IPH also contributed to the increased risk of plaque rupture that a gain of stress was 8.983, 14.526, and 34.47 kPa for the plaque with 50, 65, and 75%, respectively, when comparing stress in the plaque with IPH distributed at the middle to the shoulder of the plaque. In conclusion, neovascularization in the plaque could reduce the stability of the plaque by increasing the stress within the plaque. Also, the risk of plaque rupture increased when large luminal stenosis, thin fibrous cap, and IPH were observed.

Keywords: carotid atherosclerotic plaque, vulnerable plaque, cardiovascular diseases, neovascularization, intraplaque hemorrhage, contrast-enhanced ultrasound, computational simulation

1. INTRODUCTION

Carotid atherosclerotic plaque is one of the most common causes of stroke (Rossi et al., 2002; Murata et al., 2020), based on the fibrous cap, lipid core, and endothelial denudation with superficial platelet aggregation being closely associated with the incident (Sadat et al., 2009). Thin fibrous cap and large lipid core are the major factors of the vulnerable plaque and high risk of the plaque rupture (Falk et al., 1995; Naghavi et al., 2003; Finn et al., 2010), as rupture is commonly found in the plaque with the thickness of the fibrous cap <0.065 mm and the volume of the lipid core accounting for 40% of the total plaque volume (Kolodgie et al., 2001). Additionally, intraplaque hemorrhage (IPH) is also considered as a risk factor for the occurrence of future cardiovascular events based on previous investigations (Takaya et al., 2006; Crombag et al., 2019; Saba et al., 2019a).

Neovascularization in the carotid atherosclerotic plaque is the maker of a high risk of the vulnerable plaque (Moreno et al., 2004; Dunmore et al., 2006; Huang et al., 2008; Van der Veken et al., 2016; Demeure et al., 2017). As early as 1999, McCarthy et al. (1999) made a histological examination of 28 patients with carotid arteries, and found that neovessels were commonly found in the fibrous cap of atherosclerotic plaque and most of them existed in the medial and lateral corners of the plaque, but rarely at the bottom. Neovessels can become leakage sites of blood vessels through the aggregation of the inflammatory cells that increase the vulnerability of the plaque, and even lead to IPH (Dunmore et al., 2006; Moreno et al., 2006). Contrast-enhanced ultrasound (CEUS) imaging has been applied to assess the neovascularization in carotid atherosclerosis plaques, for additional evaluation of the vulnerable plaque during the screening procedure for stroke in clinical practice (Feinstein, 2006; Vicenzini et al., 2007; Schinkel et al., 2020; Zamani et al., 2020). Xiong et al. (2009) reported that symptomatic patients had more intense contrast agent within the plaque than asymptomatic patients. Denmark and Marcin (2011) reported that the increased density of the neovascularization was associated with the increasing vulnerability degree of the carotid atherosclerosis plaque.

Hemodynamic blood flow plays an important role in determining plaque progression and ruptures (Radwa and Eldosoky, 2020). Computational fluid dynamics (CFD) analysis of the carotid atherosclerotic plaque has been used to assess the distribution of the superficial dynamic stress and strain of the plaque (Tang et al., 2003; Woorak et al., 2017). Li Z. et al. (2006) have performed stress analysis of the carotid plaque with various fibrous cap thickness in the geometry derived from *in vivo* magnetic resonance imaging (MRI) by using CFD, showing that the morphology and component of the plaque were significantly related to the stability of the plaque (Li Z. Y. et al., 2006). Impacts of the plaque eccentricity and hemodynamics environment were also related to the stress distribution in the plaque and rupture site, according to the study of Tang et al. (2003). These studies have taken into account the geometric and structural factors, including luminal stenotic degree, thin fibrous cap, large lipid core, and so on. Previous studies reported that the density of neovessels was positively associated with destabilization of the plaque based on the 2D transverse simulation (Lu et al., 2015; Guo et al., 2018, 2019). Teng et al. (2012) established a 2D transverse CFD model based on carotid artery endarterectomy slices, and four carotid plaque samples were used to analyze the local mechanical environment of the neovessels. Their results indicate that the local mechanical environment of the neovessel could lead to the occurrence of the IPH. Nevertheless, in their investigation, the effect of the carotid artery blood flow was not included, and the impact of axial force from pulsatile blood flow on the stability of the plaque was ignored.

In this study, numerical simulation with one-way fluid–structure interaction was conducted on the theoretical geometries of carotid atherosclerotic plaque with neovascularization and IPH. The stress and strain distribution in the plaque were evaluated regarding various plaque formations. The 2-dimensional axial plaque geometries were established based on the findings from the CEUS imaging. The thickness of the fibrous cap and the degrees of lumen stenosis were taken into account to study the impacts of neovessels and IPH on the destabilization of the carotid atherosclerotic plaque.

2. METHODS

2.1. Geometries

In this study, a one-way fluid–structure interaction model was performed to explore how neovessel and IPH affected carotid atherosclerotic plaque. Considering the structures of the plaque and neovessel occurring variation in different patients and even in the same one [see **Figure 1**: (a) is the carotid plaque with one neovessel, (b) is the one with three neovessels], 2D geometries based on CEUS images were taken into account in this study [see **Figure 2**: (a) is geometry with no neovessel, (b) is geometry with one neovessel, and (c) is one with three neovessels]. The structures of these geometries included carotid lumen, fibrous cap, lipid core, and different neovessels (Naghavi et al., 2003). For analysis, one inlet and outlet were necessary. The shapes of the fibrous cap and lipid core were designed by using a sinusoidal function (Li Z. Y. et al., 2006):

$$y_1 = \frac{D - D_t}{2} \cdot cos(x) \tag{1}$$

$$y_2 = \frac{D - D_t}{2} \cdot (1 + cos(x)) - d \tag{2}$$

$$S = \frac{D}{D_t} \cdot 100\% \tag{3}$$

where (*i*) D and D_t represent the diameter of the carotid lumen and the distance between the carotid artery wall and the top of the plaque, and (*ii*) S represents the degree of the carotid artery stenosis. The thickness of the fibrous cap, represented by d, plays a critical influence factor in the vulnerable plaque development (Cicha et al., 2011); different d values were used (d = 0.2, 0.5, and 0.0065 mm), which is critical to plaque vulnerability. In this paper, we set the stenosis degree S at 50, 65, and 75% (Avci et al., 2016). Moreover, the carotid artery lumen diameter of the geometry was assumed to be 10 mm. The lengths of the carotid

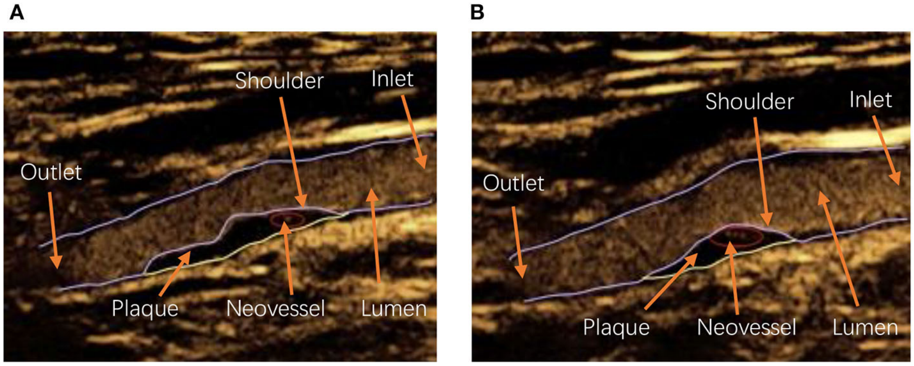

FIGURE 1 | The contrast-enhanced ultrasound (CEUS) image with carotid artery lumen, atherosclerotic plaque, and neovessel: **(A)** is the CEUS image with one neovessel, and **(B)** is the CEUS image with three neovessels. Inlet and outlet: The carotid artery blood flow inlet and outlet, respectively; Shoulder: the area at the periphery of the plaque adjacent to the normal intima beneath the fibrous cap of the plaque (Pasterkamp et al., 1998).

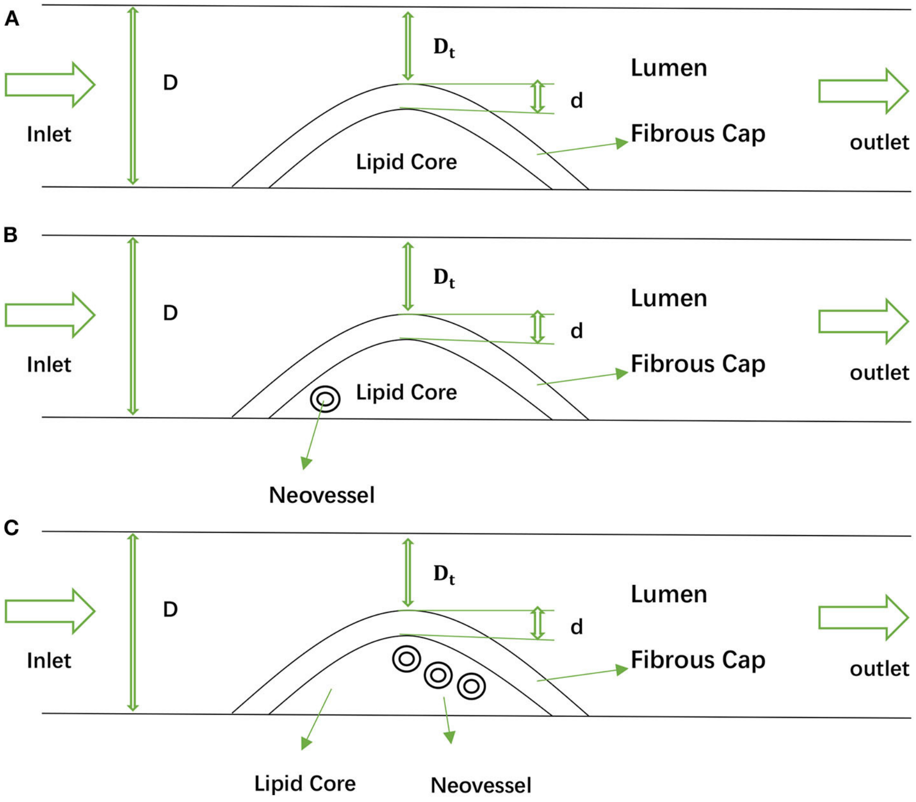

FIGURE 2 | The 2D geometries of the idealized carotid artery with plaque and neovessel: **(A)** is the geometry with no neovessel, **(B)** is the geometry with one neovessel, and **(C)** is the geometry with three neovessels.

artery and the plaque are set to 100 and 20 mm, respectively. The distance between the inlet boundary and the plaque structure was set to be 32 mm, and the outlet boundary was set to be 48 mm away from the plaque structure (Belzacq et al., 2012). Additionally, the diameter of the neovessel with 0.1 mm thickness was set at 0.4 mm. For the IPH, it was assumed to be a half-moon shape (Teng et al., 2014, 2015). Two types of IPH were used in this paper with the position of one IPH set in the shoulder of plaque, and another one in the middle of the plaque (see **Supplementary Figure 1**).

2.2. Computational Models, Materials, and Boundary Conditions

In this study, the components of the plaque were assumed to be hyper-elastic and non-linear because the ideal human tissue is hyper-elastic. The Yeoh 3rd Order strain energy density function was used to describe the material of the plaque in the carotid artery (Teng et al., 2015).

$$W = \sum_{i}^{3} C_i(I_i - 3)^i + k(J - 1), i = 1, 2, 3 \tag{4}$$

$$I_1 = {\lambda_1}^2 + {\lambda_2}^2 + {\lambda_3}^2 \tag{5}$$

where (i) I_i represents the first invariant of the unimodular component of the Cauchy–Green deformation tensor, (ii) C_i is the material constants, (iii) λ_i is the principal stretch, (iv) J = def (F) and F is the deformation gradient, (v) k is the Lagrangian multiplier for incompressibility, and (vi) J is equal to 0 for material incompressibility. The parameter values were chose to describe the material models (see **Table 1**): (i) fibrous cap: C1 = 53.724 kPa, C2 = 2201.011 kPa, C3 = 42.551 kpa, (ii) lipid core: C1 = 18.548 kPa, C2 = 207.371 kPa, C3 = 422.652 kPa, (iii) IPH: C1 = 11.225 kPa, C2 = 69,214 kPa, and C3 = 781.546 kPa, (iv) neovessel: C1 = 5.656 kPa, C2 = 1816.773 kPa, C3 = 162.037 kPa. The density and viscosity are the fundamental blood parameters. Generally, the range of blood density is 1,030–1.070 kg/m^3. In our study, the constant density 1.050 kg/m^3 was used, and the value of the blood viscosity is 3.400 Ns/m^2 (Marshall et al., 2004). The blood was assumed to be an incompressible, laminar, and Newtonian fluid.

Additionally, the inlet boundary condition was transient with time (see **Figure 3**). This trend of the velocity changed over time, and it was close to the experimental curves (Viedma et al., 1997). After one cardiac cycle, the blood flow of the carotid outlet tended to be stable, and the relative pressure of the outlet was set as 0 Pa. For simulating the blood flow, the conditions of no-slip and non-deformation were considered at the carotid artery wall. The 2D computational models were solved by using ANSYS2019 R1. The one-way fluid–structure interaction was operated. The pressure of the fluid was loaded in the whole plaque, and an approximate blood pressure of 0.00133 MPa in the microvessel was exerted on the neovessel and IPH.

TABLE 1 | The parameter values of the Yeoh model used in this paper.

	C1 (kPa)	C2 (kPa)	C3 (kPa)
Fibrous cap	53.724	2201.011	42.551
Lipid core	18.548	207.371	422.652
Neovessel	5.656	1816.773	162.037
IPH	11.225	69.214	781.546

3. RESULTS

Quantification parameters were evaluated in the present study. These parameters included total deformation, maximum principal stress, and maximum principal strain. The detail of the parameters was summarized in **Table 2**. The deformation of the plaques was negatively related to the thickness of the fibrous cap. The largest deformation was found in the geometry with a thin fibrous cap (thickness was 0.0065 mm), and it was 0.14619 (see **Figure 4C**). Also, the deformation of the neovessel was in line with the observation in the CEUS images that the shape of neovessel changes along with the pulsatile blood flow, which suggested that the stress on the plaque could further induce the stress on the neovessel. Moreover, the neovessel mainly consisted of endothelial cells without smooth muscle cells, which makes the neovessel vulnerable to the stress. Additionally, the deformation of the plaque with three neovessels (50% luminal stenosis, different thickness of fibrous cap) showed that the

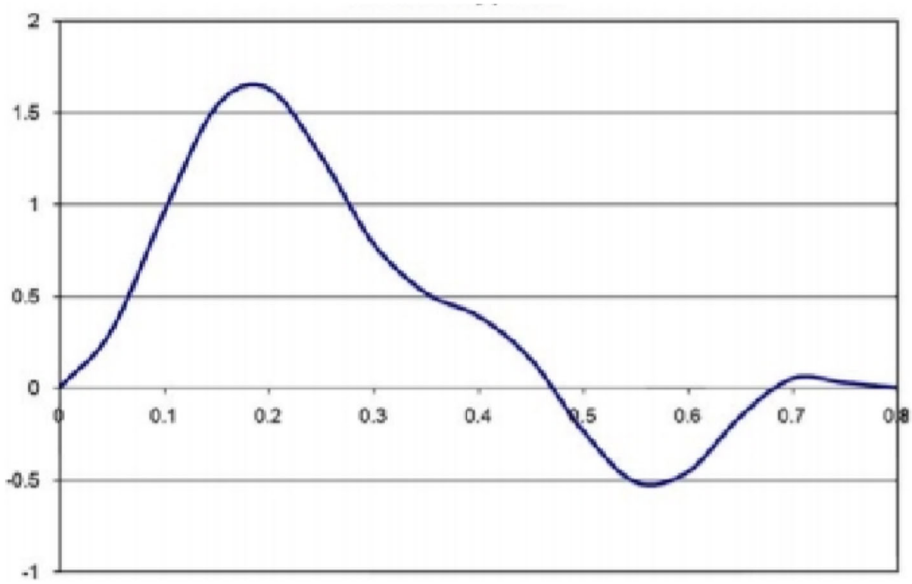

FIGURE 3 | The velocity condition specified at the inlet boundary.

TABLE 2 | Comparison of maximum principal strain [MP strain (mm\mm)] and stress [MP stress (kPa)] of plaque during one cardiac cycle among no neovessel, one neovessel, three neovessels, and intraplaque hemorrhage (IPH).

Degree of plaque stenosis (%)	Thickness of fibrous cap (mm)	Plaque geometry	MP strain (mm/mm)	MP stress (kPa)
50	2	No neovessel and IPH	0.00116	11.6
		One neovessel	0.020946	11.625
		Three neovessels	0.019249	11.565
		IPH in plaque shoulder	0.016795	11.54
		IPH in plaque middle	0.017509	11.826
	0.5	No neovessel and IPH	0.015697	21.276
		One neovessel	0.021508	21.391
		Three neovessels	0.018977	21.398
		IPH in plaque shoulder	0.048537	74.321
		IPH in plaque middle	0.078302	71.435
	0.0065	No neovessel and IPH	0.058363	276.99
		One neovessel	0.06425	272.81
		Three neovessels	0.059618	269.89
		IPH in plaque shoulder	0.052972	296.63
		IPH in plaque middle	0.058464	272.28
65	2	No neovessel and IPH	0.019593	36.25
		One neovessel	0.021154	36.389
		Three neovessels	0.020147	36.178
		IPH in plaque shoulder	0.019791	36.673
		IPH in plaque middle	0.032817	37.965
	0.5	No neovessel and IPH	0.016165	54.49
		One neovessel	0.02203	54.871
		Three neovessels	0.018698	54.393
		IPH in plaque shoulder	0.015754	56.731
		IPH in plaque middle	0.015987	54.19
	0.0065	No neovessel and IPH	0.066529	563.67
		One neovessel	0.066929	575.43
		Three neovessels	0.066642	569.73
		IPH in plaque shoulder	0.068731	608.05
		IPH in plaque middle	0.06663	565.72
75	2	No neovessel and IPH	0.054892	225.72
		One neovessel	0.057081	226.87
		Three neovessels	0.056651	225.66
		IPH in plaque shoulder	0.055234	231.15
		IPH in plaque middle	0.053922	226.95
	0.5	No neovessel and IPH	0.050985	336.36
		One neovessel	0.051242	335.89
		Three neovessels	0.051038	333.86
		IPH in plaque shoulder	0.052625	350.08
		IPH in plaque middle	0.051274	336.18
	0.0065	No neovessel and IPH	0.10114	1242.6
		One neovessel	0.10223	1270.3
		Three neovessels	0.10125	1250.3
		IPH in plaque shoulder	0.10643	1358.8
		IPH in plaque middle	0.10206	1261.5

diameter of the neovessels was further suppressed when the fibrous cap was thin (see **Figure 5**). The largest deformation occurred in the plaque with 0.0065 mm fibrous cap thickness and the value of deformation is 0.14988 (see **Figure 5C**). It can be found that there was a relatively large deformation difference between the plaque with one neovessel and with three neovessels. The reason may be that the neovessel located closed to the plaque shoulder suffered from a larger pressure

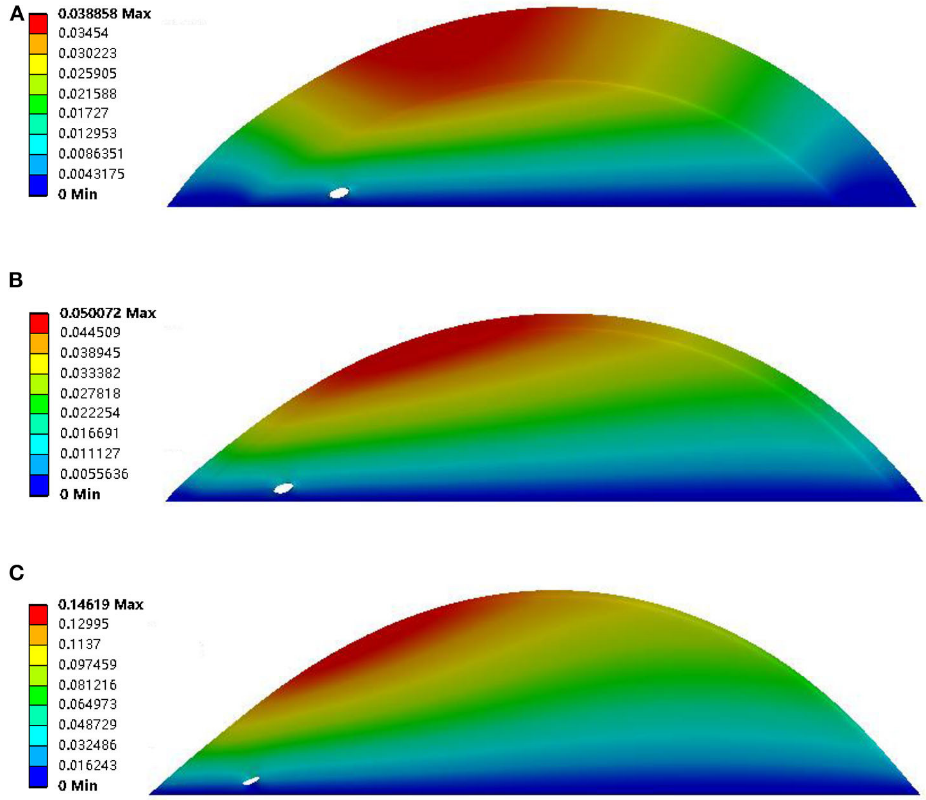

FIGURE 4 | Deformation results of plaque with 50% luminal stenosis, one neovessel, and different thickness of the fibrous cap. The fibrous cap thicknesses of subfigures **(A–C)** were 2, 0.5, and 0.0065 mm, respectively.

than the other three neovessels located in the plaque middle-lower stream.

The deformation results of plaque with 65 and 75% luminal stenoses were illustrated in the **Supplementary Figures 2–5**. The maximum principal stress and strain in plaque with different degrees of luminal stenosis and fibrous cap thickness are summarized in **Table 2**. The maximum principal stresses are recorded in the thin fibrous cap geometry that it was 276.99, 563.67, and 1242.6 kPa for 50, 65, and 75% luminal stenosis, respectively. A higher degree of luminal stenosis was subjected to a higher maximum principal stress and strain in all the geometries with 0.0065 mm fibrous cap thickness (see **Figure 6**). And the maximum principal stress grows along with the thinning of the fibrous cap in the geometry with 75% luminal stenosis (see **Figure 7**). As shown in **Table 2**, the largest maximum principal stress was recorded in the geometries with 75% stenosis and the thickness of fibrous cap varied from 2 to 0.0065 mm. The maximum principal strain of plaque with 0.0065mm fibrous ca thickness increased significantly with the degree of the luminal stenosis. Consequently, The plaques observed, with (i) 65% stenosis, 0.0065 mm thickness, and (ii) 75% stenosis, 0.5 and 0.0065 mm thickness, were unstable and vulnerable. Moreover, for an artery with high degree of luminal stenosis and a plaque with thin fibrous cap thickness, a higher maximum principal stress was observed when neovascularization or IPH was presented compared to those without neovascularization or IPH in most cases. And, a relatively higher maximum principal stress was observed when IPH existed in plaque shoulder than in plaque middle.

4. DISCUSSION

Vulnerable plaque in the carotid artery is a critical cause of many cardiovascular diseases like stroke and ischemic attacks (Schinkel et al., 2020). Neovascularization and IPH contribute significantly to the rupture of atherosclerotic plaques (Van der Veken et al., 2016; Demeure et al., 2017; Yang et al., 2020). Wang et al. (2020) found that increased carotid neovascularization was significantly related to aggravated cerebral white matter lesions in 269 participants based on CEUS. Camps-Renom et al. (2020) demonstrated that neovascularization was an independent predictor of ischemic stroke recurrence, based on 78 patients with carotid atherosclerosis. Literatures (Mark et al., 2020a,b; Yang et al., 2020) discovered that IPH had a close connection with a high risk of cardiovascular diseases. In addition, Teng et al. (2012) found that the computed parameters of stress and strain in a carotid artery plaque increased as the distance between the neovessel and the artery lumen decreased. There is a big potential for large deformation and high mechanical loading variation

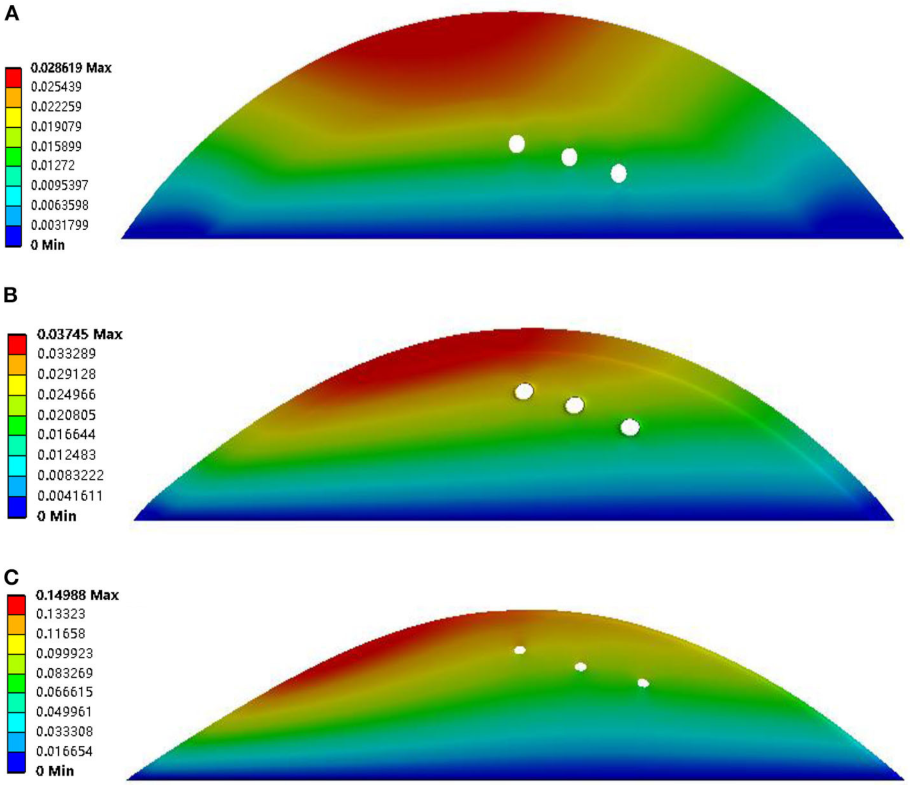

FIGURE 5 | Deformation results of plaque with 50% luminal stenosis, three neovessel, and different thickness of fibrous cap. The fibrous cap thicknesses of subfigures **(A–C)** were 2, 0.5, and 0.0065, respectively.

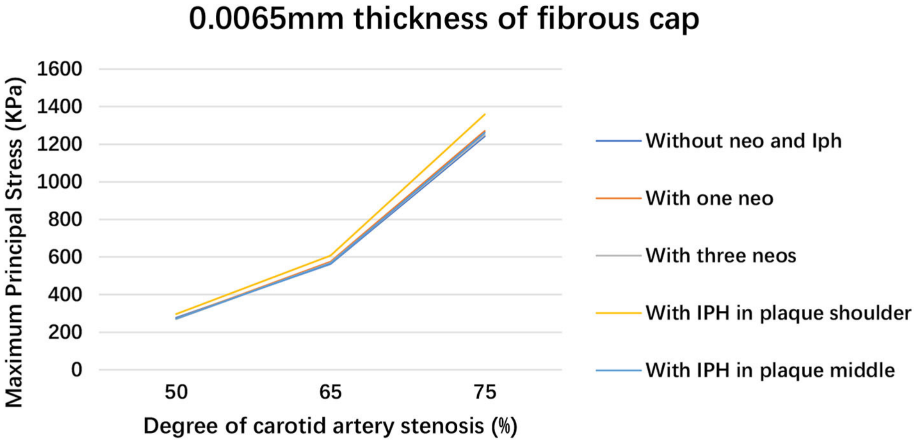

FIGURE 6 | Plaque maximum principal stress within 0.0065 mm fibrous cap thickness when changing luminal stenosis.

in an intraplaque neovessel. Huang et al. (2012) quantified the effect of IPH on plaque wall stress by using a 3D fluid–structure interaction model based on the magnetic resonance image; the authors found that the critical plaque wall stress and strain increased in geometries with IPH, relative to geometries without IPH. Additionally, fibrous cap thickness and luminal stenosis have also been demonstrated as two critical parameters that could induce plaque rupture (Li Z. Y. et al., 2006; Alegre-Marténez et al., 2019; Zareh et al., 2019). A plaque with thinner fibrous cap thickness and larger lipid core was more likely to rupture and cause stroke. Huang et al. (2012) have indicated that there was a connection between fibrous cap thickness and IPH occurrence based on the analysis by fluid–structure interaction. Therefore, to be consideration of fibrous cap thickness and

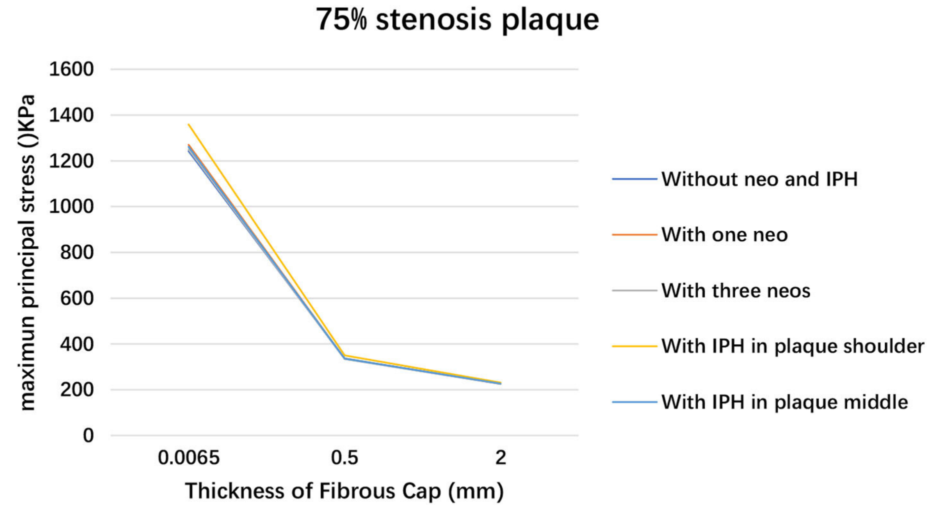

FIGURE 7 | Plaque maximum principal stress variation within 75% stenosis luminal stenosis when changing fibrous cap thickness.

luminal stenosis are necessary for analyzing the stress and strain effect of neovascularization and IPH of plaque.

In this paper, we have constructed an idealized geometry of the carotid artery with atherosclerotic plaque based on the CEUS image. The four factors of plaque rupture, namely neovascularization, IPH, fibrous cap thickness, and luminal stenosis, were evaluated. A one-way fluid–structure interaction model was employed to calculate the structural stress and strain in the carotid atherosclerotic plaque. The simulation results validated the conclusion mentioned above that the two factors of fibrous cap thickness and luminal stenosis degree play a significant role in the progression of carotid atherosclerotic plaque. The results of the one-way fluid–structure interaction model in this paper were consistent with the current literature (Li Z. Y. et al., 2006; Teng et al., 2012). Therefore, it is reasonable to assume the role of IPH and neovascularization distributions in the formation of carotid atherosclerotic plaque. IPH is one of the important factors of carotid atherosclerotic plaque, especially in vulnerable plaque (Saba et al., 2019b). It can accelerate the enlargement of the lipid core that can increase the risk of the plaque rupture.

In our work, two types of IPHs have been evaluated, and stress and strain were determined within the plaque were observed. It was a critical indication that IPH distributed at the shoulder of the plaque showed a higher risk to rupture compared to the plaque with IPH distributed in the middle area regardless of the fibrous cap thickness and the luminal stenosis degree (see **Table 2**). For the plaque with IPH in the plaque shoulder, 75% stenosis, and thin fibrous cap thicknesses, the maximum principal stress increased on an average to 34.47 kPa compared to the plaque with IPH in the plaque middle. In the plaque with 50 and 65% stenosis, the maximum principal stress increased on an average to 8.983 and 14.526 kPa, respectively. Besides, the plaque with IPH in the plaque shoulder had a 116.3 kPa higher maximum principal stress than the plaque without IPH, especially for the plaque with 75% stenosis and 0.0065 mm fibrous cap thickness. Therefore, the location of the plaque shoulder was a high-risk site for plaque rupture frequently. Additionally, IPH was not a negligible factor for assessing plaque vulnerability, and there was guidance by B-model ultrasonography to distinguish IPH (Gao et al., 2017; Zheng et al., 2020a,b).

Previous studies had (Huang et al., 2008; Hoogi et al., 2011; Van der Veken et al., 2016; Demeure et al., 2017) demonstrated that the feature of neovascularization also played an important role in the progression of plaque, and it may be associated with the possibility of stroke occurrence. Therefore, neovascularization within the plaque is important. The neovascularization can be visualized by CEUS imaging, and then help the cardiologist to observe the deformation of the neovascularization. However, the effect of the neovascularization on plaque risk only depended on the cardiologist's subjective diagnosis, according to the distribution and density of the IPH. Therefore, in this paper, the neovascularization was studied by modeling the neovessel geometry within the plaque. **Figures 4**, **5** show the deformation of the neovessel in 50% luminal stenosis in conjunction with different fibrous cap thickness. The larger deformation of the neovessel was found with a thinner fibrous cap. The deformation of the neovessel was in line with the discovery carotid artery plaque in CEUS images. **Table 2** indicates that the maximum principal stress and strain was similar between geometries with neovessel and without neovessel as a result of the similar distribution and density of the neovessels. However, **Figures 4**, **5** and **Supplementary Figures 1–5** show the occurrence of neovessel deformation. That is to say, the neovessel underwent the loading of mechanical stress and had the potential to rupture and then lead to IPH.

Additionally, according to experimental results of fluid flow, the distribution of plaque stress and strain mainly focused on the proximal surface of the plaque, regardless of luminal stenosis and fibrous cap thickness. Choi et al. (2015) have found that axial plaque stress and wall shear stress in the upstream were higher than in downstream. These findings demonstrated that the site of plaque shoulder was more likely to tend to rupture because it is undergoing shear stress induced by the blood flow (Malek, 1999). The variation of shear stress could alter the characteristics of the endothelial cell, including its morphology, function, proliferation, and even vascular injury (Malek, 1999; Chatzizisis et al., 2009). Therefore, the stress and strain distribution in the proximal surface of plaque fluid flow has an important role in adjudging plaque rupture. Additionally, the neovessel was only made up of little endothelial cells and the vulnerability of neovessel was poor. Therefore, it is of significance to improve the assessment of vulnerable plaque by analyzing the effect of hemodynamic stress and strain on the plaque with neovascularization and IPH.

There are some limitations to this study. First, it was a theoretical research, and the geometry of the carotid artery was idealized. The carotid bifurcation was not taken into account, as the neovessel and the IPH were the focus of this paper. Second, only two types of neovessels were analyzed. The shape in conjunction with the location of the neovessel was flexible and variable. McCarthy et al. (1999) found that the neovessel within a plaque may exist in the medial, the lateral corners, and the bottom of the plaque. Third, the material properties of the neovessel were assumed from literatures, and this may have resulted in the parameters of maximum principal stress and strain levels being below or over the actual value. There is a small difference in the value of the maximum principal stress between the plaque with neovessel and without neovessel. The material properties, shape, and location of the neovessel may be the most likely reason for it. Another limitation is that this idealized geometry was two-dimensional. Previous studies have illustrated the histology image of the transversal slice of the plaque, indicating the distribution of microvasculature could either axial or transversal (Lu et al., 2015; Guo et al., 2018, 2019). These neovessels were with significant variation of the size of the neovessels. While previous studies focus on the axially distributed neovessel, our results suggested that the mechanical effects of transversal distributed neovessel was also important to the vulnerability of the plaque. Also, in comparison to the previous study (Teng et al., 2015), the morphology of IPH used in the present study was generally consistent with it, even if the CEUS imaging is less applicable for detecting IPH. However, as the neovessel was more complex with branches pointing toward different directions and dimensions, further study was required to establish a more realistic geometry of the plaque with 3-dimensional distribution of the microenvironment for a more comprehensive understanding of the mechanics property of the plaque.

5. CONCLUSION

In conclusion, a numerical analysis of the stress and strain within carotid artery plaque was conducted. We verified that the plaque with thin fibrous cap and serious luminal stenosis has a high risk of rupture. At the same time, neovascularization and IPH were also studied. Pulsatile blood flow was related to the deformation phenomenon of neovessel occurrence in intraplaque observed in CEUS image. Also, the IPH has the potential to increase the possibility of plaque rupture. Therefore, IPH and neovascularization may also be considered to be the features for plaque progression and even rupture, besides the two key factors of fibrous cap thickness and the degree of luminal stenosis.

DATA AVAILABILITY STATEMENT

The original contributions presented in the study are included in the article/**Supplementary Material**, further inquiries can be directed to the corresponding author/s.

AUTHOR CONTRIBUTIONS

ZL and XW: conceptualization. YW: methodology, validation, investigation, and writing-original draft. XL: supervision, project administration, and writing - review & editing. SL, ZL, XL, and LR: funding acquisition. SH, YH, and LR: data curation.

FUNDING

This study received financial support from Shenzhen Science and Technology Project (JCYJ20170817171836611, JCYJ20170306092258717), Natural Science Foundation of Guangdong Province, China (2019A1515011463), Scientific Research Items of Shenzhen Science and Technology Innovation Committee (No. KJYY20180703165202011), and the Major Project of Guangzhou Science and Technology of Collaborative Innovation and Industry: intelligent video detection and recognition technology in cloud computing environment (201605122151511).

SUPPLEMENTARY MATERIAL

The Supplementary Material for this article can be found online at: https://www.frontiersin.org/articles/10.3389/fninf.2020.596340/full#supplementary-material

REFERENCES

Alegre-Marténez, C., Choi, K. S., Tammisola, O., and McNally, D. (2019). On the axial distribution of plaque stress: influence of stenosis, severity, lipid core stiffness, lipid core length and fibrous cap stiffness. *Med. Eng. Phys.* 68, 76–84. doi: 10.1016/j.medengphy.2019.02.015

Avci, A., Fidan, S., Tabakçı, M. M., Toprak, C., Alizade, E., Acar, E., et al. (2016). Association between the gensini score and carotid artery stenosis. *Korean Circ. J.* 46, 639–645. doi: 10.4070/kcj.2016.46.5.639

Belzacq, T., Avril, S., Leriche, E., and Delache, A. (2012). A numerical parametric study of the mechanical action of pulsatile blood flow onto axisymmetric stenosed arteries. *Med. Eng. Phys.* 34, 1483–95. doi: 10.1016/j.medengphy.2012.02.010

Camps-Renom, P., Prats-Sánchez, L., Casoni, F., González-de-Echávarri, J. M., Marrero-González, P., Castrillón, I., et al. (2020). Plaque neovascularization detected with contrast-enhanced ultrasound predicts ischaemic stroke recurrence in patients with carotid atherosclerosis. *Eur. J. Neurol.* 27, 809–816. doi: 10.1111/ene.14157

Chatzizisis, Y. S., Coskun, A. U., Jonas, M., Edelman, E. R., Feldman, C. L., and Stone, P. H. (2009). Role of endothelial shear stress in the natural history of coronary atherosclerosis and vascular remodeling. *J. Am. Coll. Cardiol.* 49, 2379–2393. doi: 10.1016/j.jacc.2007.02.059

Choi, G., Lee, J. M., Kim, H. J., Park, J. B., Sankaran, S., Otake, H., et al. (2015). Coronary artery axial plaque stress and its relationship with lesion geometry: application of computational fluid dynamics to coronary CT angiography. *JACC Cardiovasc. Imaging* 8, 1156–1166. doi: 10.1016/j.jcmg.2015.04.024

Cicha, I., Wörner, A., Urschel, K., Beronov, K., Goppelt-Struebe, M., Verhoeven, E., et al. (2011). Carotid plaque vulnerability: a positive feedback between hemodynamic and biochemical mechanisms. *Stroke* 42, 3502–3510. doi: 10.1161/STROKEAHA.111.627265

Crombag, G. A. J. C., Schreuder, F. H. B. M., van Hoof, R. H. M., Truijman, M. T. B., Wijnen, N. J. A., Vöö, S. A., et al. (2019). Microvasculature and intraplaque hemorrhage in atherosclerotic carotid lesions: a cardiovascular magnetic resonance imaging study. *J. Cardiovasc. Magn. Reson.* 21:15. doi: 10.1186/s12968-019-0524-9

Demeure, F., Bouzin, C., Roelants, V., Bol, A., Verhelst, R., Astarci, P., et al. (2017). Head-to-head comparison of inflammation and neovascularization in human carotid plaques implications for the imaging of vulnerable plaques. *Circulation* 10:e005846. doi: 10.1161/CIRCIMAGING.116.005846

Denmark, S. E., and Marcin, L. R. (2011). Correlation of carotid artery atherosclerotic lesion echogenicity and severity at standard us with intraplaque neovascularization detected at contrast-enhanced us. *Int. J. Med. Radiol.* 258, 618–626. doi: 10.1148/radiol.10101008

Dunmore, B. J., McCarthy, M. J., Naylor, A. R., and Brindle, N. P. (2006). Carotid plaque instability and ischemic symptoms are linked to immaturity of microvessels within plaques. *J. Vasc. Surg.* 45, 155–159. doi: 10.1016/j.jvs.2006.08.072

Falk, E., Shah, P. K., and Fuster, V. (1995). Coronary plaque disruption. *Circulation* 92, 657–671. doi: 10.1161/01.CIR.92.3.657

Feinstein, S. B. (2006). Contrast ultrasound imaging of the carotid artery vasa vasorum and atherosclerotic plaque neovascularization. *J. Am. Coll. Cardiol.* 48, 236–243. doi: 10.1016/j.jacc.2006.02.068

Finn, A. V., Nakano, M., Narula, J., Kolodgie, F. D., and Virmani, R. (2010). Concept of vulnerable/unstable plaque. *Arterioscler. Thromb. Vasc. Biol.* 30, 1282–1292. doi: 10.1161/ATVBAHA.108.179739

Gao, Z., Li, Y., Sun, Y., Yang, J., Xiong, H., Zhang, H., et al. (2017). Motion tracking of the carotid artery wall from ultrasound image sequences: a nonlinear state-space approach. *IEEE Trans. Med. Imaging* 37, 273–283. doi: 10.1109/TMI.2017.2746879

Guo, M., Cai, Y., Yao, X., and Li, Z. (2018). Mathematical modeling of atherosclerotic plaque destabilization: role of neovascularization and intraplaque hemorrhage. *J. Theor. Biol.* 450, 53–65. doi: 10.1016/j.jtbi.2018.04.031

Guo, M., Yan, C., He, C., and Li, Z. (2019). Coupled modeling of lipid deposition, inflammatory response and intraplaque angiogenesis in atherosclerotic plaque. *Biomed. Eng. Soc.* 47, 439–452. doi: 10.1007/s10439-018-02173-1

Hoogi, A., Adam, D., Hoffman, A., Kerner, H., Reisner, S., and Gaitini, D. (2011). Carotid plaque vulnerability: quantification of neovascularization on contrast-enhanced ultrasound with histopathologic correlation. *Am. J. Roentgenol.* 123, 1125–1132. doi: 10.2214/AJR.10.4522

Huang, P., Huang, F., Zou, C., Sun, H., Tian, X., Yang, Y., et al. (2008). Contrast-enhanced sonographic characteristics of neovascularization in carotid atherosclerotic plaques. *J. Clin. Ultrasound* 36, 346–351. doi: 10.1002/jcu.20448

Huang, X., Yang, C., Canton, G., Ferguson, M., Yuan, C., and Tang, D. (2012). Quantifying effect of intraplaque hemorrhage on critical plaque wall stress in human atherosclerotic plaques using three-dimensional fluid-structure interaction models. *J. Biomech. Eng.* 134:121004. doi: 10.1115/1.4007954

Kolodgie, F. D., Burke, A. P., Farb, A., Gold, H. K., Yuan, J., Narula, J., et al. (2001). The thin-cap fibroatheroma: a type of vulnerable plaque: the major precursor lesion to acute coronary syndromes. *Curr. Opin. Cardiol.* 16, 285–292. doi: 10.1097/00001573-200109000-00006

Li, Z., Howarth, S., Trivedi, R. A., U-King-Im, J. M., Graves, M. J., Brown, A., et al. (2006). Stress analysis of carotid plaque rupture based on *in vivo* high resolution MRI. *J. Biomech.* 39, 2611–22. doi: 10.1016/j.jbiomech.2005.08.022

Li, Z. Y., Howarth, S. P., Tang, T., and Gillard, J. H. (2006). How critical is fibrous cap thickness to carotid plaque stability? A flow-plaque interaction model. *Stroke* 37, 1195–1199. doi: 10.1161/01.STR.0000217331.61083.3b

Lu, J., Duan, W., and Qiao, A. (2015). Finite element analysis of mechanics of neovessels with intraplaque hemorrhage in carotid atherosclerosis. *Biomed. Eng. Online* 14, S1–S3. doi: 10.1186/1475-925X-14-S1-S3

Malek, A. (1999). Hemodynamic shear stress and its role in atherosclerosis. *JAMA* 282:2035. doi: 10.1001/jama.282.21.2035

Mark, I. T., Nasr, D. M., Huston, J., de Maria, L., de Sanctis, P., Lehman, V. T., et al. (2020a). Embolic stroke of undetermined source and carotid intraplaque hemorrhage on MRI: a systemic review and meta-analysis. *Clin. Neuroradiol.* doi: 10.1007/s00062-020-00921-2. [Epub ahead of print].

Marshall, I., Zhao, S., Papathanasopoulou, P., Hoskins, P., and Xu, Y. (2004). MRI and CFD studies of pulsatile flow in healthy and stenosed carotid bifurcation models. *J. Biomech.* 37, 679–687. doi: 10.1016/j.jbiomech.2003.09.032

McCarthy, M. J., Loftus, I. M., Thompson, M. M., Jones, L., London, N. J., Bell, P. R., et al. (1999). Angiogenesis and the atherosclerotic carotid plaque: an association between symptomatology and plaque morphology. *J. Vasc. Surg.* 30, 261–268. doi: 10.1016/S0741-5214(99)70136-9

Misaki, K., Uno, T., Nambu, I., Kimura, R., Yoshikawa, A., Kamide, T., et al. (2020b). Asymptomatic carotid intraplaque hemorrhage is associated with a high risk of cerebral infarction and death after cardiovascular surgery. *J. Neurol. Sci.* 412:116801. doi: 10.1016/j.jns.2020.116801

Moreno, P. R., Purushothaman, K. R., Fuster, V., Echeverri, D., Truszczynska, H., Sharma, S. K., et al. (2004). Plaque neovascularization is increased in ruptured atherosclerotic lesions of human aorta: implications for plaque vulnerability. *Circulation* 110, 2032–2038. doi: 10.1161/01.CIR.0000143233.87854.23

Moreno, P. R., Purushothaman, K. R., Zias, E., Sanz, J., and Fuster, V. (2006). Neovascularization in human atherosclerosis. *Curr. Mol. Med.* 6, 457–477. doi: 10.2174/156652406778018635

Murata, K., Murata, N., Chu, B., Watase, H., Hippe, D. S., Balu, N., et al. (2020). Characterization of carotid atherosclerotic plaques using 3-dimensional merge magnetic resonance imaging and correlation with stroke risk factors. *Stroke* 51, 475–480. doi: 10.1161/STROKEAHA.119.027779

Naghavi, M., Libby, P., Falk, E., Casscells, S. W., Litovsky, S., Rumberger, J., et al. (2003). From vulnerable plaque to vulnerable patient: a call for new definitions and risk assessment strategies: part I. *Circulation* 108, 1664–1672. doi: 10.1161/01.CIR.0000087480.94275.97

Pasterkamp, G., Schoneveld, A. H., van der Wal, A. C., Haudenschild, C. C., Clarijs, R. J., Becker, A. E., et al. (1998). Relation of arterial geometry to luminal narrowing and histologic markers for plaque vulnerability: the remodeling paradox. *J. Am. Coll. Cardiol.* 32, 655–662. doi: 10.1016/S0735-1097(98)00304-0

Radwa M. A., and Eldosoky, M. A. A. (2020). "Studying of the blood flow behavior in a stenosed carotid artery for healthy, anemic and diabetic blood," in *2020 International Conference on Innovative Trends in Communication and Computer Engineering (ITCE)* (Aswan), 72–75.

Rossi, A., Franceschini, L., Fusaro, M., Cicoira, M., Eleas, A. A., Golia, G., et al. (2002). Carotid atherosclerotic plaque instability in patients with acute myocardial infarction. *J. Am. Coll. Cardiol.* 111, 263–266. doi: 10.1016/S0735-1097(02)81383-3

Saba, L., Micheletti, G., Brinjikji, W., Garofalo, P., Montisci, R., Balestrieri, A., et al. (2019a). Carotid intraplaque-hemorrhage volume and its association with cerebrovascular events. *Am. J. Neuroradiol.* 40, 1731–1737. doi: 10.3174/ajnr.A6189

Saba, L., Saam, T., Jäger, H. R., Yuan, C., Hatsukami, T. S., Saloner, D., et al. (2019b). Imaging biomarkers of vulnerable carotid plaques for stroke risk prediction and their potential clinical implications. *Lancet Neurol.* 18, 559–572. doi: 10.1016/S1474-4422(19)30035-3

Sadat, U., Weerakkody, R. A., and Bowden, D. J. (2009). Hemorrhage and large lipid-rich necrotic cores are independently associated with thin or ruptures fibrous caps: an *in vivo* 3T MRI study. *Atherosclerosis* 207, 434–439. doi: 10.1016/j.atherosclerosis.2009.05.002

Schinkel, A. F. L., Bosch, J. G., Staub, D., Adam, D., and Feinstein, S. B. (2020). Contrast-enhanced ultrasound to assess carotid intraplaque neovascularization. *Ultrasound Med. Biol.* 46, 466–478. doi: 10.1016/j.ultrasmedbio.2019.10.020

Takaya, N., Yuan, C., Chu, B., Saam, T., Underhill, H., Cai, J., et al. (2006). Association between carotid plaque characteristics and subsequent ischemic cerebrovascular events: a prospective assessment with MRI—initial results. *J. Vasc. Surg.* 44:223. doi: 10.1016/j.jvs.2006.04.013

Tang, D., Yang, C., Kobayashi, S., Zheng, J., and Vito, R. P. (2003). Effect of stenosis asymmetry on blood flow and artery compression: a three-dimensional fluid-structure interaction model. *Ann. Biomed. Eng.* 31, 1182–1193. doi: 10.1114/1.1615577

Teng, Z., He, J., Degnan, A. J., Chen, S., Sadat, U., Bahaei, N. S., et al. (2012). Critical mechanical conditions around neovessels in carotid atherosclerotic plaque may promote intraplaque hemorrhage. *Atherosclerosis* 223, 321–326. doi: 10.1016/j.atherosclerosis.2012.06.015

Teng, Z., Yuan, J., Feng, J., Zhang, Y., Brown, A. J., Wang, S., et al. (2015). The influence of constitutive law choice used to characterize atherosclerotic tissue material properties on computing stress values in human carotid plaques. *J. Biomech.* 48, 3912–3921. doi: 10.1016/j.jbiomech.2015.09.023

Teng, Z., Zhang, Y., Huang, Y., Feng, J., Yuan, J., Lu, Q., et al. (2014). Material properties of components in human carotid atherosclerotic plaques: a uniaxial extension study. *Acta Biomater.* 10, 5055–5063. doi: 10.1016/j.actbio.2014.09.001

Van der Veken, B., De Meyer, G. R., and Martinet, W. (2016). Intraplaque neovascularization as a novel therapeutic target in advanced atherosclerosis. *Expert Opin. Ther. Targets* 20, 1247–1257. doi: 10.1080/14728222.2016.1186650

Vicenzini, E., Giannoni, M. F., Puccinelli, F., Ricciardi, M. C., Altieri, M., Di Piero, V., et al. (2007). Detection of carotid adventitial vasa vasorum and plaque vascularization with ultrasound cadence contrast pulse sequencing technique and echo-contrast agent. *Stroke* 38, 2841–2843. doi: 10.1161/STROKEAHA.107.487918

Viedma, A., Jiménez-Ortiz, C., and Marco, V. (1997). Extended willis circle model to explain clinical observations in periorbital arterial flow. *J. Biomech.* 30, 265–272. doi: 10.1016/S0021-9290(96)00143-1

Wang, Y., Jiang, C., Huang, H., Liu, N., Wang, Y., Chen, Z., et al. (2020). Correlation of cerebral white matter lesions with carotid intraplaque neovascularization assessed by contrast-enhanced ultrasound. *J. Stroke Cerebrovasc. Dis.* 29, 2020–104928. doi: 10.1016/j.jstrokecerebrovasdis.2020.104928

Woorak, C., Park, S. H., Huh, H. K., and Lee, S. J. (2017). Hemodynamic characteristics of flow around a deformable stenosis. *J. Biomech.* 61, 216–223. doi: 10.1016/j.jbiomech.2017.07.033

Xiong, L., Deng, Y. B., Zhu, Y., Liu, Y. N., and Bi, X. J. (2009). Correlation of carotid plaque neovascularization detected by using contrast-enhanced us with clinical symptoms. *Radiology* 251, 583–589. doi: 10.1148/radiol.2512081829

Yang, D., Liu, Y., Han, Y., Li, D., Wang, W., Li, R., et al. (2020). Signal of carotid intraplaque hemorrhage on MR T1-weighted imaging: association with acute cerebral infarct. *Am. J. Neuroradiol.* 41, 836–843. doi: 10.3174/ajnr.A6498

Zamani, M., Skagen, K., Scott, H., Russell, D., and Skjelland, M. (2020). Advanced ultrasound methods in assessment of carotid plaque instability: a prospective multimodal study. *BMC Neurol.* 20:39. doi: 10.1186/s12883-020-1620-z

Zareh, M., Katul, R., and Mohammadi, H. (2019). Mechanics of atherosclerotic plaques: effect of heart rate. *Cardiovasc. Eng. Technol.* 10, 344–353. doi: 10.1007/s13239-019-00413-6

Zheng, Y., Song, H., Zhang, K., Fan, J., and Liu, X. (2020b). Dynamically spatiotemporal regularized correlation tracking. *IEEE Trans. Neural Netw. Learn. Syst.* 31, 2336–2347. doi: 10.1109/TNNLS.2019.2929407

Zheng, Y., Sun, Y., Muhammad, K., and De Albuquerque, V. H. C. (2020a). Weighted LIC-based structure tensor with application to image content perception and processing. *IEEE Trans. Ind. Inform.* doi: 10.1109/TII.2020.2980577. [Epub ahead of print].

Conflict of Interest: The authors declare that the research was conducted in the absence of any commercial or financial relationships that could be construed as a potential conflict of interest.

frontiers in Neuroinformatics

ORIGINAL RESEARCH
published: 26 November 2020
doi: 10.3389/fninf.2020.611666

SARA-GAN: Self-Attention and Relative Average Discriminator Based Generative Adversarial Networks for Fast Compressed Sensing MRI Reconstruction

Zhenmou Yuan[1], *Mingfeng Jiang*[1]*, *Yaming Wang*[1], *Bo Wei*[1], *Yongming Li*[2], *Pin Wang*[2], *Wade Menpes-Smith*[3], *Zhangming Niu*[3] *and Guang Yang*[4,5]

[1] School of Information Science and Technology, Zhejiang Sci-Tech University, Hangzhou, China, [2] College of Communication Engineering, Chongqing University, Chongqing, China, [3] Aladdin Healthcare Technologies Ltd., London, United Kingdom, [4] Cardiovascular Research Centre, Royal Brompton Hospital, London, United Kingdom, [5] National Heart and Lung Institute, Imperial College London, London, United Kingdom

Research on undersampled magnetic resonance image (MRI) reconstruction can increase the speed of MRI imaging and reduce patient suffering. In this paper, an undersampled MRI reconstruction method based on Generative Adversarial Networks with the Self-Attention mechanism and the Relative Average discriminator (SARA-GAN) is proposed. In our SARA-GAN, the relative average discriminator theory is applied to make full use of the prior knowledge, in which half of the input data of the discriminator is true and half is fake. At the same time, a self-attention mechanism is incorporated into the high-layer of the generator to build long-range dependence of the image, which can overcome the problem of limited convolution kernel size. Besides, spectral normalization is employed to stabilize the training process. Compared with three widely used GAN-based MRI reconstruction methods, i.e., DAGAN, DAWGAN, and DAWGAN-GP, the proposed method can obtain a higher peak signal-to-noise ratio (PSNR) and structural similarity index measure(SSIM), and the details of the reconstructed image are more abundant and more realistic for further clinical scrutinization and diagnostic tasks.

Keywords: MRI, reconstruction, deep learning, compressive sensing, neuroinformatics, artificial intelligence, GAN

OPEN ACCESS

Edited by:
Heye Zhang,
Sun Yat-sen University, China

Reviewed by:
Yuan Gao,
University of Oxford, United Kingdom
Lei Zhang,
University of Lincoln, United Kingdom

Correspondence:
Mingfeng Jiang
m.jiang@zstu.edu.cn

Received: *29 September 2020*
Accepted: *05 November 2020*
Published: *26 November 2020*

Citation:
Yuan Z, Jiang M, Wang Y, Wei B, Li Y, Wang P, Menpes-Smith W, Niu Z and Yang G (2020) SARA-GAN: Self-Attention and Relative Average Discriminator Based Generative Adversarial Networks for Fast Compressed Sensing MRI Reconstruction.
Front. Neuroinform. 14:611666.
doi: 10.3389/fninf.2020.611666

INTRODUCTION

MRI can carry out the non-invasive examination of the internal tissues of the human body, so it is widely used in clinical pathological examination and diagnosis (Liang and Lauterbur, 2000; Kabasawa, 2012). However, the excessive scanning time of MRI limits its clinical application, and this problem is particularly prominent for high-resolution imaging. Therefore, how to reduce k-space sampling (Duyn et al., 1998) and shorten MRI acquisition time has become a research focus in this field. Compressed sensing (CS) (Lustig et al., 2008, 2010) is a conventional method for solving this problem, it uses the compressibility and sparsity of the signal to reduce k-space sampling and achieve fast imaging. At present, the methods surrounding compressed sensing for fast MRI mainly include non-Cartesian CS (Haldar et al., 2011; Wang et al., 2012), combination parallel imaging with CS (Murphy et al., 2012; El Gueddari et al., 2019; Shimron et al., 2020), and CS-based on dictionary learning (Ravishankar and Bresler, 2010; Huang et al., 2014; Du et al., 2019; Cao et al., 2020). Although the above-mentioned methods based on compressed sensing have achieved good results, they all rely on the prior knowledge extracted from the image, which limits the use of the above methods to a certain extent.

In recent years, deep learning (LeCun et al., 2015) methods have been successfully applied in many fields. In particular, with the emergence of convolutional neural networks, made it show great performance in computer vision. At present, many MRI reconstruction methods based on deep learning have been proposed (Boyd et al., 2011; Sun et al., 2016; Wang et al., 2016; Aggarwal et al., 2018; Zhu et al., 2018; Akçakaya et al., 2019; Lee et al., 2020). In 2016, Wang et al. (2016) first applied deep learning methods to the acceleration of MRI imaging. They employed an offline CNN to realize the mapping of undersampled zero-filled MRI and fully sampled k-space data and achieved good reconstruction effectively. Deep learning based MRI reconstruction methods can be roughly divided into unrolling-based approaches and those not based on unrolling (Liang et al., 2020). Among them, the unrolling-based method usually expands the CS-based iterative reconstruction algorithm into a deep network, so that the parameters in the reconstruction algorithm can be learned by the network. Sun et al. (2016) proposed the ADMM-Net defined over data flow graphs, which were derived from the iterative procedures in the Alternating Direction Method of Multipliers (ADMM) algorithm (Boyd et al., 2011) for optimizing a general CS-based MRI mode, and it significantly improved the baseline ADMM algorithm and achieved high reconstruction accuracies with fast computational speed. The framework proposed by Aggarwal et al. (2018), termed as MOdel-based reconstruction using Deep Learned priors (MODL), merged the power of model-based reconstruction schemes with deep learning. Their model provided improved results, despite the relatively smaller number of trainable parameters. The methods not unrolling-based mainly uses deep networks to learn the mapping between under-sampled data and fully sampled data to achieve reconstruction. Zhu et al. (2018) proposed a unified framework—automated transform by manifold approximation (AUTOMAP), it constructed a supervised learning task to learn the mapping between sensor domain and image domain from training data. Besides, Robust artificial-neural-networks for k-space interpolation (RAKI) (Akçakaya et al., 2019) was proposed for image reconstruction by training convolutional neural networks on ACS data. Compared with the traditional linear k-space interpolation-based method, this method had better anti-noise performance.

The Generative Adversarial Networks (GAN) (Goodfellow et al., 2014) proposed by Goodfellow was a novel deep generative model, which introduced the idea of game theory and improved the fitting ability of the network through the competitive learning of generator and discriminator. In 2016, Radford et al. proposed Deep Convolutional Generative Adversarial Networks (DCGAN) to apply convolutional neural networks to unsupervised learning (Radford et al., 2016). By applying convolutional neural networks to generators and discriminators, the network could learn a hierarchy of representations from object parts to scenes. At present, GAN and its variants have achieved excellent performance in image-to-image translation (Zhu et al., 2017), image super-resolution (Ledig et al., 2017), and others. In recent years, since its good data representation capabilities, GAN have also been used for MRI fast imaging (Arjovsky et al., 2017; Yang et al., 2017; Jiang et al., 2019; Kwon et al., 2019) and super-resolution (Chen et al., 2018; Lyu et al., 2019; Mahapatra et al., 2019). Yang et al. (2017) applied conditional GAN to MRI reconstruction and proposed the De-Aliasing Generative Adversarial Networks (DAGAN) model. Compared with conventional methods, the DAGAN model achieved a better reconstruction effect and retained more perceptible details. Wasserstein GAN (Arjovsky et al., 2017) is a variant of the original GAN, by replacing the Jensen-Shannon divergence in the original GAN with Wasserstein distance, it stabilizes the learning process and solves the problem of mode collapse. Jiang et al. (2019) proposed a de-aliasing fine-tuning Wasserstein generative adversarial network (DA-FWGAN) for MR imaging reconstruction. The DA-FWGAN could provide reconstruction with improved peak signal-to-noise ratio (PSNR) and structural similarity index measure (SSIM).

Although the current MRI reconstruction methods based on deep learning can better learn the mapping relationship between undersampling MRI and full sampling MRI, the reconstruction effect still has a lot of room for improvement. Firstly, most GANs use convolutional layers to build their generators. Due to the limited size of the convolution kernel, the network can only focus on the dependencies of the information in the local receptive field (Luo et al., 2016), but it cannot establish the long-range dependencies of the image, which leads to the inaccurate reconstruction of the image details and texture. Self-Attention Generative Adversarial Networks (SA-GAN) (Zhang et al., 2019) proposed by Zhang et al. solved this problem by introducing a self-attention mechanism and constructing long-range dependency modeling. The self-attention mechanism was used for establishing the long-range dependence relationship between the image regions. To enhance the image details and improve the quality of reconstructed MRI, the local dependence, and the global dependence of the image were combined. Secondly, the discriminator did not make full use of the prior knowledge that half of the input data is true and half is fake (Jolicoeur-Martineau, 2018). When the generated data is real enough, the discriminator can directly distinguish the generated data into real data, which results in the insufficient performance of the discriminator and the training of the generator cannot be continued. Alexia Jolicoeur-Martineau used the prior knowledge to induce a "relative discriminator" (Jolicoeur-Martineau, 2018), which estimated the probability that the given real data was more realistic than a randomly sampled fake date.

In this paper, we propose a novel MRI reconstruction method, termed as SARA-GAN, which combines the self-attention mechanism and the relative discriminator. The generator is designed as a structure, composing of down-sampling block, residual block, and up-sampling block. Among them, in the up-sampling block, we add a self-attention layer to capture the global information of the image. Besides, the discriminator

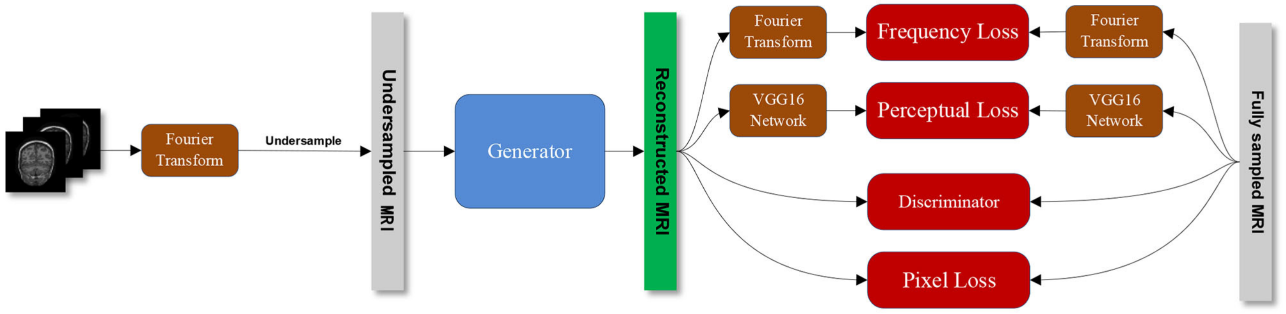

FIGURE 1 | The overall structure of the proposed SARA-GAN method.

uses the CNN structure and introduces the idea of relative discrimination to construct a relative average discriminator. At the same time, we also apply spectral normalization on the generator and discriminator to stabilize the training process. The novelties of our proposed SARA-GAN model have been summarized as follows

(a) Given the traditional convolutional structure that can only focus on the local dependency of the image, we add a self-attention layer to the high-layer of the generator network. The self-attention mechanism can calculate the correlation degree between image pixels and build long-range dependencies so that the reconstructed image can demonstrate more details.
(b) The theoretical formula of the original GAN-based methods ignores the prior information of the discriminator's input data. In our SARA-GAN model, we use relative average discriminator to transform the absolute true or false discrimination into relative true or false. In doing so, our SARA-GAN model can make full use of the prior information, and therefore can improve the discriminator performance.
(c) In our SARA-GAN, the generator adopts a residual network structure, in which multiple residual blocks are cascaded and multiple skip connections are incorporated to reduce the loss of original features in the convolution calculation. At the same time, this can avoid poor performance of the generator in the initial training stage; therefore, the training procedure can be more efficient.
(d) We also apply the spectral normalization to the network parameters of the generator and the discriminator to satisfy the Lipschitz constraint, thereby stabilizing the training of our GAN-based SARA-GAN model.

METHODS

Figure 1 shows the overall structure of our proposed SARA-GAN. We obtain the k-space data of the fully sampled MRI through Fourier transform, then undersampled the k-space data, and perform inverse Fourier transform to obtain the image-domain undersampled MRI. The generator is used to learn the mapping relationship between undersampled MRI and full-sampled MRI. The discriminator is a binary classifier, used to judge whether the reconstructed image is true or false. The combined loss function incorporates the pixel loss, the perceptual loss, and the frequency-domain loss based on the adversarial loss. The pixel loss and the perceptual loss can constrain GAN training on the image content. The frequency-domain loss provides additional constraints for the data consistency in the k-space. The pre-trained VGG16 network is used to extract features from the fully sampled MRI and the reconstructed MRI respectively, and the two sets of features are compared to obtain the perception loss. The discriminator and the combined loss function guide the training of the generator together.

Network Structure

Generator Model

The generator model is composed of a down-sampling block, residual block, and up-sampling block. The three convolutional layers in the down-sampling block are used to extract image features. The residual block contains 7 residual blocks, and each residual block contains two convolutional layers. The up-sampling block consists of three transposed convolutional layers, which are used to expand the feature map and generate reconstructed MRI. We use spectral normalization on the generator network and choose the PReLU (He et al., 2015) function as the activation function. Besides, we introduce the self-attention module in the up-sampling block to build the long-range dependency of the image, as shown in **Figure 2**.

Discriminator Model

The discriminator model is an 11-layer CNN network, which uses leaky ReLU as the activation function. The last layer is the dense layer, and the sigmoid function is used as the activation function to output the discriminatory results of the discriminator, as shown in **Figure 3**. We also use spectral normalization in the discriminator.

Self-Attention Module

To overcome the problem that the network cannot learn long-range global dependencies caused by the limited size of the convolution kernel, we add the self-attention (Zhang et al., 2019) into the up-sampling block of the generator, as shown in

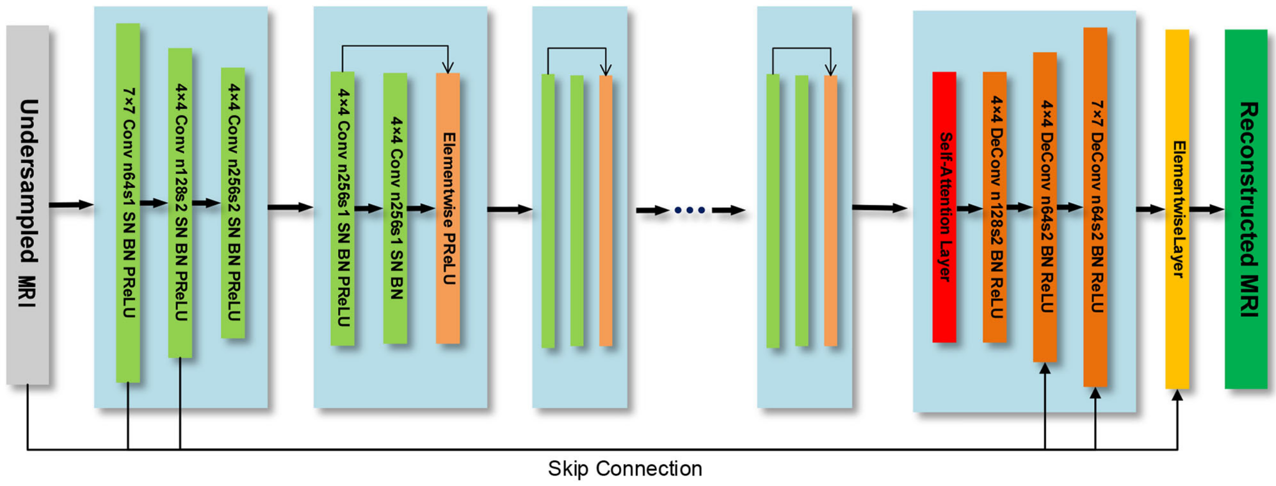

FIGURE 2 | The generator model.

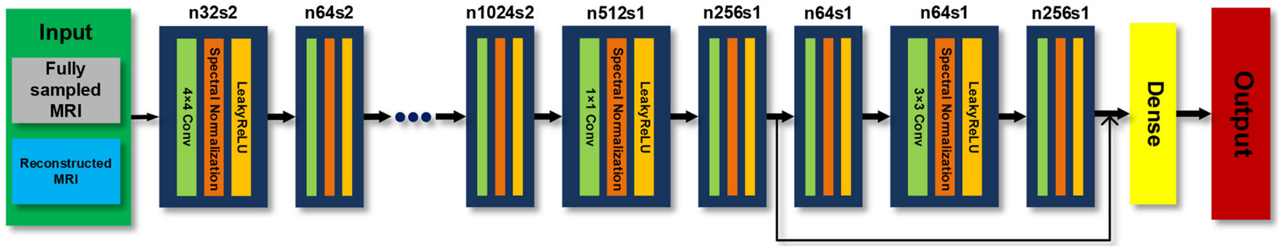

FIGURE 3 | Discriminator model.

Figure 2. In the self-attention module, the output feature map of the last residual block x with the channel number C of the previous convolution layer is input to three convolution layers with a kernel of 1×1 and the channel numbers of $C/8$, $C/8$ and C respectively, to obtain the feature space $f(x)$,$g(x)$ and $h(x)$

$$f(x) = W_f x, \tag{1}$$
$$g(x) = W_g x, \tag{2}$$
$$h(x) = W_h x. \tag{3}$$

Then the transpose of $f(x_i)$ is multiplied by $g(x_j)$, and the weight is normalized by the Softmax function to obtain $\beta_{j,i}$

$$s_{ij} = f(x_i)^T g(x_j), \tag{4}$$
$$\beta_{j,i} = \frac{\exp\left(s_{ij}\right)}{\sum_{i=1}^{N} \exp\left(s_{ij}\right)}, \tag{5}$$

where$\beta_{j,i}$ is an attention map that indicates the extent to which the model attends to the i^{th} location when synthesizing the j^{th} region. The output of the self-attention layer is defined as

$$o_j = v\left[\sum_{i=1}^{N} \beta_{j,i} h(x_i)\right], v(x_i) = W_v x_i \tag{6}$$

In the above formula, W_f, W_g,W_h, and W_v are the weight matrices of the 1×1 convolutional layer. To allow the generator learns the local dependence of the image as well as the long-range global dependence, we multiply the output of the self-attention layer o_j by a weight coefficient γ and add it to the input feature map x_i to obtain the final output of the self-attention module y_i

$$y_i = \gamma o_i + x_i. \tag{7}$$

Among them, γ is a learnable parameter and is initialized to 0. Its function is to enable the network to learn the proportion of the global dependency on the feature map.

Relative Average Discriminator

In the original GAN model, the generator accepts random noise, and then generates a false image and inputs it to the discriminator. The discriminator gives the probability that the input image belongs to the real image. The two compete with each other and learn together. Finally, the generator learns the probability distribution of the real image, making the discriminator unable to distinguish between the real image and the generated image, and then achieves Nash equilibrium.

Specifically, in the problem of MRI image reconstruction, x is defined as the fully sampled MRI image, and z is the undersampled zero-filled MRI image. The theoretical formula of the original GAN is:

$$\begin{aligned} \max \mathcal{L}_D &= \mathrm{E}_{x\sim P_{\mathrm{data}}(x)}\left[\log D(x)\right] \\ &\quad + \mathrm{E}_{z\sim P_z(z)}\left[\log\left(1-D(G(z))\right)\right], \quad (8) \\ \min \mathcal{L}_G &= \mathrm{E}_{z\sim P_z(z)}\left[\log\left(1-D(G(z))\right)\right], \quad (9) \end{aligned}$$

where $P_{\mathrm{data}}(x)$ is the fully sampled MRI image distribution, $P_z(z)$ is the undersampled zero-filled MRI image distribution. The optimization process of the original GAN is essentially to reduce the Jensen–Shannon divergence (JSD) between $P_{\mathrm{data}}(x)$ and $P_z(z)$

$$\begin{aligned} JSD(P_{data}||P_z) &= \frac{1}{2}(\log(4) + \max_D \mathrm{E}_{x\sim P_{data}(x)}[\log D(x)] \\ &\quad + \mathrm{E}_{z\sim P_z(z)}[\log(1-D(G(z)))]). \quad (10) \end{aligned}$$

When $D(x){=}D(G(z)){=}\frac{1}{2}$, $JSD(P_{data}||P_z)$ gets the minimum value 0. Therefore, ideally, when the generator generates sufficiently real samples, the discriminator cannot distinguish between true and false samples and should output a probability value of 0.5. However, in actual training, the above formula may cause the expected output of the discriminator D to be 1. This is because the original GAN theoretical formula ignores a priori knowledge, for instance, in a minibatch, half of the samples' input to the discriminator are real data and the other half are generated data.

We use the relative average discriminator (Jolicoeur-Martineau, 2018) and believe that the discriminator should estimate the probability that the given full sampling MRI is more realistic than the reconstruction MRI, on average, by making full use of the above prior knowledge. Therefore, the theoretical formula after using the relative average discriminator in our work is

$$\begin{aligned} \min \mathcal{L}_D &= -\mathrm{E}_{x\sim P_{data}}\left[\log\left(D(x)\right)\right] \\ &\quad -\mathrm{E}_{z\sim P_z}\left[\log\left(1-D(G(z))\right)\right], \quad (11) \\ \min \mathcal{L}_G &= -\mathrm{E}_{z\sim P_z}\left[\log\left(D(G(z))\right)\right] \\ &\quad -\mathrm{E}_{x\sim P_{data}}\left[\log\left(1-D(x)\right)\right], \quad (12) \\ D(x) &= sigmoid(C(x) - \mathrm{E}_{z\sim P_z}C(G(z))) \\ D(G(z)) &= sigmoid(C(G(z)) - \mathrm{E}_{x\sim P_{data}}C(x)), \quad (13) \end{aligned}$$

where $C(\cdot)$ is the output of the discriminator network.

Spectral Normalization

Miyato et al. (2018) proposed to apply spectral normalization (SN) to the discriminator network to stabilize GAN training. In this study, we also use spectral normalization in the weights of the generator network and discriminator network. The spectral normalization method uses the spectral norm on the parameter matrix of the discriminator and generator network, so that the network satisfies the Lipschitz constraint, thereby smoothing the network parameter to stabilize training.

Loss Function

The loss function is used to evaluate the gap between the reconstructed image and the fully sampled image, which is the optimization object of the GAN. The smaller the loss function value, the smaller the gap between the reconstructed image and the fully sampled image, and the better the reconstruction effect. A reasonable loss function can provide accurate gradient information for network training, thereby improving reconstruction performance. We use a combined loss function that combines perceptual loss, pixel loss, frequency domain loss, and adversarial loss to comprehensively evaluate the fitting ability of the network.

The pixel loss L_{pixel} and frequency domain loss $L_{frequency}$ are based on Mean Square Error(MSE), can be defined as follows

$$\min_G L_{pixel}(G) = \frac{1}{2}\left\|\mathbf{x_t} - \mathbf{x_u}\right\|_2^2, \quad (14)$$

$$\min_G L_{frequency}(G) = \frac{1}{2}\left\|\mathbf{y_t} - \mathbf{y_u}\right\|_2^2, \quad (15)$$

where $\mathbf{x_t}$ and $\mathbf{x_u}$ are fully sampled and reconstructed MR images in the image domain, respectively. $\mathbf{y_t}$ and $\mathbf{y_u}$ correspond to the frequency domain data of $\mathbf{x_t}$ and $\mathbf{x_u}$, respectively. The perceptual loss and adversarial loss are defined as

$$\begin{aligned} \min_G L_{perceptual}(G) &= \frac{1}{2}\left\|f_{VGG16}(\mathbf{x_t}) - f_{VGG16}(\mathbf{x_u})\right\|_2^2, \quad (16) \\ \min_G L_{adversarial} &= -\mathrm{E}_{z\sim p_z}\left[\log\left(D(G(z))\right)\right] \\ &\quad -\mathrm{E}_{x\sim p_{data}}\left[\log\left(1-D(x)\right)\right], \quad (17) \end{aligned}$$

where f_{VGG16} represents the VGG16 network (Russakovsky et al., 2015), $D(\cdot)$ represents the relative average discriminator.

Therefore, the final total loss function can be expressed as

$$L_{total} = \alpha L_{pixel} + \beta L_{frequncy} + \gamma L_{perceptual} + L_{adversarial}, \quad (18)$$

where α, β and γ are the weight parameter of each loss function.

EXPERIMENTS

Experimental Setup

The datasets used in this article are downloaded from the Diencephalon Challenge (https://www.synapse.org/#!Synapse:syn3193805/wiki/217780) in the public repository of the MICCAI 2013 grand challenge. The MRI data acquisition method is MPRAGE, the scanning matrix size is 256 × 256 × 287, and the resolution is 1 × 1 × 1 mm. We randomly selected 130 3D neuro-MRI images from the data set to verify the proposed SARA-GAN model. In the experiments, 70 samples (15,816 effective 2D MRIs) were used as the training set, 30 samples (5,073 effective 2D MRIs) were used as the validation set, and 30 samples (5,198 effective 2D MRIs) were used as the test set. In order to enhance the network performance, we applied data augmentation to the training dataset, including flipping (left to right), rotating ±20 degrees, shifting 10% along the x-axis and y-axis, random zooming between 0.9 times and 1.1 times, random brightness changes, and the random elastic

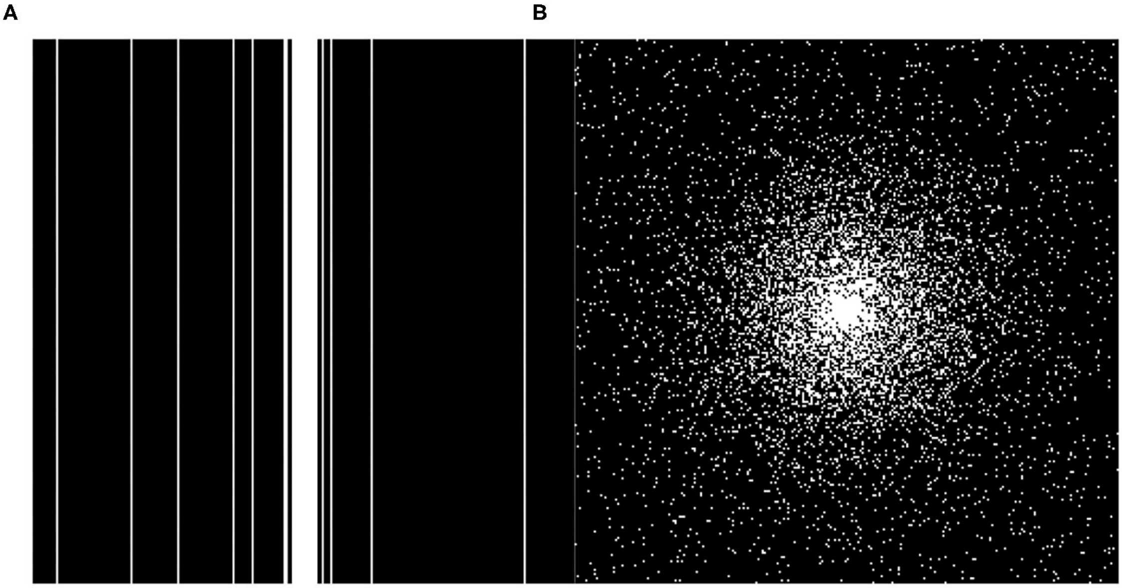

FIGURE 4 | The two different under sampling masks. **(A)** 1D Gaussian mask and **(B)** 2D Gaussian mask.

transformation with alpha of 255 × 3 and sigma of 255 × 0.10. We use TensorFlow 1.12.0 and Python framework to program, and train the proposed model on a TeslaV100-SXM2 GPU under a CentOS system environment. Two undersampling modes, including 1-dimensional Gaussian distribution and 2-dimensional Gaussian distribution, three sampling rates of 10, 20, and 30% (Corresponding to 10×, 5×, and 3.3× acceleration factors respectively) were used for obtaining undersampling MRI. We train the model separately for each sampling mode. The sampling modes are shown in **Figure 4**. The contrast experiments were carried out under the above conditions.

The input and output image size of the generator is 256 × 256, batch size set to 16. We set the learning rate of the generator and the discriminator to 0.0001 and 0.0002, respectively, so that the generator and the discriminator can learn simultaneously. Since loss items in the combined loss are inconsistent on the number scale; therefore, we use hyperparameters α, β and γ to balance them into a similar scale to make the final loss function more accurate. The hyperparameters α, β, and γ in the combined loss function are set to 15, 0.1, and 0.0025, respectively. The choice of these hyperparameters were tuned empirically for better reconstruction performance.

We use the Adam optimizer with Gradient Centralization (Yong et al., 2020) to optimize the loss function, and set the exponential decay rate for the 1st moment estimates (β_1) to 0.5, and the exponential decay rate for the 2nd moment estimates (β_2) to 0.999. To prevent over-fitting, we use the normalized mean square error (NMES) as an indicator to evaluate the fitting effect of the network on the validation set every epoch. After the network is trained for 30 epochs, the training is terminated, and the optimal model with the smallest NMSE is saved.

Reconstruction Quality Evaluation

In our experiment, the peak signal-to-noise ratio (PSNR) and structural similarity index measure (SSIM) were used as evaluation indexes of the reconstructed image. PSNR and SSIM are defined as following

$$PSNR = 10\log_{10}\left(\frac{255^2}{MN\sum_{i=1}^{M}\sum_{j=1}^{N}\left(y_{i,j} - x_{i,j}\right)^2}\right), \tag{19}$$

where x represents the full sampling MRI, y represents the network reconstructed MRI, i and j represent the coordinates of image pixels, and M, N represents the size of the image.

$$SSIM = \frac{\left(2\mu_x\mu_y + C_1\right)\left(2\sigma_{xy} + C_2\right)}{\left(\mu_x^2 + \mu_y^2 + C_1\right)\left(\sigma_x^2 + \sigma_y^2 + C_2\right)} \tag{20}$$

where μ_x and μ_y represent the means of image x and y, σ_x and σ_y represent the variances of image x and y, respectively.

RESULTS

We compared three GAN-based MRI reconstruction models, i.e., DAGAN, DAWGAN, DAWGAN-GP, and the compared methods all used the best parameter settings. **Figures 5**, **6** show the reconstruction effect of a typical MRI for the 10-fold accelerated k-space data masked with the Gaussian distribution using a different method. We chose to zoom in on a specific area of the MRI to compare the reconstruction details. From the local enlarged image, we can conclude that the reconstructed

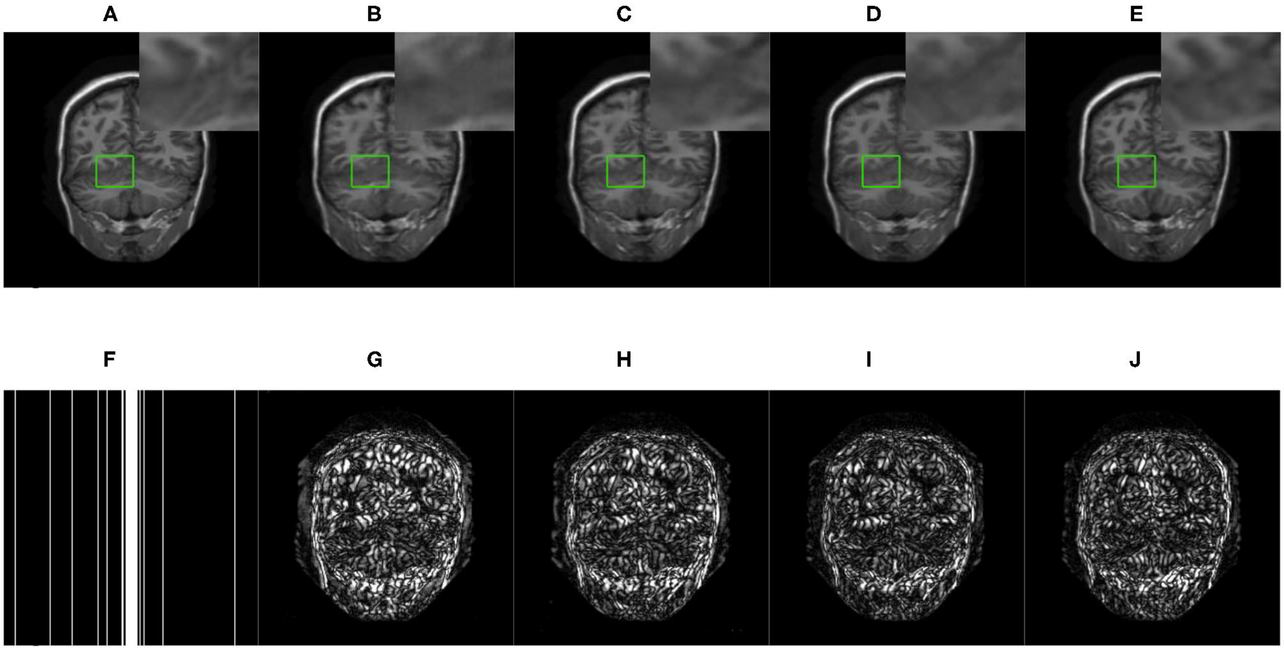

FIGURE 5 | The reconstructed MRI for the 10-fold accelerated k-space data masked with the 1D Gaussian distribution by using different GAN-based methods. **(A)** Fully-sampled MRI, **(B)** DAGAN, **(C)** DAWGAN, **(D)** DAWGAN-GP, **(E)** SARA-GAN, **(F)** 1D mask, **(G)** DAGAN(error), **(H)** DAWGAN(error), **(I)** DAWGAN-GP(error), and **(J)** SARA-GAN(error).

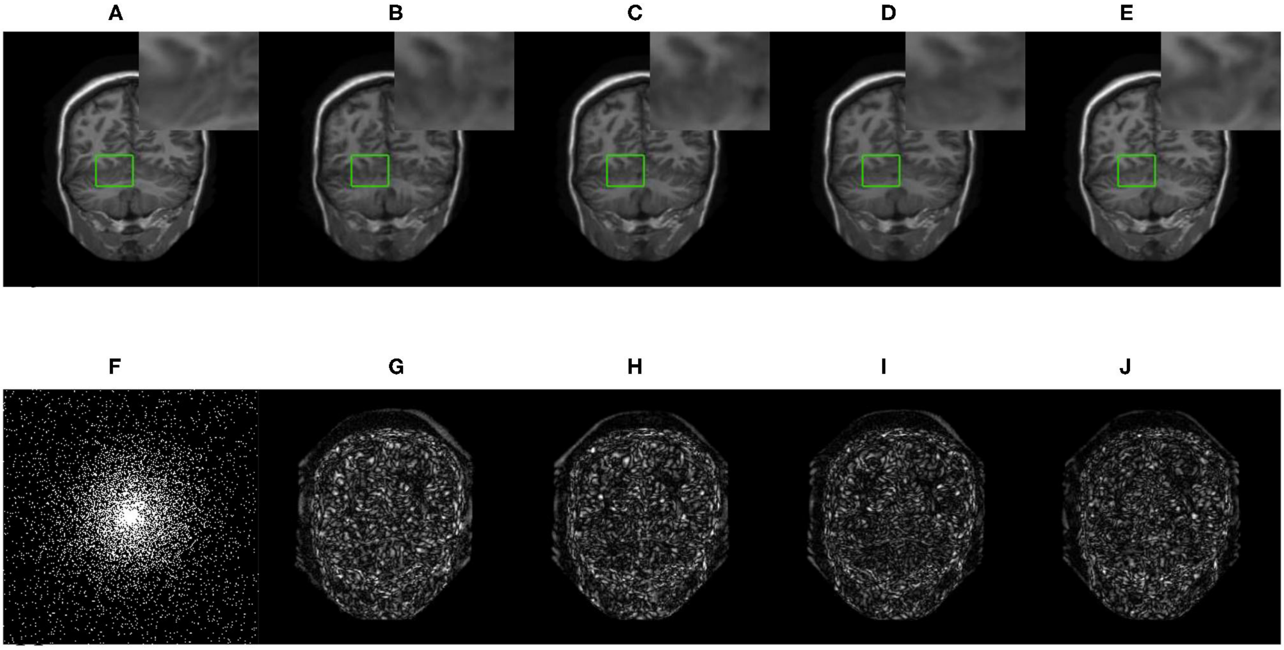

FIGURE 6 | The reconstructed MRI for the 10-fold accelerated k-space data masked with the 2D Gaussian distribution by using different GAN-based methods. **(A)** Fully-sampled MRI, **(B)** DAGAN, **(C)** DAWGAN, **(D)** DAWGAN-GP, **(E)** SARA-GAN, **(F)** 2D mask, **(G)** DAGAN(error), **(H)** DAWGAN(error), **(I)** DAWGAN-GP(error), and **(J)** SARA-GAN(error).

image obtained by the DAGAN method loses most of the texture information. DAWGAN and DAWGAN-GP perform slightly better than DAGAN, but there is still a big gap compared with full sampling MRI. Compared with the other three GAN-based methods, our method can restore more texture details, and the texture edge is clearer. The second line of **Figures 5**, **6** shows the reconstruction error map of different algorithms, and the color of pixels indicates the reconstruction error of the corresponding position. It can be seen that the reconstruction error of our method is less than that of other methods, indicating that the reconstructed MRI is closer to the full sampling MRI. **Table 1** shows the quantitative comparison of the reconstruction effects of different methods. We calculate the average PSNR and SSIM of each method on the test set to evaluate the reconstruction performance of the model. Except for the first row in the table, our results are close to the DAWGAN-GP method. In the other undersampling modes, our method obtains higher PSNR and SSIM. The average PSNR is improved 0.04 dB ∼ 0.96 dB over the DAWGAN-GP and the corresponding SSIM improvements are 0.0003 ∼ 0.0008. In order to illustrate the performance of the proposed method, we estimate the statistical significancy using the Wilcoxon rank sum test ($p < 0.05$ indicates the significant difference). We find that except for 10% 2D Gaussian sampling experiment we have a similar performance between DAWGAN-GP and SARA-GAN ($p = 0.1849$), other experiments have demonstrated that our SARA-GAN has outperformed other methods significantly (most p-values are <0.001).

With the increase of the acceleration factor, the reconstruction effect of either method becomes worse. At the same time, the reconstruction effect of 2-dimensional Gaussian sampling mode is obviously better than that of 1-dimensional Gaussian sampling. This is because the brain MRI has fewer texture details than natural images. The main information of brain MRI is concentrated in the low-frequency part of k-space, and the Gaussian sampling mode happens to also mainly collects the low-frequency part. Therefore, with the increase of sampling rate and sampling dimension, the information of the low-frequency part is more collected, so the reconstruction effect is also improved.

The real MRI sampling process often contains random noise. To simulate the real scene and evaluate the anti-noise ability of the model, we added 30 and 40 dB Gaussian white noise to the test set MRI and retested the above methods. **Tables 2**, **3** respectively show the reconstruction results of different algorithms on the test set with 30 and 40 dB Gaussian white noise. It can be seen from the table that, the average PSNR is improved by 0.004 ∼ 0.841 dB over the DAWGAN-GP and the corresponding SSIM improvements are about 0.0004 ∼ 0.0008. Despite the addition of a certain intensity of noise, our method still obtains a good reconstruction effect and is better than other GAN-based methods. This shows that our method has good anti-noise performance and the potential for practical application.

TABLE 1 | The average reconstruction performances of different methods on the test set (mean ± std).

	DAGAN		DAWGAN		DAWGAN-GP		SARA-GAN	
Mask: 1D Gaussian	**PSNR**	**SSIM**	**PSNR**	**SSIM**	**PSNR**	**SSIM**	**PSNR**	**SSIM**
Sample rate: 10%	34.0484 ± 4.81	0.9538 ± 2.20e-2	35.4455 ± 4.57	0.9654 ± 1.71e-2	36.3499 ± **4.27**	**0.9718** ± **1.37e-2**	**36.3926** ± 4.73	0.9713 ± 1.46e-2
Sample rate: 20%	40.2395 ± 4.23	0.9857 ± 6.41e-3	41.4284 ± 4.45	0.9894 ± 5.18e-3	42.6101 ± **3.92**	0.9923 ± 3.77e-3	**43.2054** ± 4.49	**0.9929** ± **3.71e-3**
Sample rate: 30%	40.8891 ± 4.46	0.9873 ± 5.88e-3	42.1798 ± 4.61	0.9907 ± 4.53e-3	42.9149 ± **3.69**	0.9928 ± **3.41e-3**	**43.3522** ± 4.34	**0.9931** ± 3.47e-3
Mask: 2D Gaussian	**PSNR**	**SSIM**	**PSNR**	**SSIM**	**PSNR**	**SSIM**	**PSNR**	**SSIM**
Sample rate: 10%	39.7242 ± 5.01	0.9801 ± 1.06e-2	40.7623 ± 4.68	0.9861 ± 7.75e-3	41.1885 ± **4.43**	0.9876 ± 6.85e-3	**41.6323** ± 5.25	**0.9881** ± **6.83e-3**
Sample rate: 20%	41.5595 ± 4.93	0.9857 ± 7.74e-3	41.7733 ± 5.15	0.9880 ± 6.84e-3	42.9742 ± **4.61**	0.9912 ± 5.05e-3	**43.4991** ± 5.15	**0.9920** ± **4.84e-3**
Sample rate: 30%	44.3886 ± 5.01	0.9934 ± 3.95e-3	44.2812 ± 5.11	0.9932 ± 4.03e-3	44.7868 ± **3.86**	0.9947 ± **2.97e-3**	**45.7536** ± 4.99	**0.9951** ± 3.03e-3

The bold value means that the experimental result value is the best.

DISCUSSION

The main purpose of this study is to accurately reconstruct clear MR images from under-sampled MRI k-space data, thereby accelerating MR imaging. The experimental results have demonstrated that the proposed SARA-GAN method can obtain high-quality reconstructed MRI, even in the presence of noise. In the SARA-GAN method, we propose to use the relative average discriminator instead of the original discriminator, and the self-attention mechanism to achieve

TABLE 2 | The average reconstruction performances of different methods on the test set with 30dB noise.

	DAGAN		DAWGAN		DAWGAN-GP		Proposed	
Mask: 1D Gaussian	**PSNR**	**SSIM**	**PSNR**	**SSIM**	**PSNR**	**SSIM**	**PSNR**	**SSIM**
Sample rate: 10%	33.4169	0.9364	34.8801	0.9582	35.0774	0.9450	**35.3201**	**0.9535**
Sample rate: 20%	38.9860	0.9742	39.2584	0.9600	40.5054	0.9805	**41.4684**	**0.9878**
Sample rate: 30%	38.0020	0.9279	39.4411	0.9579	40.7167	0.9825	**41.5242**	**0.9886**
Mask: 2D Gaussian	**PSNR**	**SSIM**	**PSNR**	**SSIM**	**PSNR**	**SSIM**	**PSNR**	**SSIM**
Sample rate: 10%	39.1818	0.9775	39.5594	0.9827	40.5227	0.9859	**40.5901**	**0.9861**
Sample rate: 20%	40.3423	0.9807	40.1344	0.9843	41.6388	0.9890	**41.7555**	**0.9895**
Sample rate: 30%	42.5157	0.9907	42.3948	0.9901	42.6534	0.9919	**43.0708**	**0.9922**

The bold value means that the experimental result value is the best.

TABLE 3 | The average reconstruction performances of different methods on the test set with 40dB noise.

	DAGAN		DAWGAN		DAWGAN-GP		Proposed	
Mask: 1D Gaussian	**PSNR**	**SSIM**	**PSNR**	**SSIM**	**PSNR**	**SSIM**	**PSNR**	**SSIM**
Sample rate: 10%	33.9782	0.9527	35.3805	0.9648	36.2549	**0.9711**	**36.2590**	0.9703
Sample rate: 20%	40.0935	0.9849	41.3256	0.9880	42.3872	0.9918	**42.9586**	**0.9926**
Sample rate: 30%	40.3222	0.9828	41.6212	0.9878	42.6548	0.9924	**43.1355**	**0.9928**
Mask: 2D Gaussian	**PSNR**	**SSIM**	**PSNR**	**SSIM**	**PSNR**	**SSIM**	**PSNR**	**SSIM**
Sample rate: 10%	39.6494	0.9797	40.2391	0.9843	41.1332	0.9874	**41.5031**	**0.9879**
Sample rate: 20%	41.4073	0.9852	41.0897	0.9866	42.8114	0.9910	**43.2453**	**0.9918**
Sample rate: 30%	44.1260	0.9931	44.0760	0.9929	44.5119	0.9944	**45.3533**	**0.9949**

The bold value means that the experimental result value is the best.

TABLE 4 | The influence of self-attention mechanism and SN on PSNR and SSIM of the reconstructed image.

	RA-GAN		SARA-GAN(NoSN)		SARA-GAN	
Mask: 1D Gaussian	**PSNR**	**SSIM**	**PSNR**	**SSIM**	**PSNR**	**SSIM**
Sample rate: 10%	35.9669	0.9686	35.6708	0.9669	**36.3926**	**0.9713**
Sample rate: 20%	42.8805	0.9924	42.9769	0.9925	**43.2054**	**0.9929**
Sample rate: 30%	42.7548	0.9920	43.1507	0.9927	**43.3522**	**0.9931**
Mask: 2D Gaussian	**PSNR**	**SSIM**	**PSNR**	**SSIM**	**PSNR**	**SSIM**
Sample rate: 10%	41.1679	0.9867	40.5628	0.9848	**41.6323**	**0.9881**
Sample rate: 20%	43.0552	0.9912	42.1689	0.9894	**43.4991**	**0.9920**
Sample rate: 30%	44.7239	0.9940	44.3378	0.9932	**45.7536**	**0.9951**

The bold value means that the experimental result value is the best.

global reference. Compared with the other state-of-the-art GAN-based MRI reconstruction methods, such as DAGAN, DAWGAN, DAWGAN-GP, our SARA-GAN method can provide outstanding reconstruction performance and generate MRI images with a stronger integrity, more details, and higher evaluation indices.

The convolution operation on CNN can only work in the local domain of the convolution kernel, which makes the network miss a lot of global information. The self-attention mechanism is proposed to solve the above problem by capturing long-range interactions. In this study, we apply the self-attention mechanism in the up-sampling block of the generator to combine local and global spatial information. To evaluate the impact of the self-attention mechanism on network reconstruction, we removed the self-attention layer in the up-sampling block of the generator and conducted training and testing under the same experimental conditions. The average PSNR and SSIM of the test set are shown in **Table 4**. As can be seen from the table, in all under-sampling modes, the self-attention mechanism affects improving the quality of reconstructed MRI images. The average PSNR is improved 0.32 $\sim$ 1.03 dB and the corresponding SSIM improvements are 0.0005 $\sim$ 0.0027.

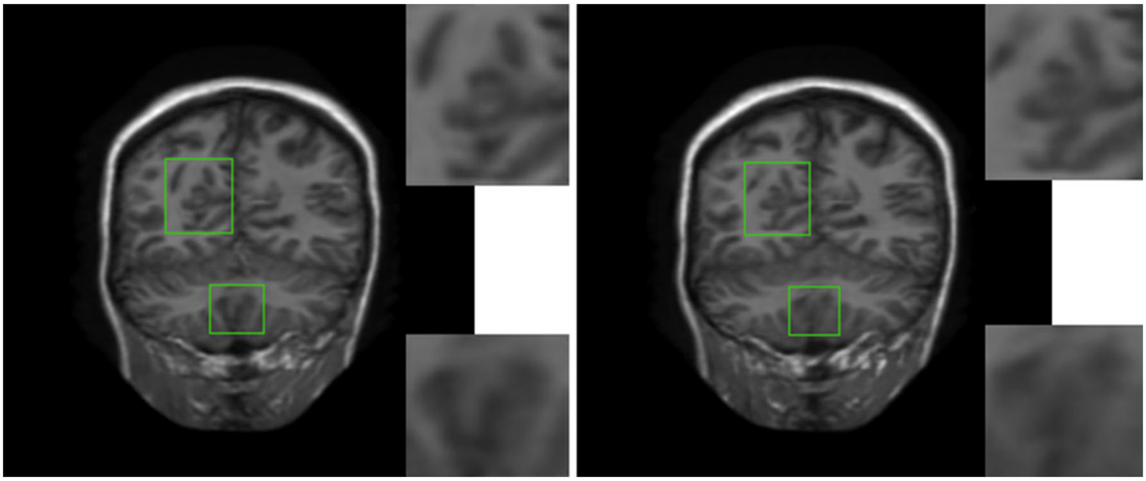

FIGURE 7 | The visual influence of self-attention mechanism on the reconstructed image. Proposed RASA-GAN (PSNR: 33.5931) and Proposed (NoSA) RA-GAN (PSNR: 32.9152).

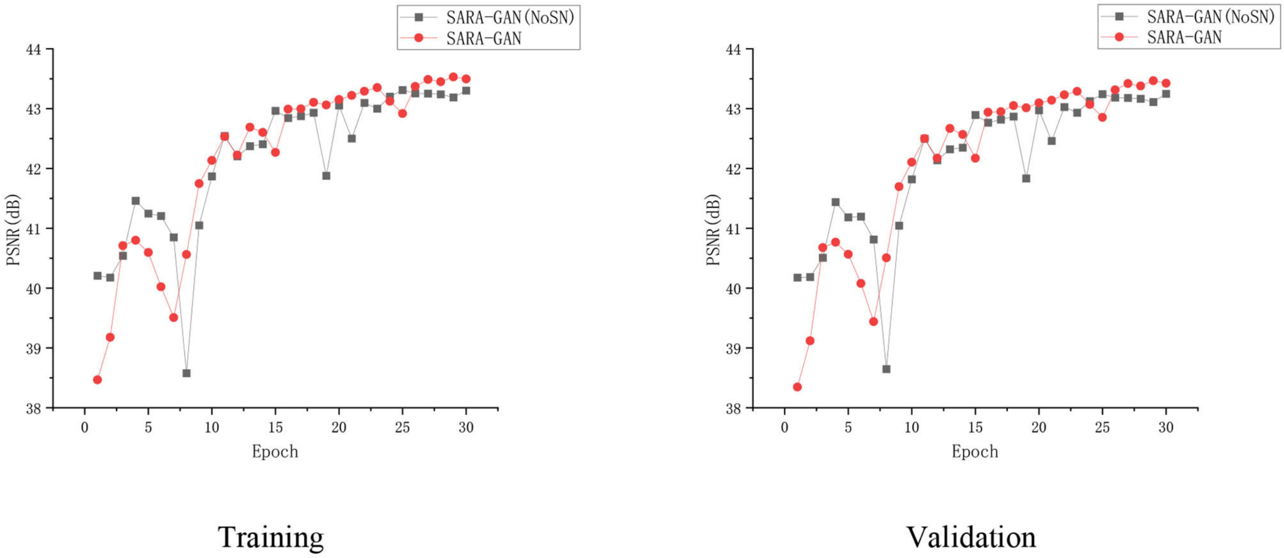

Training

Validation

FIGURE 8 | The convergence curve of the PSNR vs. the Epoch number in the case of a 30% sampling rate with the 1D Gaussian mask. Training and validation.

In order to verify the visual effect of the long-range dependence constructed by the self-attention mechanism on the reconstructed MRI, we selected a typical MRI and enlarged the texture-rich regions locally, as shown in **Figure 7**. Observation shows that the brain texture in the left picture is rich in detail and structural information is relatively complete. Comparing the enlarged image of the same area, the left image has a clear texture boundary and relatively complete color blocks, while the right image has blurry borders, and the color blocks are somewhat broken. Therefore, under the action of the self-attention mechanism, the integrity of reconstructed MRI is stronger and the visual effect is improved.

We also apply spectral normalization to the parameter matrix of the generator and discriminator.

Spectral normalization makes the parameter matrix meet 1-Lipschitz continuity by applying the spectral norm to the network parameters, which limits the network gradient change, thereby making the training process more stable. We have conducted the convergence analyses in every epoch by using SARA-GAN and SARA-GAN without SN methods in the case of the 30% sampling rate with a 1D Gaussian mask. As shown in **Figure 8**, the convergence of SARA-GAN method is more stable than SARA-GAN without the SN method. **Table 4** also shows the experimental results of SARA-GAN without the SN method on the test set. It can be seen that SN significantly improves the quality of network reconstruction MRI. Under the same number of iterations, due to the improvement of training stability, the method with SN can achieve a more optimized state.

CONCLUSION

In this study, a new MRI reconstruction method, named SARA-GAN, was proposed to reduce k-space sampling and accelerate MRI imaging. Our method combines the self-attention mechanism with relative average discriminator. Compared with other GAN-based methods, such as DAGAN, DAWGAN, and DAWGAN-GP, the experimental results show that our method can obtain more accurate reconstructed MRI with a higher PSNR and SSIM. Especially through the long-range global dependence constructed by the self-attention mechanism, the proposed method can reconstruct images with more realistic details and stronger integrity. At the same time, the proposed method has a certain ability of noise tolerance and short reconstruction time. It provides a promising approach to speed up the MRI.

DATA AVAILABILITY STATEMENT

Publicly available datasets were analyzed in this study. This data can be found here: https://mrbrains13.isi.uu.nl/data/, MICCAI 2013 grand challenge public data set.

AUTHOR CONTRIBUTIONS

ZY, MJ, YW, BW, and GY: conceptualization. ZY, MJ, YW, BW, YL, PW, and GY: methodology. ZY, MJ, YW, and BW: formal analysis, investigation, and writing—original draft preparation. WM-S, ZN, and GY: writing—review and editing. MJ and GY: funding acquisition. All authors contributed to the study conception, design, read, and approved the final manuscript.

FUNDING

This work was supported in part by the National Natural Science Foundation of China (61672466 and 62011530130), in part by the Key Research and Development Program of Zhejiang Province (2020C03060), in part by the Joint Fund of Zhejiang Provincial Natural Science Foundation (LSZ19F010001), in part by the Natural Science Foundation of Zhejiang Province (LZ20F02003 and LY18D060009), in part by the Science Technology Department Program of Zhejiang Province (LGG18H180001), in part by the 521 Talents project of Zhejiang Sci-Tech University, in part by IIAT Hangzhou, in part by the European Research Council Innovative Medicines Initiative on Development of Therapeutics and Diagnostics Combatting Coronavirus Infections Award DRAGON: rapiD and secuRe AI imaging based diaGnosis, stratification, fOllow-up, and preparedness for coronavirus paNdemics [H2020-JTI-IMI2 101005122], and in part by the AI for Health Imaging Award CHAIMELEON: Accelerating the Lab to Market Transition of AI Tools for Cancer Management [H2020-SC1-FA-DTS-2019-1 952172].

REFERENCES

Aggarwal, H. K., Mani, M. P., and Jacob, M. (2018). MoDL: model-based deep learning architecture for inverse problems. *IEEE Trans. Med. Imaging* 38, 394–405. doi: 10.1109/TMI.2018.2865356

Akçakaya, M., Moeller, S., Weingärtner, S., and Ugurbil, K. (2019). Scan-specific robust artificial-neural-networks for k-space interpolation (RAKI) reconstruction: database-free deep learning for fast imaging. *Magn. Resonance Med.* 81, 439–453. doi: 10.1002/mrm.27420

Arjovsky, M., Chintala, S., and Bottou, L. (2017). Wasserstein gan. *arXiv*. Available online at: https://arxiv.org/pdf/1701.07875.pdf

Boyd, S., Parikh, N., and Chu, E. (2011). Distributed optimization and statistical learning via the alternating direction method of multipliers. Now Foundations and Trends. p.128. doi: 10.1561/9781601984616

Cao, J., Liu, S., Liu, H., and Lu, H. (2020). CS-MRI reconstruction based on analysis dictionary learning and manifold structure regularization. *Neural Netw.* 123, 217–233. doi: 10.1016/j.neunet.2019.12.010

Chen, Y., Shi, F., Christodoulou, A. G., Xie, Y., Zhou, Z., and Li, D. (2018). "Efficient and accurate MRI super-resolution using a generative adversarial network and 3D multi-level densely connected network," in *International Conference on Medical Image Computing and Computer-Assisted Intervention*. (Granada: Springer), 91–99.

Du, D., Pan, Z., Zhang, P., Li, Y., and Ku, W. (2019). Compressive sensing image recovery using dictionary learning and shape-adaptive DCT thresholding. *Magn. Reson. Imaging* 55, 60–71. doi: 10.1016/j.mri.2018.09.014

Duyn, J. H., Yang, Y., Frank, J. A., and Veen, J. W. (1998). Simple correction method for k-space trajectory deviations in MRI. *J. Magn. Reson.* 132, 150–153. doi: 10.1006/jmre.1998.1396

El Gueddari, L., Ciuciu, P., Chouzenoux, E., Vignaud, A., and Pesquet, J.-C. (2019). "Calibrationless oscar-based image reconstruction in compressed sensing parallel MRI," in *2019 IEEE 16th International Symposium on Biomedical Imaging* (Venice), 1532–1536.

Goodfellow, I., Pouget-Abadie, J., Mirza, M., Xu, B., Warde-Farley, D., Ozair, S., et al. (2014). "Generative adversarial nets," in *Advances in Neural Information Processing Systems* (Montréal), 2672–2680.

Haldar, J. P., Hernando, D., and Liang, Z. P. (2011). Compressed-sensing MRI with random encoding. *IEEE Trans. Med. Imaging* 30, 893–903. doi: 10.1109/TMI.2010.2085084

He, K., Zhang, X., Ren, S., and Sun, J. (2015). "Delving deep into rectifiers: surpassing human-level performance on imagenet classification," in: *Proceedings of the IEEE International Conference on Computer Vision* (Santiago), 1026–1034. doi: 10.1109/ICCV.2015.123

Huang, Y., Paisley, J., Lin, Q., Ding, X., Fu, X., and Zhang, X.-P. (2014). Bayesian nonparametric dictionary learning for compressed sensing MRI. *IEEE Trans. Image Process.* 23, 5007–5019. doi: 10.1109/TIP.2014.2360122

Jiang, M., Yuan, Z., Yang, X., Zhang, J., Gong, Y., Xia, L., et al. (2019). Accelerating CS-MRI reconstruction with fine-tuning Wasserstein generative adversarial network. *IEEE Access* 7, 152347–152357. doi: 10.1109/ACCESS.2019.2948220

Jolicoeur-Martineau, A. (2018). "The relativistic discriminator: A key element missing from standard GAN," in *International Conference on Learning Representations* (Vancouver).

Kabasawa, H. (2012). Magnetic resonance imaging apparatus and magnetic resonance imaging method. *J. Biomech. Eng.* 127, 148 —157.

Kwon, G., Han, C., and Kim, D. (2019). "Generation of 3D brain MRI using auto-encoding generative adversarial networks," in *International Conference on Medical Image Computing and Computer-Assisted Intervention* (Shenzhen), 118–126.

LeCun, Y., Bengio, Y., and Hinton, G. (2015). Deep learning. *Nature* 521, 436–444. doi: 10.1038/nature14539

Ledig, C., Theis, L., Huszár, F., Caballero, J., Cunningham, A., Acosta, A., et al. (2017). "Photo-realistic single image super-resolution using a generative adversarial network", in: *Proceedings of the IEEE Conference on Computer Vision and Pattern Recognition* (Honolulu), 4681–4690

Lee, J., Kim, H., Chung, H., and Ye, J. C. (2020). "Deep learning fast MRI using channel attention in magnitude domain," in: *2020 IEEE 17th International Symposium on Biomedical Imaging* (Lowa City), 917–920.

Liang, D., Cheng, J., Ke, Z., and Ying, L. (2020). Deep magnetic resonance image reconstruction: Inverse problems meet neural networks. *IEEE Signal Process. Mag.* 37, 141–151. doi: 10.1109/MSP.2019.2950557

Liang, Z.-P., and Lauterbur, P. C. (2000). *Principles of Magnetic Resonance Imaging: A Signal Processing Perspective*. (*SPIE Optical Engineering Press*).

Luo, W., Li, Y., Urtasun, R., and Zemel, R. (2016). "Understanding the effective receptive field in deep convolutional neural networks," in *Advances in Neural Information Processing Systems* (Barcelona), 4898–4906.

Lustig, M., Donoho, D., and Pauly, J. M. (2010). Sparse MRI: the application of compressed sensing for rapid MR imaging. *Magn. Reson. Med.* 58, 1182–1195. doi: 10.1002/mrm.21391

Lustig, M., Donoho, D. L., Santos, J. M., and Pauly, J. M. (2008). Compressed Sensing MRI. *IEEE Signal Process. Mag.* 25, 72–82. doi: 10.1109/MSP.2007.914728

Lyu, Q., You, C., Shan, H., Zhang, Y., and Wang, G. (2019). "Super-resolution MRI and CT through GAN-circle," in *Developments in X-Ray Tomography XII*: *International Society for Optics and Photonics* (Paris), 111130X. doi: 10.1117/12.2530592

Mahapatra, D., Bozorgtabar, B., and Garnavi, R. (2019). Image super-resolution using progressive generative adversarial networks for medical image analysis. *Comp. Med. Imaging Graphics* 71, 30–39. doi: 10.1016/j.compmedimag.2018.10.005

Miyato, T., Kataoka, T., Koyama, M., and Yoshida, Y. (2018). "Spectral normalization for generative adversarial networks," in *International Conference on Learning Representations* (Vancouver).

Murphy, M., Alley, M., Demmel, J., Keutzer, K., Vasanawala, S., and Lustig, M. (2012). Fast $\ell_1 $-SPIRiT compressed sensing parallel imaging MRI: scalable parallel implementation and clinically feasible runtime. *IEEE Trans. Med. Imaging* 31, 1250–1262. doi: 10.1109/TMI.2012.2188039

Radford, A., Metz, L., and Chintala, S. (2016). *"Unsupervised representation learning with deep convolutional generative adversarial networks," in International Conference on Learning Representations* (San Juan).

Ravishankar, S., and Bresler, Y. (2010). MR image reconstruction from highly undersampled k-space data by dictionary learning. *IEEE Trans. Med. Imaging* 30, 1028–1041. doi: 10.1109/TMI.2010.2090538

Russakovsky, O., Deng, J., Su, H., Krause, J., Satheesh, S., Ma, S., et al. (2015). Imagenet large scale visual recognition challenge. *Int. J. Comput. Vis* 115, 211–252. doi: 10.1007/s11263-015-0816-y

Shimron, E., Webb, A. G., and Azhari, H. (2020). CORE-deblur: parallel MRI reconstruction by deblurring using compressed sensing. *Magn. Reson. Imaging*. 72, 25–33. doi: 10.1016/j.mri.2020.06.001

Sun, J., Li, H., and Xu, Z. (2016). "Deep ADMM-Net for compressive sensing MRI," in *Advances in Neural Information Processing Systems*, 10–18.

Wang, H., Liang, D., King, K. F., Nagarsekar, G., Chang, Y., and Ying, L. (2012). Improving GRAPPA using cross-sampled autocalibration data. *Magn. Reson. Med.* 64, 1042–1053. doi: 10.1002/mrm.23083

Wang, S., Su, Z., Ying, L., Peng, X., Zhu, S., Liang, F., et al. (2016). "Accelerating magnetic resonance imaging via deep learning," in *2016 IEEE 13th International Symposium on Biomedical Imaging* (Prague), 514–517.

Yang, G., Yu, S., Dong, H., Slabaugh, G., Dragotti, P. L., Ye, X., et al. (2017). DAGAN: deep de-aliasing generative adversarial networks for fast compressed sensing MRI reconstruction. *IEEE Trans. Med. Imaging* 37, 1310–1321. doi: 10.1109/TMI.2017.2785879

Yong, H., Huang, J., Hua, X., and Zhang, L. (2020). Gradient centralization: a new optimization technique for deep neural networks. Eds. A. Vedaldi, H. Bischof, T. Brox and J.M. Frahm. *Computer Vision – ECCV 2020*. (Cham: Springer) p. 635-652. doi: 10.1007/978-3-030-58452-8_37

Zhang, H., Goodfellow, I., Metaxas, D., and Odena, A. (2019). "Self-attention generative adversarial networks," in *International Conference on Machine Learning*. (Long Beach: PMLR), 7354–7363.

Zhu, B., Liu, J. Z., Cauley, S. F., Rosen, B. R., and Rosen, M. S. (2018). Image reconstruction by domain-transform manifold learning. *Nature* 555, 487–492. doi: 10.1038/nature25988

Zhu, J.-Y., Park, T., Isola, P., and Efros, A. A. (2017). "Unpaired image-to-image translation using cycle-consistent adversarial networks," in *Proceedings of the IEEE International Conference on Computer Vision* (Venice), 2223–2232.

Conflict of Interest: Co-authors ZN and WM-S are employed by Aladdin Healthcare Technologies Ltd.

The remaining authors declare that the research was conducted in the absence of any commercial or financial relationships that could be construed as a potential conflict of interest.

frontiers
in Neuroinformatics

ORIGINAL RESEARCH
published: 30 November 2020
doi: 10.3389/fninf.2020.581897

A Tensor-Based Framework for rs-fMRI Classification and Functional Connectivity Construction

*Ali Noroozi and Mansoor Rezghi**

Department of Computer Science, Tarbiat Modares University, Tehran, Iran

Recently, machine learning methods have gained lots of attention from researchers seeking to analyze brain images such as Resting-State Functional Magnetic Resonance Imaging (rs-fMRI) to obtain a deeper understanding of the brain and such related diseases, for example, Alzheimer's disease. Finding the common patterns caused by a brain disorder through analysis of the functional connectivity (FC) network along with discriminating brain diseases from normal controls have long been the two principal goals in studying rs-fMRI data. The majority of FC extraction methods calculate the FC matrix for each subject and then use simple techniques to combine them and obtain a general FC matrix. In addition, the state-of-the-art classification techniques for finding subjects with brain disorders also rely on calculating an FC for each subject, vectorizing, and feeding them to the classifier. Considering these problems and based on multi-dimensional nature of the data, we have come up with a novel tensor framework in which a general FC matrix is obtained without the need to construct an FC matrix for each sample. This framework also allows us to reduce the dimensionality and create a novel discriminant function that rather than using FCs works directly with each sample, avoids vectorization in any step, and uses the test data in the training process without forcing any prior knowledge of its label into the classifier. Extensive experiments using the ADNI dataset demonstrate that our proposed framework effectively boosts the fMRI classification performance and reveals novel connectivity patterns in Alzheimer's disease at its early stages.

Keywords: Alzheimer's disease (AD) classification, functional connectivity, tensor, high order singular value decomposition, dimension reduction

Edited by:
Heye Zhang,
Sun Yat-sen University, China

Reviewed by:
Zhifan Gao,
University of Western Ontario, Canada
Han Zhang,
University of North Carolina at Chapel Hill, United States

****Correspondence:***
Mansoor Rezghi
Rezghi@modares.ac.ir

Received: *10 July 2020*
Accepted: *14 August 2020*
Published: *30 November 2020*

Citation:
Noroozi A and Rezghi M (2020) A Tensor-Based Framework for rs-fMRI Classification and Functional Connectivity Construction.
Front. Neuroinform. 14:581897.
doi: 10.3389/fninf.2020.581897

1. INTRODUCTION

Alzheimer's disease (AD) is a progressive neurodegenerative disorder with a long pre-morbid asymptomatic period, which affects millions of elderly individuals worldwide (Caselli et al., 2004). It is predicted that the number of affected people will double in the next 20 years, and 1 in 85 people will be affected by 2050 (Brookmeyer et al., 2007). The predominant clinical symptoms of AD include a decline in some important brain cognitive and intellectual abilities such as memory, thinking, and reasoning. Early detection is important for possible delay of the progression of mild MCI to moderate and severe stages (Folch et al., 2016). However, diagnosis of MCI is difficult due to its mild symptoms of cognitive impairment, causing most computer-aided diagnosis to achieve lower-than-desired performance (Musha et al., 2013; Li R. et al., 2018). Precise diagnosis of AD, especially in its early warning stage, that is, early Mild Cognitive Impairment (eMCI), enables treatments to delay or even avoid such disorders.

In recent years, medical imaging techniques such as positron emission tomography (PET) (Chandra et al., 2019), electroencephalography (EEG) (Bi and Wang, 2019), computed tomography (CT) scan (Ozdemir et al., 2019; van de Leemput et al., 2019), intracoronary imaging (Gao et al., 2019), and functional magnetic resonance imaging, which is a non-invasive brain imaging technique (fMRI) (Golby et al., 2005), have been used in order to analyze and detect disorders within body and brain (Zhang et al., 2012; Han et al., 2013). Due to high spatial resolution, fMRI is vastly used among researchers in order to monitor brain activities, especially in AD and all its stages in which detecting abnormalities within small brain regions is essential (Dennis and Thompson, 2014). An fMRI sample is naturally a 4D tensor consisting of 3D time-varying voxels, and each voxel contains an intensity value that is proportional to the strength of the **B**lood **O**xygenation **L**evel **D**ependent (BOLD) signal, which is a measure of the changes in blood flow to estimate the activity of different brain regions. Resting-state fMRI (rs-fMRI) is an fMRI technique in which the patient is asked to rest during the whole scan and it focuses on the low-frequency ($< 0.1Hz$) oscillations of BOLD signal presenting the underlying neuronal activation patterns of brain regions. rs-fMRI is usually used in order to analyze brain diseases like AD or Autism (Leonardi et al., 2013; Kazeminejad and Sotero, 2019; Nguyen et al., 2019). Different toolboxes such as GraphVar (Waller et al., 2018), Graph CNN (Zhang et al., 2019), and BrainNetClass (Zhou et al., 2020) are also developed to aid this cause.

Since each fMRI series consists of hundreds of thousands of voxels, which are often highly correlated with the surrounding voxels in the brain volume, parcellation of the brain for further analysis has moved toward the use of anatomical atlases. These atlases are strictly defined using anatomical features of the brain like locations of common gyri and do not rely on any functional information. To generate data using an atlas-based approach, the BOLD signal from all voxels is averaged within each brain region called region of interest (ROI) (Stanley et al., 2013). By putting together the average time series for all the ROIs, the ith series becomes $X_i \in \mathbb{R}^{T\times R}, i = \{1, 2, \cdots, S\}$, in which R, T, and S are the number of ROIs, time points, and samples, respectively. This process is illustrated in **Figure 1**

There are two major studies associated with rs-fMRI data: finding common brain disorders caused by diseases such as AD, autism, schizophrenia, and so on, and more recently detecting patients with brain disorders using classification techniques (de Vos et al., 2018; Du et al., 2018). Due to the high dimensionality of data along with the nature of diseases such as eMCI, which does not show any reliable clinical symptoms, researchers have moved toward advanced machine learning techniques in order to achieve more reliable analysis (Cuingnet et al., 2011).

A powerful tool that is commonly used in order to achieve aforementioned goals is the functional connectivity (FC) network. Let X_i be the ith sample, its corresponding FC, and $\bar{X}$ is a $region \times region$ matrix in which $\bar{x}_{ij}$ represents the FC between the ith and jth ROI. Functional connectivity is an observable phenomenon quantifiable with measures of statistical dependencies such as correlations, coherence, or transfer entropy (Friston, 2011). Recent studies have shown that some brain disorders such as AD could alter the way some brain regions interact with each other. For example, compared with healthy subjects, AD patients have been found with decreased FC between the hippocampus and other brain regions, and MCI patients have been observed with increased FC between the frontal lobe and other brain regions (Dennis and Thompson, 2014).

FCs are also used as features in classification. So, instead of using X_i as the ith sample, its corresponding FC, that is, $\bar{X}_i$, is used as a feature. Common techniques for calculating FC, that is, simple statistical measures such as coherence and Pearson correlation, allow for different ambiguities (Smith, 2012; Reid et al., 2019). And since brain alterations in early MCI are tiny, more sophisticated and computationally expensive methods such as partial correlation (Li Y. et al., 2018; Pervaiz et al., 2020), high-order networks (Chen et al., 2016), and spectral clustering (Liu et al., 2018) are required in order to achieve a better FC. The computational cost of a sophisticated FC is usually high and also its quality affects the performance of the learning process massively. Also, since the conventional classifiers like **S**upport **V**ector **M**achine (SVM) or k-NN works on data in vector format, these matrix features should be vectorized in order be fed to these classifiers. This vectorization leads to high-dimensional vectors that produce poor performance due to the phenomenon known as the curse of dimensionality. Alongside the curse of dimensionality, vectorization also destroys potential information embedded in the structure of data. This problem has been studied especially in image data in which vectorization destroys the spatial relations within an image (Ahmadi and Rezghi, 2020).

In this paper, based on high-order tensor decomposition, we have created a framework in which the aforementioned goals, that is finding a general FC and detecting a disorder through classification, could be achieved via a single **H**igh-**O**rder **S**ingular **V**alue **D**ecomposition (HOSVD) of each class. Here based on latent variables obtained by HOSVD, a general representative pattern of FC for eMCI and normal controls are obtained. As it was mentioned before, finding a proper FC is a challenging task. Obtaining an FC via the proposed method is not only fast and straightforward, but also very accurate. The majority of connectivity patterns detected by this method have been observed and studied in several separated types of research (cited in the experimental studies section), which show the reliability and power of the proposed method. Along with these connections, we have also detected novel connectivities especially regarding the cerebellum, which is usually discarded in the analysis of AD.

The proposed classifier is also much faster than the state-of-the art classifiers, and also uses the obtained rs-fMRI data directly in the classification process rather than calculating its corresponding FC matrix. Being able to feed X_is directly to the classifier saves us from a lot of problems related to calculating the proper FC. It also shows that the proposed classifier is strong enough to detect tiny alterations, which other state-of-the-art methods rely on finding FC to highlight.

To verify our approach, we conducted an extensive experimental study on rs-fMRI data from the benchmark

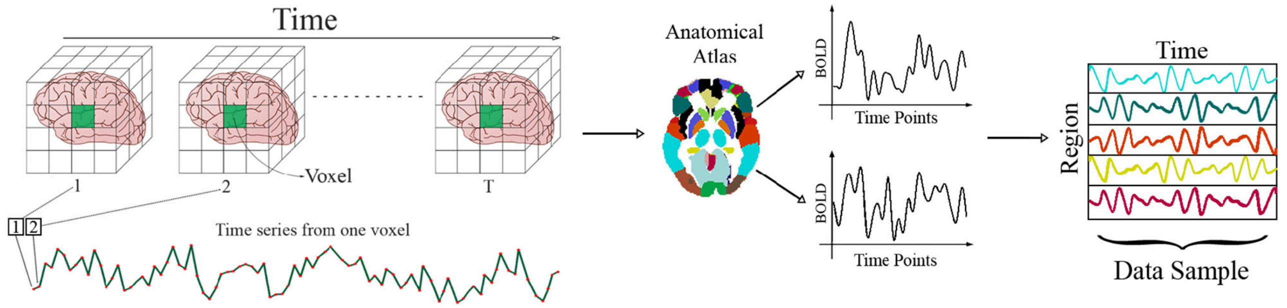

FIGURE 1 | The process of obtaining $X_i \in \mathbb{R}^{T\times R}, i = \{1, 2, \cdots, S\}$.

dataset ADNI. As will be seen, the results demonstrate the effectiveness and advantages of our method. Specifically, the proposed framework not only grants us superior classification accuracy to that from other methods, but it is also much faster and more stable against different data selection schemes. We have also confirmed our achieved general FC matrix using empirical data on the eMCI and normal FC patterns.

2. RELATED WORKS

As it was mentioned previously, obtaining and classifying FC matrices have become the dominant approach toward eMCI analysis. Variety of methods such as pairwise Pearson's correlation coefficient, sparse representation (Jie et al., 2013), and **S**parse **I**nverse **C**ovariance **E**stimation (SICE) (Huang et al., 2010) exist to obtain an FC. While the first two are easy to understand and can capture pairwise functional relationship based on a pair of ROIs, the latter can account for more complex interactions among multiple ROIs, but the estimation of partial correlation involves an inversion of a covariance matrix, which may be ill posed due to the singularity of the covariance matrix. These methods result in vastly different networks (Du et al., 2018). On the other hand, computing the correlations, based on the entire time series of fMRI data simply measures the FC between ROIs with a scalar value, which is fixed across time. This actually implicitly hypothesizes the Stationary interaction patterns among ROIs, which will result in a static functional connectivity (sFC). As a result, this method may overlook the complex and dynamic interaction patterns among ROIs, which are essentially time-varying (since the phase is not locked for every subject). In order to overcome this issue, Non-stationary methods have been proposed, which result in more complex networks and also known as dynamic functional connectivity (dFC) (Leonardi and Van De Ville, 2015; Kam et al., 2019). The most common and straightforward way to investigate dFC is using windowed FC, which consists of calculating a given FC measure, for example, the Pearson correlation coefficient, over consecutive windowed segments of the data (Zalesky et al., 2014). Although such an analysis seems straightforward, there are also pitfalls associated with it, which may cause in a non-accurate FC network (Hindriks et al., 2016).

In the following, we briefly discuss two state-of-the-art eMCI classification techniques belonging to these two paradigms:

Kernel compact SICE (**K−SIEC**): SICE matrix have proven itself to be one of the best sFC models (Huang et al., 2010; Ng et al., 2013; Colclough et al., 2018; Foti and Fox, 2019), which is extracted via the following optimization:

$$S^* = \arg\max_{S\succ 0} \quad \log\left(\det(S)\right) - \mathrm{tr}(CS) - \lambda \, \|S\|_1 \tag{1}$$

where C is the sample-based covariance matrix; $\det(\Delta)$, $\mathrm{tr}(\Delta)$, and $\|.\|_1$ denote the determinant, trace, and the sum of the absolute values of the entries of a matrix, respectively. In classification with FC features, the vectorized SICE of each sample is used (Leonardi et al., 2013). The occurrence of the curse of dimensionality and losing useful information contained in the SICE matrices [like symmetric positive definite (SPD) property] are two main drawbacks of this vectorization approach. As an inverse covariance matrix, an SICE matrix is SPD. This inherent property restricts SICE matrices to a lower dimensional Riemannian manifold rather than the full dimensional Euclidean space. This property allows some SPD manifold-based distances, like log-Euclidean distance (Arsigny et al., 2006) and Root Stein divergence (Sra, 2012) to be employed in kernel-based PCA to extract a compact representation of brain network (Zhang et al., 2015). The power of this method resides in a massive dimension reduction of SICE using its SPD property. The performance of this method also heavily relies on the choice of sparsity parameter λ for SICE calculations and the number of top eigenvectors m.

High−order networks (**HON**): This method which is proposed in Chen et al. (2016) belongs to non-stationary paradigm and uses the so-called high-order networks as features for classification purposes. It uses the sliding-window technique in order to split the time series into smaller pieces and then find the relation between them (Chang and Glover, 2010; Handwerker et al., 2012; Allen et al., 2014). Let $x^{(l)}_i(k) \in \mathbb{R}^N$ denotes the kth segment of the ith region in the lth sample. For each sample, a network with nodes $x^{(l)}_i(k)$ could be constructed, in which its edge weights are obtained as

$$C^{(l)}_{ij}(k) = \mathrm{corr}\left(x^{(l)}_i(k), x^{(l)}_j(k).\right)$$

Here, the weight $C_{ij}^{(l)}(k)$ represents the pairwise Pearson's correlation coefficients between the ith and the jth ROIs of the lth subject using the kth segment of subseries. Now

$$y_{ij}^{(l)} = \left[C_{ij}^{(l)}(1), C_{ij}^{(l)}(2), \cdots, C_{ij}^{(K)}(1)\right] \in \mathbb{R}^K$$

represents the similarity of the ith and jth ROIs of the lth sample in all segments. For each l by considering $y_{ij}^{(l)}$ as nodes of a networks with weights

$$H_{ij,pq}^{(l)} = \mathrm{corr}\left(y_{ij}^{(l)}, y_{pq}^{(l)}\right)$$

a higher-order network is obtained for each sample. Here for each pair of correlation time series y_{ij} and y_{pq}, $H_{ij,pq}^{(l)}$ indicates how the correlation between the ith and the jth ROIs influences the correlation between the pth and the qth ROIs. So for each sample its higher-order networks $\{H_{ij,pq}^{(l)}\}$ will be a matrix with size $R^4 \times R^4$(R is the number of regions), which will lead to a large-scale high-order FC network, containing at least thousands of vertices and millions of edges. In order to overcome this issue, the correlation time series within each subject are grouped into different clusters. Then, the correlation computations are carried out between the means of clusters. After reducing the network size, the weighted-graph local clustering coefficients is used to select the key features for each network and then an SVM classifier is trained in order to classify the obtained features. As a result of constructing a high-order network, the notion of a physical ROI become vague and thus such networks are not preferable choices in order to analyze functional connectivities.

Our method overcomes the dynamic-stationary problem of FC construction by working in HOSVD-based domain, which considers the dynamic nature of data and is much more sophisticated than using a windowed FC. The obtained FC also considers all subjects within a class simultaneously, rather than calculating FC for each subject separately that highlights common patterns in a class and eliminates possible outliers within data. The proposed framework also does not require any FC calculations for classification, which is a major advantage since finding a proper FC for each subject might be a very challenging task.

Multilinear approaches have been used before in order to analyze fMRI data. For example, Park (2011) uses multilinear PCA to classify fMRI data by Subject and Motor Task. Ozdemir et al. (2017) and Al-sharoa et al. (2018) use tensor decomposition and clustering techniques for analyzing brain connectivity networks and proves the dynamic nature of rs-fMRI. Recently, Ma et al. (2016) and He et al. (2017) proposed a multilinear method for voxel-wise analysis of rs-fMRI, which is used in order to detect late AD and some other diseases. Leonardi and Van De Ville (2013) considers dynamic whole-brain FC estimated from fMRI data acquired during alternating epochs of resting and watching of movie excerpts, and uses HOSVD in order to retrieve connectivity maps with associated time courses and subject loadings. This method uses the sliding-window technique in order to estimate the dynamic connectivity matrix for each subject, and then it constructs a 3-way tensor $\mathcal{R} \in \mathrm{R}^{C\times T\times T}$, by stacking the dynamic correlation matrices R of all subjects. Considering the HOSVD of R, this method obtains a matrix columns of which could be interpreted as group connectivity maps. There are similarities between this method and ours since they both take advantage of HOSVD. But our framework introduces major advantages such as (1) our framework does not require any FC calculations for its classifier. And (2), it is able to work with rs-fMRI, which is harder due to less constraint status of subjects.

3. NOTATION AND PRELIMINARIES

Tensors can be considered as a generalization of vectors and matrices of high dimensions. We use calligraphic letters to denote the tensors, for example, $(\mathcal{A}, \mathcal{B})$. Let $\mathcal{A} \in \mathbb{R}^{I_1\times I_2\times I_3}$ denote an order-3 tensor. Different "dimensions" of tensors are referred to as *modes*. We will use both standard subscripts and "MATLAB-like" notation to show tensor elements as follows:

$$\mathcal{A}(i,j,k) = a_{ijk}.$$

A *fiber* is a subtensor, where all indices but one are fixed. For example, mode-2 fibers of $\mathcal{A}$ have the following form:

$$\mathcal{A}(i,:,j) \in \mathbb{R}^{I_2}.$$

The mode-n product of an order-M tensor $\mathcal{A} \in \mathbb{R}^{\mathbb{I}_{\Bbbk}\times\cdots\times\mathbb{I}_{\mathbb{M}}}$ by a matrix $X \in \mathbb{R}^{K\times I_n}$ is defined as:

$$\mathbb{R}^{I_1\times\cdots\times I_{n-1}\times K\times I_{n+1}\times\cdots\times I_M} \ni \mathcal{B} = (X)_n \cdot \mathcal{A}, \tag{2}$$

where,

$$b_{i_1,\cdots,i_M} = \sum_{l=1}^{I_n} x_{i_n,l}, a_{i_1,\ldots,i_{n-1},l,i_{n+1},\ldots,i_M}.$$

This means that all mode-n fibers of $\mathcal{A}$ are multiplied by the matrix X. The notation (2) was suggested by De Silva and Lim (2008). An alternative notation was earlier given in De Lathauwer et al. (2000). $(X)_n \cdot \mathcal{A}$ is the same as $\mathcal{A} \times_n X$ in that system. The Frobenius norm of the order-M tensor $\mathcal{A}$ can be defined as $\|\mathcal{A}\| = \sum_{i_1,\cdots,i_M} a_{i_1,\cdots,i_M}^2$.

3.1. Higher-Order Singular Value Decomposition

HOSVD is one common extension of singular value decomposition to the tensors (De Lathauwer et al., 2000). Using HOSVD, every order-M tensor $\mathcal{A} \in \mathbb{R}^{I_1\times\cdots\times I_M}$ can be decomposed as:

$$\mathcal{A} = \left(U^{(1)}, \cdots, U^{(M)}\right) \cdot \mathcal{S} \tag{3}$$

where orthogonal matrices $U^{(i)}$ are singular matrices of tensor $\mathcal{A}$. Here, $U^{(i)}$ is the left singular matrix of $A^{(i)}$, in which its column vectors are the mode-n fibers of $\mathcal{A}$. The core tensor $\mathcal{S}$ is a real tensor of the same dimensions as $\mathcal{A}$ and

$$\mathcal{S} = \left(U^{(1)^{\mathsf{T}}}, \cdots, U^{(M)^{\mathsf{T}}}\right) \cdot \mathcal{A}$$

Although this core tensor is not diagonal as in the case of SVD of matrices, it satisfies the following conditions:

- **All orthogonality property**: Any two different slices along the same mode are orthogonal. This property of core tensor S is named as all orthogonality.
- **The ordering property**: The values $s_j^k = \left\|\mathcal{S}(:, \cdots, :, j, :, \cdots, :)\right\|$, where j is in the kth mode of $\mathcal{S}$, are named mode-k singular values of $\mathcal{A}$. It can be shown that for every k

$$s_1^k \geq s_2^k \geq \cdots \geq s_n^k \geq 0, \qquad k = 0, \cdots, M, \tag{4}$$

  are equal to the singular values of the matrix $A^{(k)}$. This means that the norms of the slices along every mode are ordered.
- **Oscillation**: It can be shown that as the indices increase, the singular vectors of each mode shows more oscillation. Based on this property, it can be shown that noises and outliers within the data are transferred into these high oscillation parts (Rezghi, 2017). Based on this fact and also the ordering property, the truncated version of HOSVD can be deployed as a noise reduction and compression tool (Lv and Wang, 2019).

The ordering property (4) demonstrates that, in the same way as matrices, singular values measure the *energy* of the tensor. So, it is easy to see that the energy of core tensor $\mathcal{S}$ focused on the elements of $\mathcal{S}$ with small indices. This property of HOSVD (similar to SVD) is very useful in the applications that encounter denoising problems. So, if $U_{k_l}^{l}$ contains the first k_l singular matrix and $\hat{\mathcal{S}} = \mathcal{S}(1:k_1, \cdots, 1:k_M)$, the following truncated HOSVD:

$$\hat{\mathcal{A}} = \left(U_{k_1}^{(1)}, \cdots, U_{k_M}^{(M)}\right)_{1:M} \cdot \hat{\mathcal{S}},$$

is a rank-$(k_1, \cdots .k_M)$ approximation of $\mathcal{A}$. Although this is not an optimal rank-$(k_1, \cdots .k_M)$ approximation of $\mathcal{A}$, it is still a good approximation and we have:

$$\left\|\mathcal{A} - \hat{\mathcal{A}}\right\| = \sum_{i=1}^{M} \sum_{j=k_i+1}^{r_i} s_j^{(i)^2},$$

where r_i is the rank of A^i (De Lathauwer et al., 2000).

4. PROPOSED FMRI ANALYSIS FRAMEWORK BASED ON HOSVD

In this section, which is divided into three subsections we first tackle the problem of classification, that is, designing a discriminant function that could predict the label of an unknown test subject. The second part describes a technique, which would enhance the designed classifier and the third part is allocated to find a general connectivity network for each class (e.g., eMCI subjects). All three aforementioned goals, that is, classification and its enhancement and finding a general FC for each class, evolve around a single HOSVD of each class, which provides us with basis for each mode (*time*, *region*, and *sample*) and enables us to capture the essence of each feature in a few low dimensional slices. We will use the obtained low-dimensional bases along the sample and region mode in order to design our discriminant function and obtain the general FC. The enhancement technique also comes from HOSVD characteristics, which enables us to involve test samples in the training process without forcing any a priori knowledge into the classifier.

4.1. eMCI Classification

Let tensors $\mathcal{X}^{(i)} \in \mathbb{R}^{T \times R \times S_i}$ consists of normal and eMCI data for $i = 1,2$, respectively. Here S_1, S_2 are the number of normal and eMCI samples. For tensor $\mathcal{X}^{(i)}$, the decomposition

$$\mathcal{X}^{(i)} = \left(U^{(i)}, V^{(i)}, W^{(i)}\right) \cdot \mathcal{S}^{(i)}, \tag{5}$$

is known as HOSVD, where orthogonal matrices $U^{(i)} \in \mathbb{R}^{T \times T}$, $V^{(i)} \in \mathbb{R}^{R \times R}$, and $W^{(i)} \in \mathbb{R}^{S_i \times S_i}$ are known as modes-1,2,3 singular matrices of $\mathcal{X}^{(i)}$, and $\mathcal{S}^{(i)}$ is the corresponding core tensor (Rezghi, 2017). Here, $U^{(i)}$ is a base of all mode-1 fibers $\mathcal{X}^{(i)}(:, l, k)$, which indicates the behavior of lth region of the kth sample of the ith class in all time points. Also $V^{(i)}$ is a base of all mode-2 fibers $\mathcal{X}(l, :, k)$, which indicates the behavior of all regions of lth sample of the ith class in the kth time. Due to the properties of HOSVD inherited from svd, the first columns of the kth singular matrix ($k = 1, 2, 3$) have more ability in construction of main parts of kth fibers (Rezghi, 2017). Therefore, a suitable dimension reduction would be to project the mode-1 and mode-2 fibers into space spanned by the first k_1^i and k_2^i singular vectors of modes-1,2, which will be denoted by $U_{k_1^i}^{(i)}$ and $V_{k_2^i}^{(i)}$, respectively. This dimension reduction could be done as:

$$\mathbb{R}^{k_1 \times k_2 \times S_i} \ni \bar{\mathcal{X}}^{(i)} = \left(U_{k_1^i}^{(i)\mathsf{T}}, V_{k_2^i}^{\mathsf{T}}\right)_{1,2} \cdot \mathcal{X}^{(i)} \tag{6}$$

It is clear that this reduction could be done separately on each mode without the need to fold any of them. This means that the structural integrity of data is preserved during the dimension reduction process, which is a key aspect in our work. It has been shown that even choosing relatively small values for k_1^i and k_2^i would result in a very good reconstruction error (Ahmadi and Rezghi, 2020).

Inspired by the structure of this reduction, in the following we present a tensor-based discriminant function. By HOSVD decomposition of $\mathcal{X}^{(i)}$, the projected data $\overline{\mathcal{X}}^{(i)}$ in Equation (6) becomes

$$\begin{aligned} \bar{\mathcal{X}}^{(i)} &= \left(\begin{bmatrix} I_{k_1^i} & 0 \end{bmatrix}, \begin{bmatrix} I_{k_2^i} & 0 \end{bmatrix}, W^{(i)}\right) \cdot \mathcal{S}^{(i)} \\ &= \left(W^{(i)}\right)_3 \cdot \mathcal{S}^{(i)}(1:k_1, 1:k_2, :) \end{aligned}$$

So, each sample of the ith class in the reduced space has the following form:

$$\begin{aligned}\bar{\mathcal{X}}^{(i)}(:,:,k) &= \left(W^{(i)}(k,:)\right)_3 \cdot \mathcal{S}^{(i)}(1:k_1^i, 1:k_2^i, :)\\ &= \sum_{k'=1}^{S_i} W^{(i)}(k,k') \cdot \mathcal{S}^{(i)}(1:k_1^i, 1:k_2^i, k').\end{aligned}$$

This means that each sample in the ith class could be represented as linear combination of the slices of the tensor $\overline{\mathcal{S}}^{(i)} = \mathcal{S}^{(i)}(1:k_1^i, 1:k_2^i, :)$. So if a test data like $X \in \mathbb{R}^{T\times R}$ belongs to the ith class, it is natural to expect that its projected version into principle region and times spaces, spanned by $U_{k_1^i}, V_{k_2^i}$, that is,

$$Z^{(i)} = \left(U_{k_1^i}^{(i)\top}, V_{k_2^i}^{(i)\top}\right)_{1,2} \cdot X$$

could be approximated well as a linear combination of the slices of the tensor $\overline{\mathcal{S}}^{(i)}$ as follows:

$$Z^{(i)} \approx \sum_{k=1}^{S_i} \lambda_k^i \overline{\mathcal{S}}^{(i)}(:,:,k). \tag{7}$$

Based on this viewpoint, each test data X could be assigned to a class that its projected version has the best approximation in the form (7). Due to the importance of core tensor elements with small indices in the reconstruction of the signal part of data in comparison with its last parts, the small number $k_3^i < S_i$ of slices $\overline{\mathcal{S}}^{(i)}(:,:,k)$ could be used in (7). In this viewpoint, each test data X would be assigned to the lth class, if $r_l = \min_{i=1,2} r_i$, where

$$r_i = \min_{\lambda^i} \|Z^{(i)} - \sum_{k=1}^{k_3^i} \lambda_k^i \overline{\mathcal{S}}^{(i)}(:,:,k)\|, \quad \lambda^i = \begin{pmatrix} \lambda_1^i \\ \vdots \\ \lambda_{s_i} \end{pmatrix} \tag{8}$$

r_i shows the reconstruction error of the projected version of X in the ith class.

4.2. Enhancing the Classifier

Consider that the test data X is added to dataset $\mathcal{X}^{(i)}$ of the ith class. So the new dataset will be $\widetilde{X}\in \mathbb{R}^{T\times R\times (S_i+1)}$:

$$\begin{aligned}\widetilde{\mathcal{X}}^{(i)}(:,:,1:S_i) &= \mathcal{X}^{(i)},\\ \widetilde{\mathcal{X}}^{(i)}(:,:,S_i+1) &= X.\end{aligned}$$

If X belongs to the ith class, then in the decomposition of $\widetilde{\mathcal{X}}^{(i)}$, X would be able to reinforce all slices of the core tensor and singular matrices. And thus enhances the reconstruction ability of (8) that would lead into a lower reconstruction error for the test subject X. On the other hand, if X does not belong to the ith class, HOSVD would naturally consider it as noise [based on ordering property (4)], since X is not similar to other samples and thus does not play a key role in reconstructing them, so its effect would be on the last slices of the core tensor and singular matrices, that is, slices with higher indices that are ignored in reconstruction (8).

In order to better demonstrate this effect, we conducted the following experiment: we randomly chose a test subject X^n from the class of normal subjects in ADNI dataset (this dataset is explained in detail in the experimental study section). The remaining normal samples are then gathered in a tensor $\mathcal{X}^{(1)} \in \mathbb{R}^{130\times 116\times 37}$. By adding X^n to this tensor, we obtained the incremented tensor $\widetilde{\mathcal{X}}^{(1)} \in \mathbb{R}^{130\times 116\times 38}$. We compute the HOSVD of these two tensors and plot the absolute mode-3 differences in **Figure 2**. As can be seen in this figure, since X^n belongs to the normal class, it effectively changes almost all singular values and so could improve the approximation in Equation (8). Then we randomly select an eMCI sample X^e and add it to $\mathcal{X}^{(1)}$ to construct another incremented version of it. The orange line in equation (**Figure 2**) shows the absolute mode-3 differences between these two tensors. It can be observed that adding an eMCI subject to the class of normal subjects only affected the last singular values and have a very low impact on the first singular values.

It can be concluded that adding unknown labeled test data to all classes before the basis extraction process would heavily impact the true class bases, and it has a rather negligible or in ideal case zero impact on the bases of other classes. As a result, after extracting the basis for each class in this manner, the reconstruction error (Equation 8) would be lower for the true class. Note that in the training process, the test data are added to all classes and they are uninformed of its label. Thus, no a priori knowledge is sneaked into the decision-making process. Algorithm (1) summarizes the proposed classification method.

Algorithm 1: Tensor-based classification method

```
1) Input: Normal train data $\mathcal{X}^{(1)}$, eMCI train data, $\mathcal{X}^{(2)}$
   $k_j^i, i,j = 1,2.$
   Test data $X$
2) Construct $\widetilde{\mathcal{X}}^{(i)}$ for $i = 1,2$, by adding $X$ to both tensors.
3) Compute $U_{k_1^i}, V_{k_2^i}$ and $\mathcal{S}(1:k_1^i, 1:k_2^i, :)$ of $\widetilde{\mathcal{X}}^{(i)}$, for i = 1,2.
4) Compute $Z^{(i)} = \left(U_{k_1^i}^{(i)\top}, V_{k_2^i}^{(i)\top}\right)_{1,2} \cdot X, i = 1,2.$
5) Comput $r_1, r_2$ from (8)
6) Assign $X$ to class $l$, if $l = \arg\min_i\{r_i\}$
```

4.3. General Functional Connectivity

In the ith class, which is represented by $\mathcal{X}^{(i)}$, the slice $\mathcal{X}^{(i)}(:,l,:)$ denotes the behavior of l^{th} region of all samples in all times. This slice could be considered as a feature for the l^{th} region of the ith class, so each region is represented as a Times-sample feature matrix. By the properties of singular matrices in modes-1,3, and for appropriate values k_1^i, k_3^i, each region $\mathcal{X}(:,l,:)$ could be reduced in both time and sample features separately based on mode-1 and mode-3 truncated singular matrices $U_{k_1^i}^{(i)}$ and $W_{k_3}^{(i)}$ as follows:

$$\mathcal{Y}^{(i)}(:,l,:) = \left(U_{k_1^i}^{(i)\top}, W_{k_3}^{(i)\top}\right)_{1,3} \cdot \mathcal{X}^{(i)}(:,l,:). \tag{9}$$

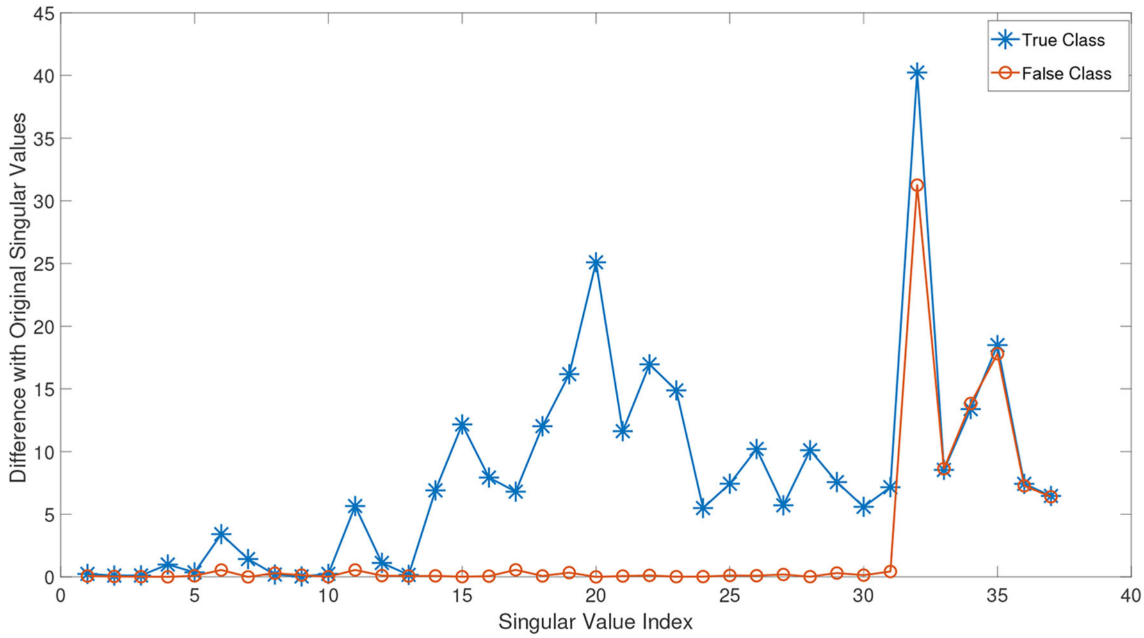

FIGURE 2 | The absolute value difference of the third mode singular values of normal and eMCI data with and without involving test data in construction of HOSVD.

Here $\mathcal{Y}^{(i)}(:,l,:)$ denotes a reduced version of $\mathcal{X}^{(i)}(:,l,:)$ into space spanned by $U_{k_1^i}^{(i)}$ and $W_{k_3}^{(i)}$ in modes-1,3. So,

$$\mathbb{R}^{k_1^i \times R \times k_3^i} \ni \mathcal{Y}^{(i)} = \left(U_{k_1^i}^{(i)\mathsf{T}}, W_{k_3^i}^{(i)\mathsf{T}}\right)_{1,3} \cdot \mathcal{X}^{(i)} \tag{10}$$

denotes all reduced regions of the ith class. By this structure and substituting the HOSVD decomposition of $\mathcal{X}^{(i)}$ in (10), we obtain

$$\begin{aligned}\mathcal{Y}^{(i)} &= \left(\left[I_{k_1^i}\ \ 0\right], V, \left[I_{k_3^i}\ \ 0\right]\right) \cdot \mathcal{S}^{(i)} \\ &= (V)_2 \cdot \mathcal{S}^{(i)}(1:k_1^i, :, 1:k_3^i)\end{aligned}$$

thus

$$\begin{aligned}\mathcal{Y}^{(i)}(:,k,:) &= \sum_{k'}^{R} V^{(i)}(k,k')\bar{\mathcal{C}}^{(i)}(:,k',:) \\ &= \left(V^{(i)}(k,:)\right)_2 \cdot \mathcal{C}^{(i)}\end{aligned} \tag{11}$$

in which

$$\mathbb{R}^{k_1^i \times R \times k_3^i} \ni \mathcal{C}^{(i)} = \mathcal{S}(1:k_1^i, :, 1:k_3^i).$$

Equation (11) shows that the reduced version of each region in the ith class could be written as the linear combinations of mode-2 slices of $\mathcal{C}^{(i)}$. So the coefficients of slices in this linear combination could be considered as a new feature for the l^{th} region of the ith class. Also as we mentioned before, the first slices are better than the last ones to reflect the principle properties of the data. So for appropriate k_3^i we could select only the first coefficients in (11) as new features for the l^{th} region. Mathematically, this means each region in the ith class could be represented by a new feature vector $V(l, 1; k_3^i) \in \mathbb{R}^{k_3^i}$.

This approach has two main benefits: (1) each region could be represented only by a vector with size k_3^i instead of a large time-sample matrix, and (2) the bases for each region is obtained in an HOSVD-based domain that is similar to Fourier frequency domain; but unlike Fourier, this transformation to HOSVD-domain is data dependent and hence the time-varying nature of rs-fMRI signals (2) would be taken into consideration (Rövid et al., 2013; Ozdemir et al., 2017). After representing each region with a single low dimensional vector, variety of methods such as SICE and other mentioned similarity measures could be deployed in order to construct a general FC for each class.

5. EXPERIMENTAL STUDY

5.1. Data Acquisition and Experimental Settings

RS-fMRI data of early MCI and NC patients were downloaded from ADNI website[1]. After removing subjects that had problems in the preprocessing steps, 44 eMCI and 38 NC subjects remained. The IDs of the 82 (38 NC and 44 early MCI) subjects are provided in the **Supplementary Material**.

The data are acquired on a 3-T (Philips) scanner with TR/TE set as 3,000/30 ms and flip angle of 80. Each series has 140 volumes, and each volume consists of 48 slices of image matrices with dimensions 64 × 64 with voxel size of $3.31 \times 3.31 \times 3.31\ mm^3$. The preprocessing is carried out using

---

[1] http://adni.loni.usc.edu

SPM12 and DPARSFA (Chao-Gan and Yu-Feng, 2010). The first 10 acquired rs-fMRI volumes of each subject were initially discarded before any further processing to ensure magnetization equilibrium. The remaining 130 volumes were then corrected for the staggered order of slice acquisition that was used during echoplanar scanning. The correction ensures the data on each slice correspond to the same point in time. To further reduce the effects of nuisance signals, regression of ventricle and WM signals as well as six head-motion profiles was performed. rs-fMRI images were then normalized to the MNI space with resolution of $3.31 \times 3.31 \times 3.31\ mm^3$ (Wee et al., 2016). Participants with too much head motion are excluded. The normalized brain images are warped into automatic anatomical labeling (AAL) (Tzourio-Mazoyer et al., 2002) atlas to obtain 116 ROIs as nodes. By following common practice (Park, 2011; Leonardi and Van De Ville, 2013; Al-sharoa et al., 2018), the ROI mean time series are extracted by averaging the time series from all voxels within each ROI and then bandpass filtered to obtain multiple sub-bands as in Al-sharoa et al. (2018). After the preprocessing steps, we obtained the normal samples $\mathcal{X}^{(1)} \in \mathbb{R}^{130\times116\times38}$ and eMCI samples $\mathcal{X}^{(2)} \in \mathbb{R}^{130\times116\times44}$.

TABLE 1 | Definitions of five statistical measurement indices.

Measurement	Definition
Acc	$\dfrac{TP+TN}{TP+FP+TN+FN}$
SEN	$\dfrac{TP}{TP+FN}$
YI	$SEN+SPE-1$
F-Score	$2 \times \dfrac{precession \times recall}{precesion + recall}$
BAC	$\dfrac{1}{2}(SEN+SPE)$

TABLE 2 | The average of different classification measurements in all dataset permutations in percent.

Method	ACC	F-Score	SEN	YI	BAC
k-SICE	75.57	77.36	78.50	50.69	75.34
HON	75.66	77.44	78.40	50.89	75.44
Proposed	**80.43**	**82.20**	**84.60**	**60.20**	**80.09**

Higher values are indicated by bold numbers.

5.2. Classification

Almost every subject in ADNI dataset has several (≈ 6) individual rs-fMRI data series, that is, a patient might be scanned several times during a period of time. Usually, a random rs-fMRI data are selected and enters the processing step (Zhang et al., 2015). This random selection may cause several problems. Since the number of train data is very low, a small alteration in the samples could drastically change the set of input parameters in order to achieve the highest accuracy. Also achieving high-quality results with a classifier does not guarantee its effectiveness on other datasets even with fine-tuning the parameters, since the training set may contain outliers and unidentified corrupted data. In order to show that the proposed framework is less sensitive against the choice of different permutations of data, we have selected 18 different random permutations (i.e., each permutation contains a different rs-fMRI series, for each subject) and tested two state of the art eMCI classification methods on them: **HON** (Chen et al., 2016) and **k−SICE** (Zhang et al., 2015). We have used five evaluation measures: accuracy (ACC), sensitivity (SEN), Youden's index (YI), F-score, and balanced accuracy (BAC). The detailed definitions of these five statistical measures are provided in equation (**Table 1**), where TP, TN, FP, and FN denote the true positive, true negative, false positive, and false negative, respectively, and precision $= \frac{TP}{TP+FP}$ and recall $= \frac{TP}{TP+FN}$. In this article, we treat the eMCI samples as positive class and the NC samples as negative class.

5.2.1. Classification Performance

After fine-tuning the input parameter set for each method, the classification accuracy measure (ACC) shows that for 16 out of 18 different *random* selected datasets, our approach performs better than k-SICE the same also holds for 15 datasets comparing to HON, that is, in 88.8% of datasets the proposed method works better than k-SICE, and in 83.3% of datasets, it works better than FON. The highest classification accuracy (86.59%) is achieved with the proposed method in the 15th sample data. The highest accuracy for the HON (84.15%) is achieved in the 14th, and the highest accuracy for the SICE method (85.37%) is achieved in the 6th sample data. As it was mentioned before, being stable when the input dataset changes is a very important aspect for a classifier, in order to measure the stability, the standard deviation of accuracy along with other measures is calculated. The standard of accuracy for the proposed method is 0.64 times less than HON and 1.73 times less than k-SICE method. Similar results hold for other classification measures as well.

Figure 3 shows the performance of these three methods in all five measurements. For a better demonstration, **Table 2** provides the average of several classification measurements scores for all dataset permutations. As it can be seen in this table, the average accuracy of proposed method, which is 80.43%, is 4.77% higher than the next method HON and 4.86% better than k-SICE. It is noteworthy that the other two methods, that is, HON and SICE, show similar results in average. The average F-score of the proposed method is also higher than other two, which shows a balanced prediction for both classes. Having a higher sensitivity (SEN) score, which measures the proportion of actual positives that are correctly identified as such, shows that the proposed method works better in detecting eMCI subjects. The YI is a measure for evaluating the biomarker effectiveness and having a higher YI yields a more informative decision (Youden, 1950). Our YI score is roughly 1.2 times better that other two methods. Similar to F-score, having a higher Balanced Accuracy Score (BAC) yields more balanced predictions. It is also noteworthy that the proposed method have much less standard deviation in all five measurements, which indicates its effectiveness and robustness toward different datasets.

One other key aspect of the proposed classifier is that it works significantly faster that the other two, especially in the training process. Our method is more than 600 times faster than HON and 20 times faster than SICE. Having a huge execution

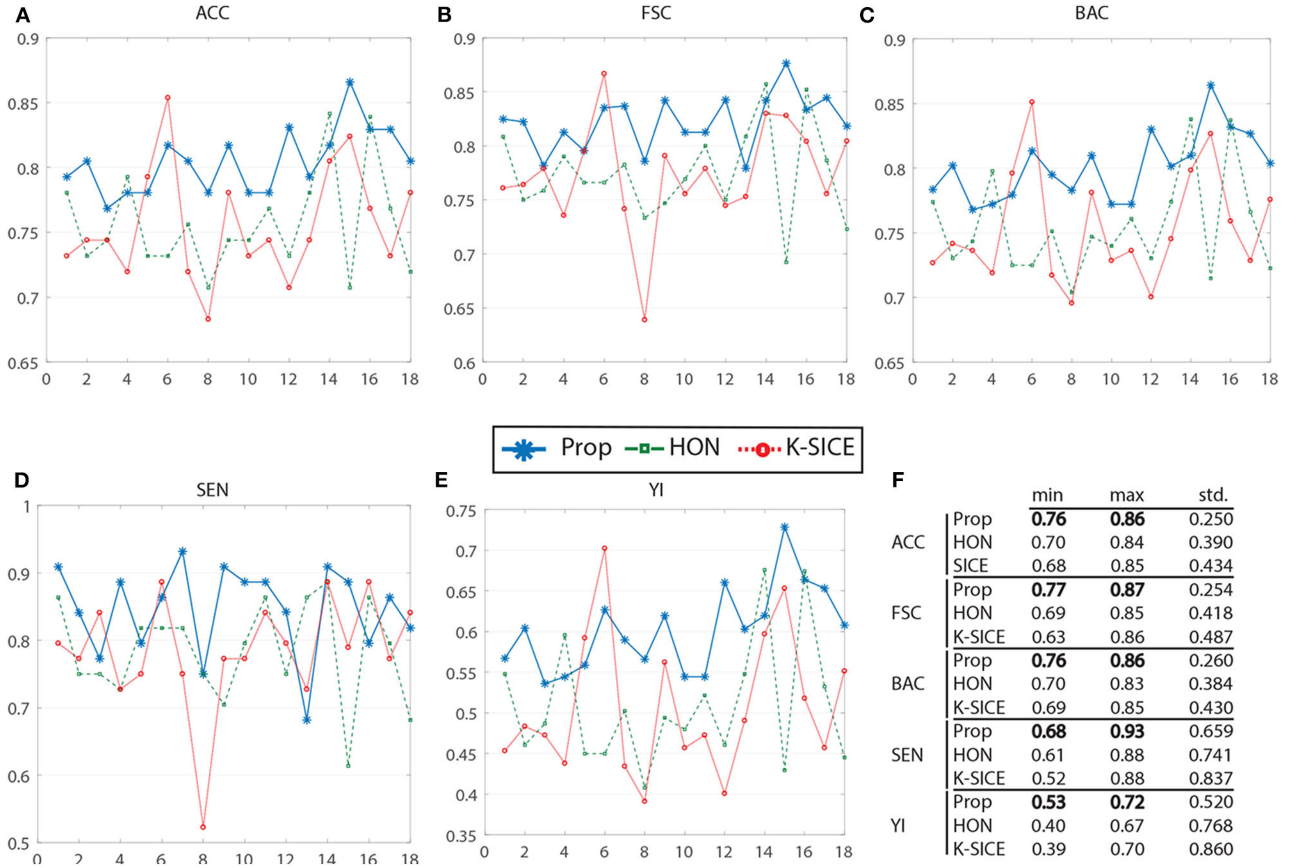

		min	max	std.
ACC	Prop	**0.76**	**0.86**	0.250
	HON	0.70	0.84	0.390
	SICE	0.68	0.85	0.434
FSC	Prop	**0.77**	**0.87**	0.254
	HON	0.69	0.85	0.418
	K-SICE	0.63	0.86	0.487
BAC	Prop	**0.76**	**0.86**	0.260
	HON	0.70	0.83	0.384
	K-SICE	0.69	0.85	0.430
SEN	Prop	**0.68**	**0.93**	0.659
	HON	0.61	0.88	0.741
	K-SICE	0.52	0.88	0.837
YI	Prop	**0.53**	**0.72**	0.520
	HON	0.40	0.67	0.768
	K-SICE	0.39	0.70	0.860

FIGURE 3 | Comparison of proposed method (Prop) with K-SICE and HON applied on 18 different dataset permutations in five different classification evaluation measures. **(A–E)** show *accuracy*, *F-Score*, *balanced accuracy*, *sensitivity*, and *Youden Index*, respectively, along with the maximum, minimum, and standard deviation of each one presented in the embedded table **(F)**.

time especially affects the parameter selection scheme since all these methods use cross-validation procedure in order to find the optimal parameters, which itself requires several runs of the algorithm.

5.3. Functional Connectivity Network

The vector features for both normal and eMCI classes were obtained via the proposed method as it is described in section 4.3. Due to the aforementioned qualities of partial correlation, SICE is deployed in order to obtain the final FC. In order to better highlight the differences between normal and eMCI subjects, a difference graph D is constructed by subtracting the normal FC from the eMCI FC. This graph could be seen in **Figure 4**. The nodes of D show the ROIs according to the AAL atlas. The size of each node is proportional to its graph clustering coefficient, that is, the bigger node demonstrates higher activity in eMCI subjects in the corresponding ROI. Similar to nodes, the size of each edge is also proportional to the correlation between two ROIs. In addition, the edges are also color coded in a way that the green edges show the positive edges in D and the red edges show the negative edges in D. In this manner, the green edges demonstrate a decrease in activity between the corresponding nodes in eMCI subjects, and the red edges show increasing activity between corresponding ROIs in the eMCI subjects.

As it can be seen in the difference graph, the big nodes, that is, ROIs with higher activities, do not necessarily establish strong connections with the other nodes. As an obvious example, higher activities in lingual gyrus (ROI index: 47, 48) (He et al., 2007), calcarine sulcus (ROI index: 43, 44) (Bakkour et al., 2013; Brewer and Barton, 2014), supplementary motor area (ROI index: 19, 20) (Brewer and Barton, 2014; Jacobsen et al., 2015), and temporal_mid_L (ROI index: 85) (Kosicek and Hecimovic, 2013) are easily detectable. The majority of ROIs located in frontal lobe also show rather high activities compared to normal subjects (Dennis and Thompson, 2014; Salvatore et al., 2015).

Similar to the nodes, the strong edge between two ROIs does not necessarily require the nodes to be highly active in eMCI, although a strong edge does indicate high activities and FC between the two corresponding ROIs. The difference in graph shows a significant increase in connectivity between Rectus (ROI index: 28, 27 in frontal lobe) and Parietal_Sup_R (ROI index: 60 in parietal lobe) (Brickman et al., 2015; De Reuck et al., 2015), Frontal_Inf_Orb_R (ROI index: 16 in frontal lobe) and

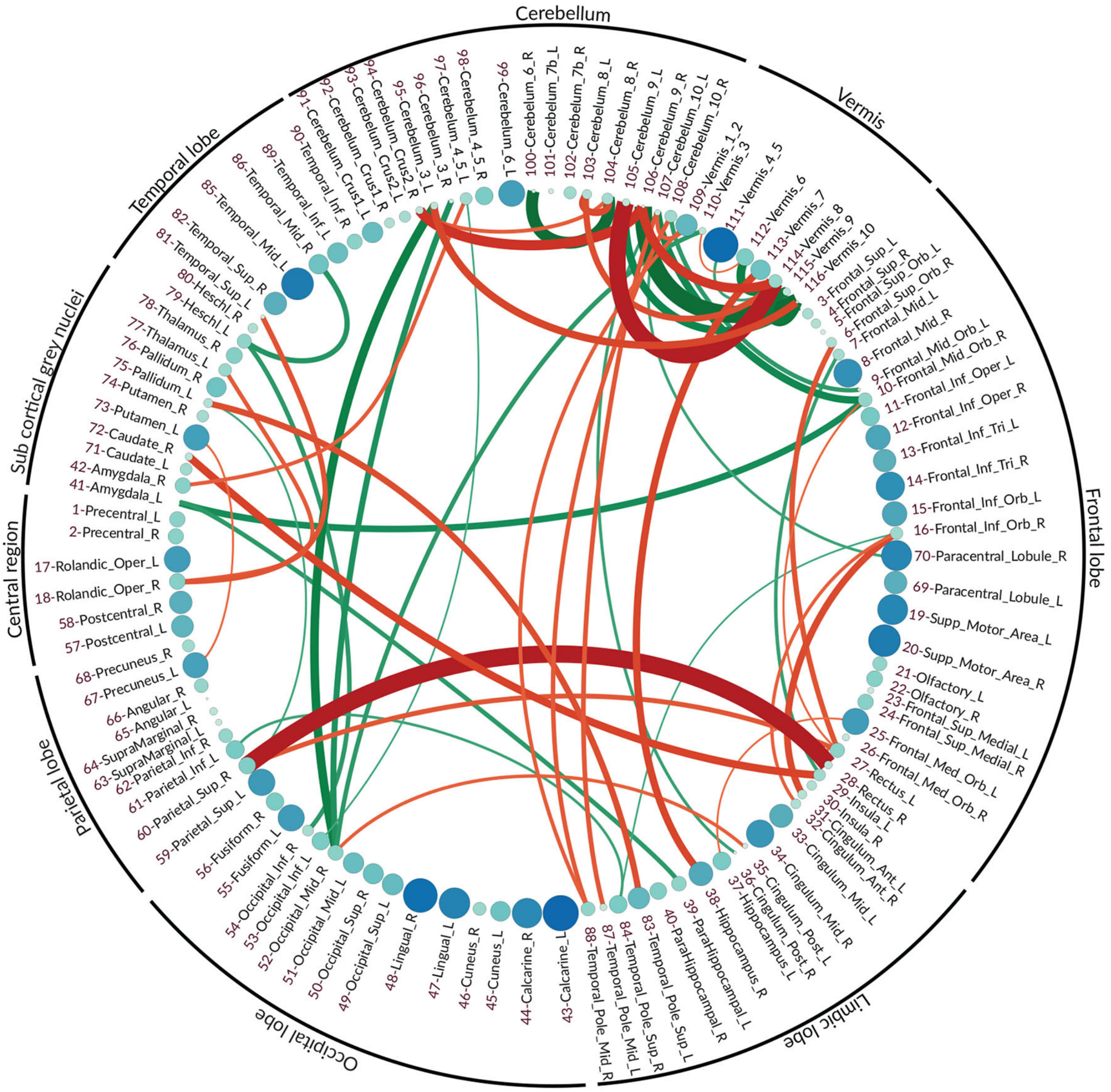

FIGURE 4 | The difference graph. This graph is obtained via subtracting the functional connectivity of eMCI subjects from normal subjects. Each circle represents an ROI in AAL atlas, and the color and size of each circle are proportional to the graph clustering coefficient of the difference graph. Red: more activity in EMCI, green: less activity in EMCI.

Cingulum_Ant (ROI index: 31, 32 in limbic lobe) (Perani et al., 2017), Insula_L, Temporal_Pole_Sup_L (ROI index: 29, 83 in limbic lobe) and Pallidum_R, Caudate_R (ROI index: 29, 83 in sub-cortical gray nuclei) (Watson et al., 2016). It can also be seen that within activities, frontal lobe also increased in patients with eMCI (Cai et al., 2015). There is a decrease in connectivity between Amygdala_L (ROI index: 41 in sub-cortical gray nuclei) with Frontal_Mid_Orb_R (ROI index: 10 in sub-frontal lobe) and ParaHippocampal_L (ROI index: 39 in sub-limbic lobe) (Ortner et al., 2016). The connectivity between Heschl_L (ROI index: 79 in temporal lobe) and two ROIs Temporal_Mid_R (ROI index: 86 also in temporal lobe) and Occipital_Inf_R (ROI index: 54 in occipital lobe) also decreased in eMCI (Steketee et al., 2016).

5.3.1. Regarding the Cerebellum and Vermis

In fMRI data analysis and especially in AD studies, ROIs within the cerebellum and vermis are usually excluded since their role was regarded as insignificant (Sanz-Arigita et al., 2010; Zhang et al., 2011). Recent studies have shown that the traditional assumption that cerebral area is essential only to the coordination of voluntary motor activity and motor learning is not valid and indicates the significant role of the cerebellum in nervous system function, cognition, and emotion (Jacobs et al., 2017).

As it can be seen in the difference graph that we obtained, ROIs within cerebellum and vermis are highly active and both their Intra and interconnections are noticeable. There is increased FC between the limbic lobe, especially Hippocampus_R, Temporal_Pole_Mid (ROI index: 38, 87, 88) and cerebral areas in eMCI patients. Also, the connectivity between occipital lobe, especially occipital_mid_R (ROI index: 52), the frontal lobe, especially in frontal_mid_orb (ROI index: 9,10), and cerebral areas seems to decrease in patients with eMCI.

6. CONCLUSION

In this article, we proposed a tensor framework for eMCI diagnosis and FC construction. There are two main issues associated with rs-fMRI analysis and in particular eMCI diagnosis. The first is that the majority of state-of-the-art fMRI classification techniques use the FC matrix as the feature for their discriminant function; hence, they have to deal with many challenges that are associated with FC calculations. The second comes from the fact that FC networks are among the best tools for studying brain activities, but the stationary and dynamic FC conflict and the fact that the majority of methods belonging to these paradigms work only with one sample would lead to vastly different brain networks. Therefore, we developed a tensor framework, which is able to directly use the samples in classification without the need for any FC calculations and is also able to calculate a general FC network that considers the time-varying nature of rs-fMRI signals since it works in the data-dependent HOSVD-domain and is able to consider all subjects within a class in order to obtain these connectivities. The proposed method is not only fast, but it also outperforms state-of-the-art techniques.

One possible drawback of this framework is the need for HOSVD calculation for both classes in each test phase. Although this problem is negligible in eMCI classification (since the number of samples is not high), it could be time consuming for larger datasets. In order to resolve this issue, incremental HOSVD calculations may be deployed that will accelerate the calculations.

DATA AVAILABILITY STATEMENT

All datasets presented in this study can be downloaded through ADNI website (http://adni.loni.usc.edu). Additional information about the subjects used in this study can be found in the **Supplementary Material**.

AUTHOR CONTRIBUTIONS

AN and MR contributed to the design and implementation of the research, to the analysis of the results, and to the writing of the manuscript. Both authors contributed to the article and approved the submitted version.

SUPPLEMENTARY MATERIAL

The Supplementary Material for this article can be found online at: https://www.frontiersin.org/articles/10.3389/fninf.2020.581897/full#supplementary-material

REFERENCES

Ahmadi, S., and Rezghi, M. (2020). Generalized low-rank approximation of matrices based on multiple transformation pairs. *Pattern Recogn*. 108:107545. doi: 10.1016/j.patcog.2020.107545

Allen, E. A., Damaraju, E., Plis, S. M., Erhardt, E. B., Eichele, T., and Calhoun, V. D. (2014). Tracking whole-brain connectivity dynamics in the resting state. *Cereb. Cortex* 24, 663–676. doi: 10.1093/cercor/bhs352

Al-sharoa, E., Al-khassaweneh, M., and Aviyente, S. (2018). Tensor based temporal and multilayer community detection for studying brain dynamics during resting state fMRI. *IEEE Trans. Biomed. Eng*. 66, 695–709. doi: 10.1109/TBME.2018.2854676

Arsigny, V., Fillard, P., Pennec, X., and Ayache, N. (2006). Log-euclidean metrics for fast and simple calculus on diffusion tensors. *Magn. Reson. Med*. 56, 411–421. doi: 10.1002/mrm.20965

Bakkour, A., Morris, J. C., Wolk, D. A., and Dickerson, B. C. (2013). The effects of aging and Alzheimer's disease on cerebral cortical anatomy: specificity and differential relationships with cognition. *Neuroimage* 76, 332–344. doi: 10.1016/j.neuroimage.2013.02.059

Bi, X., and Wang, H. (2019). Early Alzheimer's disease diagnosis based on EEG spectral images using deep learning. *Neural Netw*. 114, 119–135. doi: 10.1016/j.neunet.2019.02.005

Brewer, A. A., and Barton, B. (2014). Visual cortex in aging and Alzheimer's disease: changes in visual field maps and population receptive fields. *Front. Psychol*. 5:74. doi: 10.3389/fpsyg.2014.00074

Brickman, A. M., Zahodne, L. B., Guzman, V. A., Narkhede, A., Meier, I. B., Griffith, E. Y., et al. (2015). Reconsidering harbingers of dementia: progression of parietal lobe white matter hyperintensities predicts Alzheimer's disease incidence. *Neurobiol. Aging* 36, 27–32. doi: 10.1016/j.neurobiolaging.2014.07.019

Brookmeyer, R., Johnson, E., Ziegler-Graham, K., and Arrighi, H. M. (2007). Forecasting the global burden of Alzheimer's disease. *Alzheimers Dement*. 3, 186–191. doi: 10.1016/j.jalz.2007.04.381

Cai, S., Huang, L., Zou, J., Jing, L., Zhai, B., Ji, G., et al. (2015). Changes in thalamic connectivity in the early and late stages of amnestic mild cognitive impairment: a resting-state functional magnetic resonance study from ADNI. *PLoS ONE* 10:e0115573. doi: 10.1371/journal.pone.0115573

Caselli, R. J., Reiman, E., Osborne, D., Hentz, J., Baxter, L., Hernandez, J., et al. (2004). Longitudinal changes in cognition and behavior in asymptomatic carriers of the apoe e4 allele. *Neurology* 62, 1990–1995. doi: 10.1212/01.WNL.0000129533.26544.BF

Chandra, A., Valkimadi, P.-E., Pagano, G., Cousins, O., Dervenoulas, G., Politis, M., et al. (2019). Applications of amyloid, tau, and neuroinflammation pet imaging to Alzheimer's disease and mild cognitive impairment. *Hum. Brain Mapp*. 40, 5424–5442. doi: 10.1002/hbm.24782

Chang, C., and Glover, G. H. (2010). Time-frequency dynamics of resting-state brain connectivity measured with fMRI. *Neuroimage* 50, 81–98. doi: 10.1016/j.neuroimage.2009.12.011

Chao-Gan, Y., and Yu-Feng, Z. (2010). DPARSF: a MATLAB toolbox for "pipeline" data analysis of resting-state fMRI. *Front. Syst. Neurosci*. 4:13. doi: 10.3389/fnsys.2010.00013

Chen, X., Zhang, H., Gao, Y., Wee, C.-Y., Li, G., Shen, D., et al. (2016). High-order resting-state functional connectivity network for MCI classification. *Hum. Brain Mapp*. 37, 3282–3296. doi: 10.1002/hbm.23240

Colclough, G. L., Woolrich, M. W., Harrison, S. J., López, P. A. R., Valdes-Sosa, P. A., and Smith, S. M. (2018). Multi-subject hierarchical inverse covariance modelling improves estimation of functional brain networks. *Neuroimage* 178, 370–384. doi: 10.1016/j.neuroimage.2018.04.077

Cuingnet, R., Gerardin, E., Tessieras, J., Auzias, G., Lehéricy, S., Habert, M.-O., et al. (2011). Automatic classification of patients with Alzheimer's disease from structural MRI: a comparison of ten methods using the ADNI database. *Neuroimage* 56, 766–781. doi: 10.1016/j.neuroimage.2010.06.013

De Lathauwer, L., De Moor, B., and Vandewalle, J. (2000). A multilinear singular value decomposition. *SIAM J. Matrix Anal. Appl.* 21, 1253–1278. doi: 10.1137/S0895479896305696

De Reuck, J., Auger, F., Durieux, N., Deramecourt, V., Cordonnier, C., Pasquier, F., et al. (2015). Topography of cortical microbleeds in Alzheimer's disease with and without cerebral amyloid angiopathy: a post-mortem 7.0-tesla MRI study. *Aging Dis.* 6:437. doi: 10.14336/AD.2015.0429

De Silva, V., and Lim, L.-H. (2008). Tensor rank and the ill-posedness of the best low-rank approximation problem. *SIAM J. Matrix Anal. Appl.* 30, 1084–1127. doi: 10.1137/06066518X

de Vos, F., Koini, M., Schouten, T. M., Seiler, S., van der Grond, J., Lechner, A., et al. (2018). A comprehensive analysis of resting state fMRI measures to classify individual patients with Alzheimer's disease. *Neuroimage* 167, 62–72. doi: 10.1016/j.neuroimage.2017.11.025

Dennis, E. L., and Thompson, P. M. (2014). Functional brain connectivity using fMRI in aging and Alzheimer's disease. *Neuropsychol. Rev.* 24, 49–62. doi: 10.1007/s11065-014-9249-6

Du, Y., Fu, Z., and Calhoun, V. D. (2018). Classification and prediction of brain disorders using functional connectivity: promising but challenging. *Front. Neurosci.*12:525. doi: 10.3389/fnins.2018.00525

Folch, J., Petrov, D., Ettcheto, M., Abad, S., Sánchez-López, E., Luisa García, M., et al. (2016). Current research therapeutic strategies for alzheimer's disease treatment. *Neural Plast.* 2016:8501693. doi: 10.1155/2016/8501693

Foti, N. J., and Fox, E. B. (2019). Statistical model-based approaches for functional connectivity analysis of neuroimaging data. *Curr. Opin. Neurobiol.* 55, 48–54. doi: 10.1016/j.conb.2019.01.009

Friston, K. J. (2011). Functional and effective connectivity: a review. *Brain Connect.* 1, 13–36. doi: 10.1089/brain.2011.0008

Gao, Z., Chung, J., Abdelrazek, M., Leung, S., Hau, W. K., Xian, Z., et al. (2019). Privileged modality distillation for vessel border detection in intracoronary imaging. *IEEE Trans. Med. Imaging* 39, 1524–1534. doi: 10.1109/TMI.2019.2952939

Golby, A., Silverberg, G., Race, E., Gabrieli, S., O'Shea, J., Knierim, K., et al. (2005). Memory encoding in Alzheimer's disease: an fMRI study of explicit and implicit memory. *Brain* 128, 773–787. doi: 10.1093/brain/awh400

Han, J., Ji, X., Hu, X., Zhu, D., Li, K., Jiang, X., et al. (2013). Representing and retrieving video shots in human-centric brain imaging space. *IEEE Trans. Image Process.* 22, 2723–2736. doi: 10.1109/TIP.2013.2256919

Handwerker, D. A., Roopchansingh, V., Gonzalez-Castillo, J., and Bandettini, P. A. (2012). Periodic changes in fMRI connectivity. *Neuroimage* 63, 1712–1719. doi: 10.1016/j.neuroimage.2012.06.078

He, L., Lu, C.-T., Ding, H., Wang, S., Shen, L., Yu, P. S., et al. (2017). "Multi-way multi-level kernel modeling for neuroimaging classification," in *Proceedings of the IEEE Conference on Computer Vision and Pattern Recognition* (Honolulu, HI), 356–364. doi: 10.1109/CVPR.2017.724

He, Y., Wang, L., Zang, Y., Tian, L., Zhang, X., Li, K., et al. (2007). Regional coherence changes in the early stages of Alzheimer's disease: a combined structural and resting-state functional MRI study. *Neuroimage* 35, 488–500. doi: 10.1016/j.neuroimage.2006.11.042

Hindriks, R., Adhikari, M. H., Murayama, Y., Ganzetti, M., Mantini, D., Logothetis, N. K., et al. (2016). Can sliding-window correlations reveal dynamic functional connectivity in resting-state fMRI? *Neuroimage* 127, 242–256. doi: 10.1016/j.neuroimage.2015.11.055

Huang, S., Li, J., Sun, L., Ye, J., Fleisher, A., Wu, T., et al. (2010). Learning brain connectivity of Alzheimer's disease by sparse inverse covariance estimation. *Neuroimage* 50, 935–949. doi: 10.1016/j.neuroimage.2009.12.120

Jacobs, H. I., Hopkins, D. A., Mayrhofer, H. C., Bruner, E., van Leeuwen, F. W., Raaijmakers, W., et al. (2017). The cerebellum in Alzheimer's disease: evaluating its role in cognitive decline. *Brain* 141, 37–47. doi: 10.1093/brain/awx194

Jacobsen, J.-H., Stelzer, J., Fritz, T. H., Chételat, G., La Joie, R., and Turner, R. (2015). Why musical memory can be preserved in advanced Alzheimer's disease. *Brain* 138, 2438–2450. doi: 10.1093/brain/awv135

Jie, B., Zhang, D., Gao, W., Wang, Q., Wee, C.-Y., and Shen, D. (2013). Integration of network topological and connectivity properties for neuroimaging classification. *IEEE Trans. Biomed. Eng.* 61, 576–589. doi: 10.1109/TBME.2013.2284195

Kam, T.-E., Zhang, H., Jiao, Z., and Shen, D. (2019). Deep learning of static and dynamic brain functional networks for early MCI detection. *IEEE Trans. Med. imaging* 39, 478–487. doi: 10.1109/TMI.2019.2928790

Kazeminejad, A., and Sotero, R. C. (2019). Topological properties of resting-state fMRI functional networks improve machine learning-based autism classification. *Front. Neurosci.* 12:1018. doi: 10.3389/fnins.2018.01018

Kosicek, M., and Hecimovic, S. (2013). Phospholipids and Alzheimer's disease: alterations, mechanisms and potential biomarkers. *Int. J. Mol. Sci.* 14, 1310–1322. doi: 10.3390/ijms14011310

Leonardi, N., Richiardi, J., Gschwind, M., Simioni, S., Annoni, J.-M., Schluep, M., et al. (2013). Principal components of functional connectivity: a new approach to study dynamic brain connectivity during rest. *Neuroimage* 83, 937–950. doi: 10.1016/j.neuroimage.2013.07.019

Leonardi, N., and Van De Ville, D. (2013). "Identifying network correlates of brain states using tensor decompositions of whole-brain dynamic functional connectivity," in *2013 International Workshop on Pattern Recognition in Neuroimaging* (Philadelphia, PA: IEEE), 74–77. doi: 10.1109/PRNI.2013.28

Leonardi, N., and Van De Ville, D. (2015). On spurious and real fluctuations of dynamic functional connectivity during rest. *Neuroimage* 104, 430–436. doi: 10.1016/j.neuroimage.2014.09.007

Li, R., Rui, G., Chen, W., Li, S., Schulz, P. E., and Zhang, Y. (2018). Early detection of Alzheimer's disease using non-invasive near-infrared spectroscopy. *Front. Aging Neurosci.* 10:366. doi: 10.3389/fnagi.2018.00366

Li, Y., Liu, J., Huang, J., Li, Z., and Liang, P. (2018). Learning brain connectivity sub-networks by group-constrained sparse inverse covariance estimation for Alzheimer's disease classification. *Front. Neuroinform.* 12:58. doi: 10.3389/fninf.2018.00058

Liu, F., Choi, D., Xie, L., and Roeder, K. (2018). Global spectral clustering in dynamic networks. *Proc. Natl. Acad. Sci. U.S.A.* 115, 927–932. doi: 10.1073/pnas.1718449115

Lv, H., and Wang, R. (2019). Denoising 3D magnetic resonance images based on low-rank tensor approximation with adaptive multirank estimation. *IEEE Access* 7, 85995–86003. doi: 10.1109/ACCESS.2019.2924907

Ma, G., He, L., Lu, C.-T., Yu, P. S., Shen, L., and Ragin, A. B. (2016). "Spatio-temporal tensor analysis for whole-brain fMRI classification," in *Proceedings of the 2016 SIAM International Conference on Data Mining* (SIAM) (Miami, FL), 819–827. doi: 10.1137/1.9781611974348.92

Musha, T., Matsuzaki, H., Kobayashi, Y., Okamoto, Y., Tanaka, M., and Asada, T. (2013). EEG markers for characterizing anomalous activities of cerebral neurons in NAT (neuronal activity topography) method. *IEEE Trans. Biomed. Eng.* 60, 2332–2338. doi: 10.1109/TBME.2013.2255101

Ng, B., Varoquaux, G., Poline, J. B., and Thirion, B. (2013). "A novel sparse group Gaussian graphical model for functional connectivity estimation," in *International Conference on Information Processing in Medical Imaging* (Asilomar, CA: Springer), 256–267. doi: 10.1007/978-3-642-38868-2_22

Nguyen, D. T., Ryu, S., Qureshi, M. N. I., Choi, M., Lee, K. H., and Lee, B. (2019). Hybrid multivariate pattern analysis combined with extreme learning machine for Alzheimer's dementia diagnosis using multi-measure rs-fMRI spatial patterns. *PLoS ONE* 14:e0212582. doi: 10.1371/journal.pone.0212582

Ortner, M., Pasquini, L., Barat, M., Alexopoulos, P., Grimmer, T., Förster, S., et al. (2016). Progressively disrupted intrinsic functional connectivity of basolateral amygdala in very early Alzheimer's disease. *Front. Neurol.* 7:132. doi: 10.3389/fneur.2016.00132

Ozdemir, A., Villafane-Delgado, M., Zhu, D. C., Iwen, M. A., and Aviyente, S. (2017). "Multi-scale higher order singular value decomposition (MS-HOSVD) for resting-state fMRI compression and analysis," in *2017 IEEE International Conference on Acoustics, Speech and Signal Processing (ICASSP)* (New Orleans, LA: IEEE), 6299–6303. doi: 10.1109/ICASSP.2017.7953368

Ozdemir, O., Russell, R. L., and Berlin, A. A. (2019). A 3D probabilistic deep learning system for detection and diagnosis of lung cancer using low-dose CT scans. *IEEE Trans. Med. Imaging* 39, 1419–1429. doi: 10.1109/TMI.2019.2947595

Park, S. W. (2011). *Multifactor Analysis for fMRI Brain Image Classification by Subject and Motor Task*. Electrical and computer engineering technical report. Pittsburgh, PA: Carnegie Mellon University.

Perani, D., Farsad, M., Ballarini, T., Lubian, F., Malpetti, M., Fracchetti, A., et al. (2017). The impact of bilingualism on brain reserve and metabolic connectivity in Alzheimer's dementia. *Proc. Natl. Acad. Sci. U.S.A.* 114, 1690–1695. doi: 10.1073/pnas.1610909114

Pervaiz, U., Vidaurre, D., Woolrich, M. W., and Smith, S. M. (2020). Optimising network modelling methods for fMRI. *Neuroimage* 211:116604. doi: 10.1016/j.neuroimage.2020.116604

Reid, A. T., Headley, D. B., Mill, R. D., Sanchez-Romero, R., Uddin, L. Q., Marinazzo, D., et al. (2019). Advancing functional connectivity research from association to causation. *Nat. Neurosci.* 22, 1751–1760. doi: 10.1038/s41593-019-0510-4

Rezghi, M. (2017). A novel fast tensor-based preconditioner for image restoration. *IEEE Trans. Image Process.* 26, 4499–4508. doi: 10.1109/TIP.2017.2716840

Rövid, A., Szeidl, L., and Várlaki, P. (2013). "Data representation in HOSVD-DCT based domain," in *2013 IEEE 17th International Conference on Intelligent Engineering Systems (INES)* (San Jose, CA: IEEE), 103–106. doi: 10.1109/INES.2013.6632791

Salvatore, C., Cerasa, A., Battista, P., Gilardi, M. C., Quattrone, A., and Castiglioni, I. (2015). Magnetic resonance imaging biomarkers for the early diagnosis of Alzheimer's disease: a machine learning approach. *Front. Neurosci.* 9:307. doi: 10.3389/fnins.2015.00307

Sanz-Arigita, E. J., Schoonheim, M. M., Damoiseaux, J. S., Rombouts, S. A., Maris, E., Barkhof, F., et al. (2010). Loss of 'small-world' networks in Alzheimer's disease: graph analysis of fMRI resting-state functional connectivity. *PLoS ONE* 5:e13788. doi: 10.1371/journal.pone.0013788

Smith, S. M. (2012). The future of fMRI connectivity. *Neuroimage* 62, 1257–1266. doi: 10.1016/j.neuroimage.2012.01.022

Sra, S. (2012). "A new metric on the manifold of kernel matrices with application to matrix geometric means," in *Advances in Neural Information Processing Systems*, Vol. 25, eds F. Pereira, C. J. C. Burges, L. Bottou, and K. Q. Weinberger (Red Hook, NY: Curran Associates, Inc.), 144-152. Available online at: https://proceedings.neurips.cc/paper/2012/file/98dce83da57b0395e163467c9dae521b-Paper.pdf

Stanley, M. L., Moussa, M. N., Paolini, B., Lyday, R. G., Burdette, J. H., and Laurienti, P. J. (2013). Defining nodes in complex brain networks. *Front. Comput. Neurosci.* 7:169. doi: 10.3389/fncom.2013.00169

Steketee, R. M., Bron, E. E., Meijboom, R., Houston, G. C., Klein, S., Mutsaerts, H. J., et al. (2016). Early-stage differentiation between presenile Alzheimer's disease and frontotemporal dementia using arterial spin labeling MRI. *Eur. Radiol.* 26, 244–253. doi: 10.1007/s00330-015-3789-x

Tzourio-Mazoyer, N., Landeau, B., Papathanassiou, D., Crivello, F., Etard, O., Delcroix, N., et al. (2002). Automated anatomical labeling of activations in SPM using a macroscopic anatomical parcellation of the MNI MRI single-subject brain. *Neuroimage* 15, 273–289. doi: 10.1006/nimg.2001.0978

van de Leemput, S. C., Prokop, M., van Ginneken, B., and Manniesing, R. (2019). Stacked bidirectional convolutional lstms for deriving 3D non-contrast ct from spatiotemporal 4D CT. *IEEE Trans. Med. Imaging* 39, 985–996. doi: 10.1109/TMI.2019.2939044

Waller, L., Brovkin, A., Dorfschmidt, L., Bzdok, D., Walter, H., and Kruschwitz, J. D. (2018). Graphvar 2.0: a user-friendly toolbox for machine learning on functional connectivity measures. *J. Neurosci. Methods* 308, 21–33. doi: 10.1016/j.jneumeth.2018.07.001

Watson, R., Colloby, S. J., Blamire, A. M., and O'Brien, J. T. (2016). Subcortical volume changes in dementia with Lewy bodies and Alzheimer's disease. A comparison with healthy aging. *Int. Psychogeriatr.* 28, 529–536. doi: 10.1017/S1041610215001805

Wee, C.-Y., Yang, S., Yap, P.-T., and Shen, D. (2016). Sparse temporally dynamic resting-state functional connectivity networks for early MCI identification. *Brain Imaging Behav.* 10, 342–356. doi: 10.1007/s11682-015-9408-2

Youden, W. J. (1950). Index for rating diagnostic tests. *Cancer* 3, 32–35. doi: 10.1002/1097-0142(1950)3:1<32::AID-CNCR2820030106>3.0.CO;2-3

Zalesky, A., Fornito, A., Cocchi, L., Gollo, L. L., and Breakspear, M. (2014). Time-resolved resting-state brain networks. *Proc. Natl. Acad. Sci. U.S.A.* 111, 10341–10346. doi: 10.1073/pnas.1400181111

Zhang, D., Wang, Y., Zhou, L., Yuan, H., and Shen, D. (2011). Multimodal classification of Alzheimer's disease and mild cognitive impairment. *Neuroimage* 55, 856–867. doi: 10.1016/j.neuroimage.2011.01.008

Zhang, J., Zhou, L., Wang, L., and Li, W. (2015). Functional brain network classification with compact representation of sice matrices. *IEEE Trans. Biomed. Eng.* 62, 1623–1634. doi: 10.1109/TBME.2015.2399495

Zhang, S., Tong, H., Xu, J., and Maciejewski, R. (2019). Graph convolutional networks: a comprehensive review. *Comput. Social Netw.* 6:11. doi: 10.1186/s40649-019-0069-y

Zhang, T., Guo, L., Li, K., Jing, C., Yin, Y., Zhu, D., et al. (2012). Predicting functional cortical ROIs via DTI-derived fiber shape models. *Cereb. Cortex* 22, 854–864. doi: 10.1093/cercor/bhr152

Zhou, Z., Chen, X., Zhang, Y., Hu, D., Qiao, L., Yu, R., et al. (2020). A toolbox for brain network construction and classification (brainnetclass). *Hum. Brain Mapp.* 41, 2808–2826. doi: 10.1002/hbm.24979

Conflict of Interest: The authors declare that the research was conducted in the absence of any commercial or financial relationships that could be construed as a potential conflict of interest.

frontiers
in Neuroinformatics

ORIGINAL RESEARCH
published: 09 December 2020
doi: 10.3389/fninf.2020.613666

Validation and Diagnostic Performance of a CFD-Based Non-invasive Method for the Diagnosis of Aortic Coarctation

Qiyang Lu[1,2†], Weiyuan Lin[1,2†], Ruichen Zhang[3], Rui Chen[2], Xiaoyu Wei[2], Tingyu Li[2,4], Zhicheng Du[5], Zhaofeng Xie[4], Zhuliang Yu[1,6], Xinzhou Xie[3*] and Hui Liu[2,6*]

[1] College of Automation Science and Technology, South China University of Technology, Guangzhou, China, [2] Department of Radiology, Guangdong Provincial People's Hospital, Guangdong Academy of Medical Sciences, Guangzhou, China, [3] Department of Information Engineering, Northwestern Polytechnical University, Xi'an, China, [4] Guangdong Cardiovascular Institute, Guangdong Provincial People's Hospital, Guangdong Academy of Medical Sciences, Guangzhou, China, [5] Guangdong Key Laboratory of Medicine, Department of Medical Statistics and Epidemiology, Health Information Research Center, School of Public Health, Sun Yat-sen University, Guangzhou, China, [6] School of Medicine, South China University of Technology, Guangzhou, China

OPEN ACCESS

Edited by:
Heye Zhang,
Sun Yat-sen University, China

Reviewed by:
Xin Liu,
Foshan University, China
Qian Tao,
Leiden University Medical Center, Netherlands

Correspondence:
Hui Liu
liuhuijiujiu@gmail.com
Xinzhou Xie
xinzhxie@hotmail.com

† These authors share first authorship

Received: *03 October 2020*
Accepted: *13 November 2020*
Published: *09 December 2020*

Citation:
Lu Q, Lin W, Zhang R, Chen R, Wei X, Li T, Du Z, Xie Z, Yu Z, Xie X and Liu H (2020) Validation and Diagnostic Performance of a CFD-Based Non-invasive Method for the Diagnosis of Aortic Coarctation. Front. Neuroinform. 14:613666. doi: 10.3389/fninf.2020.613666

Purpose: The clinical diagnosis of aorta coarctation (CoA) constitutes a challenge, which is usually tackled by applying the peak systolic pressure gradient (PSPG) method. Recent advances in computational fluid dynamics (CFD) have suggested that multi-detector computed tomography angiography (MDCTA)-based CFD can serve as a non-invasive PSPG measurement. The aim of this study was to validate a new CFD method that does not require any medical examination data other than MDCTA images for the diagnosis of CoA.

Materials and methods: Our study included 65 pediatric patients (38 with CoA, and 27 without CoA). All patients underwent cardiac catheterization to confirm if they were suffering from CoA or any other congenital heart disease (CHD). A series of boundary conditions were specified and the simulated results were combined to obtain a stenosis pressure-flow curve. Subsequently, we built a prediction model and evaluated its predictive performance by considering the AUC of the ROC by 5-fold cross-validation.

Results: The proposed MDCTA-based CFD method exhibited a good predictive performance in both the training and test sets (average AUC: 0.948 vs. 0.958; average accuracies: 0.881 vs. 0.877). It also had a higher predictive accuracy compared with the non-invasive criteria presented in the European Society of Cardiology (ESC) guidelines (average accuracies: 0.877 vs. 0.539).

Conclusion: The new non-invasive CFD-based method presented in this work is a promising approach for the accurate diagnosis of CoA, and will likely benefit clinical decision-making.

Keywords: hydrodynamics, multidetector computed tomography angiography, non-invasive assessment, aortic coarctation, congenital heart disease

INTRODUCTION

The coarctation of the aorta (CoA) is a common congenital condition encountered in 6 − 10% of live births with congenital heart diseases (CHD) (Reller et al., 2008). Although CoA can occur as a solitary lesion, it is often associated with premature death and substantial late morbidity, including hypertension, heart failure, and premature coronary artery diseases (Toro-Salazar et al., 2002). Therefore, accurate diagnoses of CoA are important. In addition to anatomic evaluations, CoA can be clinically diagnosed by hemodynamic evaluations through cardiac catheterization (presently considered the standard method for its diagnosis and relative clinical decision-making). The specific diagnostic criterion of CoA is the occurrence of a peak systolic pressure gradient (PSPG) ≥20 mmHg (Rosenthal, 2001; Nielsen et al., 2005; Vogt et al., 2005; Menon et al., 2012a). Multi-detector computed tomography angiography (MDCTA) cannot be used to directly determine the occurrence of a PSPG; however, MDCTA-based computational fluid dynamics (CFD) can be employed to acquire hemodynamic information (e.g., pressure gradient) from coronary and cerebral arteries (Castro et al., 2006; Knight et al., 2010; Taylor et al., 2013). Still, the simulated pressure gradient depends on the applied boundary conditions, which cannot be directly determined from MDCTA images. Obtaining accurate boundary conditions is a persistent challenge for the clinical application of CFD-based methods, and should be overcome in order to perform unbiased CFD simulations. One approach to solve this problem would be to derive the boundary conditions from additional tests [e.g., transthoracic echocardiography (TTE) and 4D flow magnetic resonance imaging (MRI)] (Liu et al., 2016a; Xu et al., 2018; Zhu et al., 2018). Since CoA is a common CHD among pediatric patients, however, the need for additional tests is particularly inconvenient. Another approach would be to estimate the boundary conditions from several physiological models. This is similar to what is done when calculating coronary computed tomography angiography-derived fractional flow reserves (FFR-CT): several physiological models are used to estimate the approximate maximal hyperemia condition and obtain the correspondent boundary conditions. These physiological models reflect average behaviors and ignore the significant differences typically observed between pediatric patients, further degrading the accuracy of the CFD simulation results and limiting their real-life applicability.

The pressure drop occurring in correspondence of a coarctation can be approximate determined by using a common fluid dynamic equation (Gould, 1978; Banerjee et al., 2007):

$$\Delta\overline{p} = f\overline{Q} + s\overline{Q}^2 \tag{1}$$

where $\Delta\overline{p}$ is the mean pressure drop, f the viscous friction, s the expansion loss, and $\overline{Q}$ the mean flow rate. Aortic coarctation increases the viscous friction and causes the expansion loss of the stenosis section, enhancing the pressure drop: possibly, the first two parameters can be used to assess the hemodynamic severity of aortic coarctation. The proposed method can be used to obtain those two parameters by setting a series of boundary conditions comprised within a normal physiological range, and then performing a CFD simulation. Since the values of f and s in Equation 1 are almost independent of the flow rate and pressure, the results of the proposed method will not be affected with same parameter as boundary conditions. Compared to the general CFD method, the one proposed here does not require any medical examination data other than MDCTA images; hence, it represents a promising approach to achieve a non-invasive diagnosis of CoA.

The overall objective of the present study was to evaluate and validate the diagnostic performance of a novel CFD model developed from MDCTA imaging data for the diagnosis of CoA.

METHODS AND METHODS

Ethic Approval

This retrospective study was approved by the local institutional review board following the ethical guidelines of the Declaration of Helsinki, and written informed consents were waived.

Study Population

This study included a total of 65 subjects: patients with CoA (n = 38, median age = 9 months, ages ranging between 1 month and 14 years; 50% male) and others suspected of having CHD, but without evidence of CoA (n = 27; median age = 18 months, ages ranging between 2 months and 10 years; 59% male). All patients included in this study: (1) underwent MDCTA between February 2012 and September 2019; (2) underwent cardiac catheterization with recording of the aortic isthmus' PSPG <2 weeks before the time of the MDCTA; (3) were not subjected to any surgery or intervention before MDCTA. Patients with lesions in the branches of the aorta, or for whom we obtained poor-quality images, were excluded. More details about the study cohorts are presented in **Table 1** and in the **Supplementary Material** of this paper (**Supplementary Figure 1**).

MDCTA and Cardiac Catheterization Protocol

MDCTA imaging was performed using an electrocardiographic-gated "step and shoot protocol" using a second-generation dual-source CT scanner (Somatom Definition Flash, Siemens Healthcare, Forchheim, Germany). A short-term sedation of the

TABLE 1 | Patients' information.

	Patients with CoA	Patients without CoA	*P*-value
Number	38	27	
Age			0.183
Median	9 months	18 months	
Range	1 months−14 years	2 months−10 years	
Gender			0.614
Male	19 (50%)	16 (59%)	
BSA	0.462	0.569	0.193

CoA, coarctation of the aorta; BSA, body surface area.

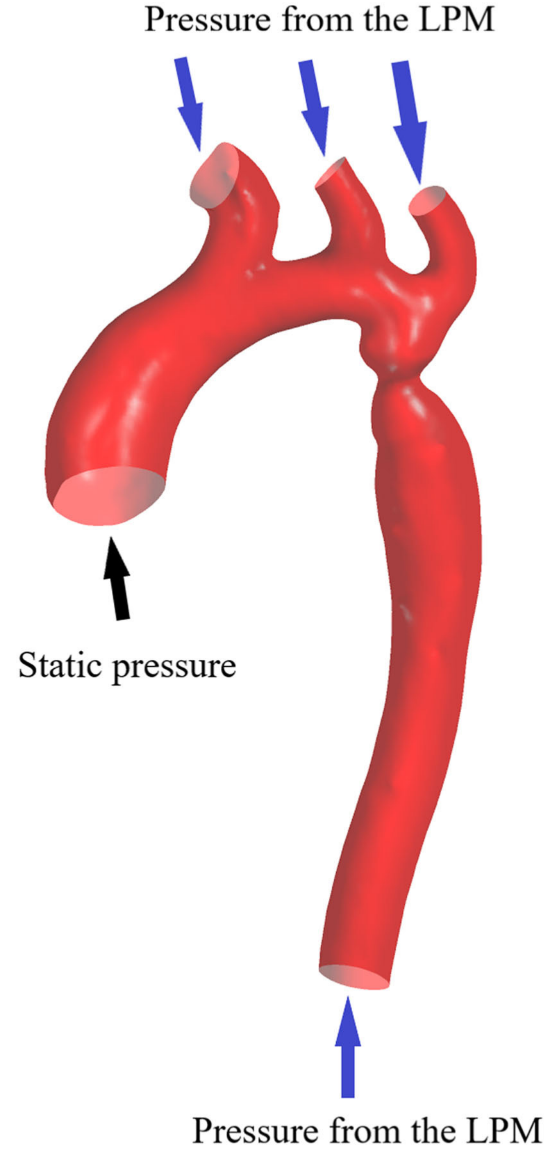

FIGURE 1 | Boundary conditions. Geometry of the aorta with one inlet and four outlet boundaries.

patients was achieved when necessary by administering them a 0.1 mg/ml oral chloral hydrate solution. Scans were performed in the cranio-caudal direction, from the thoracic inlet to the bottom of the heart. The MDCTA involved a gantry rotation time of 0.28 s, the use of a detector collimation (dimensions = 2 × 64 × 0.6 mm), and that of a CARE kV (with a weight-adapted grouping for the tube voltage and tube current). The acquisition window was grouped in the sequential mode at 35%–45% of the R-R interval. SAFIRE (Strength 3) was adopted as the iterative reconstruction algorithm, with I26 kernel, a slice thickness of 0.75 mm, and an increment of 0.5 mm. An iodinated contrast medium (Iopamidol, 300 mg I/ml, BRACCO, Italy) was injected intravenously (volume to body weight ratio of 1.5–2.0 ml/kg) for imaging, followed by 1.0 ml/kg body weight of a saline chaser injected at a rate of 1–2 ml/s. The acquisition delay was determined based on the time at which the contrast medium entered both ventricles.

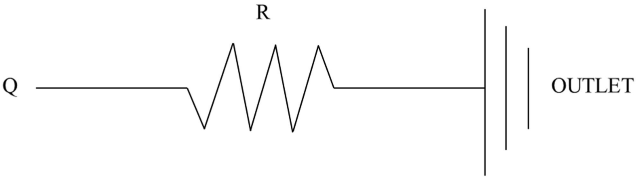

FIGURE 2 | Scheme of the LPM. Outlet boundary condition: a lumped parameter model with only one resistance is coupled to each outlet.

The cardiac catheterization was performed using a Philips Allura Xper FD10 system (Philips Medical System, Best, the Netherlands). The PSPG was measured across the coarctation using the standard procedure, which inserted the catheter probe into the aortic isthmus of the patients, and recorded the peak systolic blood pressure of ascending and descending aorta.

Boundary Conditions

The inflow and outflow boundaries are defined in **Figure 1**. The wall boundary was considered as a rigid vessel, and the flow domain was defined as a cavity of the reconstructed geometry. In the proposed method, a static pressure in the normal physiological range (80 mmHg) was mapped to the inlet of the CFD models. A lumped parameter model (LPM) with only one resistance was applied for each outlet, in order to confirm the outlet boundaries (**Figure 2**). A total resistance was allocated to each outlet according to their inverse diameters; then, the pressure value of each outlet was obtained by the LPM model (Murray, 1926; Taylor et al., 2013; Xie et al., 2018). The resistance was initially set to 9.6 mmHg·s /cm^3, and subsequently reduced to 1/2, 1/3, 1/4, 1/5, and 1/6: the steady flow was simulated six times under six different total resistances for each case.

Post-processing

The CFD simulation process is displayed in the **Supplementary Material** (method section, **Supplementary Figure 2**). The results of the CFD simulation were elaborated using CFD-Post 19.2 (ANSYS, Inc., Canonsburg, Pennsylvania, USA) and MATLAB (R2016a, the Math Works, Natick, MA). Only the stenosis sections with nearby branches are retained for further CFD analysis (as show in **Figure 1**), and the start and end of each lesion were defined by an experienced observer; then, the mean pressure in correspondence of the start and end sections and the mean flow rate across the coarctation were obtained from the simulation results. The pressure drop was defined as the pressure difference between the start and the end sections of the coarctation. After substituting the six steady flow simulation results into Equation 1, we obtained f and s through an iterative least squares estimation of the non-linear regression (George and Seber, 2003). Furthermore, the predictive parameters f and s obtained from the CFD simulation results were used to establish

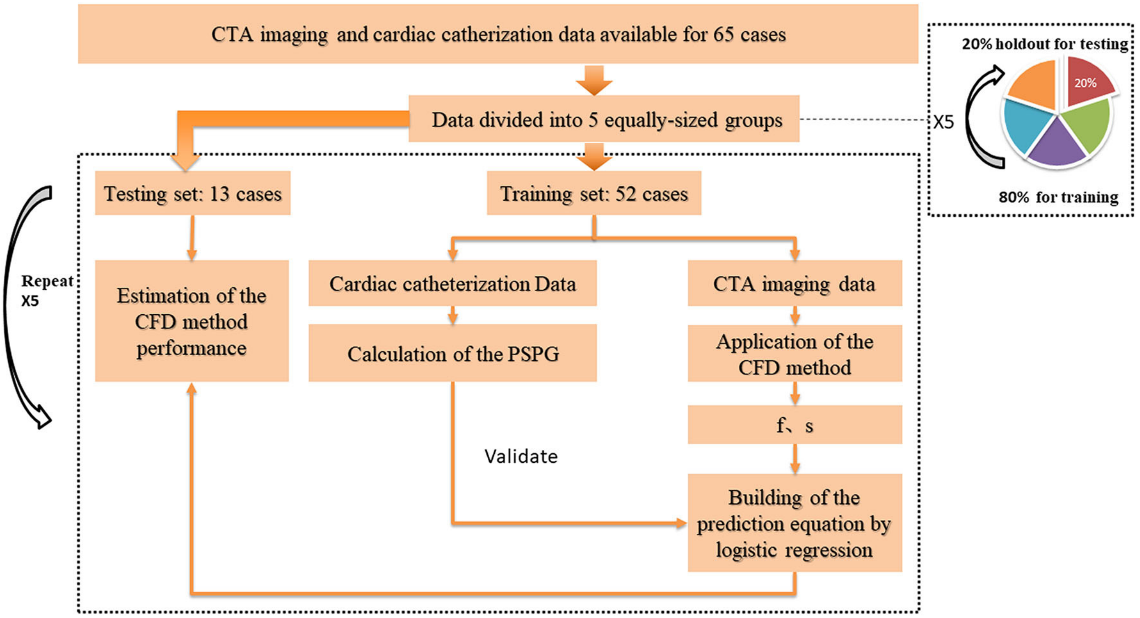

FIGURE 3 | Cross-validation pathway. Five equally-sized groups were stratified so to have approximately the same proportion of genders, ages, and patients with CoA. One of them (20% of the data) was holdout for testing, while the others (80% of the data) were used as the training set. To estimate the CFD performance, we applied a 5-fold cross-validation procedure on all groups: each time, the CFD simulation was performed on a different training set. The parameters f and s, obtained from the simulation results, were used to build a prediction equation by using logistic regression, before testing the prediction model on the unseen test set.

a combined diagnosis model by logistic regression.

$$P = \frac{1}{1 + e^{-(af+bs+c)}} \tag{2}$$

where P is the probability of the patients suffered CoA, f the viscous friction, s the expansion loss, and a, b, c are the coefficients obtained by logistic regression analysis using MedCalc Statistical Software version 19.0.7 (MedCalc Software bvba, Ostend, Belgium).The predictive performance of this model was evaluated on the AUC of the ROC curve by 5-fold cross-validation.

Cross-Validation

To investigate and validate the diagnostic performance of the proposed method for CoA diagnosis, we randomly divided the study population into five non-overlapping groups having the same size. These five groups were stratified so to have approximately the same proportion of genders, ages, and patients with CoA. The diagnostic performance was then assessed by stratified 5-fold cross-validation (**Figure 3**). Compared to the conventional sample division method, the main advantages of the new approach are that: (1) it decreases the variance of the prediction error, (2) it maximizes the utilization of data from both the training and test groups, and (3) it avoids the testing of hypotheses suggested by arbitrarily split data. Overall, the proposed approach allows an unbiased estimate of the CFD performance in the diagnosis of CoA, removing uncertainties linked to the random division of one training group and one test group (Molinaro et al., 2005; Betancur et al., 2007; Kanamori et al., 2007; Motwani et al., 2010).

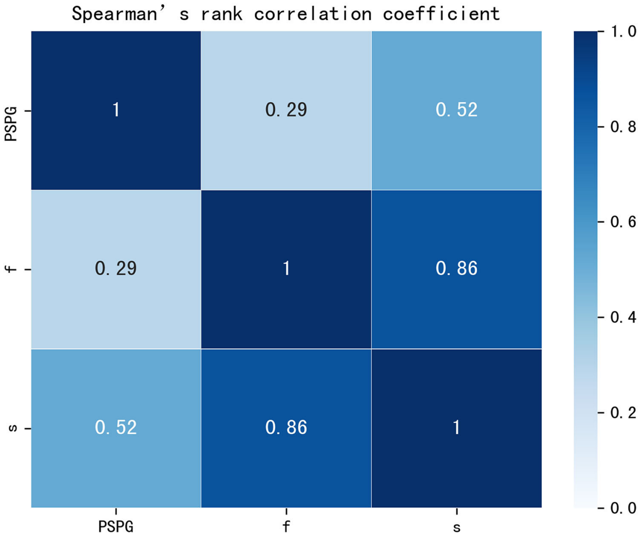

FIGURE 4 | Rank correlation matrix among PSPG, f, and s. PSPG, f, and s were all positively correlated ($p < 0.05$). Lighter shades of blue correspond to lower correlation coefficients that the darker shades. PSPG, peak systolic pressure gradient; f, viscous friction in Equation 1; s, expansion loss in Equation 1.

Statistical Analysis

The continuous variables were expressed in the form of mean ± standard deviation (M ± SD). Normality was tested by the Kolmogorov-Smirnov method, and the variance homogeneity through the Levene test. The patient gender was analyzed using

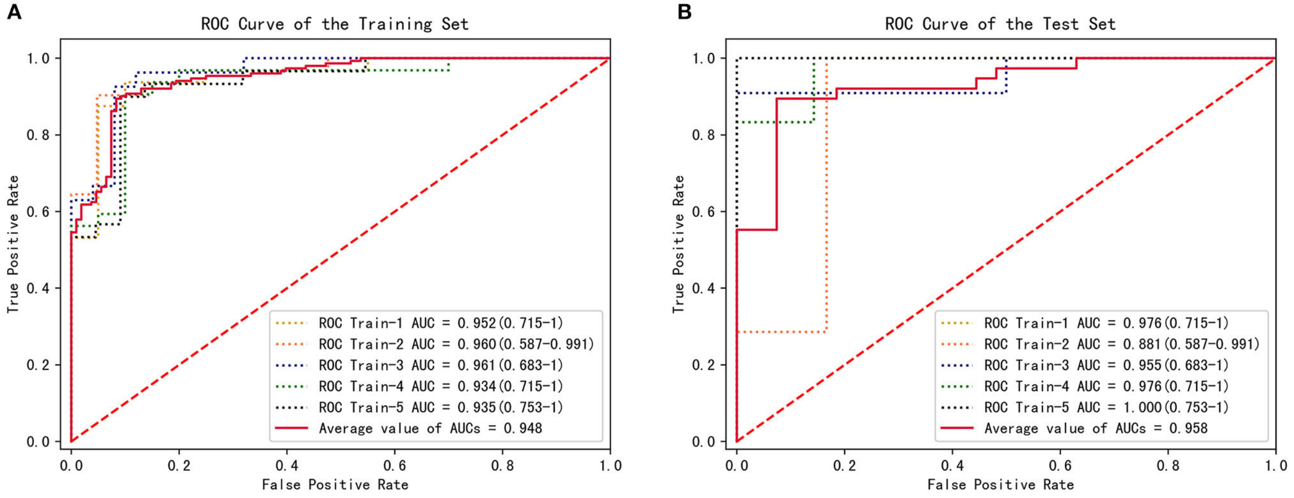

FIGURE 5 | CFD performance for the diagnosis of CoA. **(A)** ROC for CoA diagnosis in the training set. **(B)** ROC for CoA diagnosis in the test set.

the Chi-square test, while the age and body surface area (BSA) data were analyzed through an independent samples *t*-test. The accuracy of the aorta reconstruction was validated by comparing the anatomic information with the Bland-Altman method. The correlations among the PSPG and CFD simulation results were evaluated based on a Spearman's rank correlation analysis. The diagnosis performance of the CFD method in training sets and test sets was evaluated using a ROC analysis and pairwise comparisons of the AUC according to DeLong et al. (Er et al., 1988). The diagnostic reference standard of the CoA is PSPG > 20 mmHg; therefore, we considered a cut-off value of 20 mmHg.

The statistical analyses were performed using the MedCalc Statistical Software version 19.0.7 (MedCalc Software bvba, Ostend, Belgium). All the tests were two-sided, and the results were considered statistically significant for $p < 0.05$.

RESULTS

No statistically significant differences we observed in terms of gender, age, and BSA ($p = 0.183$, $p = 0.614$, and $p = 0.193$, respectively) between patients with CoA and without CoA. Excellent agreement was observed between the diameters of the aorta measured through the CT workstation and those in the reconstructed models: the bias between the different datasets were of -0.024 ± 0.134 mm, -0.025 ± 0.141 mm, and -0.039 ± 0.129 mm, respectively (**Supplementary Figure 3**). A good correlation (rho = 0.861, $p < 0.001$) was noted between f and s, a moderate correlation (rho = 0.519, $p < 0.001$) was noted between PSPG and s, and a relatively low correlation (rho = 0.292, $p < 0.005$) was noted between PSPG and f (**Figure 4**).

Performance of the CFD Method With Respect to the Training Set

The parameters f and s in Equation 1 were obtained from the CFD simulation results; then, combined diagnosis models were established by logistic regression. The CoA diagnosis performances of these combined diagnosis models are shown in **Figure 5A**: all the training sets exhibited high AUCs (95.2, 96.0, 96.1, 93.4, 93.5%, respectively). The sensitivities, specificities, accuracy, and other details about these measurements are presented in **Table 2**. The sensitivities and specificities of the training sets exhibited high values (average values of 84.7 and 92.6%, respectively). The combined diagnosis models highlighted how 5, 4, 7, 7, and 8 out of 52 patients (in the case of 4, 3, 5, 5, and 6 false-negative patients, respectively) were misclassified in the five training sets. The average percentage of correctly classified patients was 88.1%.

Performance of the CFD Method With Respect to the Test Sets

To estimate the performance of the CFD method, 5-fold cross-validation procedure was conducted on the five groups of data previously established. One combined diagnosis model was established for each training set, and then tested on the unseen test set. The performance of the combined diagnosis models with respect to the test sets is shown in **Figure 5B**. The five combined diagnosis models exhibited high AUCs (89.6, 91.7, 79.2, 97.9, 88.9%, respectively). The corresponding prediction models suggest that 12, 10, 10, 12, and 13 out of 13 patients were diagnosed correctly for each test set, respectively. Notably, 2, 3, and 1 patient(s) with CoA were misclassified (i.e., false negative) in the second, third, and fourth test sets, while no false negative cases were noted in first and fifth test sets. The performance of f and s in test sets are presented in **Table 3**.

Comparison With the ESC Guidelines Criteria

The European Society of Cardiology (ESC) guidelines indicate some non-invasive criteria for the determination of CoA. In particular, the Class II ESC recommends interventions

TABLE 2 | Diagnostic capacity of the CFD method in the training and testing sets.

	AUC (95% CI)	Specificities	Sensitivities	Accuracy
Training set (*n* = 52)				
Train-1	0.952 (0.853–0.992)	0.95	0.875	0.904
Train-2	0.960 (0.866–0.995)	0.952	0.903	0.923
Train-3	0.961 (0.868–0.995)	0.92	0.815	0.865
Train-4	0.934 (0.830–0.984)	0.9	0.844	0.865
Train-5	0.935 (0.830–0.985)	0.909	0.8	0.846
Average value	0.948	0.926	0.847	0.881
Testing set (*n* = 13)				
Test-1	0.976 (0.715–1)	0.857	1	0.923
Test-2	0.881 (0.587–0.991)	0.833	0.714	0.769
Test-3	0.955 (0.683–1)	1	0.727	0.769
Test-4	0.976 (0.715–1)	1	0.833	0.923
Test-5	1 (0.753–1)	1	1	1
Average value	0.958	0.938	0.855	0.877

The whole population was randomly divided into 5 equally-sized groups; then, the performance of the CFD method was assessed by a stratified 5-fold cross-validation.
AUC, area under the curve; CI, confidence interval; accuracy, % of cases correctly classified.

TABLE 3 | Diagnostic capacity of the f and s in the testing sets.

		AUC (95% CI)	Specificities	Sensitivities	Accuracy
Test-1	f	0.786 (0.479–0.957)	0.857	0.833	0.846
	s	0.881(0.587–0.991)	0.857	0.833	0.846
Test−2	f	0.714 (0.407–0.921)	0.833	0.571	0.692
	s	0.810(0.505–0.967)	0.833	0.714	0.769
Test-3	f	0.545 (0.257–0.813)	0.500	0.909	0.846
	s	0.773(0.465–0.951)	1	0.636	0.692
Test-4	f	0.571 (0.278–0.831)	0.429	0.833	0.615
	s	0.833(0.531–0.976)	0.857	0.833	0.846
Test-5	f	0.900 (0.610–0.995)	1	0.750	0.846
	s	1(0.753-1)	1	1	1
Average value	f	0.703	0.724	0.779	0.769
	s	0.859	0.909	0.803	0.831

AUC, area under the curve; CI, confidence interval; accuracy, % of cases correctly classified; f, viscous friction in Equation 1; s, expansion loss in Equation 1.

on patients with a $\geq$50% aortic narrowing relative to the aortic diameter at the diaphragm level (observed by CMR, CT, or invasive angiography) (Kanamori et al., 2007). The narrowing rate (from the Class II ESC) and the results of the CFD method were compared to determine the occurrence of CoA (**Figure 6**). The narrowing rate is able to diagnose CoA with an average sensitivity of 0.213, an average specificity of one, and an average accuracy of 0.539 for the five test sets. Although the narrowing rate criteria exhibited excellent specificities in our test sets, the correspondent sensitivities were poor (average = 0.213). Remarkably, all patients with CoA in the second and fourth test sets were misclassified (false-negative) by applying the Class II ESC recommendation criteria.

DISCUSSION

CoA is associated with premature death and substantial late morbidity, including hypertension, heart failure, and premature coronary artery disease (Toro-Salazar et al., 2002). Therefore, accurate diagnoses of CoA are important. The observations conducted during the present study are relevant to the management of patients with suspected CoA. The viscous friction and the expansion loss of the aorta can be effectively used to classify pediatric patients with CoA, since they reflect the flow resistances causes by a given stenosis. Notably, these two parameters can be obtained by combined CFD simulations. The main advantages of the proposed method are that: 1) it allows a non-invasive diagnosis of CoA, 2) does not require extra medical examination data to establish boundary conditions, 3) is able to fully describe the pressure-flow relationship in a stenosis within a normal physiological range.

Current guidelines indicate that cardiac catheterization should be used to address specific anatomical and physiological questions, or before intervention. The reference standard for the diagnosis of CoA is a PSPG > 20 mmHg (Baumgartner et al., 2010). However, the standard procedure is invasive and costly; therefore, its clinical application should be limited to patients whose diagnosis is difficult or who need to be evaluated for subsequent intervention. TTE and 4D flow MRI can be applied to obtain the blood flow velocity; afterwards, the PSPG across the coarctation can be obtained by combining them in a simplified pressure estimation formula, which may result in an overestimation of the PSPG (Sakthi, 2010). Another approach is to apply the velocity values as boundary conditions, and then utilize the CFD method to acquire the PSPG across the coarctation. This method, however, needs additional tests (e.g., TTE or 4D flow MRI) and the process is complex: additional, non-contrast enhanced MRI, including 4D flow MRI, can be technically challenging, easily influenced by environmental noise and also limited by a relatively lower temporal resolution (Cibis et al., 2014; Khodarahmi, 2015). Meanwhile, the proposed method provides additional hemodynamic information and only requires the collection of MDCTA images.

The calculation of the hemodynamic parameters using CFD models developed from MDCTA imaging data is an attractive concept and potentially obviates the need for invasive angiography in pediatric patients suspected to have CoA (LaDisa et al., 2011). The present study focused on evaluating the diagnostic performance of a new MDCTA-based CFD model for the diagnosis of CoA. The results revealed that, in both the training and test sets, patients showed high AUCs and only a small number of them were misclassified. This indicates that the MDCTA-based CFD model has a high level of diagnostic efficiency. The misclassification of some patients in both the training and test sets could have derived from the use of actual simulation conditions in the present study. To reduce the computing time, we simulated a steady flow state and defined the pressure-flow relationship of a stenosis. A real pulsating blood flow, however, is inconsistent with the steady state flow assumption. To implement the pressure at the outlet boundary, previous studies have applied a lumped parameter

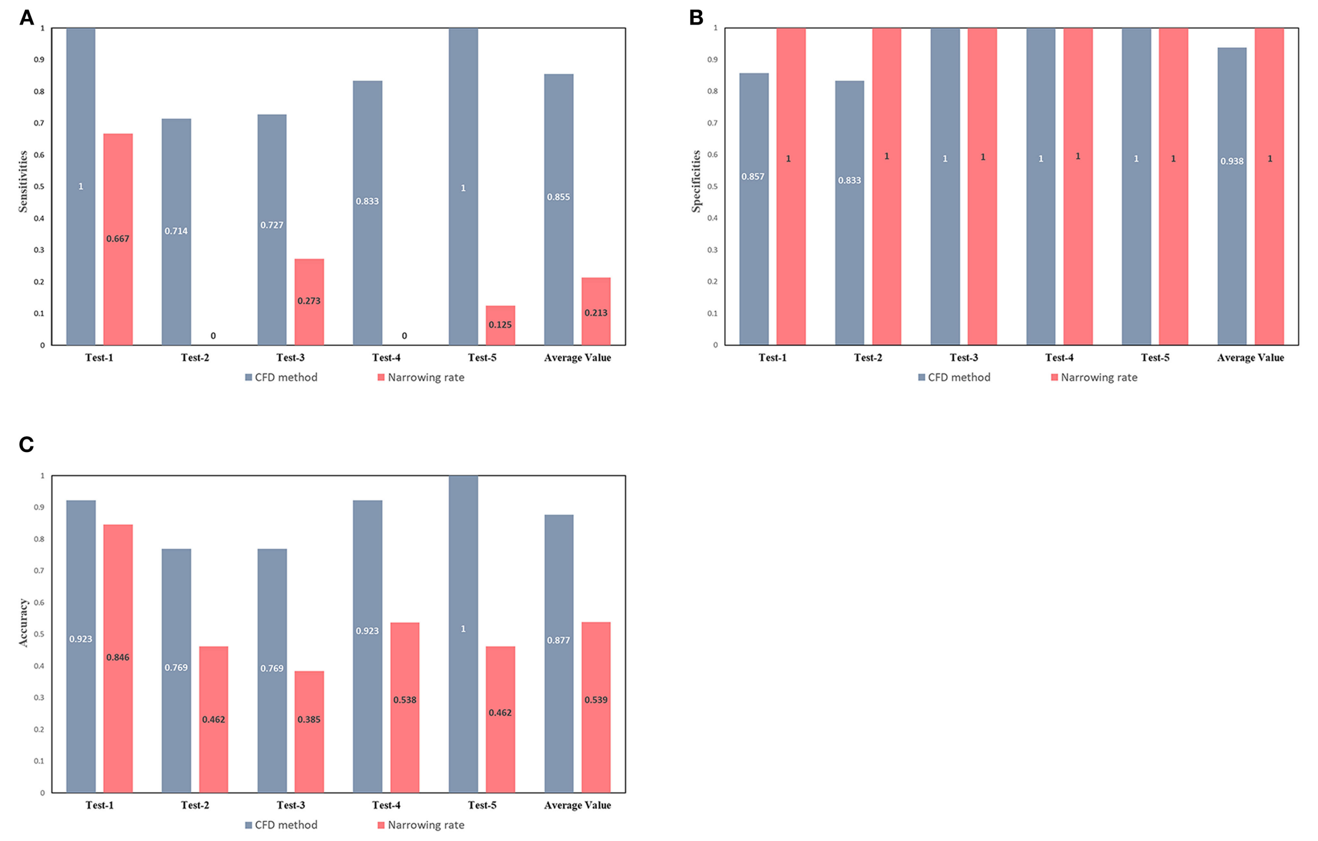

FIGURE 6 | Comparison between the diagnostic capacity of the CFD method and of the ESC guidelines criteria. Sensitivities **(A)**, specificities **(B)**, and accuracies **(C)** of CoA diagnoses conducted by the CFD (gray-blue bars) and the narrowing rate (pink bars) methods. The latter method was applied according to current guidelines.

model (Menon et al., 2012b; Liu et al., 2016b); still, the modeling of the aorta hemodynamics based on such model is inconsistent with real conditions (Kim et al., 2009, 2010), resulting in further biases during the CFD simulation.

A set of non-invasive criteria for the identification of patients with significant CoA and requiring intervention have been provided in the ESC Guidelines. **Figure 6** shows how those non-invasive criteria performed poorly in our dataset and in that of another study (Astengo et al., 2017). Thus, relying on ESC recommendations for the identification of CoA patients might lead to under-diagnosis and the conservative treatment of many patients actually needing intervention. In fact, the narrowing rate criteria rely on simple morphological measurements, not taking into account any hemodynamical information (which may play a greater role in the development of a significant pressure gradient across the CoA). The proposed MDCTA-based CFD method can provide additional hemodynamic information and compared to the narrowing rate criteria, it shows an overall better diagnosis performance.

The present study has several limitations. First, we considered a relatively small sample size: we suggest to increase that in further studies. Moreover, the boundary conditions used for the CFD simulation were derived from the LPM model, which is inconsistent with real conditions. Still, the correspondent validation results suggest that the simulation error was negligible compared to that observed in another study (Kilner et al., 1993; Dwyer et al., 2009).

The results of the present study show that the proposed CFD model developed from MDCTA imaging data represents an accurate non-invasive method for the diagnosis of CoA, and which can be beneficial for clinical decision-making.

DATA AVAILABILITY STATEMENT

The data analyzed in this study is subject to the following licenses/restrictions: The authors do not have permission to share data. Requests to access these datasets should be directed to Qiyang Lu, 915081903@qq.com.

ETHICS STATEMENT

The study was approved by the Clinical Ethics Committee of Guangdong Provincial People's Hospital. Written informed consent from the participants' legal guardian/next of kin was not required to participate in this study in accordance with the national legislation and the institutional requirements.

AUTHOR CONTRIBUTIONS

QL and WL drafted the manuscript and analyze the data. RZ provided the post-processing tools. RC, XW, TL, and ZY revised the manuscript. ZD provided the statistical analysis method. ZX provided the cardiac catheterization data. HL and XX provided the conception and design of the study. All authors contributed to the article and approved the submitted version.

FUNDING

This study was funded by the National Natural Science Foundation of China (Grant Nos. 61601368 & 81974262), the Key R&D Program of Guangdong Province, China (2018B030339001), Guangzhou City Science and Technology Planning Project of China (201707010306), and Guangdong provincial people's Hospital Project Grant (2016dzx01).

SUPPLEMENTARY MATERIAL

The Supplementary Material for this article can be found online at: https://www.frontiersin.org/articles/10.3389/fninf.2020.613666/full#supplementary-material

REFERENCES

Astengo, M., Berntsson, C., Johnsson, Å. A., Eriksson, P., and Dellborg, M. (2017). Ability of noninvasive criteria to predict hemodynamically significant aortic obstruction in adults with coarctation of the aorta[J]. *Cong. Heart Dis.* 12, 174–180. doi: 10.1111/chd.12424

Banerjee, R. K., Roy, A. S., Back, L. H., Back, M. R., Khoury, S. F., and Millard, R. W. (2007). Characterizing momentum change and viscous loss of a hemodynamic endpoint in assessment of coronary lesions. *J. Biomech.* 40, 652–662. doi: 10.1016/j.jbiomech.2006.01.014

Baumgartner, H., Bonhoeffer, P., De Groot, N. M., Haan, F., and Lionis, C. (2010). ESC Guidelines for the management of grown-up congenital heart disease (new version 2010). *Europ. Heart J.* 31, 2915–2957. doi: 10.1093/eurheartj/ehq249

Betancur, J., Otaki, Y., Motwani, M., Fish, M. B., Lemley, M., Dey, D., et al. (2007). Prognostic value of combined clinical and myocardial perfusion imaging data using machine learning[J]. *JACC* 2017:2406. doi: 10.1016/j.jcmg.2017.07.024

Castro, M. A., Putman, C. M., and Cebral, J. R. (2006). Computational fluid dynamics modeling of intracranial aneurysms: effects of parent artery segmentation on intra-aneurysmal hemodynamics. *AJNR Am. J. Neuroradiol.* 27, 1703–1709. doi: 10.1055/s-2006-932585

Cibis, M., Potters, W. V., Gijsen, F. J., Marquering, H., VanBavel, E., van der Steen, A. F., et al. (2014). Wall shear stress calculations based on 3D cine phase contrast MRI and computational fluid dynamics: a comparison study in healthy carotid arteries. *NMR Biomed*. 27, 826–834. doi: 10.1002/nbm.3126

Dwyer, H. A., Matthews, P. B., Azadani, A., Jaussaud, N., Ge, L., Guy, T. S., et al. (2009). Computational fluid dynamics simulation of transcatheter aortic valve degeneration[J]. *Interact. Cardiovasc. Thor. Surg.* 9, 301–308. doi: 10.1510/icvts.2008.200006

Er, D., DeLong, D. M., and Clarke-Pearson, D. L. (1988). Comparing the areas under two or more correlated receiver operating characteristic curves: a nonparametric approach[J]. *Biometrics*. 44, 837–845. doi: 10.2307/2531595

George, A. F., and Seber, C. J. W. (2003). *Nonlinear Regression*. Hoboken, NJ: Wiley-Interscience.

Gould, K. L. (1978). Pressure-flow characteristics of coronary stenoses in unsedated dogs at rest and during coronary vasodilation[J]. *Circul. Res.* 43, 242–253. doi: 10.1161/01.RES.43.2.242

Kanamori, T., Takenouchi, T., Eguchi, S., and Murata, N. (2007). Robust loss functions for boosting[J]. *Neural Comp.* 19, 2183–2244. doi: 10.1162/neco.2007.19.8.2183

Khodarahmi, I. (2015). Comparing velocity and fluid shear stress in a stenotic phantom with steady flow: phase-contrast MRI, particle image velocimetry and computational fluid dynamics. *MAGMA*. 28, 385–393. doi: 10.1007/s10334-014-0476-x

Kilner, P. J., Yang, G. Z., Mohiaddin, R. H., Firmin, D. N., and Longmore, D. B. (1993). Helical and retrograde secondary flow patterns in the aortic arch studied by three-directional magnetic resonance velocity mapping[J]. *Circulation*. 88, 2235–2247. doi: 10.1161/01.CIR.88.5.2235

Kim, H. J., Vignon-Clementel, I. E., Coogan, J. S., Figueroa, C. A., Jansen, K. E., and Taylor, C. A. (2010). Patient-specific modeling of blood flow and pressure in human coronary arteries[J]. *Ann Biomed. Eng.* 38, 3195–3209. doi: 10.1007/s10439-010-0083-6

Kim, H. J., Vignon-Clementel, I. E., Figueroa, C. A., LaDisa, J. F., Jansen, K. E., Feinstein, J. A., et al. (2009). On coupling a lumped parameter heart model and a three-dimensional finite element aorta model[J]. *Ann. Biomed. Eng.* 37, 2153–2169. doi: 10.1007/s10439-009-9760-8

Knight, J., Baumüller, S., Kurtcuoglu, V., Turina, M., Turina, J., Schurr, U., et al. (2010). Long-term follow-up, computed tomography, and computational fluid dynamics of the Cabrol procedure. *J. Thor. Cardiovasc. Surg*. 139, 1602–1608. doi: 10.1016/j.jtcvs.2009.09.023

LaDisa, J. F., Alberto Figueroa, C., Vignon-Clementel, I. E., Jin Kim, H., Xiao, N., Ellwein, L. M., et al. (2011). Computational simulations for aortic coarctation: representative results from a sampling of patients. *J. Biomech. Eng*. 133:091008. doi: 10.1115/1.4004996

Liu, X., Gao, Z., Xiong, H., Ghista, D., Ren, L., Zhang, H., et al. (2016a). Three-dimensional hemodynamics analysis of the circle of Willis in the patient-specific nonintegral arterial structures[J]. *Biomech. Model. Mechanobiol.* 15, 1439–1456. doi: 10.1007/s10237-016-0773-6

Liu, X., Zhang, H., Ren, L., Xiong, H., Gao, Z., Xu, P., et al. (2016b). Functional assessment of the stenotic carotid artery by CFD-based pressure gradient evaluation. *Am. J. Physiol. Heart Circul. Physiol.* 311:H645–H653. doi: 10.1152/ajpheart.00888.2015

Menon, A., Eddinger, T. J., Wang, H., Wendell, D. C., Toth, J. M., and LaDisa, J. F. Jr. (2012a). Altered hemodynamics, endothelial function, and protein expression occur with aortic coarctation and persist after repair. *Am. J. Physiol. Heart Circul. Physiol.* 303:H1304–H1318. doi: 10.1152/ajpheart.00420.2012

Menon, A., Wendell, D. C., Wang, H., Eddinger, T. J., Toth, J. M., Dholakia, R. J., et al. (2012b). A coupled experimental and computational approach to quantify deleterious hemodynamics, vascular alterations, and mechanisms of long-term morbidity in response to aortic coarctation. *J. Pharmacol. Toxicol. Methods*. 65, 18–28. doi: 10.1016/j.vascn.2011.10.003

Molinaro, A. M., Simon, R., and Pfeiffer, R. M. (2005). Prediction error estimation: a comparison of resampling methods[J]. *Bioinformatics*. 21, 3301–3307. doi: 10.1093/bioinformatics/bti499

Motwani, M., Dey, D., Berman, D. S., Germano, G., Achenbach, S., Al-Mallah, M. H., et al. (2010). Machine learning for prediction of all-cause mortality in patients with suspected coronary artery disease: a 5-year multicentre prospective registry analysis. *Europ. Heart J*. 31, 2915–2957. doi: 10.1093/eurheartj/ehw188

Murray, C. D. (1926). The physiological principle of minimum work: I. The vascular system and the cost of blood volume[J]. *Proc. Natl. Acad. Sci. U.S.A.* 12:207. doi: 10.1073/pnas.12.3.207

Nielsen, J. C., Powell, A. J., Gauvreau, K., Marcus, E. N., Prakash, A., and Geva, T. (2005). Magnetic resonance imaging predictors of coarctation severity. *Circulation* 111, 622–628. doi: 10.1161/01.CIR.0000154549.53684.64

Reller, M. D., Strickland, M. J., Riehle-Colarusso, T., Mahle, W. T., and Correa, A. (2008). Prevalence of congenital heart defects in metropolitan Atlanta, 1998-2005. *J. Pediatr*. 153, 807–813. doi: 10.1016/j.jpeds.2008.05.059

Rosenthal, E. (2001). Stent implantation for aortic coarctation: the treatment of choice in adults? *J. Am. Coll. Cardiol.* 38, 1524–1527. doi: 10.1016/S0735-1097(01)01573-X

Sakthi, C., Yee, H., and Kotlewski, A. (2010). Overestimation of aortic valve gradient measured by Doppler echocardiography in patients with aortic stenosis[J]. *Catheteri. Cardiovasc. Interv*. 65, 176–179. doi: 10.1002/ccd.20324

Taylor, C. A., Fonte, T. A., and Min, J. K. (2013). Computational fluid dynamics applied to cardiac computed tomography for noninvasive quantification of fractional flow reserve: scientific basis. *J. Am. Coll. Cardiol.* 61, 2233–2241. doi: 10.1016/j.jacc.2012.11.083

Toro-Salazar, O. H., Steinberger, J., Thomas, W., Rocchini, A. P., Carpenter, B., and Moller, J. H. (2002). Long-term follow-up of patients after coarctation of the aorta repair. *Am. J. Cardiol.* 89, 541–547. doi: 10.1016/S0002-9149(01)02293-7

Vogt, M., Kühn, A., Baumgartner, D., Baumgartner, C., Busch, R., and Kostolny, M., et al. (2005). Impaired elastic properties of the ascending aorta in newborns before and early after successful coarctation repair: proof of a systemic vascular disease of the prestenotic arteries? *Circulation* 111, 3269–3273. doi: 10.1161/CIRCULATIONAHA.104.529792

Xie, X., Zheng, M., Wen, D., Li, Y., and Xie, S. (2018). A new CFD based non-invasive method for functional diagnosis of coronary stenosis. *Biomed. Eng. Online*. 17:36. doi: 10.1186/s12938-018-0468-6

Xu, P., Liu, X., Zhang, H., Ghista, D., Zhang, D., and Shi, C. (2018). Assessment of boundary conditions for CFD simulation in human carotid artery. *Biomech. Model. Mechanobiol.* 17, 1581–1597. doi: 10.1007/s10237-018-1045-4

Zhu, Y., Chen, R., Juan, Y. H., Li, H., Wang, J., Yu, Z., et al. (2018). Clinical validation and assessment of aortic hemodynamics using computational fluid dynamics simulations from computed tomography angiography. *Biomed. Eng. Online*. 17:53. doi: 10.1186/s12938-018-0485-5

Conflict of Interest: The authors declare that the research was conducted in the absence of any commercial or financial relationships that could be construed as a potential conflict of interest.

The reviewer QT declared a past co-authorship with the authors (XX, RZ, HL) to the handling editor.

frontiers in Neuroinformatics

ORIGINAL RESEARCH
published: 24 June 2021
doi: 10.3389/fninf.2021.635657

DarkASDNet: Classification of ASD on Functional MRI Using Deep Neural Network

Md Shale Ahammed[1], *Sijie Niu*[1*], *Md Rishad Ahmed*[2], *Jiwen Dong*[1], *Xizhan Gao*[1] *and Yuehui Chen*[1]

[1] *Shandong Provincial Key Laboratory of Network Based Intelligent Computing, University of Jinan, Jinan, China,* [2] *École de Technologie Supérieure (ÉTS), Montreal, QC, Canada*

Non-invasive whole-brain scans aid the diagnosis of neuropsychiatric disorder diseases such as autism, dementia, and brain cancer. The assessable analysis for autism spectrum disorders (ASD) is rationally challenging due to the limitations of publicly available datasets. For diagnostic or prognostic tools, functional Magnetic Resonance Imaging (fMRI) exposed affirmation to the biomarkers in neuroimaging research because of fMRI pickup inherent connectivity between the brain and regions. There are profound studies in ASD with introducing machine learning or deep learning methods that have manifested advanced steps for ASD predictions based on fMRI data. However, utmost antecedent models have an inadequacy in their capacity to manipulate performance metrics such as accuracy, precision, recall, and F1-score. To overcome these problems, we proposed an avant-garde DarkASDNet, which has the competence to extract features from a lower level to a higher level and bring out promising results. In this work, we considered 3D fMRI data to predict binary classification between ASD and typical control (TC). Firstly, we pre-processed the 3D fMRI data by adopting proper slice time correction and normalization. Then, we introduced a novel DarkASDNet which surpassed the benchmark accuracy for the classification of ASD. Our model's outcomes unveil that our proposed method established state-of-the-art accuracy of 94.70% to classify ASD vs. TC in ABIDE-I, NYU dataset. Finally, we contemplated our model by performing evaluation metrics including precision, recall, F1-score, ROC curve, and AUC score, and legitimize by distinguishing with recent literature descriptions to vindicate our outcomes. The proposed DarkASDNet architecture provides a novel benchmark approach for ASD classification using fMRI processed data.

Keywords: autism spectrum disorder, fMRI, neuroimaging, image processing, deep learning, DarkASDNet, ABIDE

Edited by:
Heye Zhang,
Sun Yat-sen University, China

Reviewed by:
Xiaobo Shen,
Nanjing University of Science and Technology, China
Chengjin Yu,
Zhejiang University, China

Correspondence:
Sijie Niu
sjniu@hotmail.com

Received: *30 November 2020*
Accepted: *26 April 2021*
Published: *24 June 2021*

Citation:
Ahammed MS, Niu S, Ahmed MR, Dong J, Gao X and Chen Y (2021) DarkASDNet: Classification of ASD on Functional MRI Using Deep Neural Network. Front. Neuroinform. 15:635657. doi: 10.3389/fninf.2021.635657

1. INTRODUCTION

Autism spectrum disorder (ASD) is also familiar as a "spectrum" disorder that can cause different abnormalities such as social deficits, repetitive behaviors, speech, and nonverbal communication (Baio et al., 2018; Noriega, 2019). The fact-finding for the frequency of ASD is estimated at about 1% or higher (1 subject in 54, **Figure 1**) by the Center for Disease Control and Prevention in the United States (Senn, 2020). Previous treatments are based on the behavior observations of the patients, and the doctor asks a lot of psychological questions to the patient or their parents or guardians

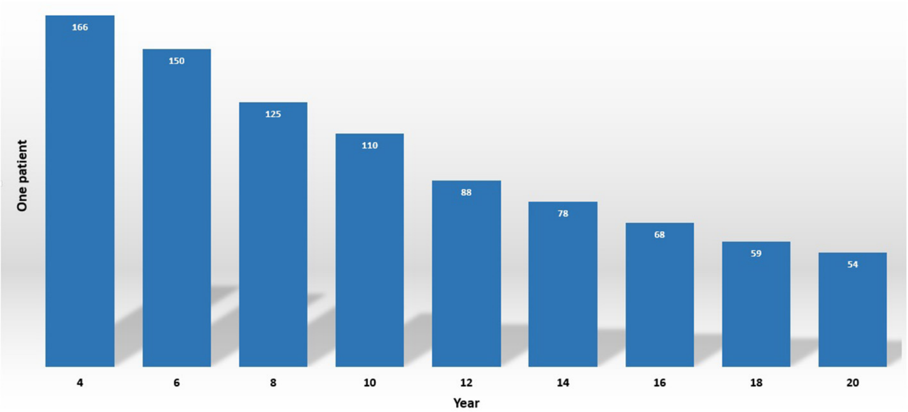

FIGURE 1 | Estimated ASD prevalence of 2020 by CDC.

(Höfer et al., 2017; Hyman et al., 2020). These questionnaires often produce a false positive rate. The principal goal of neuroscience research is to sort out brain disorder treatment in an effective way (Yahata et al., 2016; Ahmed et al., 2018). Nevertheless, when patients seek a doctor for their treatment, sometimes the diagnosis of ASD is burdensome due to a lack of proper symptoms and the process requiring too much time (Mandell et al., 2007; Nylander et al., 2013). In consequence, it is indispensable to come up with conscientious techniques that can easily get make the diagnosis ASD more meticulous and efficient in an assessable way beyond depending utterly on behavioral questions.

The increasing investigation of neuroimaging research using up-to-date technologies in the last few years led to the classification of ASD, resulting in more effective performance in treatment (Bi et al., 2018). With the help of fMRIs, we can inspect the abnormalities between ASD vs. TC by analyzing functional connectivity (Kaiser et al., 2010; Lee et al., 2018). After introducing machine learning (ML) in neuroimaging, it becomes a legitimate means to obtain information from the raw data to illustrate the pattern of the disease (Klöppel et al., 2012). Amongst the ML approaches, in the area of neuroimaging research, support vector machines (SVM) is a powerful classifier to classify the problems (Sundermann et al., 2014; Chen et al., 2016).

Region of interest (ROI) bestows the structural medium, quantifying connectivities within the individual brain's active functional patterns. Many researchers investigate ASD individuals based on data-driven strategies or brain parcelation, such as independent component analysis (ICA), clustering, and dictionary learning by adopting ROI techniques (Cociu et al., 2018; Bi et al., 2019). Although the ROI strategy has some limitations regarding the arbitrary decision and standardization, considering the special regions can be biased for the subjects (Thirion et al., 2014). To overcome these challenges, support vector machines (SVM) have been extensively utilized to manipulate individual brain functional connectivity variation and classify ASD (Yao et al., 2016; Wang et al., 2019). Recently, DL (Deep Learning) approaches have been successfully deployed in neuroimaging research to identify ASD disorder (Li et al., 2018b). Although most of the DL methods used functional connectivity, time-series data analysis, ROI analysis, and spatial or temporal information of fMRI data (Iidaka, 2015; Zhao et al., 2018a), some have issues such as clinical application, lack of model comprehensibility.

As we observed from the recent findings, there are still some drawbacks to overcome in ASD classification using deep learning knowledge, such as lack of data mining techniques from the heterogeneous, complex fMRI data and model interpretation to classify ASD. Besides, a large group of scientists adopted ROIs, or functional connectivity (FC) features to classify ASD. As ASD is heterogeneous, a more pertinent approach is required to classify ASD patients from a typical control. In this paper, we consider a novel DL algorithm for ASD classification to overcome these challenges. The pivotal contributions in this experiment are as follows:

- We preprocessed 3D fMRI data according to the model input requirement through slice-time correction and min-max normalization. We preferred min-max scaling so that data variables can contribute equally and overcome the model biases during training of the classification model.
- We improved the original DarkNet and proposed a novel framework named DarkASDNet for ASD classification. Our proposed framework's main advantage is that it has a fast operating speed and is easily interpretable to weigh against other state-of-the-art methods.
- Finally, to evaluate DarkASDNet performances using the preprocessed fMRI data, we contemplated metrics functioning such as recall, precision, F1-score, and accuracy with ROC curve and AUC score and legitimized our outcomes by distinguishing with recent literature descriptions.

The designed DarkASDNet framework with fMRI processing steps provides a novel benchmark approach for ASD classification on the Autism Brain Imaging Data Exchange (ABIDE) dataset.

2. RELATED WORK

The coalescence of brain imaging and machine learning approach concession of ASD classification can alleviate the critical affliction and give precautions to the patient's day-by-day prosperity. Research for brain networks using functional connectivity is a robust method for understanding the neurological bases of various brain disorders, for example, autism (Pascual-Belda et al., 2018). Abraham et al. used a support vector classifier (SVC) in 871 resting-state fMRI data to classify ASD vs. TC and got an accuracy of about 67% (Abraham et al., 2017). According to work in Jin et al. (2015), they proposed the SVM to classify ASD and got the highest accuracy of 76% during testing results with the original multi-kernel.

In Parikh et al. (2019), k-fold cross-validation was promulgated to measure classification performance using specificity, sensitivity, accuracy, and area under the curve (AUC). In Yu et al. (2020), a reverse mapping system was anticipated to further learn reverse mapping to assist mining and representation of task dependencies. Then, an adversarial assumption training approach combined a multi-tasking learning network with a reverse mapping network. Finally, an MRI of the two network parameters learned from the source was shared with target imaging CT (computed tomography). In Zhang et al. (2018), their method treated data at various points in time as different perspectives and built an overarching representation to collect complementary data from the entire time period. The potential representation investigates the complementarity between various time points in order to increase prediction accuracy. The problem is solved using the Alternate Direction Method of Multiplier (ADMM).

For the classification and identification of the regions of interest (ROIs) of functional connectivity magnetic resonance imaging (FC-MRI), Yang et al. (2019) deal with different ML algorithms, including SVM, ridge, and logistic regression where the highest accuracy of 71.98% obtained by ridge classifier. Multiple stacked auto-encoder (SAE) was considered by Guo et al. (2017) as a feature selection technique by ROIs from whole-brain FC. They obtained a classification accuracy of 86.36% utilizing only one data site named UM (University of Michigan) from ABIDE. However, ROIs for the time series data can illustrate and classify ASD from the whole brain. Usually, ROI figures out the functional connectivity pattern and activation of the brain (Eickhoff et al., 2015; Cociu et al., 2018). Dvornek et al. integrated rs-fMRI phenotypic data and obtained an accuracy of 70.1% by deploying LSTM (Long short-term memory) (Dvornek et al., 2018). Without the cross-validation and global signal regression system, they used CCS pipeline data.

In particular, maintaining the 3D and 2D data with the Convolutional Neural Network (CNN) from the DL methods, opens a new era for the classification and segmentation tasks (Parisot et al., 2017; Li et al., 2018a). In order to classify and distinguish ASD from healthy controls, Zhao et al. (2018b) assessed a satisfactory 3D CNN to unite the distinctiveness of functional and spatial brain networks. They integrated only two hundred rs-fMRI (ASD-100, HC-100) data. For the neuropathological biomarker, another way to recognize the brain's patterns is graph convolutional neural networks (G-CNN). Ktena et al. (2017) introduced the connectome-based classification model by applying CNN. Anirudh and Thiagarajan (2019) investigated ensemble learning and G-CNN to classify the problems and achieved 70.86% testing accuracy. Khosla et al. (2018) employed the connectivity fingerprint as a voxel input for the 3D convolutional neural network (CNN) with an accuracy of 73.3% and with ensemble CNN of 75.8%. Wutao et al. learned the features from the raw features by using an autoencoder (AE; Yin et al., 2020). Finally, they amalgamated the pretrained AE and DNN, which leads to an AUC of 82.4% and an accuracy of 79.2%. According to Ahmed et al. (2020), this was performed per site classification to see the data variability. The ABIDE-NYU dataset achieved the highest accuracy of 86 and 88% for stat map and glass brain images, using improved CNN architecture. On the other hand, in Kong et al. (2019), the authors extracted the ROI connectivity features for ASD classification using deep neural network (DNN). They used ABIDE-I, NYU dataset with 10-fold cross-validation. Using the softmax classifier and the stacked autoencoder (SAE) to get the most promising results for the ABIDE-NYU site of 90.39% accuracy according to our best knowledge.

The contemporary scientific knowledge for ASD classification is summarized in **Table 1**. According to **Table 1**, it is evident that most of the researcher goes through for classification purposes with functional connectivity (FC) or ROIs data for their work. We noticed there had been an inclination to use machine or deep learning approaches to solve classification problems. In the meantime, with the ABIDE dataset, a preponderance of works focused on a particular atlas, site, or pipeline image to overcome the classification problems. Medical image data are practically preferable to convalesce concrete contributions in the field of brain disorder research like ASD for treatment and reliability (Ravì et al., 2016; Phinyomark et al., 2017). To overcome these challenges, we preprocess every single slice from the whole brain images for each ABIDE-NYU dataset subject. We build DarkASDNet to extract features for the classification problems and check the stability of our model. We executed confusion metrics for precision, recall, F1-score, ROC curve, and AUC value.

3. MATERIALS AND METHODOLOGY

3.1. Dataset

In our experiments, we used ABIDE-I data processed through the Connectome Computation System (CCS) (Craddock et al., 2013). The raw 3D NIFTI fMRI data has been downloaded from ABIDE-I through the CCS pipeline, a publicly available dataset for ASD and TC. Among the 17 sites, we endeavor with the CCS-NYU (New York University Langone Medical Center) site. The publicly available CCS was preprocessed, including a register of the anatomical brain mask to functional image: FLIRT, slice time correction: 3dTshift, Skull-strip: AFNI's 3dAutomask, motion correction: 3dvolreg, voxel intensity normalization, nuisance signal removal, band-pass filtering (0.01–0.1 Hz) [http://preprocessed-connectomes-project.org/abide/ccs.html].

TABLE 1 | A concise representation of the erstwhile deep learning algorithms in autism classification.

References	Method	Pattern	Purpose	Accuracy (%)
Leming et al. (2020)	Ensemble learning	FC and structural	Classification	67
Lu et al. (2020)	Auto-encoder	Atlases	Classification	61(ABIDE)
Niu et al. (2020)	DANN	FC/ROI	Classification	73.2
Byeon et al. (2020)	RNN	FC	Classification	74.54
Thomas et al. (2020)	3DCNN, SVM	FC	Classification	66
Jiao et al. (2020)	CapsNets	FC	Classification	71
Yin et al. (2020)	DNN, AE	ROI	Classification	79.2
Anirudh and Thiagarajan (2019)	GCNN	ROI	Classification	70.86
Zhao et al. (2018b)	3D CNN	ICN	Differentiation	70.5
Zhao et al. (2018a)	3D CNN	ROI	Classification	70.1
Guo et al. (2017)	DNN	FC	Classification	86.36
Dvornek et al. (2017)	LSTMs	ROI	Identification	68.5
Ktena et al. (2017)	GCNN	ROI	Classification	62.9
Abraham et al. (2017)	SVM	ROI	Prediction	67

TABLE 2 | NYU phenotypic data information for ABIDE-I database.

Total subjects	ASD	TC	Female	Male	Age range (Years)		Average age (SD)	ADOS score (SD)
					ASD	TC		
184	79	105	35	149	7.1–39.1	6.5–31.8	15.25 (6.58)	11.30 (4.08)

TABLE 3 | Overview of the basic parameters and steps of used by CCS.

	Basic processing	Nuisance Signal	Regressor Removal
Steps	Slice timing correction (Yes) Motion realignment (Yes) Intensity normalization (Yes)	Motion (24 param)	Tissue signals (mean WM and CSF) Motion realignment (Yes) Low frequency drifts

The phenotypic information of the CCS-NYU dataset is shown in **Table 2**.

3.2. Data Preprocessing

The CCS ABIDE data preprocessing pipelines are analogous due to the parameters and software used for each of the steps. The CCS parameters and steps are presented in **Table 3**. In this work, data are selected from the filt_global preprocessing stratagem, which is band-pass filtered (0.01–0.1 Hz) and spatially registered using a nonlinear method to MNI152 template space for each of four pipelines. The overall 3D fMRI data processing procedure is shown in **Figure 2**. For data processing, firstly, we loaded the 3D fMRI data and saved it as 2D images. To pursue this process, we proceeded with the slice time corrections and normalizations. The whole steps are explained briefly in the following section.

3.2.1. Slice-Time Correction

The original 3D fMRI data has 73 slices per volume according to the data description of ABIDE-I. In our experiments, from the 73 slices, we contemplated the last 50 slices because of the precise sketches of the brain images.

3.2.2. Normalization

Normalization is a process wherein the database is reoriented in such a way that users can suitably handle that for further interrogation and analysis. We used the Min-Max normalization technique to overcome the image inappropriateness, which transformed the images into numerical values from 0 to 1.

$$Y_i = [X_i - min(X)]/[max(X) - min(X)] \tag{1}$$

Where X_i is the ith data point, min and max stands for minimum and maximum, and Y_i is the converted output.

3.3. Proposed DarkASDNet Model

The appositeness of the deep learning approach has to be remodled in artificial intelligence, helping to find neuropsychiatric brain disorders such as ASD. Deep learning is designated with the increasing number of layers as well as the network. An exemplary CNN performed for the feature extraction by the convolution layer, and reduced the size of the computational operation and a fully connected layer before the classification. The overall demonstration of our conceptual DarkASDNet architecture is presented in **Figure 3**. Here, DN represents the set-up for the convolutional layer, batch normalization layer, and max-pooling layer in sequential order.

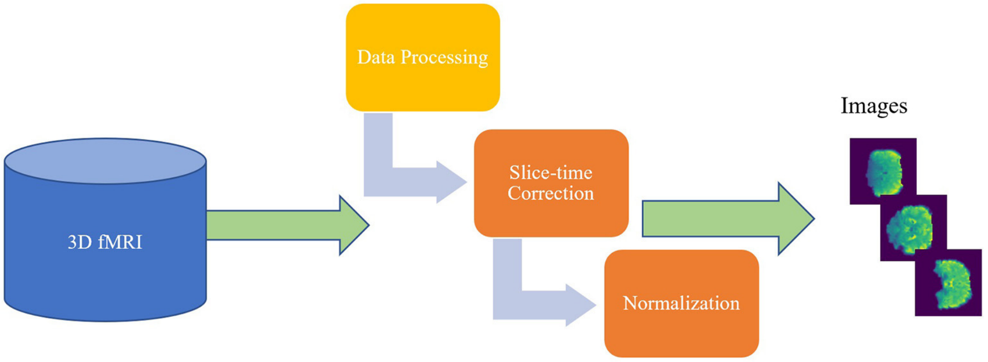

FIGURE 2 | The overview of the 3D fMRI data processing for both ASD and TC.

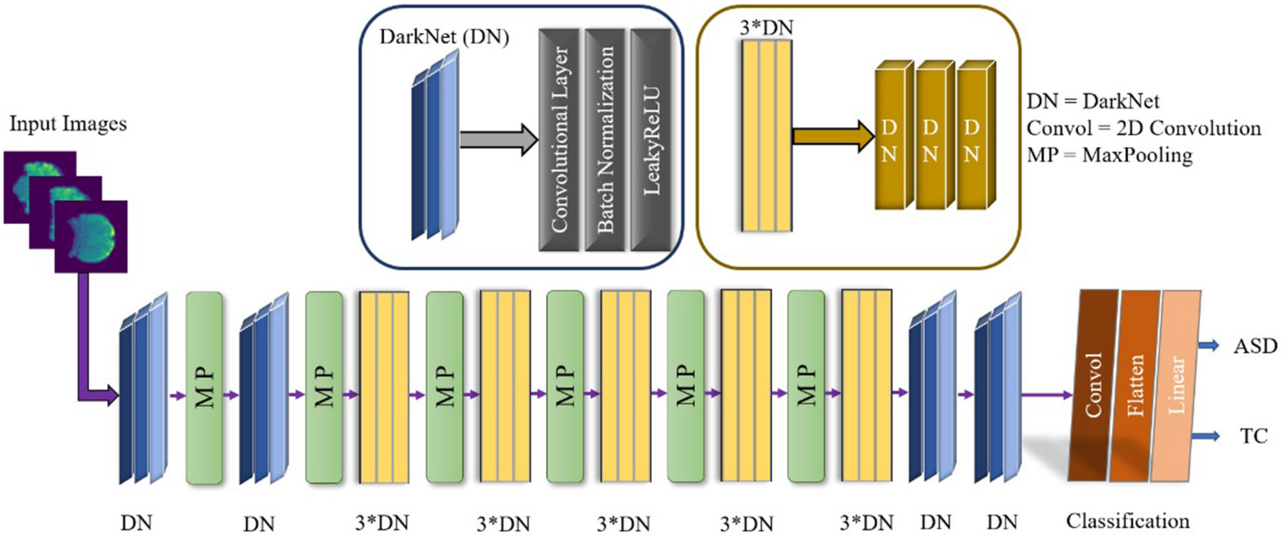

FIGURE 3 | The proposed DarkASDNet framework for ASD classification.

For the time being, 3*DN is betoken for the three times of DN ensuing one after another DN block. There are a considerable number of deep learning algorithms. In this work, we have followed the Darknet-19 model (Redmon and Farhadi, 2017) for our experiment and updated this model to get the utmost accuracy. The Darknet-19 preeminently builds for classifier object detection where they used 19 convolutional layers, 5 Maxpooling layers, and disparate stride values, sizes, and filter numbers. In this work, we proposed DarkASDNet for classifying the autism brain images between ASD vs. TC. For this reason, we have originated 20 Convolutional layers and six Max pooling layers.

Where *Convol* represents the 2D Convolution, and *MP* stand for Max pooling layers. Each Convolutional layer come out with Batch Normalization (BN) and LeakyReLU operations. There has been the same set-up when we are using three Convolutional layers in successive order. For the two-dimensional convolution operation, kernel is epitomized as K and input images as X, while $*$ is symbolized as discrete convolution operation, as given in the following Equation (2).

$$(X * K)_{(i,j)} = \sum_{m} \sum_{n} K_{(m,n)} X_{(i-m,j-n)} \qquad (2)$$

The superiority of adopting batch normalization is increased learning rate, improved gradient flow, reduced dependency on initialization, standardized inputs, and reduced training time to overcome the overfitting problem. Although ReLu (Rectified Linear Unit) or Sigmoid activation functions are prominent in deep learning, we used LeakyReLU as our activation function. Unlike ReLu, LeakyReLU has the biggest advantages in calculating the negative part which forestalls dying neurons. The mathematical formula for LeakyRelu is shown in Equation (3).

$$f(x) = \begin{cases} 0.01x, & \text{for } x < 0 \\ x, & \text{for} x > 0 \end{cases} \qquad (3)$$

TABLE 4 | The number of layers and layer parameters of the proposed DarkASDNet model.

Layer (type)	Output shape	Parameters
Convol2d	[8, 256, 256]	216
Convol2d	[16, 128, 128]	1,152
Convol2d	[32, 64, 64]	4,608
Convol2d	[16, 66, 66]	512
Convol2d	[32, 66, 66]	4,608
Convol2d	[64, 33, 33]	18,432
Convol2d	[32, 35, 35]	2,048
Convol2d	[64, 35, 35]	18,432
Convol2d	[128, 17, 17]	73,728
Convol2d	[64, 19, 19]	8,192
Convol2d	[128, 19, 19]	73,728
Convol2d	[256, 9, 9]	294,912
Convol2d	[128, 11, 11]	32,768
Convol2d	[256, 11, 11]	294,912
Convol2d	[512, 5, 5]	1,179,648
Convol2d	[256, 7, 7]	131,072
Convol2d	[512, 7, 7]	1,179,648
Convol2d	[256, 9, 9]	131,072
Convol2d	[512, 9, 9]	1,179,648
Convol2d	[2, 9, 9]	9,216
Flatten	[162]	0
Linear	[2]	326

Resembling the DarkNet-19, Maxpool has the same operation in our model. It has several advantages, such as reducing the number of parameters to get prime information, diminishing the computational cost, and preventing over-fitting by fixing up with an abstracted form of the depiction. To classify the binary classification problem, we inked the loss function called Cross-Entropy Loss, and for the optimization, we set the Adam optimizer. The main ascendancy of using the Cross-Entropy loss function in binary classification problems is that it can reduce the distance between predicted and actual. The equation for the binary classification of the Cross-Entropy Loss function as follows.

$$CE = -\sum_{i=1}^{C'=2} t_i log(s_i) = -t_1 log(s_1) - (1 - t_1) log(1 - s_1) \quad (4)$$

where $C' = 2$ (for two classes C_1 and C_2), $t_1[0, 1]$ and s_1 are the ground truth and score for C_1, $s_2 = 1 - s_1$ and $t_2 = 1 - t_1$ for C_2. Finally, the layers and layers parameter are described in **Table 4**.

We utilized the Cross-Entropy loss function with the Linear classifier because they are best fitted to our proposed binary ASD classification instead of preserving the original DarkNet's loss calculation strategy. In the meantime, we change the average pooling layer to maxpooling layer and add one more convolutional layer than DarkNet. Moreover, the trainable parameters of the proposed DarkASDNet model are about 4.5 million compared to the underlying DarkNet model, which contains around 25 million. Therefore, our model is six times lighter than the original DarkNet, ensuring our model's computational efficiency.

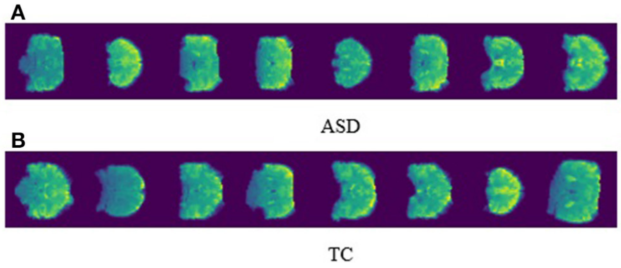

FIGURE 4 | The visualization of single sliced ASD and TC images.

4. DATA VISUALIZATION AND PERFORMANCE METRICS

4.1. Visualization of the Sliced fMRI Data

For the outrun treatment, reinforcement with prior diagnosis is important for ASD patients in order to delay deterioration and retain quality of life The visualization of the neuroimaging data can outrun perceptible biomarkers to illustrate prognosis and particular pathology for ASD patients. In our proposed work, we preprocess the 3D fMRI data into 2D images with slice time correction and normalization. **Figure 4** represents the perfect visualization of our preprocessed images, and the manifestation of our per slice images are easily depicted for both ASD and TC. In the meantime, we disclosed only the first eight images for ASD and TC.

4.2. Evaluation Metrics

To ensure the performance of our proposed model, we consummate an in-depth search to learn hyperparameters and investigate the average accuracy, f1-score, precision, and recall. True positive (TP) can correctly predict the ASD class and true negative (TN) for TC. False positive (FP) is the outcome of incorrect prediction of ASD and false negative (FN) for TC. The corresponding formula for the evaluation metrics is given below.

$$Accuracy = \frac{Total\ correct\ prediction}{Total\ number\ of\ labels} \times 100 \quad (5)$$

$$Precision = \frac{True\ Positive}{True\ Positive + False\ Positive} \quad (6)$$

$$Recall = \frac{True\ Positive}{True\ Positive + False\ Negative} \quad (7)$$

$$F_{1\_score} = 2 \times \frac{(Precision * Recall)}{(Precision + Recall)} \quad (8)$$

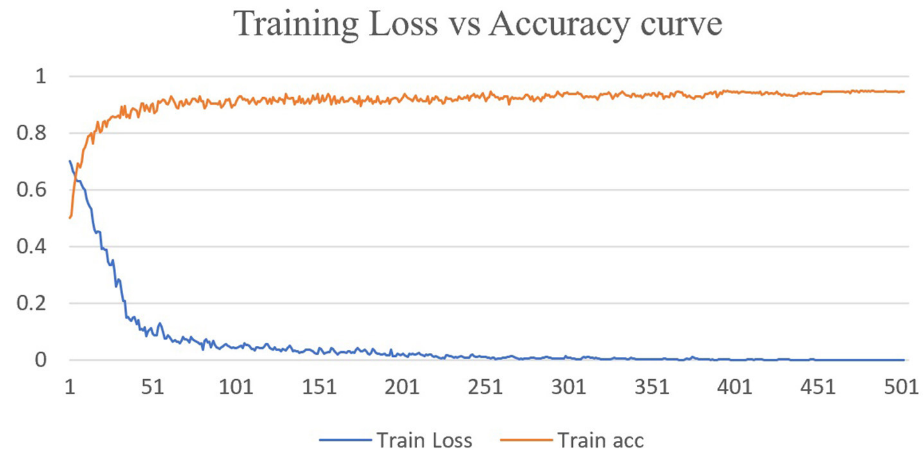

FIGURE 5 | Training loss vs. accuracy curve for DarkASDNet.

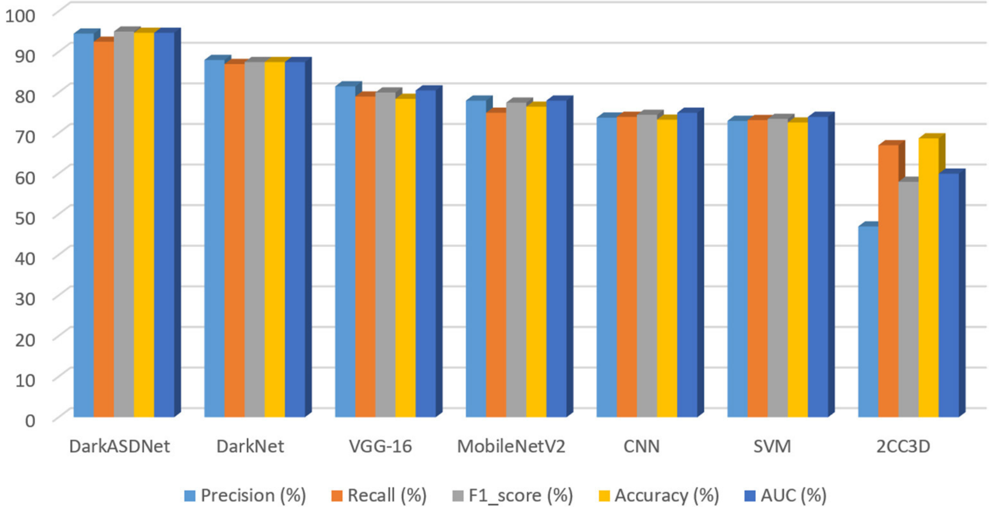

FIGURE 6 | Accuracy comparison of DarkASDNet with state-of-the-art methods used in ASD classification.

5. EXPERIMENTAL RESULTS AND DISCUSSION

Deep learning approaches have been successfully employed in ASD classification using ABIDE data based on fMRI images. In this work, we have proposed DarkASDNet to classify ASD showing different measurement metrics in the same manner with recall, precision, F1-score, and accuracy with ROC curve and AUC score to legitimize the performance of the proposed method. The training loss and accuracy comparison curve of the proposed DarkASDNet is shown in **Figure 5**. From **Figure 5**, it is depicting that the training accuracy is increasing with decreasing the training loss. The highest accuracy of 94.7% we have obtained while testing the DarkASDNet model. **Figure 6** shows the performance values for different evaluation metrics, including precision, recall, f1-score, and AUC for ASD classification using proposed DarkASDNet. After testing our model for ASD classification, we have achieved the highest accuracy of 94.7%, the precision of 94.5%, recall of 92.5%, f1-score of 95%, and the AUC score 94.703%.

Furthermore, to evaluate our proposed DarkASDNet, we have implemented the VGG16 (Simonyan and Zisserman, 2015), MobileNetV2 (Sandler et al., 2018), and SVM (Jebapriya et al., 2019) algorithms as competence methods to classify ASD using the same dataset. We have also implemented two most recent works preferably using CNN in Ahmed et al. (2020), and 2CC3D in Li et al. (2018a). **Figure 6** represents the performance comparison for the competence method with our proposed DarkASDNet model. Using SVM, MobileNetV2, and VGG16 models for ASD classification, we get an accuracy of 72.6, 76.5, and 78.43%, respectively. Comparing with the performance of competitive methods, in DarkASDNet, we get state-of-the-art

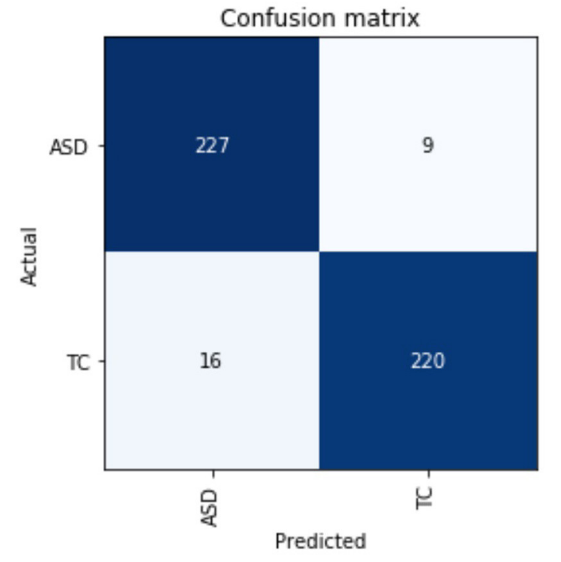

FIGURE 7 | The evaluation performances of confusion metrics.

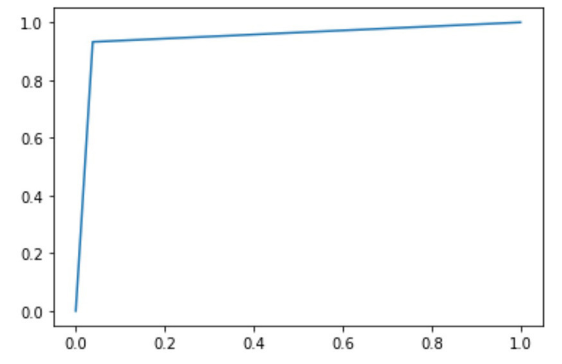

FIGURE 8 | Receiver operating characteristic curve for ASD.

accuracy during classification. As we know, deep learning techniques are nowadays performing very satisfactorily in ASD classification using ABIDE data. For example, in Ahmed et al. (2020), authors adopted the CNN model for single site (NYU) classification, where they got the highest accuracy of 88% for glass brain images. On the other hand, using extracted ROIs connectivity features and NYU dataset with 10-fold cross-validation, Kong et al. (2019) achieved the highest accuracy of 90.39% by considering stacked autoencoder (SAE) and softmax as a classifier. Furthermore, Auto-ASD-Network proposed by Eslami and Saeed (2019) based on the multilayer perceptron (MLP) with two hidden layers, and SVM got the highest accuracy of 80% for ASD classification using the NYU dataset. The accuracy comparison curve of our proposed DarkASDNet and other state-of-the-art methods for ASD classification using the ABIDE-NYU dataset is shown in **Figure 6**. From the bar diagram in **Figure 6**, the nearest model has a mean accuracy difference of about 3.4% with our method (Kong et al., 2019). Therefore, based on the results, our proposed DarkASDNet method outperforms other methods on average for classifying ASD.

Besides the matrices explained above, we have also described the confusion matrix table for DarkASDNet in **Figure 7**. It is clear from **Figure 7** that there are two predicted classes: ASD and TC, a binary classification problem. The proposed DarkASDNet classifier made 472 subjective predictions, and out of these subjects, the classifier predicts 243 times as ASD patients and 229 times as the TC subjects. However, in the original dataset, there were 236 subjects for ASD patients and 236 subjects as TC. From the confusion matrix, we see that the overall misclassification rate is ∼5.3%, with a true positive and false positive rate of 0.96 and 0.93, respectively, which is comparatively highly acceptable. The corresponding ROC curve is shown in **Figure 8**.

6. CONCLUSION AND FUTURE WORK

It is challenging to find the proficient classifier for ASD, while most of the classifier depends on functional connectivity and brain ROIs analysis. In this work, we proposed a novel DarkASDNet model for ASD classification using 3D fMRI data. Different from the conventional machine learning method in which the extraction of the image features for the training set is done manually, our method handles the extraction of the image features automatically during the computation. We processed the fMRI data according to the DarkASDNet requirement through proper slice-time correction and normalization. We assessed the DarkASDNet performances using the generated fMRI data and utilized metrics functioning as recall, precision, F1-score, and accuracy with ROC curve and AUC value. Finally, we validated our outcomes by comparing with five other recent competency methods, including three leading benchmark approaches showing state-of-the-art results. To the end, the proposed framework provides a new benchmark method for ASD classification.

Future work will increase the number of subjects, such as the whole ABIDE database, considering each subject's phenotypic information. Although our model has presented outstanding results for ASD classification, improvements still need to be made to the model to handle the 3D fMRI data directly. We will solve these issues in our future work by employing the sample demographic information.

DATA AVAILABILITY STATEMENT

The raw data supporting the conclusions of this article will be made available by the authors, without undue reservation.

AUTHOR CONTRIBUTIONS

MSA and SN conceived the study. MSA pursued the implementation of the methodology, conducted the data processing and experiments, and generated and validated the results. MSA, SN, and MRA performed the formal analysis and wrote the original draft. SN provided critical feedback and suggestions for performing the experiments. SN, MRA, JD, XG, and YC provided valuable suggestions in writing the manuscript. All authors have read and agreed to the published version of the manuscript.

ACKNOWLEDGMENTS

Data used in this manuscript were obtained from the ABIDE (Autism Brain Imaging Data Exchange), an open-source database for Autism and typical controls comprising 17 individual international sites' data from world-renowned laboratories and hospitals. The author also acknowledges the support from the coauthors for their meaningful suggestions during manuscript preparation.

REFERENCES

Abraham, A., Milham, M. P., Di Martino, A., Craddock, R. C., Samaras, D., Thirion, B., et al. (2017). Deriving reproducible biomarkers from multi-site resting-state data: an autism-based example. *NeuroImage* 147, 736–745. doi: 10.1016/j.neuroimage.2016.10.045

Ahmed, M. R., Zhang, Y., Feng, Z., Lo, B., Inan, O. T., and Liao, H. (2018). Neuroimaging and machine learning for dementia diagnosis: recent advancements and future prospects. *IEEE Rev. Biomed. Eng.* 12, 19–33. doi: 10.1109/RBME.2018.2886237

Ahmed, M. R., Zhang, Y., Liu, Y., and Liao, H. (2020). Single volume image generator and deep learning-based asd classification. *IEEE J. Biomed. Health Inform.* 24, 3044–3054. doi: 10.1109/JBHI.2020.2998603

Anirudh, R., and Thiagarajan, J. J. (2019). "Bootstrapping graph convolutional neural networks for autism spectrum disorder classification," in *ICASSP 2019 - 2019 IEEE International Conference on Acoustics, Speech and Signal Processing (ICASSP)* (Brighton), 3197–3201. doi: 10.1109/ICASSP.2019.8683547

Baio, J., Wiggins, L., Christensen, D. L., Maenner, M. J., Daniels, J., Warren, Z., et al. (2018). Prevalence of autism spectrum disorder among children aged 8 years-autism and developmental disabilities monitoring network, 11 sites, United States, 2014. *MMWR Surveill. Summar.* 67:1. doi: 10.15585/mmwr.ss6706a1

Bi, X.-a., Liu, Y., Sun, Q., Luo, X., Tan, H., Chen, J., et al. (2019). The genetic-evolutionary random support vector machine cluster analysis in autism spectrum disorder. *IEEE Access* 7, 30527–30535. doi: 10.1109/ACCESS.2019.2902889

Bi, X.-a., Wang, Y., Shu, Q., Sun, Q., and Xu, Q. (2018). Classification of autism spectrum disorder using random support vector machine cluster. *Front. Genet.* 9:18. doi: 10.3389/fgene.2018.00018

Byeon, K., Kwon, J., Hong, J., and Park, H. (2020). "Artificial neural network inspired by neuroimaging connectivity: application in autism spectrum disorder," in *2020 IEEE International Conference on Big Data and Smart Computing (BigComp)* (Busan), 575–578. doi: 10.1109/BigComp48618.2020.00013

Chen, H., Duan, X., Liu, F., Lu, F., Ma, X., Zhang, Y., et al. (2016). Multivariate classification of autism spectrum disorder using frequency-specific resting-state functional connectivity-a multi-center study. *Prog. Neuro-Psychopharmacol. Biolog. Psychiatry* 64, 1–9. doi: 10.1016/j.pnpbp.2015.06.014

Cociu, B., Das, S., Billeci, L., Jamal, W., Maharatna, K., Calderoni, S., et al. (2018). Multimodal functional and structural brain connectivity analysis in autism: a preliminary integrated approach with EEG, fMRI, and DTI. *IEEE Trans. Cogn. Dev. Syst.* 10, 213–226. doi: 10.1109/TCDS.2017.2680408

Craddock, C., Benhajali, Y., Chu, C., Chouinard, F., Evans, A., Jakab, A., et al. (2013). The neuro bureau preprocessing initiative: open sharing of preprocessed neuroimaging data and derivatives. *Neuroinformatics* 7. doi: 10.3389/conf.fninf.2013.09.00041

Dvornek, N. C., Ventola, P., and Duncan, J. S. (2018). "Combining phenotypic and resting-state fmri data for autism classification with recurrent neural networks," in *2018 IEEE 15th International Symposium on Biomedical Imaging (ISBI 2018)* (Washington, DC), 725–728. doi: 10.1109/ISBI.2018.8363676

Dvornek, N. C., Ventola, P., Pelphrey, K. A., and Duncan, J. S. (2017). "Identifying autism from resting-state fmri using long short-term memory networks," in *International Workshop on Machine Learning in Medical Imaging* (Quebec City, QC: Springer), 362–370. doi: 10.1007/978-3-319-67389-9_42

Eickhoff, S. B., Thirion, B., Varoquaux, G., and Bzdok, D. (2015). Connectivity-based parcellation: critique and implications. *Hum. Brain Mapp.* 36, 4771–4792. doi: 10.1002/hbm.22933

Eslami, T., and Saeed, F. (2019).

Guo, X., Dominick, K. C., Minai, A. A., Li, H., Erickson, C. A., and Lu, L. J. (2017). Diagnosing autism spectrum disorder from brain resting-state functional connectivity patterns using a deep neural network with a novel feature selection method. *Front. Neurosci.* 11:460. doi: 10.3389/fnins.2017.00460

Höfer, J., Hoffmann, F., and Bachmann, C. (2017). Use of complementary and alternative medicine in children and adolescents with autism spectrum disorder: a systematic review. *Autism* 21, 387–402. doi: 10.1177/1362361316646559

Hyman, S. L., Levy, S. E., Myers, S. M., et al. (2020). Identification, evaluation, and management of children with autism spectrum disorder. *Pediatrics* 145:e20193447. doi: 10.1542/peds.2019-3447

Iidaka, T. (2015). Resting state functional magnetic resonance imaging and neural network classified autism and control. *Cortex* 63, 55–67. doi: 10.1016/j.cortex.2014.08.011

Jebapriya, S., David, S., Jaspher, W., and Sundar, N. (2019). Support vector machine for classification of autism spectrum disorder based on abnormal structure of corpus callosum. *Int. J. Adv. Comput. Sci. Appl.* 10:2019. doi: 10.14569/IJACSA.2019.0100965

Jiao, Z., Li, H., and Fan, Y. (2020). "Improving diagnosis of autism spectrum disorder and disentangling its heterogeneous functional connectivity patterns using capsule networks," in *2020 IEEE 17th International Symposium on Biomedical Imaging (ISBI)* (Iowa City, IA), 1331–1334. doi: 10.1109/ISBI45749.2020.9098524

Jin, Y., Wee, C.-Y., Shi, F., Thung, K.-H., Ni, D., Yap, P.-T., et al. (2015). Identification of infants at high-risk for autism spectrum disorder using multiparameter multiscale white matter connectivity networks. *Hum. Brain Mapp.* 36, 4880–4896. doi: 10.1002/hbm.22957

Kaiser, M. D., Hudac, C. M., Shultz, S., Lee, S. M., Cheung, C., Berken, A. M., et al. (2010). Neural signatures of autism. *Proc. Natl. Acad. Sci. U.S.A.* 107, 21223–21228. doi: 10.1073/pnas.1010412107

Khosla, M., Jamison, K., Kuceyeski, A., and Sabuncu, M. R. (2018). "3d convolutional neural networks for classification of functional connectomes," in *Deep Learning in Medical Image Analysis and Multimodal Learning for Clinical Decision Support* (Granada: Springer), 137–145. doi: 10.1007/978-3-030-00889-5_16

Klöppel, S., Abdulkadir, A., Jack, C. R. Jr, Koutsouleris, N., Mour ao-Miranda, J., and Vemuri, P. (2012). Diagnostic neuroimaging across diseases. *Neuroimage* 61, 457–463. doi: 10.1016/j.neuroimage.2011.11.002

Kong, Y., Gao, J., Xu, Y., Pan, Y., Wang, J., and Liu, J. (2019). Classification of autism spectrum disorder by combining brain connectivity and deep neural network classifier. *Neurocomputing* 324, 63–68. doi: 10.1016/j.neucom.2018.04.080

Ktena, S. I., Parisot, S., Ferrante, E., Rajchl, M., Lee, M., Glocker, B., et al. (2017). Distance metric learning using graph convolutional networks: application to functional brain networks. *arXiv preprint arXiv:1703.02161*. doi: 10.1007/978-3-319-66182-7_54

Lee, M.-H., Kim, D. Y., Chung, M. K., Alexander, A. L., and Davidson, R. J. (2018). Topological properties of the structural brain network in autism via ϵ-neighbor method. *IEEE Trans. Biomed. Eng.* 65, 2323–2333.

Leming, M., Górriz, J. M., and Suckling, J. (2020). Ensemble deep learning on large, mixed-site fMRI datasets in autism and other tasks. *arXiv preprint arXiv:2002.07874*. doi: 10.1142/S0129065720500124

Li, X., Dvornek, N. C., Papademetris, X., Zhuang, J., Staib, L. H., Ventola, P., et al. (2018a). "2-channel convolutional 3D deep neural network (2CC3D) for fMRI analysis: ASD classification and feature learning," in *2018 IEEE 15th International Symposium on Biomedical Imaging (ISBI 2018)*, 1252–1255. doi: 10.1109/ISBI.2018.8363798

Li, X., Dvornek, N. C., Zhuang, J., Ventola, P., and Duncan, J. S. (2018b). "Brain biomarker interpretation in asd using deep learning and fMRI," in *International Conference on Medical Image Computing and Computer-Assisted Intervention* (Washington, DC: Springer), 206–214. doi: 10.1007/978-3-030-00931-1_24

Lu, H., Liu, S., Wei, H., and Tu, J. (2020). Multi-kernel fuzzy clustering based on auto-encoder for fMRI functional network. *Expert Syst. Appl.* 2020:113513. doi: 10.1016/j.eswa.2020.113513

Mandell, D. S., Ittenbach, R. F., Levy, S. E., and Pinto-Martin, J. A. (2007). Disparities in diagnoses received prior to a diagnosis of autism spectrum disorder. *J. Autism Dev. Disord.* 37, 1795–1802. doi: 10.1007/s10803-006-0314-8

Niu, K., Guo, J., Pan, Y., Gao, X., Peng, X., Li, N., et al. (2020). Multichannel deep attention neural networks for the classification of autism spectrum disorder using neuroimaging and personal characteristic data. *Complexity* 2020:1357853. doi: 10.1155/2020/1357853

Noriega, G. (2019). Restricted, repetitive, and stereotypical patterns of behavior in autism-an fMRI perspective. *IEEE Trans. Neural Syst. Rehabil. Eng.* 27, 1139–1148. doi: 10.1109/TNSRE.2019.2912416

Nylander, L., Holmqvist, M., Gustafson, L., and Gillberg, C. (2013). Attention-deficit/hyperactivity disorder (ADHD) and autism spectrum disorder (ASD) in adult psychiatry. A 20-year register study. *Nordic J. Psychiatry* 67, 344–350. doi: 10.3109/08039488.2012.748824

Parikh, M. N., Li, H., and He, L. (2019). Enhancing diagnosis of autism with optimized machine learning models and personal characteristic data. *Front. Comput. Neurosci.* 13:9. doi: 10.3389/fncom.2019.00009

Parisot, S., Ktena, S. I., Ferrante, E., Lee, M., Moreno, R. G., Glocker, B., et al. (2017). "Spectral graph convolutions for population-based disease prediction," in *International Conference on Medical Image Computing and Computer-Assisted Intervention* (Quebec City, QC: Springer), 177–185. doi: 10.1007/978-3-319-66179-7_21

Pascual-Belda, A., Díaz-Parra, A., and Moratal, D. (2018). Evaluating functional connectivity alterations in autism spectrum disorder using network-based statistics. *Diagnostics* 8:51. doi: 10.3390/diagnostics8030051

Phinyomark, A., Ibanez-Marcelo, E., and Petri, G. (2017). Resting-state fMRI functional connectivity: big data preprocessing pipelines and topological data analysis. *IEEE Trans. Big Data* 3, 415–428. doi: 10.1109/TBDATA.2017.2734883

Raví, D., Wong, C., Deligianni, F., Berthelot, M., Andreu-Perez, J., Lo, B., and Yang, G.-Z. (2016). Deep learning for health informatics. *IEEE J. Biomed. Health Inform.* 21, 4–21. doi: 10.1109/JBHI.2016.2636665

Redmon, J., and Farhadi, A. (2017). "Yolo9000: better, faster, stronger," in *Proceedings of the IEEE Conference on Computer Vision and Pattern Recognition*, 7263–7271. doi: 10.1109/CVPR.2017.690

Sandler, M., Howard, A., Zhu, M., Zhmoginov, A., and Chen, L. (2018). "Mobilenetv2: inverted residuals and linear bottlenecks," in *2018 IEEE/CVF Conference on Computer Vision and Pattern Recognition* (Salt Lake City, UT), 4510–4520. doi: 10.1109/CVPR.2018.00474

Senn, M. (2020). *CDC Estimate on Autism Prevalence Increases by Nearly 10 Percent, to 1 in 54 Children in the U.S.* Available online at: https://www.autismspeaks.org/press-release/cdc-estimate-autism-prevalence-increases-nearly-10-percent-1-54-children-us (accessed April 26, 2020).

Simonyan, K., and Zisserman, A. (2015). "Very deep convolutional networks for large-scale image recognition," in *International Conference on Learning Representations* (San Diego, CA).

Sundermann, B., Herr, D., Schwindt, W., and Pfleiderer, B. (2014). Multivariate classification of blood oxygen level-dependent fMRI data with diagnostic intention: a clinical perspective. *Am. J. Neuroradiol.* 35, 848–855. doi: 10.3174/ajnr.A3713

Thirion, B., Varoquaux, G., Dohmatob, E., and Poline, J.-B. (2014). Which fMRI clustering gives good brain parcellations? *Front. Neurosci.* 8:167. doi: 10.3389/fnins.2014.00167

Thomas, R. M., Gallo, S., Cerliani, L., Zhutovsky, P., El-Gazzar, A., and van Wingen, G. (2020). Classifying autism spectrum disorder using the temporal statistics of resting-state functional MRI data with 3D convolutional neural networks. *Front. Psychiatry* 11:440. doi: 10.3389/fpsyt.2020.00440

Wang, C., Xiao, Z., Wang, B., and Wu, J. (2019). Identification of autism based on SVM-RFE and stacked sparse auto-encoder. *IEEE Access* 7, 118030–118036. doi: 10.1109/ACCESS.2019.2936639

Yahata, N., Morimoto, J., Hashimoto, R., Lisi, G., Shibata, K., Kawakubo, Y., et al. (2016). A small number of abnormal brain connections predicts adult autism spectrum disorder. *Nat. Commun.* 7, 1–12. doi: 10.1038/ncomms11254

Yang, X., Islam, M. S., and Khaled, A. A. (2019). "Functional connectivity magnetic resonance imaging classification of autism spectrum disorder using the multisite abide dataset," in *2019 IEEE EMBS International Conference on Biomedical* & *Health Informatics (BHI)* (Chicago, IL), 1–4. doi: 10.1109/BHI.2019.8834653

Yao, Z., Hu, B., Xie, Y., Zheng, F., Liu, G., Chen, X., et al. (2016). Resting-state time-varying analysis reveals aberrant variations of functional connectivity in autism. *Front. Hum. Neurosci.* 10:463. doi: 10.3389/fnhum.2016.00463

Yin, W., Mostafa, S., and Wu, F.-x. (2020). Diagnosis of autism spectrum disorder based on functional brain networks with deep learning. *J. Comput. Biol.* 28, 146–165. doi: 10.1089/cmb.2020.0252

Yu, C., Gao, Z., Zhang, W., Yang, G., Zhao, S., Zhang, H., et al. (2020). Multitask learning for estimating multitype cardiac indices in MRI and CT based on adversarial reverse mapping. *IEEE Trans. Neural Netw. Learn. Syst.* 32, 493–506. doi: 10.1109/TNNLS.2020.2984955

Zhang, C., Adeli, E., Wu, Z., Li, G., Lin, W., and Shen, D. (2018). Infant brain development prediction with latent partial multi-view representation learning. *IEEE Trans. Med. Imaging* 38, 909–918. doi: 10.1109/ISBI.2018.8363751

Zhao, Y., Dong, Q., Zhang, S., Zhang, W., Chen, H., Jiang, X., et al. (2018a). Automatic recognition of fmri-derived functional networks using 3-D convolutional neural networks. *IEEE Trans. Biomed. Eng.* 65, 1975–1984. doi: 10.1109/TBME.2017.2715281

Zhao, Y., Ge, F., Zhang, S., and Liu, T. (2018b). "3D deep convolutional neural network revealed the value of brain network overlap in differentiating autism spectrum disorder from healthy controls," in *Medical Image Computing and Computer Assisted Intervention-MICCAI 2018*, eds A. F. Frangi, J. A. Schnabel, C. Davatzikos, C. Alberola-López, and G. Fichtinger (Cham: Springer International Publishing), 172–180. doi: 10.1007/978-3-030-00931-1_20

Conflict of Interest: The authors declare that the research was conducted in the absence of any commercial or financial relationships that could be construed as a potential conflict of interest.

frontiers
in Neuroinformatics

ORIGINAL RESEARCH
published: 11 August 2021
doi: 10.3389/fninf.2021.719719

Comparative Study of Multi-Delay Pseudo-Continuous Arterial Spin Labeling Perfusion MRI and CT Perfusion in Ischemic Stroke Disease

Xi Xu[1†], *Zefeng Tan*[2,3†], *Meng Fan*[1†], *Mengjie Ma*[1], *Weimin Fang*[1], *Jianye Liang*[1,4], *Zeyu Xiao*[1], *Changzheng Shi*[1,5]* *and Liangping Luo*[1,5]*

[1] Medical Imaging Center, The First Affiliated Hospital of Jinan University, Guangzhou, China, [2] Department of Neurology, The First Affiliated Hospital of Jinan University, Guangzhou, China, [3] Department of Neurology, Shun De Hospital of Jinan University, Foshan, China, [4] Department of Medical Imaging, Sun Yat-sen University Cancer Center, Guangzhou, China, [5] Engineering Research Center of Medical Imaging Artificial Intelligence for Precision Diagnosis and Treatment, Guangzhou, China

With the aging population, stroke has gradually become the leading cause of death and disability among adults. It is necessary to verify whether multi-delay pseudo-continuous arterial spin labeling (pCASL) MRI can be used as a standard neuroimaging protocol in the patients with ischemic stroke. We aimed to investigate the clinical utility of multi-delay pCASL for evaluating cerebral perfusion in ischemic stroke disease. Twenty-one ischemic stroke patients [18 men and 3 women; median age, 62 years (age range, 37–84 years)] were enrolled in this study. All patients underwent examinations, including the multi-delay pCASL protocol (using 6 PLDs between 1,000 and 3,500 ms) and computed tomography perfusion (CTP). The cerebral blood flow (CBF) and arterial transit time (ATT) maps were obtained by the multi-delay pCASL protocol, while CBF and mean transit time (MTT) maps were derived by CTP measurements. Based on the voxel level analysis, Pearson correlation coefficients were used to estimate the associations between the two modalities in the gray matter, white matter, and whole brain of each subject. Moderate to high positive associations between ASL-CBF and CTP-CBF were acquired by voxel-level-wise analysis in the gray matter, white matter, and whole brain of the enrolled patients (all $P < 0.005$), and the average Pearson correlation coefficients were 0.647, 0.585, and 0.646, respectively. Highly significant positive correlations between ASL-ATT and CTP-MTT were obtained by voxel-level-wise associations in the gray matter, white matter, and whole brain (all $P < 0.005$), and the average Pearson correlation coefficients were 0.787, 0.707, and 0.799, respectively. In addition, significant associations between ASL and CT perfusion were obtained in the gray, white matter and whole brain, according to the subgroup analyses of patient's age and disease stage. There is a correlation between perfusion parameters from multi-delay pCASL and CT perfusion imaging in patients with ischemic stroke. Multi-delay pCASL is radiation-free and non-invasive, and could be an alternative method to CT scans for assessing perfusion in ischemic stroke disease.

Keywords: ischemic stroke, pseudo-continuous arterial spin labeling, CT perfusion, cerebral blood flow, arterial transit time, mean transit time

Edited by:
Heye Zhang,
Sun Yat-sen University, China

Reviewed by:
KowsalyaDevi Pavuluri,
Mayo Clinic, United States
Xin Liu,
Foshan University, China

Correspondence:
Changzheng Shi
tsczcn@jnu.edu.cn
Liangping Luo
tluolp@jnu.edu.cn

†These authors have contributed equally to this work

Received: *02 June 2021*
Accepted: *28 June 2021*
Published: *11 August 2021*

Citation:
Xu X, Tan Z, Fan M, Ma M, Fang W, Liang J, Xiao Z, Shi C and Luo L (2021) Comparative Study of Multi-Delay Pseudo-Continuous Arterial Spin Labeling Perfusion MRI and CT Perfusion in Ischemic Stroke Disease. Front. Neuroinform. 15:719719. doi: 10.3389/fninf.2021.719719

INTRODUCTION

The Global Burden of Disease Study in 2015 provided a comprehensive assessment of 249 all-cause and cause-specific deaths across 195 countries and regions from 1980 to 2015; stroke was determined to be the second-leading cause of death worldwide (Wang et al., 2016). The 2019 statistical report from the American Heart Association on heart disease and stroke revealed that approximately 795,000 people experience a new or recurrent stroke each year (Benjamin et al., 2019). With the aging of the population, stroke has gradually become a leading cause of death and disability among adults in China. The social burden of stroke has gradually increased because of the increased morbidity and mortality (Vilela and Rowley, 2017).

Stroke is a type of cerebrovascular disease characterized by the symptoms of cerebral ischemia or cerebral hemorrhage, and cerebral ischemia is the main cause of stroke (Benjamin et al., 2019). Early diagnosis and appropriate treatment of the disease can effectively improve the prognosis of patients. MRI and CT are routine imaging modalities that play important roles in evaluating the brain condition of patients. Because of the pathophysiological changes in stroke patients, the assessment of microcirculation and cerebral perfusion is of great value for diagnosis and treatment.

The development of CT image analysis to assess the function of different organs (e.g., brain, heart, carotid artery, etc.) constitutes a promising strategy for evaluating normal and abnormal physiology (Xu et al., 2018; Zhang et al., 2018). As known errors are associated with bolus-based perfusion measurements (Wintermark et al., 2005), CT perfusion (CTP) is not regarded as the gold standard for calculating hemodynamic parameters. However, it is routinely used in clinical practice for perfusion evaluation, because it provides relatively accurate hemodynamic parameters, such as cerebral blood flow (CBF) and mean transit time (MTT). It's noting that the radiation damage and contrast medium may not be suitable for some individuals. Arterial spin labeling (ASL) perfusion MRI has gradually applied in the clinic without radiation damage. Previously studies have generally adopted a single post-labeling delay (PLD) time (Wang et al., 2014), typically between 1.5 and 2 s, which may underestimate perfusion due to prolonged arterial transit time (ATT) in ischemic stroke (MacIntosh et al., 2010). In recent years, multi-delay ASL sequences have been used to overcome this limitation. Wang et al. (2014) concluded the correlations between multi-delay pCASL and CTP in moyamoya disease, and indicated ASL could be a part of neuroimaging protocols in the moyamoya disease. They advised warranted studies of ischemic stroke, as the radiation-free and non-invasive ASL can provide perfusion information without the use of contrast agent. MacIntosh et al. (2010) adopted multi-delay pCASL (PLD times were set between 500 ms and 2,500 ms, a total of 9 intervals) in patients with acute ischemic stroke in a recent research. Wang et al. (2013) made a comparison between multi-delay ASL perfusion MRI and dynamic susceptibility contrast (DSC) enhanced perfusion imaging in acute ischemic stroke disease. The results showed highly correlations between pCASL and DSC CBF measurements. In our study, a wider range of PLD times was adopted, totally 6 PLD times between 1,000 and 3,500 ms were used to investigate the accuracy of multi-delay pCASL perfusion MRI for estimating cerebral perfusion in ischemic stroke patients, using CTP as the reference standard. In this study, we aimed to explore the feasibility and clinical utility of multi-delay pCASL by comparison with CTP imaging in ischemic stroke.

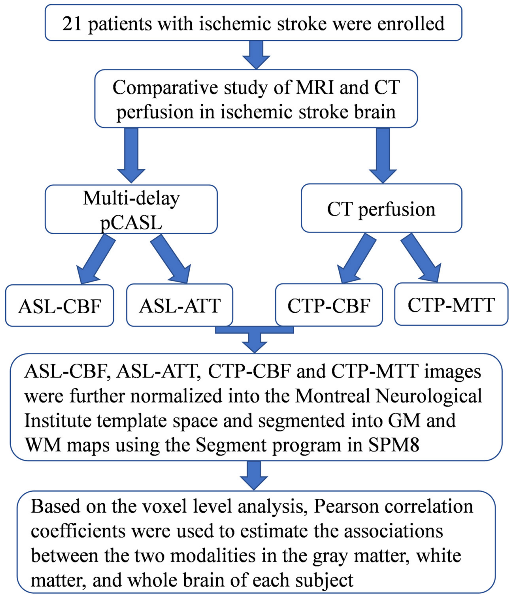

FIGURE 1 | Flowchart of the comparison between ASL and CT perfusion.

MATERIALS AND METHODS

Patients

The study was conducted in accordance with the principles of the Declaration of Helsinki, and the study protocol was approved by the institutional review board of our hospital. A total of 21 patients with ischemic stroke [18 men and 3 women; median age, 62 years (age range, 37–84 years)] were enrolled between June 2017 and March 2018. All patients underwent multi-delay pCASL and CTP examinations (**Figure 1**).

The inclusion criteria were as follows: (1) All patients were confirmed as ischemic stroke according to clinical symptoms and imaging diagnosis (MRI or CT images); (2) To reduce additional CT-associated radiation damage, patients who required CTP examination based on their condition were enrolled in the study; (3) Both CTP and ASL examinations were performed within 24 h.

The exclusion criteria were as follows: (1) Patients complicated with severe parenchymal organ disease (heart, lung, liver and kidney); (2) Patients complicated with brain trauma, brain tumor, intracranial hemorrhages, craniocerebral infection and other mixed factors; (3) Patients with a cardiac pacemaker, non-titanium alloy stent or internal plate fixation *in vivo*; (4) Unable to complete the examination due to claustrophobia.

Image Acquisition

All included patients underwent CTP on a Toshiba Aquilion One scanner, which was set at 112∼187 mA and 80 kV. And the minimum section thickness was 0.5 mm. CTP scan was initiated after injection of non-ionic iodinated contrast agent (Ultravist, 370 mg I/L; 50 ml at a rate of 6 ml/s) and physiological saline (30 ml at rate of 6 ml/s), using a power injector. The dynamic volume scan mode was turned on immediately after a delay of 7 s following the intravenous injection of contrast agent. The first period was used as a mask; 11–36 s was used for the arterial phase, and continuous scanning was performed at intervals of 2 s; 40–60 s was used for the venous phase for continuous scanning at intervals of 5 s. In total, 19 image acquisitions were performed with a total scan time of 60 s.

All enrolled patients underwent MRI on a GE Discovery MR750 3.0T System, using an 8-channel phased array head coil. The MRI protocol included T1-weighted imaging (T1WI), T2-weighted imaging (T2WI), fluid attenuated inversion recovery (FLAIR), diffusion weighted imaging (DWI), and multi-delay pCASL. For multi-delay pCASL, the imaging parameters were as follows: the delay time was between 1,000 and 3,500 ms, for a total of 6 PLDs. Filp angle (FA) = 111°, repetition time (TR) = 5,436 ms, echo time (TE) = 24.2 ms, slice thickness = 5 mm, spacing between slices = 0 mm, FOV = 220 mm × 220 mm, acquisition matrix = 550 × 6, number of excitations (NEX) = 1.

Processing of ASL and CTP

The post-processing of CTP data was performed on Vitrea Fx 6.3 image post-processing workstation by a senior radiologist. CTP-CBF and CTP-MTT perfusion maps derived from CT perfusion images using delay-insensitive blockcirculant singular-value decomposition (bSVD) post-processing method referring to existing described procedures (Wintermark et al., 2001).

Mean perfusion difference images were generated for each PLD. Both ASL-ATT and ASL-CBF perfusion maps were computed online. The ASL-ATT map was converted using the weighted delay method as previously described (Dai et al., 2012; Wang et al., 2014).

Pre-processing was performed using Data Processing and Analysis of Brain Imaging (DPABI_V2.3)[1], which is based on Statistical Parametric Mapping (SPM8)[2]. DPABI was developed in MATLAB 2013 (The MathWorks Inc., Natick, MA, United States). ASL-CBF, ASL-ATT, CTP-CBF, and CTP-MTT images were further normalized into the Montreal Neurological Institute template space using SPM8. Based on the registered 3D T1W images, the gray matter (GM) and white matter (WM) masks were extracted. ASL-CBF, ASL-ATT, CTP-CBF, and CTP-MTT images were segmented into GM and WM maps using the Segment program in SPM8.

Statistical Analysis

Voxel-wise analysis of the gray matter, white matter, and whole brain was conducted by DPABI: Pearson correlation coefficients were calculated across voxels between the two modalities in the gray matter, white matter and whole brain of each subject as previously described (Wang et al., 2014). Subgroup analyses based on age of patient and disease stage were performed to study the associations between ASL and CT perfusion.

TABLE 1 | clinical characteristics of patients at admission (*n* = 21).

Variable	Patients (*n* = 21)
Patient demographics	
Median age, years (range)	62 (37–84)
Male (n,%)	18 (86)
Female (n,%)	3 (14)
Disease stage	
Acute stage (n,%)	5 (24)
Subacute stage (n,%)	8 (38)
Chronic stage (n,%)	8 (38)
Laboratory test	
Blood pressure, mmHg	
Median systolic pressure (range)	143 (111–160)
Median diastolic pressure (range)	80 (68–107)
Hypertension (n,%)	15 (71)
Median fasting glucose, mmol/L (range)	4.97 (3.96–9.49)
Diabetes (n,%)	3 (14)
Median triglyceride, mmol/L (range)	1.64 (0.64–4.85)
Elevated triglyceride (≥1.70 mmol/L, n,%)	10 (48)

RESULTS

Clinical Characteristics of Enrolled Patients

In total, 21 patients [18 men and 3 women; median age, 62 years (age range, 37–84 years)] with confirmed ischemic stroke were enrolled in this study. Of 21 patients, fifteen (71.4%) had hypertension, 3 (14.3%) patients had diabetes, and 10 (47.6%) patients had elevated triglyceride levels (**Table 1**).

The Correlations Between Multi-Delay pCASL and CTP in Patients With Ischemic Stroke

The Pearson correlation coefficients of hemodynamic parameters between two modalities were obtained based on voxel levels in the gray matter, white matter, and whole brain (**Table 2**; all $P < 0.005$). Moderate to high positive associations between ASL-CBF and CTP-CBF were acquired in the gray matter, white matter and whole brain of the enrolled patients, and the mean Pearson correlation coefficients were 0.647, 0.585, and 0.646, respectively. Highly significant positive correlations between ASL-ATT and CTP-MTT were obtained in the gray matter, white matter and whole brain, and the mean Pearson correlation coefficients were 0.787, 0.707, and 0.799, respectively (**Table 3**). The box plots showed the same results (**Figure 2**).

Subgroup Analyses Based on Patient's Age and Disease Stage

We divided the ages into 30–49, 50–69, and over 70 for a subgroup analysis. The Pearson correlation coefficients exceed

---

[1] http://restfmri.net/forum/DPABI

[2] http://www.fil.ion.ucl.ac.uk/spm/

TABLE 2 | Pearson correlation coefficients between the two modalities in gray, white matter and whole brain of each subject.

	ASL-ATT vs. CTP-MTT			ASL-CBF vs. CTP-CBF		
Patient No.	**Gray matter**	**White matter**	**Whole brain**	**Gray matter**	**White matter**	**Whole brain**
P1	0.781*	0.695*	0.806*	0.604*	0.581*	0.589*
P2	0.803*	0.683*	0.793*	0.779*	0.714*	0.781*
P3	0.743*	0.617*	0.788*	0.730*	0.651*	0.736*
P4	0.757*	0.609*	0.750*	0.736*	0.721*	0.737*
P5	0.767*	0.710*	0.797*	0.600*	0.497*	0.601*
P6	0.783*	0.658*	0.801*	0.802*	0.671*	0.809*
P7	0.788*	0.674*	0.790*	0.569*	0.513*	0.566*
P8	0.792*	0.727*	0.787*	0.662*	0.616*	0.683*
P9	0.787*	0.699*	0.801*	0.612*	0.497*	0.597*
P10	0.825*	0.753*	0.812*	0.705*	0.641*	0.705*
P11	0.801*	0.723*	0.840*	0.718*	0.629*	0.719*
P12	0.754*	0.708*	0.818*	0.748*	0.711*	0.766*
P13	0.757*	0.666*	0.770*	0.475*	0.391*	0.493*
P14	0.742*	0.700*	0.703*	0.427*	0.459*	0.394*
P15	0.814*	0.797*	0.834*	0.574*	0.645*	0.569*
P16	0.799*	0.744*	0.811*	0.650*	0.655*	0.646*
P17	0.789*	0.691*	0.794*	0.522*	0.499*	0.518*
P18	0.834*	0.783*	0.846*	0.582*	0.539*	0.574*
P19	0.822*	0.741*	0.829*	0.637*	0.453*	0.623*
P20	0.790*	0.722*	0.800*	0.765*	0.674*	0.765*
P21	0.807*	0.739*	0.817*	0.697*	0.532*	0.689*

$P<0.005$.

TABLE 3 | Mean Pearson correlation coefficients between the two modalities in gray, white matter and whole brain of 21 patients.

	Gray matter	White matter	Whole brain
ASL-ATT vs. CTP-MTT	0.787 ± 0.026	0.707 ± 0.047	0.799 ± 0.032
ASL-CBF vs. CTP-CBF	0.647 ± 0.102	0.585 ± 0.097	0.646 ± 0.107

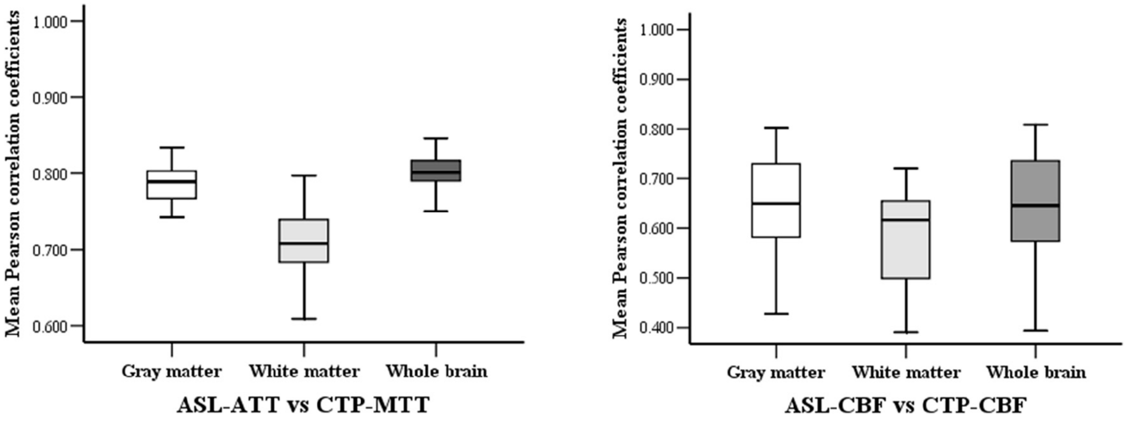

FIGURE 2 | The box-plots of mean Pearson correlation coefficients between the two modalities in gray, white matter and whole brain.

0.5 in each subgroup (**Table 4**). The results showed a moderate to high positive correlation of different age groups between the two modalities.

The comparison of patients at the acute phase, subacute phase, and chronic phase was conducted. The results exhibited a moderate to high correlation in different periods of ischemic stroke patients under the two modalities, indicating the little effect of disease stage.

Figure 3 shows a representative patient of ischemic stroke disease with ASL and CTP images. CTP shows hypoperfused

TABLE 4 | Mean Pearson correlation coefficients of different subgroups between the two modalities in gray, white matter and whole brain.

	ASL-ATT vs. CTP-MTT			ASL-CBF vs. CTP-CBF		
	Gray matter	**White matter**	**Whole brain**	**Gray matter**	**White matter**	**Whole brain**
Age (years)						
30–49 (*n* = 5)	0.799 ± 0.018	0.732 ± 0.041	0.811 ± 0.020	0.618 ± 0.033	0.558 ± 0.081	0.612 ± 0.044
50–69 (*n* = 9)	0.792 ± 0.030	0.716 ± 0.039	0.802 ± 0.041	0.659 ± 0.126	0.613 ± 0.092	0.657 ± 0.138
>70 (*n* = 7)	0.773 ± 0.023	0.677 ± 0.051	0.787 ± 0.217	0.653 ± 0.107	0.568 ± 0.117	0.655 ± 0.103
Disease stage						
Acute (*n* = 5)	0.788 ± 0.027	0.703 ± 0.066	0.799 ± 0.020	0.653 ± 0.106	0.625 ± 0.079	0.657 ± 0.111
Subacute (*n* = 8)	0.784 ± 0.025	0.699 ± 0.046	0.805 ± 0.026	0.701 ± 0.069	0.623 ± 0.081	0.702 ± 0.076
Chronic (*n* = 8)	0.790 ± 0.030	0.716 ± 0.039	0.794 ± 0.043	0.590 ± 0.105	0.523 ± 0.098	0.582 ± 0.109

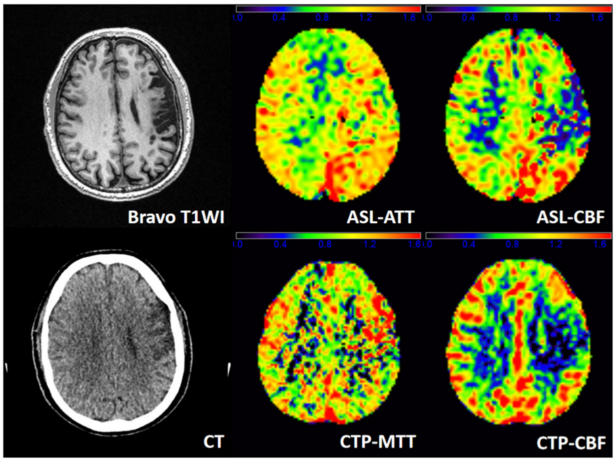

FIGURE 3 | A patient admitted to the hospital with weakness in the right upper limb for 1 day, and he had a history of ischemic stroke last year. T1WI demonstrates an obsolete infarct in the left frontal lobe. ASL-ATT, CTP-MTT, ASL-CBF, and CTP-CBF are normalized images and present consistent results. CTP shows hypoperfused regions in the left frontal lobe. CTP-CBF of the left frontal lobe is lower than the contralateral side, and ASL shows decreased ASL-CBF of the left frontal lobe. CTP-MTT is higher in the infarcted area but not in the surrounding regions, whereas the ASL-ATT is decreased (probably no signal) in the infarcted region and increased in the surrounding regions/territories (fitting with the atrophy patterns).

regions in the left frontal lobe. By visual appearance, ASL images present similar perfusion lesion as CTP. However, CTP-MTT is higher in the infarcted area, whereas the ASL-ATT is decreased (probably no signal) in the infarcted region and increased in the surrounding regions/territories (fitting with the atrophy patterns).

Figure 4 shows another representative case with ischemic stroke disease, and ASL images are in substantial agreement with the results of CTP. Besides, ASL-CBF shows focal intravascular signals and low tissue perfusion in the right frontal, temporal and occipital lobes, which may indicate the status of collateral perfusion.

ASL-CBF, ASL-ATT, CTP-CBF, and CTP-MTT images were segmented into gray matter maps in **Figure 5**. ASL shows hypoperfusion area of the left frontal, temporal and occipital lobes and basal ganglia. The ASL-CBF of the infarct regions decreases and the ASL-ATT increases compare to the contralateral side. CTP is in concordance with the result of ASL.

DISCUSSION

The correlations between pCASL and CT perfusion were analyzed in 21 patients with ischemic stroke in this study. Moderate to high positive associations between ASL-CBF and CTP-CBF were acquired in the gray matter, white matter, and whole brain of the enrolled patients. Wang et al. (2014) also found significant correlations between multi-delay pCASL and CTP in patients with moyamoya disease. CTP scan was initiated after injection of non-ionic iodinated contrast agent. The time concentration curves can be obtained by serially detecting the dynamic CT values of the interest regions (Konstas et al., 2009). In addition, a dynamic assessment of capillary level blood flow through different mathematical models was obtained. ASL adopts magnetically labeled arterial blood water as an endogenous tracer (Wu et al., 2007). When the labeled blood reaches the scanning level, it causes changes in the focal tissue magnetization vector and longitudinal relaxation time. Although the imaging mechanisms of the two modalities are different, they can both reflect blood perfusion of brain. Continuously dynamic scanning is necessary to calculate the CT perfusion parameters; therefore, the required radiation dose increases. Despite the application of low-dose CT scans, radiation damage is still inevitable. Multi-delay pCASL is non-radiative and non-invasive, and can be performed in patients with iodine contrast agent allergies, hyperthyroidism, and renal insufficiency.

The CBF and ATT maps were simultaneously derived using multi-delay pCASL protocol in this study. ATT refers to the time needed for the inverted spins to reach the acquisition region (Chen et al., 2012). The blood flow of ischemic stroke patients is slowed because of stenosis or the collateral pathway of the cerebral arteries, and the arterial transit time is prolonged (Lin et al., 2016). All patients enrolled in this study presented increased ATT in the infarct region, which can be used to detect focal cerebral ischemia. MacIntosh et al. (2010) adopted multi-delay pCASL in patients with acute ischemic stroke. They reported a representative patient with minor lacunar infarcts, and the patient showed obviously high signals on ATT images, which

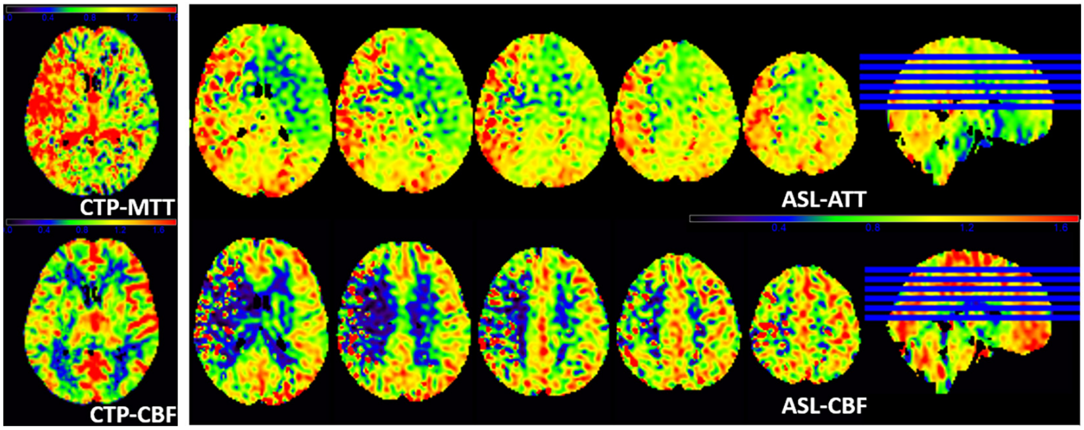

FIGURE 4 | A patient with left limb weakness for 9 days at admission. ASL-ATT, CTP-MTT, ASL-CBF, and CTP-CBF are normalized images and presented consistent results. CTP shows decreased CTP-CBF and increased CTP-MTT in the right frontal, temporal and occipital lobes; ASL shows decreased ASL-CBF and increased ASL-ATT of the right frontal, temporal and occipital lobes compare with the contralateral side. However, ASL-CBF shows focal intravascular signals and low tissue perfusion in the right frontal, temporal and occipital lobes, which may indicate the status of collateral perfusion.

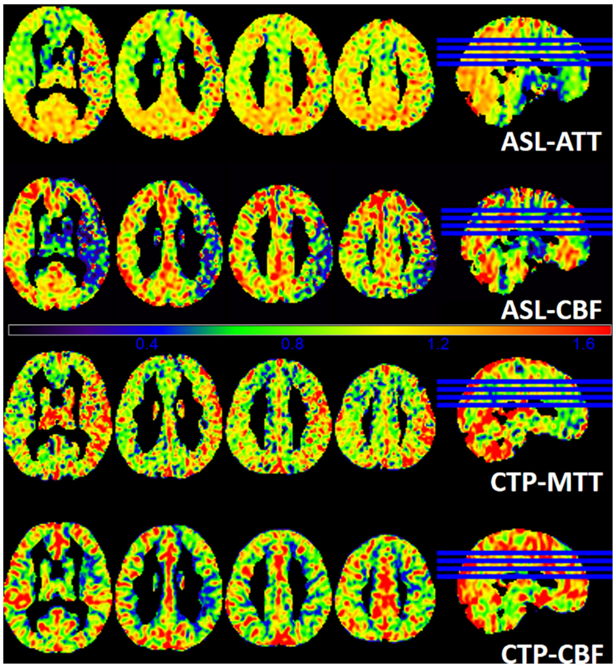

FIGURE 5 | A patient with 6 days of weakness in the right limb at admission. The images demonstrate the gray matter of ASL-ATT, ASL-CBF, CTP-MTT, and CTP-CBF. ASL shows hypoperfusion area of the left frontal, temporal and occipital lobes and basal ganglia. The ASL-CBF of the infarct regions decreases and the ASL-ATT increases compare to the contralateral side. CTP is in concordance with the result of ASL.

was consistent with our findings. Consequently, we suggest that the measurement of ATT helps to detect subtle ischemic lesions in patients with stroke.

In patients with ischemic stroke, ATT can be prolonged due to intracranial artery stenosis. PLD is defined as the interval time between blood labeling and image acquisition (van der Thiel et al., 2018). When the PLD is closer to the ATT, the CBF value is closer to the cerebral blood flow under physiological conditions. If the PLD cannot be adjusted in a timely manner, some of the labeled blood fails to reach the acquisition level due to delayed arrival, which may lead to underestimation of the perfusion (Ferré et al., 2013). The International Society for Magnetic Resonance in Medicine and the European Consortium ASL in Dementia recommends that the PLD of adults with cerebrovascular disease should be set to 2 s (Alsop et al., 2015). When patients have severe cerebrovascular stenosis, the ATT will be significantly prolonged because of flow deficits. Therefore, 2 s may still result in underestimation of the CBF. In recent years, a single PLD was generally employed in most ASL studies, and the delay time was usually between 1.5 and 2 s (Chen et al., 2018; Jezzard et al., 2018). In our study, a total of 6 PLDs between 1,000 and 3,500 ms were adopted to improve the accuracy of cerebral perfusion quantitative measurement in ischemic patients. However, the multi-delay pCASL also has some limitations. As the delay time increases, the scanning time will also increase, as will the possibility of motion artifacts. Therefore, this imaging protocol is suitable only for patients in a stable condition and with high levels of cooperation.

In our study, we found a patient that presented focal intravascular signals and low tissue perfusion in the infarct regions. Recent clinical evaluations of ASL in cerebrovascular disease have shown that focal intravascular signals and the delayed arterial transmission of tissue hypoperfusion may indicate the status of collateral perfusion (Chen et al., 2009; Zaharchuk, 2011; Lou et al., 2017). Therefore, we speculate that another potential ability of multi-delay pCASL could be evaluating collateral flow through dynamic perfusion images.

Evaluating cerebral perfusion plays an important role in determining treatment options for patients with ischemic stroke. Some patients also need regular follow-up brain perfusion examinations to assess the treatment efficacy and make timely adjustments. Up to present, few studies on multi-delay ASL have been reported (Wang et al., 2013). Compared with traditional single PLD ASL, multi-delay pCASL allows for non-invasive perfusion imaging and can provide more relevant clinical information. Besides, we have increased the comparison of patients at the acute phase, subacute phase, and chronic phase. The results showed a moderate to high correlation in different periods of ischemic stroke patients between ASL and CTP, indicating the little effect of disease stage. In addition, a moderate to high correlation of different age groups under the two modalities was obtained. Therefore, we speculated multi-pCASL could be used as an alternative imaging method for CTP.

In this study, a total of 3 female patients were included, far fewer than men. However, we calculated the correlation coefficients of each subject under the two modalities. The results of the three ischemic female patients were basically consistent with the overall trend. Multi-delay pCASL is non-radiative and non-invasive, and can be combined with other MRI sequences, such as anatomical imaging, vascular imaging, and diffusion weighted imaging; thus, more imaging information can be obtained during one examination.

There are some limitations in our study. First, only 21 patients were enrolled in this study, but presented a relatively representative cohort of patients with ischemic stroke. Second, gender bias should be excluded, as the female patients were far fewer than male patients. Despite we calculated the correlation coefficients of each subject under the two modalities, we will continue to include more female patients to verify this conclusion.

CONCLUSION

In conclusion, the present study showed moderate to high significant correlations between perfusion parameters from multi-delay pCASL and CTP imaging in patients with ischemic stroke. Due to the clinical feasibility and utility of multi-delay pCASL, it could potentially be used as part of a standard neuroimaging protocol for the management of ischemic stroke disease.

DATA AVAILABILITY STATEMENT

The raw data supporting the conclusions of this article will be made available by the authors, without undue reservation.

ETHICS STATEMENT

The studies involving human participants were reviewed and approved by the institutional review board of the First Affiliated Hospital of Jinan University. The patients/participants provided their written informed consent to participate in this study.

AUTHOR CONTRIBUTIONS

CS and LL designed the study. XX was a major contributor in writing the manuscript. ZT and MF contributed to collect the imaging and clinical data. XX, ZT, and MF performed data analysis and interpretation. MM, WF, JL, and ZX revised it critically for important content. All authors have read and approved the manuscript.

FUNDING

This work was supported by the Key Program of Natural Science Foundation of Guangdong Province of China (Grant No. 2018B0303110011), the Guangzhou Key Laboratory of Molecular and Functional Imaging for Clinical Translation (Grant No. 201905010003), and the Guangzhou External Science and Technology Cooperation Program (Grant No. 201807010046).

REFERENCES

Alsop, D. C., Detre, J. A., Golay, X., Günther, M., Hendrikse, J., Hernandez-Garcia, L., et al. (2015). Recommended implementation of arterial spin-labeled perfusion MRI for clinical applications: a consensus of the ISMRM perfusion study group and the European consortium for ASL in dementia. *Magn. Reson. Med.* 73, 102–116. doi: 10.1002/mrm.25197

Benjamin, E. J., Muntner, P., Alonso, A., Bittencourt, M. S., Callaway, C. W., Carson, A. P., et al. (2019). Heart disease and stroke statistics—2019 Update: a report from the American heart association. *Circulation* 139:e0056-28. doi: 10.1161/cir.0000000000000659

Chen, J., Licht, D. J., Smith, S. E., Agner, S. C., Mason, S., Wang, S., et al. (2009). Arterial spin labeling perfusion MRI in pediatric arterial ischemic stroke: initial experiences. *J. Magn. Reson. Imaging* 29, 282–290. doi: 10.1002/jmri.21641

Chen, Y., Wang, D. J., and Detre, J. A. (2012). Comparison of arterial transit times estimated using arterial spin labeling. *Magma* 25, 135–144. doi: 10.1007/s10334-011-0276-5

Chen, Z., Zhao, X., Zhang, X., Guo, R., Teeuwisse, W. M., Zhang, B., et al. (2018). Simultaneous measurement of brain perfusion and labeling efficiency in a single pseudo-continuous arterial spin labeling scan. *Magn. Reson. Med.* 79, 1922–1930. doi: 10.1002/mrm.26842

Dai, W., Robson, P. M., Shankaranarayanan, A., and Alsop, D. C. (2012). Reduced resolution transit delay prescan for quantitative continuous arterial spin labeling perfusion imaging. *Magn. Reson. Med.* 67, 1252–1265. doi: 10.1002/mrm.23103

Ferré, J. C., Bannier, E., Raoult, H., Mineur, G., Carsin-Nicol, B., and Gauvrit, J. Y. (2013). Arterial spin labeling (ASL) perfusion: techniques and clinical use. *Diagn. Interv. Imaging* 94, 1211–1223. doi: 10.1016/j.diii.2013.06.010

Jezzard, P., Chappell, M. A., and Okell, T. W. (2018). Arterial spin labeling for the measurement of cerebral perfusion and angiography. *J. Cereb. Blood Flow Metab.* 38, 603–626. doi: 10.1177/0271678X17743240

Konstas, A. A., Goldmakher, G. V., Lee, T. Y., and Lev, M. H. (2009). Theoretic basis and technical implementations of CT perfusion in acute ischemic stroke, part 1: theoretic basis. *Am. J. Neuroradiol.* 30, 662–668. doi: 10.3174/ajnr.A1487

Lin, L., Bivard, A., Krishnamurthy, V., Levi, C. R., and Parsons, M. W. (2016). Whole-brain CT perfusion to quantify acute ischemic penumbra and core. *Radiology* 279, 876–887. doi: 10.1148/radiol.2015150319

Lou, X., Yu, S., Scalzo, F., Starkman, S., Ali, L. K., Kim, D., et al. (2017). Multi-delay ASL can identify leptomeningeal collateral perfusion in endovascular therapy of ischemic stroke. *Oncotarget* 8, 2437–2443. doi: 10.18632/oncotarget.13898

MacIntosh, B. J., Lindsay, A. C., Kylintireas, I., Kuker, W., Günther, M., Robson, M. D., et al. (2010). Multiple inflow pulsed arterial spin-labeling reveals delays in the arterial arrival time in minor stroke and transient ischemic attack. *Am. J. Neuroradiol.* 31, 1892–1894. doi: 10.3174/ajnr.A2008

van der Thiel, M., Rodriguez, C., Giannakopoulos, P., Burke, M. X., Lebel, R. M., Gninenko, N., et al. (2018). Brain perfusion measurements using Multidelay arterial Spin-labeling are systematically biased by the number of delays. *Am. J. Neuroradiol.* 39, 1432–1438. doi: 10.3174/ajnr.A5717

Vilela, P., and Rowley, H. A. (2017). Brain ischemia: CT and MRI techniques in acute ischemic stroke. *Eur. J. Radiol.* 96, 162–172. doi: 10.1016/j.ejrad.2017.08.014

Wang, D. J., Alger, J. R., Qiao, J. X., Gunther, M., Pope, W. B., Saver, J. L., et al. (2013). Multi-delay multi-parametric arterial spin-labeled perfusion MRI in acute ischemic stroke - comparison with dynamic susceptibility contrast enhanced perfusion imaging. *Neuroimage Clin.* 3, 1–7. doi: 10.1016/j.nicl.2013.06.017

Wang, H., Naghavi, M., Allen, C., Barber, R. M., Bhutta, Z. A., Carter, A., et al. (2016). Global, regional, and national life expectancy, all-cause mortality, and cause-specific mortality for 249 causes of death, 1980–2015: a systematic analysis for the Global Burden of Disease Study 2015. *Lancet* 388, 1459–1544. doi: 10.1016/S0140-6736(16)31012-1

Wang, R., Yu, S., Alger, J. R., Zuo, Z., Chen, J., Wang, R., et al. (2014). Multi-delay arterial spin labeling perfusion MRI in moyamoya disease–comparison with CT perfusion imaging. *Eur. Radiol.* 24, 1135–1144. doi: 10.1007/s00330-014-3098-9

Wintermark, M., Maeder, P., Thiran, J. P., Schnyder, P., and Meuli, R. (2001). Quantitative assessment of regional cerebral blood flows by perfusion CT studies at low injection rates: a critical review of the underlying theoretical models. *Eur. Radiol.* 11, 1220–1230. doi: 10.1007/s003300000707

Wintermark, M., Sesay, M., Barbier, E., Borbély, K., Dillon, W. P., Eastwood, J. D., et al. (2005). Comparative overview of brain perfusion imaging techniques. *Stroke* 36, e83–e99. doi: 10.1161/01.STR.0000177884.72657.8b

Wu, W. C., Fernández-Seara, M., Detre, J. A., Wehrli, F. W., and Wang, J. (2007). A theoretical and experimental investigation of the tagging efficiency of pseudocontinuous arterial spin labeling. *Magn. Reson. Med.* 58, 1020–1027. doi: 10.1002/mrm.21403

Xu, P., Liu, X., Zhang, H., Ghista, D., Zhang, D., Shi, C., et al. (2018). Assessment of boundary conditions for CFD simulation in human. *Biomech. Model. Mechanobiol.* 17, 1581–1597. doi: 10.1007/s10237-018-1045-4

Zaharchuk, G. (2011). Arterial spin label imaging of acute ischemic stroke and transient ischemic attack. *Neuroimag. Clin. N. Am.* 21, 285–301. doi: 10.1016/j.nic.2011.01.003

Zhang, H., Gao, Z., Xu, L., Yu, X., Wong, K., Liu, H., et al. (2018). A meshfree representation for cardiac medical image computing. *IEEE J. Transl. Eng. Health Med.* 6:1800212. doi: 10.1109/JTEHM.2018.2795022

Conflict of Interest: The authors declare that the research was conducted in the absence of any commercial or financial relationships that could be construed as a potential conflict of interest.

Advantages of publishing in Frontiers

OPEN ACCESS
Articles are free to read
for greatest visibility
and readership

FAST PUBLICATION
Around 90 days
from submission
to decision

HIGH QUALITY PEER-REVIEW
Rigorous, collaborative,
and constructive
peer-review

TRANSPARENT PEER-REVIEW
Editors and reviewers
acknowledged by name
on published articles

Frontiers
Avenue du Tribunal-Fédéral 34
1005 Lausanne | Switzerland

Visit us: www.frontiersin.org
Contact us: frontiersin.org/about/contact

REPRODUCIBILITY OF RESEARCH
Support open data
and methods to enhance
research reproducibility

DIGITAL PUBLISHING
Articles designed
for optimal readership
across devices

FOLLOW US
@frontiersin

IMPACT METRICS
Advanced article metrics
track visibility across
digital media

EXTENSIVE PROMOTION
Marketing
and promotion
of impactful research

LOOP RESEARCH NETWORK
Our network
increases your
article's readership